On Mesh-free Method for Singularly Perturbed Problems

A

Thesis submitted in partial fulfillment

of the requirements for the award of the degree of

DOCTOR OF PHILOSOPHY

in

School of Mathematics

By

Jagbir Kaur

Reg. No. 901611005

Under the Supervision

of

Dr. Vivek Sangwan

(Assistant Professor)

THAPAR INSTITUTE

OF ENGINEERING & TECHNOLOGY

(Deemed to be University)

SCHOOL OF MATHEMATICS

THAPAR INSTITUTE OF ENGINEERING & TECHNOLOGY

PATIALA - 147004, PUNJAB, INDIA

March, 2023

Certificate

I hereby certify that the work which is being presented in the thesis, entitled **"On Mesh-free Method for Singularly Perturbed Problems"** in partial fulfillment of the requirements for the award of degree of **Doctor of Philosophy** and submitted in School of Mathematics, Thapar Institute of Engineering and Technology, Patiala is an authentic record of my own work carried out during the period **July, 2016** to **March, 2023** under the supervision of **Dr. Vivek Sangwan**, Assistant Professor, School of Mathematics, Thapar Institute of Engineering and Technology, Patiala.

Date : 03-08-23

Jagbir Kaur
(Reg. No. 901611005)

This is to certify that the above statement made by the candidate is correct and true to the best of my knowledge.

Date : 03-08-2023

Dr. Vivek Sangwan
(Supervisor)

Acknowledgement

I begin with the name of God, the creator of the universe, who bestowed his blessing on me in completing this thesis.

I would like to express my sincere gratitude to my research supervisor **Dr. Vivek Sangwan**, Assistant Professor, School of Mathematics, Thapar Institute of Engineering and technology (T.I.E.T.), Patiala, for the continuous support of my Ph.D. study and related research, for his cooperation, motivation, enthusiasm and immense knowledge. It has been an honour to be his Ph.D. student. I appreciate all his contributions of time and ideas to make my Ph.D. experience productive and stimulating. I appreciate his vast knowledge and skill in many research areas. His joy and enthusiasm for his research were contagious and motivational for me, even during challenging times in the Ph.D. pursuit. On a personal level, he always inspired me with his positive and passionate attitude. I could not have imagined having a better advisor and mentor for my Ph.D. study. This thesis would not happen to be possible without the ardent support and care he provided me academically and personally. His advice on both research as well as on my career has been invaluable. I would also thank him for letting me evolve as a better human being.

I am thankful to **Dr. Rafat Siddique** (Dean, Research and Development Cell) and **Dr. Mahesh Kumar Sharma** (Head of the Department) for providing me with the necessary facilities for the smooth completion of my Ph.D. I sincerely thank my dissertation committee members **Dr. Paramjeet Singh**, **Dr. Satish Kumar** and **Dr. Ajay Kumar**, for their insightful comments and encouragement, but also for the tricky question which incented me to widen my research from various perspectives. A special thanks to **Dr. Harish Garg**, Associate Professor, T.I.E.T., Patiala. He has been a great source of knowledge and inspiration. Thank you for always being so helpful and making my Ph.D. journey smooth.

It gives me great pleasure to acknowledge the valuable advise and remarks from **Dr. Arvind Kumar Lal**, Professor, T.I.E.T., Patiala, former Head of the Department. Their support and sincere attitude towards the department have always been encouraging and helped me pave my way for the dissertation. I express my gratitude to all the faculty members and staff of the School of Mathematics, T.I.E.T. Patiala, for their support.

I would like to thank anonymous reviewers and editors of our papers for their valuable and enriching suggestions.

I am heartfelt to my closest friends Ashish Goyal, Sukhveer Singh, Jaspreet Kaur, Madhu Aneja, Richa Goyal, and Nikita Madaan for the stimulating discussions, for the times we worked together before deadlines, and for all the moments we had fun together. I greatly value their friendship and sincerely appreciate their belief in me. I share the credit of my work with my friends Arshdeep Kaur, Prabhsimrat, Navjot Kaur, Nishtha, Prashu, Watanjeet Singh, Gagandeep Kaur, Kamal Kumar, Shahid Batt, Manpreet Kaur, Vivek Dingra, Shweta Sinha, Harmanjit Kaur. I cannot write the name of each of my friends, but I would like to thank all my friends, I feel blessed to have all of you in my life.

I owe my gratitude to my family, who have supported me spiritually throughout the entire process by keeping me harmonious and helping me put pieces together. Without their support and endless blessings, I would be unable to complete my education seamlessly. Without them, I would not be the person I am today. Words can not express how grateful I am to my mother **Paramjit Kaur** and my father **Parambir Singh** for all of the sacrifices you have made on my behalf. My special thanks go to my husband **Lovedeep Singh** for believing in me. I owe thanks to him for his continuous support, assistance and understanding when undertaking my research and writing my project. Your prayer for me was what sustained me this far. I wish to extend my sincere appreciation to my father-in-law **Maninder Singh** and mother-in-law **Manjeet Kaur** for his constant encouragement and wise counsel, which helped me to overcome many challenges. I would also like to express my respect and love to my sister, **Amarbir Kaur**, my brother, **Joban Singh**, my brother-in-laws, **Neerajpal Singh** and **Harjinder Singh**, my sister-in-laws, **Chanpreet Kaur** and **Navdeep Kaur** for their unfailing support, unconditional love and continuous encouragement throughout the process of researching and writing this thesis. I truly appreciate everything you have done for me during my time in Patiala, especially for the comfort and respite you have provided me during these hectic times. This accomplishment would not have been possible without them. I also would like to thank my little angels, **Kudrat Kaur** and **Kirat Kaur** for showing her love and affection and relaxing my mind during the hard times of my thesis.

Jagbir Kaur

Abstract

In the present thesis, an attempt has been made to demonstrate some robust and efficient mesh-free techniques for approximating the solutions of singularly perturbed problems. It is observed that the proposed mesh-free method are more efficient than the conventional methods and are, at the same time, conceptually simple. We consider one and two-dimensional singularly perturbed problems commonly arise in the field of science and engineering. Besides it, a well-developed theory for their convergence and error estimates has also been proved. Numerical experiments have been carried out extensively to support the theoretical results. The research work started with the following three objectives:

- To propose and implement a mesh-free method for solving linear/non-linear singularly perturbed problems in one dimension.
- To implement the proposed mesh-free method for solving the higher dimensional singularly perturbed problem.
- To implement the proposed mesh-free method for solving a real-life problem.

To accomplish these objectives, the research work has been carried out and organized in form of Chapters. The thesis is categorized into seven Chapters. A brief overview of the Chapters is given below:
In **Chapter 1** of the proposed thesis work focuses on singularly perturbed differential equations and their importance in various fields. It provides an introduction to basic definitions and notations related to singularly perturbed problems (SPP), highlighting their significance in real-world applications. The Chapter emphasizes on the need for efficient and accurate methods for solving SPP, and reviews various analytic and numerical techniques proposed in this regard. The discussion also includes a summary of mesh-free schemes and their developments, highlighting their advantages and limitations. The presented literature survey on this topic has led to the identification of gaps in the existing approaches which motivates for the objectives of the Ph.D. thesis. Overall, Chapter 1 lays the foundation for the subsequent Chapters by providing a clear and concise overview of the problem domain.

Chapter 2 deals with one-dimensional singularly perturbed linear and non-linear elliptic differential equations. Singularly perturbed problems have solutions that exhibit sharp boundary layers, which makes them difficult to solve using traditional numerical methods. This Chapter discusses the element-free Galerkin (EFG) methodology for solving the SPP. Due to the absence of element connectivity, the EFG method's main feature lies in its

ability to add or delete node particles without much difficulty. This feature makes the method more adaptable than other conventional numerical techniques. The EFG method uses moving least-square (MLS) approximation to generate shape functions. The impact of different weight functions on the accuracy of the method has been discussed. The methodology is based on the global weak form, and the numerical integrations are computed using background cells created by the Gauss quadrature formula. Since the MLS shape functions do not satisfy the Kronecker delta function property, the boundary conditions can not be implemented directly. Therefore, Lagrange multipliers approach has been used to impose the essential boundary constraints. The quasilinearization technique has been adopted for handling the nonlinearity present in the considered problems and its rate of convergence has also been derived. Shishkin's approach has been utilized to generate more nodes in the boundary layer region and to capture these layers sharply. The EFG method's robustness is verified through various numerical examples and $L_\infty-$errors have been presented. Comparisons of solutions have been made with those available in the literature.

Chapter 3 of the thesis focuses on the numerical analyzation of the time-dependent singularly perturbed parabolic reaction-diffusion equation. To accomplish this, the authors utilized the element-free Galerkin (EFG) method for spatial discretization in conjunction with the implicit Crank-Nicolson scheme for temporal discretization. Due to the steep boundary layers in the solution to the problem, the authors employ a piecewise uniform layer-adapted Shishkin's technique to generate more dense node points near the boundary layer region. Stability and a posteriori errors of the proposed method have been analyzed using L_2-norm. The ϵ-uniform convergence of the full-discrete scheme is shown to be $\mathcal{O}(\tau^2+\mathfrak{d}_\mathfrak{s}{}^m)$, where τ represents the time step size and $\mathfrak{d}_\mathfrak{s}$ represents the size of the influence domain. Some numerical experiments have been conducted to validate the theoretical results and to verify the computational consistency and robustness of the proposed scheme. The numerical order of convergence has also been presented.

Chapter 4 is dedicated to demonstrate the application of the proposed method for solving real-life problems. In particular, the study focuses on a realistic model that displays the phenomenon of traveling wave propagation. The time-dependent singularly perturbed Fisher's problem, represented by the below given equations, has been used as the model problem for analysis:

$$u_t(x,t) = \epsilon\nabla^2 u(x,t) + \beta u(x,t)(1-u(x,t)), \quad (x,t) \in \Omega \equiv \Omega_x \times \Omega_t \equiv (0,1)\times(0,T],$$

with initial condition

$$u(x,0) = u_0(x), \ x \in \bar{\Omega}_x,$$

and boundary conditions as

$$u(0,t) = f(t), \quad u(1,t) = g(t), \ t \in \bar{\Omega}_t,$$

where $u(x,t)$ symbolizes the occurrence of traveling waves. Implicit Crank-Nicolson technique has been employed for temporal semi-discretization. Spatial discretization has been carried out using mesh-free element-free Galerkin scheme. The authors analyzed the stability of the semi-discrete scheme. The non-linear terms has been tackled by using the quasilinearization process. The convergence analysis of the quasilinearization process and the full discrete scheme has also been discussed. Numerical experiments have been performed to validate the theoretical findings and to show the robustness of the proposed scheme. The numerical results demonstrate the efficiency and accuracy of the proposed method in solving the time-dependent singularly perturbed Fisher's problem.

Chapter 5, a more generalized version of the Fisher's model problem, i.e. Burger-Fisher's problem, has been considered to check the robustness of the proposed EFG method. The considered Burger-Fisher's model problem is given by

$$\frac{\partial u}{\partial t} - \gamma \frac{\partial u^2}{\partial^2 x} + \alpha u^{\delta} \frac{\partial u}{\partial x} = F(u), \ (x,t) \in \Omega \equiv \Omega_x \times \Omega_t \equiv (0,1) \times (0,T],$$

$$\begin{aligned} u(x,0) &= u_0(x), \ x \in \bar{\Omega}_x, \\ u(0,t) &= f(t), \quad u(1,t) = g(t), \ t \in \bar{\Omega}_t. \end{aligned}$$

Mesh-free EFG method along with Crank-Nicolson scheme has been proposed to analyze the realistic model problem which generally arises in the biological field. The shape functions are generated using the moving least-square (MLS) approximation and the Lagrange multiplier method has been invoked to implement the essential boundary conditions. The existence and uniqueness of the EFG solution has been presented. Stability and uniform convergence of the proposed scheme for the non-linear model problem has also been presented for fixed value of singular perturbation parameter. Numerical results have been presented which depicts the efficiency of the scheme.

In **Chapter 6**, the proposed scheme has been extended to solve the two-dimensional time-dependent non-linear singularly perturbed reaction-diffusion initial-boundary value problem. The temporal and spatial discretizations have been carried out using the Crank-Nicolson and element-free Galerkin scheme respectively. Again the MLS approach has been invoked to generate the basis functions. To impose the boundary conditions, Lagrange multiplier method has been utilized. Stability of the time semi-discrete problem has been

analyzed. Uniform convergence of the proposed scheme has been shown in the L_2- norm. Numerical results have been presented to validate the efficiency of the method.

In **Chapter 7**, we have investigated a real-life application of a two-dimensional singularly perturbed parabolic equation in the context of finance. Specifically, the Black-Scholes (B-S) model has been considered, commonly used for option pricing and based on the principle of hedging to eliminate risks associated with underlying assets and stock options. The two-dimensional Black-Scholes (B-S) equation for a European call option pricing is given by:

$$\frac{\partial C}{\partial t}(S_1,S_2,t)+\frac{1}{2}\sigma_1^2S_1^2\frac{\partial^2 C}{\partial S_1^2}(S_1,S_2,t)+2\rho\sigma_1\sigma_2S_1S_2\frac{\partial^2 C}{\partial S_1\partial S_2}(S_1,S_2,t)+\frac{1}{2}\sigma_2^2S_2^2\frac{\partial^2 C}{\partial S_2^2}(S_1,S_2,t)$$
$$+r\Big[S_1\frac{\partial C}{\partial S_1}(S_1,S_2,t)+S_2\frac{\partial C}{\partial S_2}(S_1,S_2,t)\Big]-rC(S_1,S_2,t)=0,$$
$$(S_1,S_2,t)\in(0,\infty)\times(0,\infty)\times(0,T),$$

with initial condition

$$C(S_1,S_2,0)=S_2\max(S_1-E,0),\quad (S_1,S_2)\in(0,\infty)\times(0,\infty)$$

and terminal conditions

$$C(0,S_2,t)=0=C(S_1,0,t),\quad t\in[0,T]$$

where $C(S_1,S_2,t)$ denotes the value of a call option with underlying asset prices $S_1,\ S_2$ at time $'t'$. Here, $'\sigma_1'$ and $'\sigma_2'$ are the volatility rates of the underlying assets S_1 and S_2, respectively. $'r'$ is the risk-free interest rate, $'\rho'$ is correlation value between S_1, S_2 and E is the strike or exercise price.
A dimensionless interpretation of the two-dimensional B-S equation has been demonstrated by using linear transformations. The above model has been reformulated into initial-value singularly perturbed parabolic problem as follows:

$$LU(x,y,\tau)\equiv\left\{-\frac{\partial}{\partial\tau}+\epsilon_1\frac{\partial^2}{\partial x^2}+\epsilon_2\frac{\partial^2}{\partial y^2}-1\right\}U(x,y,\tau)=0.$$

Here, $\epsilon_1=\frac{\sigma_1^2}{2r},\ \ \epsilon_2=\frac{\sigma_2^2}{2r}$ are dimensionless perturbation parameters, $\epsilon_1,\epsilon_2\in(0,1]$.
The numerical treatment of the deemed problem has been accomplished by adopting the element-free Galerkin (EFG) approach. The proposed mesh-free scheme is novel for the singularly perturbed B-S equation for $0<\epsilon_1,\epsilon_2<<1$. An implicit Crank-Nicolson scheme has been used to discretize temporal variable. Error analysis of the scheme reveals an order

of convergence $\mathcal{O}(\tau^2+\mathfrak{d}_{\mathfrak{s}}{}^m)$, where τ and $\mathfrak{d}_{\mathfrak{s}}{}^m$ are the time step size and size of the influence domain, respectively. Numerical experiments verify the theoretical and computational consistency of the proposed scheme, and $L_\infty-$errors of solutions with sharp boundary layers are presented.

Conclusion of the thesis has been presented in the last followed by bibliography.

List of Publications

Published Papers

1. J. Kaur and V. Sangwan, *Exponentially fitted element-free Galerkin approach for nonlinear singularly perturbed problems*, Journal of Mathematics, 2021,
   doi:10.1155/2021/4165954 (**SCIE, Impact Factor: 1.555**).

2. J. Kaur and V. Sangwan, *Stability estimates for singularly perturbed Fisher's equation using element-free Galerkin algorithm*, AIMS Mathematics, Vol. 7(10), pp. 19105–19125, 2022,
   doi:10.3934/math.20221049 (**SCIE, Impact Factor: 2.739**).

3. J. Kaur and V. Sangwan, *An Adaptive Element-Free Galerkin Approach for Solving Singularly Perturbed Boundary Layer Problems*, Journal of Applied and Industrial Mathematics, Vol. 16(2), pp. 211–226, 2022,
   doi:10.1134/S1990478922020041 (**SCOPUS**).

Communicated Papers

1. J. Kaur and V. Sangwan, *A robust mesh-free technique for numerical analysis of two dimensional Singularly Perturbed Black-Scholes equation governing European option pricing.*

2. J. Kaur and V. Sangwan, *Numerical convergence of nonlinear parabolic singularly perturbed reaction-diffusion problems using element-free Galerkin method.*

3. J. Kaur and V. Sangwan, *A numerical analysis of generalized Burgers-Fisher equation using a robust element-free Galerkin techniques.*

4. J. Kaur and V. Sangwan, *Error analysis of robust element-free Galerkin method for solving two-dimensional parabolic singularly perturbed problems.*

5. J. Kaur and V. Sangwan, *Convergence analysis of singularly perturbed Fisher's model governing traveling wave phenomenon using Element-free Galerkin technique.*

6. J. Kaur and V. Sangwan, *A comprehensive study of recent advances in Element-free Galerkin method for solving PDEs and its applications.*

List of Figures

List of Tables

Contents

Chapter 1

Introduction

The environment around us is continually changing, such as plant growth, stock market fluctuations, population expansion, temperature changes, the value of the money in bank accounts, the strength of an electric field, physical forces acting on an object, etc. All these changes depend upon some factors like time, climate, the position of an object etc. These rates of change can be described mathematically by derivatives. Any relation between these derivatives and their functions or physical quantities can be described as a differential equation. Differential equations have a remarkable ability to anticipate the world around us, including the transmission of illnesses through a population, the exponential development and decay of species, and changes in investment return over time, to mention some examples. Hence the differential equations are used in a wide variety of disciplines like biology, physics, chemistry, engineering, stock markets, business, statistics etc. Due to the advanced development of science and technology, the governing differential equations modeling physical phenomenon are becoming more and more complex. One such problem that usually occurs in fluid and gas dynamics is a boundary layer problem.

1.1 Singularly perturbed problems

The mathematical representation of boundary layers is the presence of a small parameter, ϵ, called the singular perturbation parameter, multiplying with the coefficients of some or all the terms involving highest order derivatives in the differential equations. In the limiting case, when this singular

perturbation parameter ϵ approaches zero, then, in general, all the boundary conditions are not satisfied and hence, a boundary layer appears in the solution, and the problem is said to be singularly perturbed.

Geometrically, a boundary layer is defined to be a region of rapid change in the solution near the endpoints. The concept of boundary layer theory was first introduced by Ludwig Prandtl [176], a 29-year-old professor at the Technische University in Hanover, on August 12, 1904, at the Third International Congress of Mathematicians in Heidelberg, Germany, where he presented his paper entitled "On Fluid Motion with small Friction". Prandtl's presentation was only ten minutes long. His seven-pages paper described a new concept of fluid dynamics called boundary layer theory. The presence of boundary layers in fluid and gas dynamics was unknown before the early twentieth century.

The term "Singular Perturbation" was coined by Friedrichs and Wasow [78] at New York University in 1946 in a seminar on non-linear vibrations. Their work was motivated by analysing the edge effect for buckled plates. Levinson [129] began the study of a wide spectrum of important topics using asymptotic analysis and made definitive contributions to singular perturbations. In 1961, Friedrichs and Erdelyi [65] evolved an asymptotic matching of the inner and outer expansions at the edge of the boundary layer. In 1965, Wasow's [223] book placed singular perturbations in the context of the analytic theory of differential equations. By 1970, courses on perturbation methods became common in engineering and applied mathematics departments. Bender and Orszag [165], in 1978, emphasized more general asymptotic techniques for ordinary differential equations. Much of the work on singular perturbation partial differential equations started appearing in the late 1980s. Nayfeh [161] made the elementary concepts of singular and regular perturbation theory as a part of the undergraduate study for most scientists and engineers.

1.2 Significance of singularly perturbed problems

One of the primary motivations for studying singularly perturbed differential equations is that the partial differential equations that occur in the field of hydrodynamics are typically singularly perturbed. The singularly perturbed nature of differential equations becomes apparent when the magnitude of convection terms is much larger than diffusion terms. Such differential equations arise in various fields of applied mathematics, fluid dynamics, quantum mechanics, aerodynamics, plasma dynamics, reaction-diffusion processes, oceanography and other domains of fluid motion. Some of the standard singular perturbation models arising in various areas have been mentioned below:

Singularly perturbed Kolmogorov-Fokker-Planck model

Khasminskii and Yin [113] derived asymptotic expansions for solutions of singularly perturbed Kolmogorov-Fokker-Planck equation having two time scales. The equation is given by

$$\epsilon\frac{\partial p^{\epsilon}}{\partial t}(s,x,t,y)+\frac{\partial(b(t,y)p^{\epsilon})}{\partial y}(s,x,t,y)-\frac{1}{2}\frac{\partial^2(a(t,y)p^{\epsilon})}{\partial y^2}(s,x,t,y)=0,\quad t>s$$
$$\text{with}\quad \lim_{t\to s+0}p^{\epsilon}(s,x,t,y)=\delta(x-y),$$

where $p^{\epsilon}(s,x,t,y)$ denotes the transition density, $\epsilon>0$ is a small parameter, $b(t,x)$ and $a(t,x)$ represents the drift and diffusion coefficient, respectively. The asymptotic expansion of carried out explicitly and showed that the initial layer term decays at an exponential rate. This study has a broad spectrum of applications in manufacturing systems, queueing networks, statistical physics, population biology, financial economics, and many other related fields.

Predator-Prey model for interacting populations

Dunbar [63] presented the singularly perturbed predator-prey model produced by modifying the Lotka-Volterra equations, including predator satiation effect, is demonstrated in the following system of equations:

$$u_t = \delta_1 u_{xx} + Au(1 - u/K) - B\frac{uw}{1 + Eu},$$
$$w_t = \delta_2 w_{xx} - Cw + D\frac{uw}{1 + Eu}.$$

The functions $u(t, x)$, and $w(t, x)$ are the densities of the prey and predator, respectively. Here, δ_1 and δ_2 are the diffusion coefficients, A is a growth factor for the prey species, C is a death rate for the predator in the absence of prey, K is the carrying capacity of the prey species, B and D are the interactions rates for the two species. The parameter E measures the satiation effect, which is prey consumption by a unit number of predators. The author considered $\delta = 0$, i.e. situation in which the prey species diffuses much more slowly than the predator species. The existence of periodic traveling wave solutions in heteroclinic orbits of the considered model has been discussed and showed that "chaotic" orbits could not exist in $\mathbb{R}^3$.

Biological model for wound healing assay

Maini et al. [147] suggested extension of Fishers equation in the medical context in which cell propagation for wound healing was modeled by Fickian diffusion has been discussed. The model is given by

$$\frac{\partial n}{\partial t} = D\frac{\partial^2 n}{\partial x^2} + rn(N - n),$$

where $n(x, t)$ represents cell number density at position x and at time t, rN denotes linear growth of cells, D is the diffusion coefficient and N is the carrying capacity. The authors discussed the migration of healing wound

assay which exhibits constant speed $\nu = 2\sqrt{(rND)}$ traveling waves.

Semiconductor device modeling

Roosbroeck [184] was developed the basic model for electric current through a semiconductor in terms of the electric potential ϕ as

$$\begin{aligned} \epsilon\nabla^2\phi &= q(n - p - D), \\ -q\frac{\partial n}{\partial t} + \nabla.J_n &= qR, \\ q\frac{\partial p}{\partial t} + \nabla.J_p &= -qR, \end{aligned}$$

Here, n is an electron, and p is the hole density of negative and positive charges. ϵ symbolizes permittivity of the material, q is the unit charge, D denotes the doping concentration in the background, and R is a recombination term. The combination of J_n and J_p currents give the drift-diffusion model of the form

$$J_n = q\mu_n(U_t\nabla n - n\nabla\phi),$$

where μ_n is the electron mobility, a potential internal barrier is represented by U_t.

Air pollution

The Chernobyl disaster brought international attention to the modeling of atmospheric pollution. Pudykiewicz [178] demonstrated the importance of employing a full three-dimensional model of the following modestly simplified form for a group of radioactive tracers of specified activity A^i,

$$\frac{\partial A^i}{\partial t} + V_H.\nabla_H A^i + \frac{\partial}{\partial\sigma}(\nu_\sigma^i A^i) = \frac{\partial}{\partial\sigma}(K_z\frac{\partial}{\partial\sigma}A^i) + S^i.$$

In this case, a terrain-following vertical coordinate σ is utilized, with V_H representing an average horizontal wind vector in the σ system and ∇_H denoting thegradient operator. The various sources and sinks are gathered in S^i, which includes a matrix of coefficients characterizing the radioactive decay and transformation of all the isotopes in the model, K_z is a vertical diffusion coefficient which varies with height, and V_σ^i is made up of the vertical motion in the σ system and the gravitational settling velocity. Wind velocity and other atmospheric parameters were determined using standard meteorological forecast data.

Moreover, the horizontal and vertical scales used here are significantly different. Horizontal length scales are generally thousands of kilometers, with velocities of 10 m/s, resulting in a Reynolds number in the $10^{11}10^{12}$ range. However, the length scale and velocity are much smaller in the vertical direction. The turbulent diffusion coefficient is much larger: in the atmospheric boundary layer, K_z maybe 10^3 m^2/s, giving a $Pclet$ number around 10^2, and in the free atmosphere, where K_z is typical 10 m^2/s, the $Pclet$ number would be around 10.

Navier-Stokes model for nozzle flow

The following equation represents a shock wave in a one-dimensional nozzle flow. The steady state Navier-Stokes equation give

$$\epsilon A(x)uu'' - [1 + \frac{\gamma}{2} - \epsilon A'(x)]uu'' + \frac{u'}{u} + \frac{A'(x)}{A(x)}(1 - \frac{\gamma - 1}{2}u^2) = 0 \ ; \ 0 < x < 1,$$

where x is the normalized downstream distance from the throat, u is a normalized velocity, $A(x)$ is the area of the nozzle at x and ϵ is essentially the inverse Reynolds number, e.g. $\epsilon = 4.792 \times 10^{-8}$. The boundary conditions are

$$u(0) = 0.9129, \ u(1) = 0.375.$$

For this BVP, an $O(\sqrt{\epsilon})$-wide shock develops whose location depends on ϵ.

Black-Scholes model for European option pricing problems

The Black-Scholes (B-S) equation is well-known for demonstrating option pricing theory, which generally occurs in the model of the financial world. As a result, it has become an extensive elementary subject for studying financial engineering and financial theory. In 1973, Black and Scholes [26] published the B-S model and option pricing formula in their paper to analyze the behavior of financial derivatives in the market. The B-S model is based on the principle of hedging and focus on eliminating risks associated with the volatility of underlying assets and stock option. The generalized B-S equation governing European call option $C(S,t)$ at asset price S at time t is given as

$$\frac{\partial C(S,t)}{\partial t} + \frac{1}{2}\sigma^2(S,t)S^2\frac{\partial^2 C(S,t)}{\partial S^2} + r(S,t)S\frac{\partial C(S,t)}{\partial S} - r(S,t)C = 0, \quad (S,t) \in \mathbb{R}^+ \times (0,T), \tag{1.2.1}$$

equipped with the terminal and boundary conditions

$$C(S,0) = max(S-E,0), \quad S \in \mathbb{R}^+, \tag{1.2.2}$$

$$C(0,t) = 0; \quad C(S,t) \sim S \text{ for } S \to \infty^+, \quad t \in [0,T], \tag{1.2.3}$$

where $\sigma(S,t) > 0$ denotes the volatility function of underlying asset; T, the maturity time; E, symbolizes the exercise price and $r(S,t) > 0$ is the risk-free interest rate.

Groundwater flow and solute transport

The passage of water and solutes across the unsaturated zone has a vital role in conventional applications of groundwater hydrology, soil physics, and agronomy. The modeling of water flow through a liquid phase in unsaturated porous media , in one dimension, can be stated by a combination of Darcys law and the equation of continuity given as

$$\frac{\partial}{\partial t}c(x,t) = D\frac{\partial^2}{\partial x^2}c(x,t) - v\frac{\partial}{\partial x}c(x,t) - \lambda c(x,t), \quad x > 0, \quad t > 0, \tag{1.2.4}$$

where x denotes the distance, which is zero at the soil center and computed positive towards the right side of the soil center, herein, $c(x,t)$ is the solute density at time t; D represents diffusivity of soil water, v is velocity and k signifies the decay coefficient.

The mathematical modeling for unknown coefficient $c(x,t)$ is represented by defining dimensionless variables as

$$\bar{t} = \frac{t}{\lambda^{-1}}, \quad \overline{x} = \frac{x}{v/\lambda}, \quad \overline{c} = \frac{c}{c_0}. \tag{1.2.5}$$

The equation (1.2.5) is known as the solute transport equation. Now, reformulate the above equation (1.2.4) using these scaled variables, we get

$$\frac{\partial}{\partial t}c(x,t) = \epsilon\frac{\partial^2}{\partial x^2}c(x,t) - v\frac{\partial}{\partial x}c(x,t) - \lambda c(x,t), \quad x > 0, \quad t > 0,$$

where $\epsilon = \frac{\lambda D}{v^2}$ is singular perturbation parameter and $\epsilon \ll 1$. Bear and Verruijt discussed various ground water transport models in [17].

Though we have mentioned some singular perturbed models, but many more singular perturbed models can be found out arising in various different fields. Thus, we can say that singularly perturbed problems (SPP) plays an important role in our day to day life and hence, it becomes a necessity to develop more and more stable and robust numerical methods for solving SPP.

1.3 Solution methodology

The solution of SPP typically contains boundary layers. Prandtl began the study of fluid-dynamical boundary layers by analyzing viscous flows. Broadly asymptotic and numerical techniques are two principle approaches to tackle SPP.

1.3.1 Analytical approach

The analysis of singularly perturbed differential equations began early in the 20^{th} century when approximate solutions were constructed from asymptotic expansions. An asymptotic analysis provides the qualitative behavior of singularly perturbed differential equations. Mainly, asymptotic analysis for differential operators was developed for regular perturbation. In brief, we present the development of analytical methods for SPP below.
Friedrichs and Wasow [78] is widely considered the first mathematicians to initiate the study of asymptotic solutions for singularly perturbed boundary layer problems. In 1908, Birkhoff [25] discussed the asymptotic character of the solution of linear differential equations containing a parameter. In 1926, significant work on turning point problems was done by Wentzel [225], Kramers [116] and others. Later on, Langer [128] investigated the asymptotic dependence of the solution of ordinary differential equations upon complex parameters. The author concluded that the asymptotic representation utilizes multiple-valued expressions for the description of single-valued solutions of SPP. During the 1950s, some interesting physical problems such as low-Reynolds number flow problems were solved by Carrier, Cole, Latta, Van Dyke etc. The authors discussed the asymptotic expansion procedures for more general singular perturbation problems. The lectures of Friedrichs and Erdelyi [65] discussed asymptotic matching in detail, where they obtained uniform valid asymptotic approximations by adding the inner and

outer expansions. By the end of the 1970s, singular perturbation theory was placed in the contents of the analytic theory of differential equations. In 1968, Cole developed limit-process expansions for SPP. Later, in 1979, Friedman obtained the asymptotic behavior of eigenvalues for a singular perturbation problem in partial differential equations. Kamin [108], in 1979, considered singularly perturbed Dirichlet problem and proved that as $\epsilon \to 0$, the solution converges to a constant using a formal asymptotic expansion. In 1982, Frank and Wendt [76] studied linear elliptic singular perturbation problems. They converted the singular problem to a regular problem and thus found the asymptotic formula for the solution of the singular problem. Flyud and Tsimbal [72] obtained asymptotic expansions in the form of power series with respect to a small parameter ϵ for the solution of the Cauchy problem for the linear second-order singularly perturbed hyperbolic equation. Makarov [148] presented Eigen function expansion of the solution for linearly parabolic singularly perturbed partial differential equations. Asymptotic expansions for the corresponding Eigen functions in the form of powers of the perturbation parameter were presented. In 1986, Butuzov and Nesterov [33] constructed an asymptotic representation of the solution for the boundary value problems. Liu and Zheng [141] also proposed an asymptotic analysis approach for the solution of self-adjoint first-order elliptic boundary value problems. In 1989, Garbey [79] established a constructive procedure for obtaining the uniform asymptotic approximation for quasi-linear hyperbolic singular perturbation problems. During the same time, Butuzov and Nefedov [32] developed the asymptotic solution for boundary value problems. Melenk and Schwab [152], in 1999, assumed analyticity of the singularly perturbed elliptic problem in two-dimension. They gave asymptotic expansion of the solution and found error bounds that were uniform with respect to the singular perturbation parameter.

Though analytical methods provide us exact solutions, at the same time, it is challenging to apply these techniques to find the solution to non-linear

or complex problems or for problems with complex domains etc. Numerical techniques have tremendous advantages over analytical techniques for solving such types of problems and other complex and real-life problems.

1.3.2 Numerical approach

The studies of SPPs problems have been tackled by many researchers, but the majority of these problems cannot be solved analytically, therefore, one has to use numerical methods. The numerical analysis provides quantitative information about a particular problem but is applicable to broad classes of problems. A brief survey of various numerical techniques for SPP has been presented below:

Pearson [173, 174] is considered to be the first researcher who provided the numerical solution to SPP using the classical three-point finite difference scheme over a non-uniform mesh. Axelsson and Gustafsson [7] presented a modified upwind scheme for convection-dominated problems. Ortiz [166] discussed error bounds for the τ-method for singularly perturbed (SP) differential equations. Kelley [111] derived sufficient conditions for the existence and asymptotic behaviour of the solution of SP boundary value problems (BVP). In 1980, Flaherty and Mathon [70] developed a collocation method using cubic splines and polynomial for linear singularly perturbed 2-point BVP. Niijima [163] analyzed an exponential type difference scheme for solving non-linear SPPs. Sakai et al. [186] introduced hyperbolic and trigonometric B-splines of the fourth degree for SPP. Kadalbajoo and Rao [99] discussed a parallel discrete invariant algorithm for SP boundary value problems.

With the day-by-day advancements of science and engineering, various new numerical schemes are being proposed, mainly depending on specific problems. A few decades back, traditional finite difference methods, finite element methods, finite volume methods, etc., were widely used for solving

problems. But mesh generation, discretization of the domain, element connectivity, re-meshing, and adaptivity in complex two- and three-dimensional geometries are still challenging exercises for researchers and engineers in utilizing these methods.

Because of the inefficiency of the existing traditional numerical methods for solving specific problems, e.g., crack growth problems, problems with moving discontinuities, etc., mesh-free methods have drawn a lot of attention from engineers and mathematicians in the latter two decades.
From literature, it seems that Lucy and Monaghan [151] were the first ones who proposed the first mesh-free method named the smooth particle hydrodynamics (SPH) method in 1977. Later on, in 1992, the diffuse element method was developed by Nayroles et al. [162] at the University of Technology of Compiegne. The MLS approximation [127] was utilized in the method for generating smooth approximations of functions. Afterward, Belytschko [23], in 1994, introduced the EFG method where MLS approximation was employed for generating shape functions and Lagrange multipliers for imposing boundary conditions. During the same time, Liu et al. [143] pioneered the reproducing kernel particle method (RKPM) in 1995 as an improvement of SPH. In 1996, Duarte and Oden [62] used MLS interpolation equations to generate the hp-meshless cloud method, which is almost entirely meshless. Melenk [150] was the first to propose the partition-of-unity finite element method (PUFEM) technique in his Ph.D. thesis. Further, in 1997, Babuska and Melenk [10] extended this work and introduced a new meshless method known as the partition of unity method. Later on, Mayer and Mandel [149] proposed a finite ray element method in 1997, an extension of the partition of unity method, to solve the Helmholtz equation. In 1998, Atluri and Zhu [6] suggested a meshless local Petrov-Galerkin method which was based on local symmetric weak form and MLS approximation. In the late 1990, various mesh-free methods were developed, such as the point/radial point interpolation method (PIM/RPIM), the natu-

ral neighbor method, diffuse element method, mesh-free particle methods, multiple-scale kernel particle methods, multiple scales mesh-free methods, local boundary integral equation method, Petrov-Galerkin diffuse element method (PG-DEM), natural element method, etc. In 1996, Belytschko and his co-authors [21] presented an overview of meshless strategies and their developments.
Even though the mesh-free techniques have been applied effectively in different fields like fluid dynamics, heat transfer, solid mechanics, structural analysis, etc., most of them are still in progress.

Among the above discussed meshfree methods, the EFG method is the foremost common method broadly used to deal with numerous engineering problems. The MLS approximation is utilized to produce the shape functions. Belytschko developed the EFG method in 1994 by improving the methods of Nayroles [162] based upon the concept of the diffuse element method (DEM). Looking on the bright side, the EFG technique is very efficient for approximating partial differential equations solutions. Due to the absence of element connectivity, node particles can be added or removed without re-meshing. Thus, an adaptive refinement of the discretization can be achieved efficiently and easily. The simple integration cells are required for integration over the solution domain. These features make the EFG method more adaptable than the finite element method (FEM). On the other hand, the EFG technique still has some downsides in comparison to FEM. The EFG method is computationally more expensive and has a more complex implementation algorithm than FEM. Moreover, the method depends upon the MLS shape functions, which do not satisfy the Kronecker delta property. As a result, the imposition of boundary conditions is not trivial as in the case of FEM. To overcome this challenge, one has to utilize some special techniques such as Lagrange multipliers method [9, 23], coupling EFG with FEM [117], penalty method [247]. Despite all the downsides, the element-free Galerkin method is widely used

for solving various engineering problems. Considering the importance and positive points of the EFG method for solving various kinds of problems, many of its improved versions, such as the complex variable EFG (CVEFG) method [45], improved EFG method [243], interpolating complex variables EFG (ICVEFG) method [58], improved interpolating EFG method [211] have been developed by several researchers. The work on the improvement of the EFG technique for various kinds of problems is still in progress.
Hashemian and Shodja [86] applied gradient reproducing kernel particle method for solving the one-dimensional Burgers problem. The authors used different initial and boundary transformation techniques for the enforcement of essential boundary conditions. The reproducing kernel method was adopted by Geng and Qian [80] to solve SP turning point problems with twin boundary layers. Afterwards, the authors devised a modified reproducing kernel method [81] to handle singularly perturbed delay boundary value problems, and the proposed method's error estimations were also analyzed. Nadjafi and his co-authors [160] described a meshless method based on the MLS technique for solving singularly perturbed differential-difference equations. Following that, Ghassabzade et al. [82] introduced the radial basis collocation method with the coordinate stretching approach for the numerical analysis of SP differential-difference equations.

1.4 Gaps in the literature

Because of the increasing use of SPP in science and engineering, the field of singular perturbation theory has been an attraction to researchers. Many researchers have continuously proposed and developed many analytical and numerical techniques for solving SPP. Due to arising in nonlinearity and complexity in the singularly perturbed models, numerical techniques have always been preferred over analytical techniques. Further, among the nu-

merical techniques, it is clear from the survey, finite difference methods, finite element methods, collocation methods, spline approximation methods etc., have been widely used for solving SPP. Though the use of mesh-free methods has been increasing day by day for solving differential equations, these mesh-free techniques have yet to be used for solving singularly perturbed problems. We have carried out a thorough survey on numerical techniques for SPP but could not find any application of mesh-free methods for solving SPP. Thus, the proposed research work leading to Ph.D. is to propose some mesh-free techniques for solving the SPP.

1.5 Objectives of the study

Based on the survey and gaps in the literature, the following objectives have been proposed for the Ph.D. research work:

- To propose and implement a mesh free method for solving linear/nonlinear singularly perturbed problems in one dimension.
- To implement the proposed mesh free method for solving higher dimensional singularly perturbed problem.
- To implement the proposed mesh free method for solving real-life problem.

1.6 Element-free Galerkin method and its development

Belytschko et al. [23] were the first who proposed the EFG method and implemented it on elasticity and heat conduction problems in 1994. The weak formulation trial and test functions were constructed using MLS interpolants. It was shown that the proposed method's performance depends

upon the weight function choice. The authors demonstrated the impact of two different weight functions graphically. The Lagrange multiplier methodology was employed to incorporate the essential boundary conditions. The numerical outcome shows that the proposed scheme has achieved a higher resolution of steep gradient and convergence rate than standard FEM.
Later, in the same year, Lu et al. [145] discussed the element-free Galerkin technique for solving the partial differential equations using MLS approximations. The Lagrange multiplier method was used to implement the essential boundary conditions. Weighted orthogonal basis functions were described for MLS interpolants. The authors discussed the problems of the standard patch test, cantilever beam problem, edge crack, and the infinite plate with hole issues. With the help of numerical results, it was shown that the proposed method has higher accuracy than FEM for elliptic partial differential equations and provides smooth solutions for stains and stresses.
Further in 1995, the authors of [146] employed EFG method to solve the following transient problem in elasticity with small displacements:

$$\nabla.\sigma + b = \rho a, \quad \text{in } \Omega,$$

where σ_{ij} are the stress components, $v = \dot{u}$ and $a = \dot{v}$ are the velocity and acceleration respectively, b is body force vector and ρ is the density. The initial conditions, natural and kinematic boundary conditions are given as

$$\begin{aligned} u(x,0) &= u_0(x), \quad \text{in } \Omega, \\ v(x,0) &= v_0(x) \quad \text{in } \Omega, \\ \sigma.n &= \bar{t} \quad \text{on } \Gamma_t, \\ u &= \bar{u} \quad \text{on } \Gamma_u, \end{aligned}$$

where $u_0(x)$ and $v_0(x)$ are the initial displacements and velocity respectively, n is the unit normal to the domain Ω. The shape functions were constructed

using orthogonal basis functions, due to which the stiffness matrix becomes symmetric and positive semi-definite, and hence the consistency, convergence and stability analysis of time integration remain similar as for in the FEM. The relationship between the EFG method and SPH method was also discussed.

Belytschko et al. [24] described the applications of the EFG method in statics. The stationary growing crack problems, straight crack growth, and curvilinear crack growth problems were discussed. To capture the stress singularity and stress intensity factors, dense grids of nodes were aligned around the crack tip. The Lagrange multiplier method was considered for enforcing essential boundary conditions. Numerical results show that authentic stress intensity factors are achieved by this method without any enrichment of the displacement field by a near-crack tip singularity. The obtained results were compared with the existing results of the boundary element method and finite element method. A comparison of results obtained by regular square and radial patterns of nodes around the crack tip was shown. The rate of convergence of the method was also discussed.

In 1997, Fleming et al. [71] proposed an enriched EFG formulation for fracture problems. The authors proposed two refinement strategies near the crack tip for enriching the EFG formulation for better results. The trial functions have been augmented for the first approach to include the near-tip asymptotic field. For the second approach, the EFG basis functions have been augmented to include functions similar to the near-tip asymptotic fields. Numerical outcomes demonstrated that the two strategies largely diminish stress oscillations and computational degree of freedom. Later on, in the same year, Belytschko et al. [22] proposed a three-dimensional formulation and implementation of the EFG method for dynamic problems with explicit time integrations. The consistency approach has been utilized for generating the approximation function, which speeds up the calculations of shape functions. The central difference scheme in the classical form has

been utilized for time discretization. The coupled EFG-FEM technique has been used to impose the essential boundary conditions. Numerical results for two real-life problems, the fluid sloshing problem and the Taylor bar impact problem, have been compared with reference solutions available in the literature.

A formulation of the EFG method and its implementation has been discussed by Bouillard and Suleau [28] for analyzing the harmonic forced response of acoustic problems governed by the Helmholtz equation. The authors used the EFG and finite element methods to review the dispersion and pollution phenomena. Numerical tests described that the EFG solutions have significantly more accuracy than the FEM solutions.

Dolbow and Belytschko [61] examined various numerical integration schemes and described the Galerkin weak form for linear elastostatic problems. Numerical studies using the mesh-free EFG method have been carried out for second-order elliptic boundary value problems and investigated the effect of integration errors. Several integration errors and oscillations due to large as well as small changes in nodal spacing have been discussed which highly affect the rate of convergence. The integration of the weak form with the newly constructed technique known as boundary box cells has been shown to improve the results and to recover the convergence rates.

In 1999, Barry and Saigal [15] presented a three-dimensional formulation of the EFG method for static elastic and elastoplastic analysis. In the MLS approximations, singular weight functions were utilized for a formulation that allows a direct and accurate imposition of essential boundary conditions at the boundary nodes. The elastoplastic implementation is based on an increment approach, together with a consistent tangent operator. More accurate results were obtained for the J-integral in the case of the EFG approach with linear basis functions than for the finite element analysis.

Park and Leap [171] presented an application of the element-free Galerkin (EFG) method for groundwater flow model in a two-dimensional confined

aquifer domain Ω given by

$$\nabla.(T\nabla h) + R = S\frac{\partial h}{\partial t}, \quad \text{in } \Omega,$$

with the boundary conditions defined by

$$(T\nabla h).n = \overline{q}, \quad \text{on } \Gamma_q,$$
$$h = \overline{h}, \quad \text{on } \Gamma_h,$$

where ∇ is a vector differential operator, R is source or sink strength and t is time. The transmissivity T is the product of hydraulic conductivity K and aquifer thickness b. The storativity S is the product of specific storage S_s and aquifer thickness b. $\overline{q}$ is the specified flux of groundwater flow at the constant flow boundary Γ_q, h is the specified hydraulic head at the constant head boundary Γ_h and n is the unit vector normal to the constant flow boundary Γ_q. The construction of shape functions is based on the MLS approximations. A computer code has been developed with irregular boundaries for solving groundwater flow problems. The accuracy of the developed code was tested on groundwater problems with analytical solutions in a confined aquifer. The coupled EFG-FEM method was utilized to enforce the Dirichlet boundary conditions. The flexibility of the method was tested on the groundwater flow problem in a heterogeneous aquifer. The accuracy of solutions obtained by the EFG method was very similar to that of the FEM.

As described earlier, though the EFG method has the benefit of non-connectivity of nodes over the finite element method, it requires more CPU time to search nodes in the MLS procedure for generating shape functions as compared to the finite element method. This issue has been addressed by Hagihara et al. in their paper [84]. The authors proposed the method of the directed graph and the Delaunay triangulation for searching nodes and the division of the integral domain respectively to reduce CPU time. These

techniques are useful for saving CPU time and simplification the analysis for the EFG method. Further, for the first time, the authors employed the EFG method for solving non-linear creep problems under elevated temperature, elastocreep problems, and center-cracked plate problems. Numerical results obtained from the EFG method and the FEM were shown to agree with each other.

Singh and Tanaka [205] carried out the heat transfer analysis of composite slabs using the EFG method in the three-dimensional domain by proposing trigonometric and polynomial basis functions. The authors considered a general form of the energy equation for three-dimensional steady-state heat transfer in isotropic composite slabs given by

$$k(\frac{\partial^2 T}{\partial x^2} + \frac{\partial^2 T}{\partial y^2} + \frac{\partial^2 T}{\partial z^2}) + \dot{Q} = \rho c \dot{T},$$

with initial conditions

$$T = T_{ini},\ on\ \Omega,$$

essential boundary conditions at the surface of slab 1,

$$T = T_{S_1},$$

and natural boundary conditions at the outer surfaces of slab 1 and slab 2,

$$-k \frac{\partial T}{\partial n''}\bigg|_{S_h} cos(n', n'') = h(T - T_\infty),$$

The compatibility requirement at the interface of two slabs is given by

$$-k\left(\frac{\partial T}{\partial x}\right)_{x=L/2}\bigg|_{slab1} = -k\left(\frac{\partial T}{\partial x}\right)_{x=L/2}\bigg|_{slab2}.$$

Here k, denotes the coefficient of thermal conductivity, $\dot{Q}$ is rate of internal heat generation, ρ is density of material, c represents specific heat of material, $\dot{T}$ is $\frac{\partial T}{\partial t}$, h is convection heat transfer coefficient, $\cos(n', n'')$ is the cosine of angle between n' and n'', n' is the outward normal to the surface, $n'' = (x, y, z)$ and $S_h = S_2 \cup S_3 \cup ... \cup S_{11}$. MLS approximants are utilized to approximate the temperature $T(x)$. Results obtained using trigonometric and polynomial basis functions for constructing approximants have been compared with the existing one. The trigonometric basis functions produce slightly more accurate results than the other two by comparing the results. Penalty and Lagrange multiplier techniques have been used to enforce the essential boundary conditions. The effect of the penalty parameter on EFG results has also been discussed. Polynomial basis functions provide quite accurate results for the penalty approach in comparison to the other two.
In 2007, Singh et al. [203] considered the following general form of energy equation for three-dimensional heat transfer in isotropic materials with temperature dependent material properties:

$$\nabla.\{k(T)\nabla T\} + \dot{Q} = \rho(T)C(T)\dot{T},$$

with initial and boundary conditions defined as

$$\begin{aligned} T(x,0) &= T_i, \quad on\ V, \\ T(x,t) &= T_{S_1}, \quad x \in\ S_1, \\ q(x,t) &= h(T - T_\infty), \quad x \in S_j, \quad j = 2, 3, ..., 6. \end{aligned}$$

Here, $k(T) = k_0(1 + \beta_1 T)$ is thermal conductivity, $\rho(T) = \rho_0(1 + \beta_2 T)$ is density, $C(T) = C_0(1 - \beta_3 T)$ is specific heat, h is heat transfer coefficient, T_∞ is surrounding fluid temperature and T_i is initial temperature. The meshless EFG method has been successfully utilized to obtain the numerical solution of the above unsteady state non-linear heat transfer problem. The authors assumed that the material parameters, namely thermal con-

ductivity, specific heat, and density vary linearly with temperature. The quasilinearization process has been used to obtain the solution to the non-linear model problem, whereas the backward difference method has been used for the time integration. The results obtained by the EFG method are in good agreement with those obtained by the finite element approach.
Singh et al. [206] presented a thermal analysis of carbon nanotube (CNT) based composites by meshless EFG method. The governing heat conduction equation is given by

$$k_r \frac{\partial^2 T}{\partial r^2} + \frac{k_r}{r}\frac{\partial T}{\partial r} + k_z \frac{\partial^2 T}{\partial z^2} = 0,$$

with the following essential boundary conditions

$$at \quad z = 0, \ T = T_L,$$
$$at \quad z = L, \ T = T_R.$$

A cylindrical representative volume element (RVE) has been chosen to evaluate the thermal properties of nanocomposites. Continuum mechanics approach, multi-domain, and simplified approaches have been applied to calculate heat conductivity. It has been observed that the simplified approach provides more accurate results as compared to the multi-domain approach. The thermal conductivity of the composites was found to be a function of CNT length, CNT radius, RVE length, and RVE radius. The analysis found that temperature distribution on the surface of CNTs comes out to be almost uniform.
Zhang et al. [244] presented the following two-dimensional elasticity model problem on the domain Ω

$$\nabla.\sigma + b = 0, \quad in \ \Omega,$$

where σ is the stress tensor and b the body force. The boundary conditions are given by:

$$u(x) = \overline{u}(x), \quad x \in \Gamma_u,$$
$$t(x) = \sigma(x).n = \bar{t}(x), \quad x \in \Gamma_\sigma,$$

where σ is the stress tensor, b is body force, u is the displacement vector, t the traction vector, $\overline{u}$ and $\bar{t}$ the prescribed displacement and traction vectors on the displacement boundary Γ_u and on the traction boundary Γ_σ, respectively, and n the unit outward normal to the boundary Γ. For approximating the solution of the presented model, the authors proposed an improved EFG method. The authors utilized improved MLS approximation in which the orthogonal function system with a weight function is used as the basis function. The improved MLS approximation has greater computational efficiency and precision than the existing one. The considered strategy has the added benefit that the resulting system does not become ill-conditioned.

Pan and Yuan [168] developed EFG algorithm for strain-gradient-based nonlocal damage models to overcome the problem of convergence of finite element computation occurring, especially due to large strains in damaging elements.

The considered micro-mechanical damage model is given by

$$\Phi(\sigma, \overline{\varepsilon}^p, \Delta\overline{\varepsilon}^p, f^*) = (\frac{q}{Y(\overline{\varepsilon}^p, \Delta\overline{\varepsilon}^p)})^2 + 2q_1 f \cosh(\frac{3q_2 p}{2Y(\overline{\varepsilon}^p, \Delta\overline{\varepsilon}^p)}) - (1 + {q_1}^2 f^{*2}).$$

Here, σ is stress tensor of the material, $Y(\overline{\varepsilon}, \Delta\overline{\varepsilon})$ is effective yield stress depending on gradient plastic strain, q_1 and q_2 are constants, q is the Mises stress, p is hydrostatic pressure, and f^* is the function of the void volume fraction f. The EFG algorithm obtained the plastic strain by interpolating the strain values on integration points using the MLS shape functions. Also,

high-order spacial derivation on integration points has been directly calculated with the interpolated nodal plastic strain by using the MLS shape function so that no additional plastic strain boundary conditions are required. The mesh dependence of damage localization was removed using the EFG algorithm's gradient regulator. The computational results exhibit the stability of the EFG method for complex material models.

Yang and He [230], in 2010, solved a smoothed effective heat capacity model by using the EFG method with phase change. The problem domain Ω was divided into two distinct phases as liquid phase region Ω_l and solid phase region Ω_s. The governing equations in these two regions are given as follows:

$$c_l \frac{\partial T}{\partial t} = \nabla.(k_l \nabla T), \quad \text{in } \Omega_l,$$
$$c_s \frac{\partial T}{\partial t} = \nabla.(k_s \nabla T), \quad \text{in } \Omega_s,$$

where c_l and c_s denote the volumetric heat capacities and $k = k_l$ and k_s are the thermal diffusivities of materials in Ω_l and Ω_s respectively. The boundary conditions are specified as

$$T = T_b, \quad on\ \Gamma_1,$$
$$-k\nabla T.n = q, \quad on\ \Gamma_2.$$

Here, n is the unit outside the normal vector, q stands for a heat flux along n, and k is thermal diffusivity. The sigmoid function has been employed to build a continuous and smooth effective heat capacity function that avoids numerical oscillations caused by the step jump. The impacts of the arrangement of EFG nodes and the parameters relevant to the Sigmoid function on the solutions have been investigated. The proposed numerical model has been verified via two numerical examples, and reliable results have been achieved in comparison with analytical solutions.

Sharma et al. [196] studied heat transfer of an incompressible, electrically

conducting micropolar fluid along with a semi-infinite vertical porous moving plate in the presence of viscous dissipation, magnetic field, and heat absorption. The model problem is governed by the following set of equations:
Mass:

$$\frac{\partial v}{\partial y} = 0.$$

Momentum:

$$\rho\left(\frac{\partial u}{\partial t'} + v\frac{\partial u}{\partial y}\right) = (\mu + k)\frac{\partial^2 u}{\partial y^2} + k\frac{\partial N}{\partial Y} - \left(\sigma B_0^2 + \frac{(\mu + k)}{k_p}\epsilon + \frac{F\rho\epsilon^2}{k_p^{1/2}}u\right)u + \beta g\rho(T - T_\infty).$$

Angular momentum:

$$\frac{\partial N}{\partial t'} + v\frac{\partial N}{\partial y} = \frac{\gamma}{\rho j}\frac{\partial^2 N}{\partial y^2} - \frac{k}{\rho j}\left(2N + \frac{\partial u}{\partial y}\right).$$

Energy equation:

$$\frac{\partial T}{\partial t'} + v\frac{\partial T}{\partial y} = \frac{k_f}{\rho c_p}\frac{\partial^2 T}{\partial y^2} + \frac{1}{\rho c_p}\left(\frac{(\mu + k)\epsilon}{k_p}u^2 + \frac{F\rho\epsilon^2}{k_p^{1/2}}u^3 + (\mu + k)\left(\frac{\partial u}{\partial y}\right)^2\right) - \frac{Q_0}{\rho c_p}(T - T_\infty).$$

The corresponding boundary conditions are given as:

$$y = 0: \ u = u_p, \quad N = -s\frac{du}{dy}, \quad T = T_w + \delta(T_w - T_\infty)e^{nt'},$$
$$y \to \infty: \ u = 0, \quad N \to 0, \quad T \to T_\infty,$$

where u and v are components of velocities along and perpendicular to the plate respectively, t' denotes the time, μ is fluid dynamic viscosity, k is vortex viscosity, N is the angular velocity, σ is electrical conductivity, B_0 is the

strength of the magnetic field, ϵ is porosity, β denotes thermal expansion coefficients, g is gravitational acceleration medium, ρ is density, γ is spin gradient viscosity, c_p represents specific heat at constant pressure, Q_0 is heat absorption coefficient, F is empirical constant, k_p is the permeability of the porous, j denotes micro-inertia per unit mass and k_f is thermal conductivity. The authors utilized the Darcy-Brinkman-Forchheimer model to include the effects of boundary and inertia forces. The transformed system of non-dimensional ordinary differential equations is numerically solved using the EFG method. The influence of viscosity ratio, Darcy number, Forchhimer number, magnetic field parameter, heat absorption parameter, and the micropolar parameter on the velocity and temperature has been analyzed.

In 2011, Shibata and Murakami [197] proposed a stabilization methodology for mesh-free analysis of the soil-water coupled boundary-value problem using the EFG method. A stabilization term has been incorporated into the equilibrium equation to avoid instability in the pressure field. This stabilization term consists of first-order derivatives, which makes the derivative of the interpolation functions smooth. The added benefit of this stabilization parameter is that the interpolation order for the pore pressure becomes the same as that for the displacements, making the numerical results more accurate. The saturated column test and the foundation loading problem have been solved by using the stabilization procedure. The proposed stabilized scheme has been validated using the numerical results.

Peng and Li [175] considered the following two-dimensional elastoplasticity model problem

$$L^T \dot{\sigma} + \dot{b} = 0, \quad x \in \Omega,$$

together with the boundary conditions

$$\dot{u} = \dot{\bar{u}}, \quad x \in \Gamma_u,$$
$$n.\dot{\sigma} = \dot{\bar{t}}, \quad x \in \Gamma_t.$$

Here, L is the differential operator matrix, u is displacement, ϵ is strain, σ is stress at time t, $\dot{b}$ is body force rate. $\dot{\bar{u}}$ and $\dot{\bar{t}}$ are the prescribed velocity distribution and the prescribed traction rate at an arbitrary point z on the essential boundary Γ_u and the natural boundary Γ_t respectively. The authors proposed a complex variable element-free Galerkin (CVEFG) method based on the complex variable MLS approximation for solving the above-mentioned model problem. The Galerkin weak form is used to obtain the linear system. The penalty method is used to incorporate the essential boundary conditions. The inverse matrix A^{-1} of a complex variable has been obtained easily. It has been shown that the proposed CVEFG scheme has higher computational precision and efficiency than the EFG scheme.
In 2012, Wang et al. [221] proposed a hybrid particle element-free Galerkin (HPEFG) method for simulating free-surface flow problems. The technique combines the advantages of the EFG method in the Eulerian description and the particle method in the Lagrangian description. The EFG method in the Eulerian description completely avoids node coacervation, and the particles in the Lagrangian description capture the free surface. The feasibility and ability of the proposed scheme have been verified by solving four fluid flow problems with a free surface.
During the same year, Cai et al. [34] considered the following two-dimensional time-dependent non-linear Schrodinger equation

$$i\frac{\partial\psi}{\partial t}+\frac{\partial^2\psi}{\partial x^2}+\frac{\partial^2\psi}{\partial y^2}-B(x,y,t)\psi-C(x,y)|\psi|^q\psi=0,$$

with the initial conditions

$$\psi(x,y,0)=f(x,y),\quad (x,y)\in\Omega,$$

and boundary conditions

$$\psi(x,y,t) = \overline{\psi}(x,y,t), \quad (x,y) \in \Gamma_u, \quad 0 \le t \le T,$$
$$\frac{\partial \psi(x,y,t)}{\partial n} = p(x,y,t), \quad (x,y) \in \Gamma_n, \quad 0 \le t \le T,$$

where ψ is an unknown complex-valued function of (x,y) and t. $B(x,y)$, $C(x,y)$, $f(x,y)$, $\overline{\psi}$ and $p(x,y,t)$ are given complex-valued functions, q is positive real constant, Γ_u and Γ_n are non-intersecting curves forming a simple closed curve Γ bounding Ω and n is unit outward normal vector to Γ. The author and his co-workers obtained the numerical solutions of the proposed model problem by using a meshless global element-free Galerkin method. The MLS approximation scheme was employed to construct the shape functions. A time-stepping method was applied to deal with the time derivative term. Numerical solutions of the Schrodinger equation were presented for different cases and were compared with the analytical results. Based on the numerical results, it has been concluded that the EFG method can be applied to this kind of problem with reasonable accuracy. Later on, in 2014, the two-dimensional non-linear time-dependent Schrodinger equation was also analyzed by Zhang et al. [236] by utilizing the improved complex variable MLS approximation in the EFG method. Samimi and Pak [188] presented fully coupled three-dimensional hydro-mechanical problems arising in geotechnical engineering. The system of governing equations for analyzing a two-phase deforming porous medium is stated as follows:

$$\sigma_{ij} + \rho g_i = 0,$$
$$\left[\frac{\alpha - n}{K_s} + \frac{n}{K_w}\right] \frac{\partial \rho}{\partial t} + \alpha \dot{u_{i,i}} + \frac{1}{\rho_w} \left[\rho_w n \dot{u_i^{ws}}\right]_i = 0.$$

Herein, σ_{ij} is the total stress tensor, ρ is the porous medium density, g_i is the gravity acceleration vector, α is Biots parameter, n is the porosity of soil mass, p is the pore fluid pressure, t is time, u_i is the velocity vector of solid

phase, ρ_w is the pore fluid density, $\dot{u_i^{ws}}$ is the relative velocity between fluid and solid phase, and K_s and K_w are the bulk modulus of solid grains and pore fluid, respectively. Considering the displacement of the soil skeleton (u_i) and the pore fluid pressure (p) as the main variables of the governing equations, the required initial and boundary conditions can be expressed as follows:
Initial conditions:

$$u_i = u_i^0, \quad p = p^0, \quad at\ t = 0, \quad on\ \Omega.$$

Boundary conditions for the displacement field:

$$u_i = \overline{u_i}, \quad on\ \Gamma_u, \quad \sigma_{ij} n_j = \overline{t_i}, \quad on\ \Gamma_\sigma.$$

Boundary conditions for the pore pressure field:

$$p = \overline{p}, \quad on\ \Gamma_p, \quad K_{ij}/\mu(-p_j + p_w g_j) n_i = \overline{q}, \quad on\ \Gamma_q,$$

where $\overline{u_i}$, $\overline{t_i}$, $\overline{p}$ and $\overline{q}$ are the prescribed displacement, traction, pore pressure and flux respectively on the corresponding boundaries Γ_u, Γ_σ, Γ_p and Γ_q. n_i is the unit normal vector of the boundary Γ. The authors used the EFG method for the numerical simulation of the proposed coupled hydro-mechanical model problem. The weighted residual method and the Galerkin technique were used for the weak formulation of the governing equations. The penalty method was used for the imposition of essential boundary conditions. The spatial discretization of the resulting constrained Galerkin weak forms was based on EFG shape functions for displacements and pore water pressures, and a fully implicit scheme was used for time discretization. Numerical results obtained using the employed numerical technique were compared with analytical solutions. The numerical results indicate the capability of mesh-free code for simulating fully coupled hydro-mechanical problems without spurious oscillations in three dimensions. In 2013, a new

enrichment criterion was proposed by Pant and Singh [170] for modeling and simulating kinked crack problems using the EFG method. The authors proposed some modifications to the conventional intrinsic enrichment criterion by adding some extra terms to enhance its capabilities to capture the kinked cracks and the straight cracks. The modeling capability of the proposed criterion has been demonstrated by modeling cracks with multiple kinked segments and the quasi-static crack growth where crack tracking has been required at each incremental step of crack growth. Also, quasi-static crack growth in the two-dimensional domain subject to the mixed-mode loading conditions has been modeled. This implantation and analysis of complex and realistic fracture mechanics problems and comparison of numerical results with the FEM results prove the capabilities of the proposed method. Jaberzadeh et al. [93] investigated the buckling behavior of skew functionally graded plates (FGP) under thermal loading using the EFG method. MLS approximation, the Lagrange multiplier method, and orthogonal transformation techniques have been utilized to generate the shape functions and enforce the essential boundary conditions, respectively. The formulation was based on the classical plate theory. The material properties of the FGP were assumed to vary continuously and smoothly through the thickness according to the power-law distribution of the volume fraction of the constituents. In the thermal buckling analysis of an FGP, it is assumed that the temperature varies only in the thickness direction and is uniform, linear or non-linear over any plane. The deflection of plates was only unknown at a node. Therefore, the dimension of the discrete eigenvalue equations was equal to the number of nodes that discretize the plate domain. The effects of aspect ratio, thickness ratio, gradient index, and skew angle on the critical buckling temperature difference have been analyzed. Numerical results verify that the EFG method was efficient for modeling the skew and trapezoidal plates with various boundary conditions. In 2014, Sharma [195] examined the effects of thermal radiation on heat transfer over

a stretching sheet under a uniform magnetic field. The governing equations of the flow in two dimensions are given as follows:
Continuity equation:

$$\frac{\partial u}{\partial x} + \frac{\partial v}{\partial y} = 0.$$

Equation of momentum:

$$\rho(u\frac{\partial u}{\partial x} + v\frac{\partial u}{\partial y}) = (\mu + k)\frac{\partial^2 u}{\partial y^2} + k\frac{\partial N}{\partial y} - \frac{(\mu + k)}{k_p}u - \sigma B_0^2 u.$$

Equation of angular momentum:

$$\rho(u\frac{\partial N}{\partial x} + v\frac{\partial N}{\partial y}) = \frac{\gamma}{j}\frac{\partial^2 N}{\partial y^2} - \frac{k}{j}(2N + \frac{\partial u}{\partial y}).$$

Equation of energy:

$$\rho(u\frac{\partial T}{\partial x} + v\frac{\partial T}{\partial y}) = \frac{k_f}{c_p}\frac{\partial^2 T}{\partial y^2} - \frac{1}{c_p}\frac{\partial q_r}{\partial y} + \frac{1}{c_p}(\frac{(\mu + k)}{k_p}u^2 + (\mu + k)(\frac{\partial u}{\partial y})^2) + \frac{\sigma B_0^2}{c_p}u^2.$$

Herein, x and y are the coordinate directions, u, v, N and T are the fluid velocity components, the components of micro rotation and temperature, in the x and y directions respectively. m, k and r denote the viscosity, the Eringen vortex viscosity, and the fluid density respectively. k_f and k_p are the thermal conductivity and the permeability. c_p is the specific heat at constant pressure, T_w and T_∞ are the plate temperature and the fluid free-stream temperature respectively. Using appropriate transformations, the author non-dimensionalized the governing conservation equations and transformed them into ordinary differential equations. The EFG method has been employed to simulate the resulting system of equations. The FEM and EFG solutions have achieved an excellent correlation. The effects of temperatures, micro-rotation, linear velocity, skin friction coefficient, and heat transfer rate have been studied graphically. Zhang et al. [235] employed the improved EFG method to solve the degenerate parabolic equations aris-

ing from the spatial diffusion of biological populations. The proposed non-linear fractional-order biological population model is given as

$$\rho_t = \rho_{xx}^2 + \rho_{yy}^2 + \sigma(\rho), \quad t > 0, \ x, y \in \mathbb{R},$$

with the initial condition $\rho(x, y, 0) = \rho_0$ and the boundary conditions

$$\rho(x, y, t) = \overline{\rho}(x, y, t), \ (x, y) \in \Gamma,$$

where ρ denotes the population density and σ represents the population supply due to births and deaths. The implementation process involves employing the improved MLS approximation to construct shape functions. The main aim of the authors was to check the applicability of the method for biological problems. For this, the method was applied to many biological problems wherein the boundary conditions were considered time-dependent for most of the problems. The penalty method was employed to impose the essential boundary conditions. The convergence of the proposed method has been proved numerically by varying the number of nodes and time steps. Numerical results obtained are found to be in good agreement with those available in the literature. It has been concluded that the improved EFG method has the potential to solve linear and non-linear biological model problems. Debbabi et al. [54] presented a comparison between the EFG method using the MLS approximation and the improved EFG method using the improved MLS approximation. These two meshless methods have been applied to solve one- and two-dimensional potential problems. The shape functions have been obtained without matrix inversion which accelerates the computing speed. It has been shown through numerical examples that 75% of calculation time can be saved by using an improved EFG method as compared to the EFG method. The improved EFG method also provides better precision than the EFG method. Thus, the improved EFG method has been preferred over the EFG method for solving one- and two-

dimensional potential problems. During the same time, Li et al. [136] discussed error analysis for improved MLS approximation in multidimensional Sobolev spaces under some appropriate assumptions on weight functions. These assumptions on weight functions arise naturally in the derivation of error approximations. The theoretical results show that the error is directly related to the nodal spacing. Some properties of the improved MLS shape functions have been discussed. These improved MLS approximation error results have been further used to obtain optimal order error estimates for the improved EFG method to solve Neumann boundary value problems. To incorporate the Dirichlet boundary conditions, the penalty method has been used. Error analysis of the improved EFG method for Dirichlet boundary value problems has also been provided. Li and others [138] analyzed the EFG method to solve the non-linear time-dependent sine-Gordon (SG) and generalized sine-Gordon (GSHG) equations. The considered sine-Gordon model problem is given as:

$$\frac{\partial^2 u(x,t)}{\partial t^2} + \beta \frac{\partial u(x,t)}{\partial t} = \Delta u(x,t) - \psi(x) \sin u(x,t), \quad x \in \Omega, \ t > 0.$$

Boundary conditions are assumed to be of Neumann type

$$q(x,t) := \frac{\partial u(x,t)}{\partial n} = \overline{q}(x,t), \quad x \in \Gamma, \ t \geq 0,$$

where the bounded function $\psi(x)$ is Josephson current density, $u(x,t)$ is the wave displacement at position $x = (x_1, x_2, ..., x_d)^T$ and t, Δ is the Laplacian operator, β is dissipative term, $\overline{q}(x,t)$ is a given function of x and t and $n = (n_1, n_2, ..., n_p)^T$ is the unit outward normal on Γ. Theoretical error estimates of the EFG strategy based on MLS approximation have been derived from energy norms. Boundary conditions for the GSHG equation were of Dirichlet form, and the penalty method has been adopted to implement these boundary conditions. The theoretical results and capabilities of the technique have been affirmed by numerical examples. Convergence

studies have been conducted to approve the accuracy and proficiency of the EFG method for the SG and GSHG equations. The numerical results are in great understanding with the extant literature. The sine-Gordon equation was also solved by Dehghan and Shokri [57] by using the mesh-free collocation method based on the radial basis function. In 2016, Zhang et al. [238] considered a natural convection heat transfer between the concentric inner heated elliptic cylinder and the outer inclined square enclosure. The authors analyzed the phenomenon using the variational multiscale element-free Galerkin (VMEFG) method. The distribution of isotherms, streamlines, and the average Nusselt number on the inner elliptic cylinder were obtained from the computational results for different tilted angles ranging from $\gamma = 0^\circ$ to 45°, different dimensionless major axes of the elliptic cylinder from $a = 0.2$ to 0.4 and different Ra number from 10^3 to 10^6. Numerical results indicated that the tilted angle (γ), the magnitude of major axis a, and Ra numbers have remarkable effects on the streamlines, temperature forms, and vortex formation in the enclosure. The average Nusselt number on the inner elliptic cylinder increases with the increase of Rayleigh number, but the distribution of these numbers was almost independent of the variation of the tilted point of the square enclosure. Bahmyari et al. [11] carried out the stochastic analysis of moderately thick plates. The authors considered a combination of the EFG method with generalized polynomial chaos to quantify the uncertainties in the bending analysis of shear deformable plates. Based on the first-order shear deformation plate theory, the displacement field is expressed as:

$$
\begin{aligned}
u(x, y, z) &= z\theta_x(x, y), \\
v(x, y, z) &= z\theta_y(x, y), \\
w(x, y, z) &= w(x, y),
\end{aligned}
$$

where $u,\ v$ and w are the displacement of the plate in $x,\ y$ and z direction, θ_x and θ_y denote the rotations of the cross-section of the plate about y and x-axis, respectively. The MLS approximation has been used to produce the displacement shape functions and the penalty method has been employed for imposing the essential boundary conditions. The Karhunen-Loeve (KL) expansion and gPC have been used to represent random input and response respectively. The applicability and versatility of the presented method have been demonstrated by solving numerical examples for various values of coefficient of variations, aspect ratio, thickness and several combinations of boundary conditions, different types of lateral loading, and various values of stiffnesses of restrained edges and elastic foundation. Numerical results have been compared with the Monte-Carlo simulation and are found to be in very good agreement. Firoozjaee and Sahebdel [68] carried out numerical simulations of the bed-load sediment transport problem using the EFG method on the regular and irregular meshes. The governing shallow water equations, Coriolis forces and friction losses are presented as follows:

$$\begin{aligned}
\partial_t h + \partial_x(hu) + \partial_y(hv) &= 0,\\
\partial_t(hu) + \partial_x(hu^2 + \frac{1}{2}gh^2) + \partial_y(huv) &= -gh\partial_x Z,\\
\partial_t(hv) + \partial_x(huv) + \partial_y(hv^2 + \frac{1}{2}gh^2) &= -gh\partial_y Z.
\end{aligned}$$

Here, t is the time, u and v are the depth-averaged velocities in x and y directions respectively, h is the height of the water, g is the gravitational acceleration and Z is the bottom topography. The non-linear shallow water equation was considered for describing the hydrodynamic components, while the Exner equation was used to model the bed-load components, which determine the sediment continuity for depicting the bed updating. The governing equations were formulated for a coupled approach and were rewritten as a non-conservative hyperbolic system. The numerical results depict the capabilities of the EFG method to capture the shock resolution and trav-

eling discontinuities without generating nonphysical oscillations. To check the robustness and efficiency of the EFG approach, the solutions to several benchmark problems have been compared with the existing solutions in the literature. Cheng et al. [41] introduced a hybrid improved complex variable EFG method by combining the dimension splitting and the improved complex variable EFG methods for solving three-dimensional potential problems. The dimension splitting method was employed to transform the three-dimensional potential problem into a series of two-dimensional ones which were solved using the improved CVEFG method. The improved complex variable MLS approximation and the penalty method were used to construct the shape functions and to impose the essential boundary conditions respectively. The finite difference method was used for time discretization, while space derivative terms were discretized using Galerkin's weak form to obtain the final discretized equations. The effects of the scale parameter, the penalty factor, the number of nodes, the step number, and the weight function on the computational precision and efficiency were discussed. The numerical results obtained by using the proposed method and the improved EFG method were compared with the analytic ones. It has been concluded that the proposed scheme is computationally more efficient for the same accuracy than the improved EFG scheme.

Talebi et al. [213] utilized the EFG method to analyze the material flow during the friction stir welding (FSW) process. A mortar contact was used to account for the stirring effect and heat generation from the frictional contact. During the coupled thermomechanical process, a two-way adaptive method (rh-adaptive) was utilized to overcome potential numerical problems due to the extensive mesh distortion and material deformation. The mesh was globally refined by perusing an anisotropic tetrahedral mesh (h-adaptive). r-adaptivity was incorporated by building a completely new mesh based on the old mesh. The authors utilized a certain time integration scheme and mortar surface-to-surface contact to handle the apparatus

and workpiece interaction. The simulation was performed on an aluminium sheet with a cylindrical instrument to exemplarily show the applicability of the adaptive EFG method. The obtained deformation and temperature fields from the simulation were compared to the experimental results of FSW.

The numerical study of regularized long wave (RLW) equation was presented by using the simplified interpolating EFG (IEFG) strategy with the Galerkin weak form by Sun and Wang [210] in 2017. The trial functions in the interpolating moving least-square (IMLS) strategy have one less unknown coefficient than within the traditional MLS approximation. The shape functions fulfil the interpolating property at the nodes. In this manner, the essential boundary conditions were automatically imposed. The accuracy and viability of the IEFG strategy were tested by the problems of the single solitary wave, the interaction of two solitary waves and the solitary waves with Maxwellian starting conditions. The error estimates of the semi-discrete scheme and the convergence rate of the fully discrete scheme for the RLW equation were examined in terms of the radius of the influence domain and the time step. The theoretical results show that the IEFG strategy has a good convergence rate for the RLW problem. The numerical convergence rates agree with those of theoretical results. Muthu et al. [159] proposed a multiple crack weight technique with a level set method to model multiple cracks by employing a coarse mesh-free nodal discretization. The EFG method has been considered to solve the problem of modeling interacting cracks in isotropic and bi-materials. This approach has been expanded to analyze kinked cracks that have knee singularity. The level sets for multiple cracks are extrapolated to a generic point through triangulation of the closest level set coordinates. These level sets are upgraded at each step of crack propagation. The stress intensity factors and energy release rates for interacting cracks in isotropic and homogeneous materials, including a crack at a bi-material interface, are determined by utilizing the

standard interaction integrals. The results have been compared with the existing results in the literature. It has been observed that with coarser nodal thickness, the error is less than 1%, and the solutions converged with the increment in nodal density. Bahmyari et al. [11] combined the EFG method and the generalized polynomial chaos expansion to analyze the stochastic bending of moderately thick plates with flexibly restrained edges resting on a two-parameter elastic foundation. The deterministic governing equations were derived from the first-order shear deformable plate theory. The MLS approximation has been utilized to produce the displacement shape functions, and the penalty method has been utilized for imposing the essential boundary conditions. The plate modules of elasticity, stiffness of the elastically restrained edges, and foundation stiffness have been represented using the Karhunen-Loeve expansion. The accuracy and convergence of the developed method have been examined by comparing the numerical results with those obtained by the Monte Carlo EFG method. The applicability and versatility of the developed method have been demonstrated by solving numerical examples for various values of the parameters like aspect ratio, thickness, coefficient of variations, correlation lengths, different types of boundary conditions, etc. Zhang et al. [234], in 2017, set up a numerical model for steady heat transfer analysis of the orthotropic structure and employed the EFG method. The essential boundary conditions were enforced by using the penalty method. The reliability of the heat transfer model and MATLAB programs were confirmed by solving complex engineering heat transfer problems. The impacts of node distribution patterns, scaling factors, penalty factors and weight functions on the temperature of different orthotropic structures were investigated. The cubic spline and parabolic weight functions have been favored in the heat transfer analysis. The CPU computation time for the EFG and the FEM has also been calculated and compared. The relative computational error increases with the decrease of the orthotropic factor for different weight func-

tions. The steady heat transfer analysis has been expanded to the transient heat transfer analysis and thermal structure topology optimization of the three-dimensional complex orthotropic structures considering the material discontinuity. Later, the same year, the authors also analyzed the transient heat model for anisotropic material using the EFG approach [233]. The governing equations for the heat transfer model in anisotropic material are described as

$$k_{ij}\frac{\partial^2 T}{\partial x_i \partial x_j} + \dot{Q} = \rho c \frac{\partial T}{\partial t}, \quad T(x,y) \in \Omega, \quad (i,j = 1,2),$$

where k is thermal conductivity, $T(x,t)$ is the transient temperature, $\dot{Q}(x,t)$ is the heat generation per unit volume, ρ and c are the material density and the specific heat respectively. The initial and boundary conditions for considered model are given as:

$$\begin{aligned} T(x,0) &= T_0, \quad x \in \Omega, \\ T(x,t) &= \overline{T}, \quad x \in \Gamma_1, \\ -k_{ij}\frac{\partial T}{\partial x_i} n_j &= q, \quad x \in \Gamma_2, \\ -k_{ij}\frac{\partial T}{\partial x_i} n_j &= h(T - T_f), \quad x \in \Gamma_3, \end{aligned}$$

where T_0 is the initial temperature on Ω, $\overline{T}$ is the constant temperature on Γ_1, n_j is directional cosine of the unit outward normal vector to the boundary point x, q is the prescribed heat flux on Γ_2. T_f and h are a prescribed ambient temperature and a convection heat transfer coefficient on Γ_3 respectively.

Also for this model, the EFG and the finite element solutions have been compared and it has been concluded that the EFG approach provides a higher accuracy at very time instants than the finite element approach for transient heat transfer problems, especially in complex geometries with mixed thermal boundaries. The impact of orthotropic factors and off-angles on

anisotropic thermal conductivity was investigated. It has been concluded that the thermal performance of complex geometries can be boosted by controlling the orthotropic factors and off-angles.

Zhang and Li [240] developed a variational multiscale interpolating element-free Galerkin method by coupling the EFG method with Hughes's variational multiscale (HVM) approach for analyzing the Darcy flow. The improved IMLS method is used to construct shape functions that satisfy the no-penetration boundary condition in the Darcy flow. The spurious numerical oscillations were controlled by utilizing the HVM approach. Numerical results demonstrate high accuracy and improved stability for both velocity and pressure. Later, in 2018, the authors [241] developed a generalized element-free Galerkin (GEFG) method for tackling Stokes's problem in primitive variable form. The MLS shape functions in the GEFG strategy were chosen as a partition of unity functions. The penalty method was used to employ the Dirichlet boundary conditions. Similar to the variational multi-scaled element-free Galerkin (VMEFG) method, theoretical analysis shows the stability of the GEFG method. Numerical results show the superiorities of the GEFG method over the VMEFG and FEM. By eliminating numerical oscillations from the standard EFG method, the GEFG method provides better accuracy and computational efficiency. Furthermore, the proposed method requires less CPU time, resulting in superior precision and computational proficiency compared to the VMEFG method based on the numerical results.

Li and Li [137] discretized the p-Laplacian problem into a non-linear algebraic system by utilizing the improved EFG method. To overcome the drawbacks of the MLS approximation, the authors introduced weighted orthogonal basis functions in the MLS approximation similar to [44] and generated the IMLS approximation. Further, to enhance the stability and performance of the improved MLS approximation, a stabilized improved MLS approximation has been adopted to form meshless shape functions.

The method is implemented through computer code written in MATLAB. Numerical results show that the improved EFG method for the p-Laplacian problem is convergent and has high computational accuracy.
Cheng et al. [42] presented a hybrid improved CVEFG method by combining the dimension splitting method and improved CVEFG method for three-dimensional advection-diffusion problems. The dimension-splitting method has been used to transform the three-dimensional advection-diffusion problem into a series of two-dimensional problems, which have been further solved by the improved CVEFG method. The formulae of the proposed method have been obtained by constructing the shape functions using improved CVEFG approximation. Essential boundary conditions have been imposed by using the penalty method and the Galerkin weak form has been used to obtain the discretized equations for advection-diffusion problems. Six numerical examples have been considered and results were compared with the improved EFG method. Results show that the proposed method is convergent and the computational accuracy and efficiency are much higher than the improved EFG method. In 2018, Li [135] discussed the formulations and error analysis of the CVEFG method for three-dimensional elliptic problems and wave equations. For given functions $\sigma(x)$, $f(x)$, $\overline{u}$ and $\overline{q}$, the author considered the following elliptic problem in $\Omega \subset \mathbb{R}^3$ with boundary $\Gamma = \Gamma_D \cup \Gamma_N$ where $\Gamma_D \cap \Gamma_N = \emptyset$,

$$\begin{cases} -div(\Lambda(x)\nabla u(x)) + \sigma(x)u(x) = f(x), & x \in \Omega, \\ u(x) = \overline{u}(x), & x \in \Gamma_D, \\ \Lambda(x)\nabla u(x).n(x) = \overline{q}(x), & x \in \Gamma_N. \end{cases}$$

Herein, $\Lambda(x)$ is 3×3 positive definite and symmetric matrix, u is the unknown function and $n = (n_1, n_2, n_3)^T$ is the unit outward normal to Γ. The complex variable moving least-square (CVMLS) approximation on the three-dimensional domain is developed to form shape functions. The

approximation involves fewer coefficients, requires fewer nodes than the standard MLS approximation, thus, more computationally efficient. Numerical examples are presented to verify the convergence and efficiency of the CVEFG method. Numerical results reveal that the method has better accuracy and higher computational efficiency than the EFG method. In 2019, Zhang et al. [232] established the thermo-mechanical coupling analysis for orthotropic structures. The considered two-dimensional model for heat transfer in orthotropic structure is given as

$$\nabla.(\lambda \nabla T) + \dot{Q} = 0, \quad T \in \Omega,$$

where T is the temperature field in the domain Ω, $\dot{Q}$ is the density of heat sources, λ is the second-order tensor of thermal coefficients. The three types of boundary conditions have been considered and are given as:
Dirichlet boundary condition:

$$T = \overline{T}, \quad T \in \Gamma_1.$$

Neumann boundary condition:

$$-K\nabla T.n = q, \quad T \in \Gamma_2.$$

Robin boundary condition:

$$-K\nabla T.n = h(T - T_f), \quad T \in \Gamma_3,$$

where $\overline{T}$ is constant temperature on Γ_1, q is the heat flux on Γ_2, T_f and h are ambient temperature and convection heat transfer coefficient on Γ_3 respectively. n represents the unit outward normal vector of the boundary Γ. The authors proposed the EFG method to analyze the presented model. The feasibility of the proposed method and programs have been verified through thermoelastic problems of complex orthotropic structures. It has been concluded that the EFG solutions have higher calculation pre-

cision and adaptability than the FEM solutions, irrespective of whether the nodes are distributed regularly or irregularly. The authors discussed the effects of off-angles and orthotropic material factors on the magnitude and direction of total thermal deformation displacement and Mises stress. The result shows that the value of thermal deformation and thermal stress for the orthotropic structure is reduced by 11% and 24% respectively by using the proposed model.

Mohammadi and Dehghan [156] applied a mesh-free method to solve the time-dependent Cahn-Hilliard equation and tumor growth model. The Cahn-Hilliard equation is a time-dependent fourth-order partial differential equation defined as

$$\begin{cases} \frac{\partial u(x,t)}{\partial t} & = \nabla.(M(u(x,t))\nabla\mu), \\ \mu(x,t) & = F^{'}(u(x,t)) - E^2\Delta u(x,t), \quad x \in \Omega,\ 0 < t \leq T, \end{cases}$$

where $\Omega \subset \mathbb{R}^d (d = 1, 2, 3)$, ∇ is the gradient operator, Δ is Laplace operator, T is the final time, $F(u)$ is the Helmholtz free energy, μ is chemical potential, $E(u)$ is the Ginzburg-Landau free energy and $M(u)$ is diffusional mobility. The boundary conditions on u and μ are considered as

$$\frac{\partial u}{\partial \overrightarrow{n}} = \frac{\partial \mu}{\partial \overrightarrow{n}} = 0, \quad \text{on } \partial\Omega,$$

where $\overrightarrow{n}$ is the unit normal vector on the boundary.

A mathematical model of tumor growth of a fourth-order differential equation split into two second-order differential equations is given as follows:

$$\begin{cases} \frac{\partial u(x,t)}{\partial t} & = \nabla.(M_u\nabla\mu_u(x,t)) + \gamma_u(x,t), \\ \mu_u(x,t) & = F'(u(x,t)) - E^2\Delta u(x,t) + D_u\chi(u(x,t), n(x,t)), \\ \frac{\partial n(x,t)}{\partial t} & = \nabla.(M_n\nabla\mu_n(x,t)) - \gamma_u(x,t), \\ \mu_n & = D_n\chi(u(x,t), n(x,t)) + \frac{n(x,t)}{\sigma}, \quad x \in \Omega, \quad 0 < t \leq T. \end{cases}$$

Herein, u denotes the tumor cell volume fraction, n is nutrient-rich extracellular water volume fraction, $F(u)$ represents the free-energy density function, $\chi(u,n)$ represents the chemotaxis energy, σ denotes a small parameter governing the relative strength, μ_u and μ_n are the chemical potentials due to u and n respectively, E^2 is the diffusivity parameter for the surface energy term. The boundary conditions for u, μ_u, n and μ_n are considered as follows

$$\frac{\partial u}{\partial \overrightarrow{n}} = \frac{\partial \mu_u}{\partial \overrightarrow{n}} = \frac{\partial n}{\partial \overrightarrow{n}} = \frac{\partial \mu_n}{\partial \overrightarrow{n}} = 0, \quad on\ \partial\Omega,$$

in which $\overrightarrow{n}$ is the unit normal vector on the boundary. The EFG technique was considered for approximating the spatial variables. An adaptive time algorithm was employed to reduce the number of iterations and the temporal variable was discretized using a second-order semi-implicit backward differential formula. Some numerical simulations have been carried out to show the capabilities of the proposed numerical scheme.

The classical EFG method is based on the shape functions constructed using the MLS approximation. Since the shape functions are unable to satisfy the Kronecker delta property, essential boundary conditions cannot be imposed naturally. To overcome this problem, Dehghan and Abbazadeh [56], in 2019, employed an interpolating element-free Galerkin (IEFG) technique for solving the magneto-hydrodynamic equation wherein the shape functions were so modified as to satisfy the Kronecker delta property. The authors first employed the Gant-Nicosen scheme to discretize the temporal derivative term. The energy method was used to investigate the stability and convergence of the time-discrete scheme. Then, the IEFG method was employed to discretize the spatial derivatives. Some error estimates have been presented, and the convergence order of the proposed numerical scheme is of $O(\tau^2 + \delta^m)$. Numerical results confirm the efficiency of the developed method.

Cheng et al. [43] employed an improved CVEFG method for solving wave

propagation problems. The shape functions were obtained by using improved complex variable MLS approximation. The discretized equations of two-dimensional wave propagation problems were obtained using Galerkin's weak form for space variables and the finite difference method for time variables. The penalty method has been utilized for enforcing the essential boundary conditions. The convergence of the proposed improved CVEFG method about node distribution and time step has been analyzed and the influence of weight functions, scale parameter of the influence domain and penalty factor on the numerical solutions have also been discussed.

Dinesh et al. [59] is the first who apply the EFG method for solving the vertically integrated three-dimensional multiphase flow model for the horizontal aquifer, the sloped aquifer, the non-homogeneous aquifer and the horizontal aquifer with multiple wells with and without the consideration of a local nodal refinement zone around the discontinuities. The three-dimensional multiphase flow model under consideration is given by

$$\frac{\partial \phi \rho_\alpha S_\alpha}{\partial t} + \nabla.(\rho_\alpha \overrightarrow{u}_\alpha) = \rho_\alpha q_\alpha, \quad \alpha = 1(brine), 2(CO_2),$$

where $\phi[L^0]$ is the porosity of the aquifer, $t[T]$ is time, $\rho_\alpha[ML^{-3}]$ and $S_\alpha[L^0]$ are the density and the fluid saturation respectively, for each phase, $q_\alpha[L^3T^{-1}]$ is a source/sink term, and $\overrightarrow{u_\alpha}$ is the volumetric flux of each phase. The authors showed that the EFG formulation for the resulting coupled system of PDE, together with the Crank-Nicolson scheme, provides higher-order shape functions and ease of nodal refinement. These features make the mesh-free method more attractive for modeling hydrodynamic problems, specifically for those with a sharp change in the solutions. The temporal analysis has been carried out using implicit pressure and explicit saturations.

Azhari et al. [8] proposed coupling of the EFG method and the classic finite strip method for investigating the static and buckling analysis of the thin plates to reduce the computational cost. The modified variational forms

were obtained by utilizing the Lagrange multiplier method to satisfy the combined conditions of displacement. In the finite strip sub-domain, three triangular shape functions were used to approximate the displacement field of each strip. A rectangular plate with a hole at the centre under static and buckling load was analyzed, and good convergence results were achieved. The results showed that the analysis time in the EFG-finite strip method is reduced in comparison to the EFG method. Essential boundary conditions were easily enforced infinite strip sub-domains which demonstrate the effectiveness of the present coupling method.

In 2019, Zhou and Song [245] developed a three-dimensional strain-rotation-EFG (3D-SR-EFG) method to investigate the non-linear bending analysis of functionally graded carbon nanotube-reinforced composite (FG-CNTRC) plates. The method was based on the Strain-Rotation (S-R) decomposition theorem. The discretized equations were obtained by global weak form, and the incremental variational equation was derived from an updated co-moving coordinate formulation. The numerical stability and accuracy of the proposed 3D-SR-EFG method have been confirmed through convergence and comparison studies. Numerical results indicate that the 3D-SR-EFG method has effectively predicted the non-linear bending behavior of the CNTRC plates.

1.7 Norms and notations

In the thesis, we define some of standard notations of Sobolev spaces and the spaces of vector-valued functions. Let $\Omega \subseteq \mathbb{R}^d$ be a bounded and open set ($d = 1$ or 2). For $p < \infty$, we define $L^p(\Omega)$ as the space of all measurable functions $u : \Omega \to \mathbb{R}$ such that

$$\|\vartheta\|_{L^p(\Omega)} = \left(\int_\Omega |\vartheta|^p dx \right)^{1/p} < \infty.$$

For $p = 2$, the space $L^2(\Omega)$ forms a Hilbert space with the inner product

$$< \vartheta, \xi >= \int_\Omega \vartheta(x)\xi(x)dx,$$

and the endowed norm

$$\begin{aligned} \|\vartheta\| &= [< \vartheta, \vartheta >]^{1/2} \\ &= \left(\int_\Omega \vartheta(x)\vartheta(x)dx \right)^{1/2}. \end{aligned}$$

We assume that Ω is an open domain in $\mathbb{R}^d$, $\alpha = (\alpha_1, ..., \alpha_d)$ is a d-tuple of non-negative integers and $|\alpha| = \sum_{i=1}^d \alpha_i$. If $\xi \in L^2(\Omega)$, then define

$$D^\alpha \xi = \frac{\partial^{|\alpha|}\xi}{\partial x_1^{\alpha_1} \partial x_2^{\alpha_2} ... \partial x_d^{\alpha_d}}.$$

Further, we define

$$\begin{aligned} H^1(\Omega) &= \{\xi \in L^2(\Omega), \frac{dv}{dx} \in L^2(\Omega)\}, \\ H^m(\Omega) &= \{\xi \in L^2(\Omega), \quad D^\alpha \xi \in L^2(\Omega) \ \forall \ |\alpha| \leq m\}. \end{aligned}$$

The inner product in the Hilbert space $H^m(\Omega)$ is defined by

$$< \vartheta, \xi >_m = \sum_{|\alpha| \leq m} \int_\Omega D^\alpha \vartheta D^\alpha \xi dx,$$

which induces the norm

$$\|\vartheta\|_{H^m(\Omega)} = \left(\sum_{|\alpha| \leq m} \|D^\alpha \vartheta\|^2_{L^2(\Omega)} \right)^{1/2}.$$

We proposed the parameter-uniform or ϵ-uniform method, which generated numerical solutions that converge uniformly for all values of the parameter ϵ in the range $(0, 1]$ and that require a parameter-uniform amount of computational work to compute each numerical solution. If the technique

is ϵ-uniform, the difference between the exact solution u_ϵ and the numerical solution u_ϵ^{*N} corresponds to an estimate of the form:
For some $N_0 \in \mathbb{Z}^+$, all integers $N \geq N_0$ and all $\epsilon \in (0, 1]$,we have

$$\|u_\epsilon^{*N} - u_\epsilon\|_{\overline{\Omega}} \leq \mathcal{C} N^{-p},$$

where $\mathcal{C}$ and p are positive constants independent of ϵ and N. The maximum norm on the whole domain $\overline{\Omega}$ is denoted by $\|.\|_{\overline{\Omega}}$. Such a numerical technique approximates the problem's solution and its first derivative, ϵ-uniformly, is called a robust method.
The application of a maximum or minimum principle can effectively provide priori estimates for the solutions and their derivatives of differential equations. A comprehensive discussion of these comparison principles can be found in Protter and Weinberger [177]. In this thesis, the maximum principle [187] is utilized to achieve ϵ-uniform error estimates. The maximum norm is chosen as the error measurement due to the need to estimate the error in the extremely small domains where the boundary layers occur. In the boundary layer region, the local behavior of the error may not be captured by other norms, such as the root mean square, which involves averages of the error that smooth out rapid changes in the solutions. Farrell et al. [66] and Hegarty et al. [88] provide additional discussion on the choice of an appropriate norm.

1.8 Conclusion

In this Chapter, significance of singularly perturbed problems and various models have been presented. Basic concepts and some definitions involved in the thesis work have been discussed. Survey on different mesh-free techniques has been carried out for solving SPP based models governing real-life phenomenon. Based on the extensive survey, gaps in the literature have been pointed out and consequently, objectives of the thesis have been

framed. These objectives have been achieved via the work which has been categorized in six different Chapters to follow.

Chapter 2

Element-free Galerkin method for one-dimensional singularly perturbed elliptic problem

2.1 Introduction

Due to rapid advancements in science and technology, modeling of real-life phenomenon with differential equations turn out to be a complex problem. It become more complex if singularly perturbation parameter is introduced. The mathematical representation of boundary layers is the presence of a small parameter ϵ, called singular perturbation parameter, multiplying with the coefficients of some or all the terms involving highest order derivatives in the differential equations. Singular perturbation problems (SPP) emerge in almost all the fields of science and engineering, e.g. plasma dynamics, oceanography, biochemistry, elasticity, electric power systems, fluid dynamics, aerospace systems, ecology, reaction-diffusion processes, etc. [40]. Therefore, one has to pay a great attention while approximating the solutions of such SPP having boundary layers.

Several authors worked on numerical schemes for approximating the solutions of SPP [66, 183]. Survey papers of Kadalbajoo and his co-authors [100–103, 105] throw light on various computational techniques used for solving SPP. Pearson [173, 174] is considered to be the first researcher who provided the numerical solution to SPP using the classical three-point finite difference scheme over a non-uniform mesh. Axelsson and Gustafsson [7] presented a modified upwind scheme for convection-dominated problems.

Ortiz [166] discussed error bounds for the τ-method for singularly perturbed (SP) differential equations. Kelley [111] derived sufficient conditions for the existence and asymptotic behavior of the solution of SP boundary value problems (BVP). In 1980, Flaherty and Mathon [70] developed a collocation method using cubic splines and polynomial for linear singularly perturbed 2-point BVP. Niijima [163] analyzed an exponential type difference scheme for solving non-linear SPP. Sakai et al. [186] introduced hyperbolic and trigonometric B-splines of the fourth degree for SPP. Kadalbajoo and Rao [99] discussed a parallel discrete invariant algorithm for singularly perturbed BVP.

Shishkin [198–202] employed special type of mesh, called Shishkin mesh, to generate parameter-uniform numerical schemes under finite difference framework. Several authors [4, 30, 115] also utilized Shishkin meshes for generating parameter-uniform numerical schemes for SPP having additional singularities. Recently, researchers have paid considerable attention to the developments of mesh-free methods taking into account the benefits and advantages of mesh-free methods over other numerical schemes. But for SPP, some mesh-free techniques have been proposed.

Hashemian and Shodja [86] applied gradient reproducing kernel particle method for solving the one-dimensional Burgers problem. The authors used different initial and boundary transformation techniques to enforce essential boundary conditions. Geng and Qian [80] employed the reproducing kernel method for obtaining numerical solutions to singularly perturbed turning point problems having twin boundary layers. Later, the authors developed a modified reproducing kernel method [81] to solve singularly perturbed delay boundary value problems.

The method was based on the reproducing kernel theory, and the error estimates of the method were discussed. Nadjafi and his co-authors [160] described a meshless method based on the moving least-square (MLS) technique for solving singularly perturbed differential-difference equations. Af-

ter that, a meshless approach namely radial basis collocation method, with the coordinate stretching procedure was presented by Ghassabzade et al. [82] for the numerical treatment of singularly perturbed differential-difference equations.

In the present Chapter, we propose an element-free Galerkin (EFG) method. The method lies in the category of mesh-free methods and was given by Belytschko et al. [23]. The authors then applied the proposed method to solve the elasticity and heat conduction problems. To the best of our knowledge, the proposed method has rarely been applied for solving SPP as these types of problems require some special treatment in order to capture the boundary layers.

In the current work, this treatment is carried out by proposing some special type of node distribution so that the proposed method can be made capable of capturing the sharp boundary layers. The proposed technique is very efficient for approximating the solutions of partial differential equations. Node particles can be added or deleted without difficulty due to the lack of element connectivity. As a result, a flexible refinement of domain discretization can be achieved efficiently and quickly. This feature makes the EFG method better adaptable than the finite element method (FEM). The proposed scheme utilizes MLS approximation for generating shape functions. The methodology is based on the global weak form, and the numerical integrations are computed employing background cells. The Lagrange multipliers approach is used to impose the essential boundary constraints as the MLS shape functions do not satisfy the Kronecker delta function property.

The Chapter is organized as follows: In Section 2.2, the continuous singularly perturbed problem has been considered. The numerical methodology consisting of the node generation, MLS approximation, weight functions and weak formulation, is discussed in Section 2.3. Section 2.4 focuses on the one-dimensional non-linear singularly perturbed elliptic problem. The

quasilinearization technique and its convergence are discussed in Section 2.5. The numerical algorithm of the proposed method and numerical tests are conducted in Section 2.6 to evaluate its efficiency and robustness. Certain conclusion based on the present analysis are finally discussed in Section 2.7.

2.2 Singularly perturbed linear elliptic differential equation

In this Chapter, we will investigate the following one dimensional singularly perturbed problem

$$\epsilon\frac{d^2u(x)}{dx^2} + a(x)\frac{du(x)}{dx} + b(x)u(x) = f(x), \qquad x \in \Omega = (0,1) \tag{2.2.1}$$

with essential boundary conditions defined by

$$u(0) = u_0, \quad u(1) = u_1, \tag{2.2.2}$$

where ϵ is a small positive parameter known as singular perturbation parameter with $0 < \epsilon \ll 1$, and $a(x)$, $b(x)$ and $f(x)$ are continuous functions in the specified domain.

2.3 Formulation of element-free Galerkin method

2.3.1 Node generation

As discussed by Roos et al. [183], when ϵ tends to 0, boundary layers appear in the solution and we need to adopt some special technique in order to capture these boundary layers. In the present work, we have utilized Shishkin's approach in order to generate more nodes in the boundary layer region and to capture these layers nicely. The distribution of nodes has

been carried out by splitting up the spatial domain $\bar{\Omega} = [0, 1]$ into two subintervals $[0, 1-\delta]$ and $[1-\delta, 1]$, where the transition parameter δ is chosen as

$$\delta = \min\{\frac{1}{2}, \kappa\epsilon \ln N\},$$

where κ is a constant chosen appropriately and N denotes the total number of nodes. Here, we have considered that the boundary layers appear at $x = 0$. Similar procedure can be carried out for boundary layers appearing at $x = 1$. On each of these sub-domains, the nodes are generated as follows:

$$x_i = \begin{cases} i * h_i, & i = 0, 1, ..., \frac{N}{2} \\ \delta + (i - N/2) * h_i, & i = \frac{N}{2} + 1, ..., N, \end{cases}$$

where mesh spacings $h_i^{'}s$ are given by

$$h_i = \begin{cases} \frac{2\delta}{N}, & i = 0, 1, ..., \frac{N}{2} \\ \frac{2(1-\delta)}{N}, & i = \frac{N}{2} + 1, ..., N. \end{cases}$$

Remark: Shishkin's idea is used only to generate nodes and not the mesh as the present method does not require elements or element connectivity.

2.3.2 Moving least-square approximation

The field function $u(x)$ is approximated by $u^h(x)$ using MLS approximants in the domain Ω. These approximants contain three components: firstly, basis functions which are usually polynomials, secondly, weight functions which are related to nodes present in the influence domain of a particular node and lastly, the set of coefficients that depend upon the position of nodes. The domain of influence of any nodal point x_I is defined as a local neighbourhood of x_I or the domain that the particular node x_I exerts an

influence upon. The MLS approximation of the unknown function $u^h(x)$ is as follows:

$$u^h(x) = \sum_{i=1}^{m} c_i(x)a_i(x) = \mathbf{c}^T(x)\mathbf{a}(x), \tag{2.3.1}$$

where $\mathbf{c}(x)$ is a vector of monomial basis functions, m is the number of components in the basis and $\mathbf{a}(x)$ is an unknown vector of coefficients of the basis functions.

Further, the approximated values of the field function $u^h(x)$ at the nodes $x_I,\ I = 1, 2, ..., n$ lying in the influence domain of the point x, are given by

$$u^h(x, x_I) = \mathbf{c}^T(x_I)\mathbf{a}(x).$$

Following are the most common basic functions:

- Linear basis:

$$\mathbf{c}^T(x) = (1, x) \text{ in 1D.}$$
$$\mathbf{c}^T(x, y) = (1, x, y) \text{ in 2D.}$$

- Quadratic basis:

$$\mathbf{c}^T(x) = (1, x, x^2) \text{ in 1D.}$$
$$\mathbf{c}^T(x, y) = (1, x, y, x^2, y^2, xy) \text{ in 2D.}$$

We define the weighted residual functional as

$$J(a) = \sum_{I=1}^{n} w(x - x_I)[\mathbf{c}^T(x_I)\mathbf{a}(x) - u_I]^2, \tag{2.3.2}$$

where n denotes the number of nodes x_i in the support domain of the point of interest x. The nodes in the support domain of any point x are used to support or approximate the function value at x. The dimension $\mathfrak{d}_s$ of the

support domain of the point x is defined by

$$\mathfrak{d}_s = \alpha_s \mathfrak{d}_c,$$

where α_s signifies the dimensionless size of the support domain and nodal spacing at the point, x is described by the characteristic length $\mathfrak{d}_c$. $w(x-x_I)$ in the expression (2.3.2) is weight function which is generally chosen as monotonically decreasing as $|x-x_I|$ increases. In the literature, researchers have developed and employed numerous weight functions, as mentioned in Section 2.3.3. The condition $m > n$ generally leads to an ill-conditioned system of equations in MLS approximation.
On simplification, Eq. (2.3.2) can be rewritten as follows:

$$J = \mathbf{(Ca\text{-}u)}^T \mathbf{W(Ca\text{-}u)},$$

where

$$\mathbf{u}^T(x) = (u_1, u_2, u_3, ..., u_n)$$

$$\mathbf{C} = \begin{bmatrix} c_1(x_1) & c_1(x_2) & \cdots & c_1(x_n) \\ c_2(x_1) & c_2(x_2) & \cdots & c_2(x_n) \\ \vdots & \vdots & \ddots & \vdots \\ c_n(x_1) & c_n(x_2) & \cdots & c_n(x_n) \end{bmatrix}$$

and $\mathbf{W}$ is the diagonal matrix defined as

$$\mathbf{W} = \begin{bmatrix} w(\mathbf{x}-\mathbf{x_1}) & 0 & \cdots & 0 \\ 0 & w(\mathbf{x}-\mathbf{x_2}) & \cdots & 0 \\ \vdots & \vdots & \ddots & \vdots \\ 0 & 0 & \cdots & w(\mathbf{x}-\mathbf{x_n}) \end{bmatrix}$$

The minimization of J with respect to $\mathbf{a}(x)$ leads to $\frac{\partial J}{\partial \mathbf{a}} = 0$.
This gives

$$\mathbf{a}(x) = \mathbf{P}^{-1}(x)\mathbf{S}(x)u_I,$$

where

$$\mathbf{P}(x) = \sum_{I=1}^{n} w(x - x_I)\mathbf{c}(x_I)\mathbf{c}^T(x_I),$$
$$\mathbf{S}(x) = [w(x - x_1)\mathbf{c}(x_1), w(x - x_2)\mathbf{c}(x_2), ..., w(x - x_n)\mathbf{c}(x_n)].$$

Therefore, from (2.3.1), the approximated field function u^h can be computed as

$$\begin{aligned} u^h(x) &= \sum_{I=1}^{n}\sum_{j=1}^{m} c_j(x)(\mathbf{P}^{-1}(x)\mathbf{S}(x))_{jI}u_I \\ &= \sum_{I=1}^{n} \phi_I(x)u_I, \end{aligned}$$

where the shape functions $\phi_I(x),\ I = 1, 2, 3, ..., n$, are defined by

$$\begin{aligned} \phi_I(x) &= \sum_{j=1}^{m} c_j(x)(\mathbf{P}^{-1}(x)\mathbf{S}(x))_{jI} \\ &= \mathbf{c}^T\mathbf{P}^{-1}\mathbf{S}_I. \end{aligned}$$

2.3.3 Choice of weight functions

The weight function corresponding to any node provides weights for the residuals at different nodes within the support domain of the node of interest. It ensures that nodes should enter and leave the support domain smoothly so that the shape functions satisfy the compatibility condition and the approximation is globally continuous. The weight functions must be continuous and positive in the corresponding support domains. The

weight functions should satisfy the following properties:

1. $w(x - x_I) > 0$ in the support domain Ω_x of the node x,
2. $w(x - x_I) = 0$ outside the support domain Ω_x,
3. $w(|x - x_I|)$ is a monotonically decreasing function,
4. $w(|x - x_I|) \to \delta(|x - x_I|)$ as $h \to 0$,

where $\delta(|x-x_I|)$ represents the Dirac delta function and h is measure of the size of the support domain Ω_x. The weight functions are usually based on a normalized distance $s = \frac{|x-x_j|}{\mathfrak{d}_s}$, where $\mathfrak{d}_s$ denotes the radius of the influence domain. In the literature [28, 60, 71, 98, 171, 204, 230, 231, 234], there are variety of weight functions available for the MLS approach. Some of the weight functions, which are widely used in literature, are defined below. Though many researchers utilize these weight functions, some of them have been referred here.

- **Quadratic spline**: The weight function of a quadratic spline is defined as follows:

$$w(s) = \begin{cases} 1 - s^2, & 0 \leq s \leq 1 \\ 0, & s > 1. \end{cases}$$

  Singh [204] compared different weight functions (exponential, elliptical, cosine and quadratic) under EFG method for heat transfer problems. It is found that elliptical, quadratic and cosine weight functions provide acceptable results for the support domain with radius $\mathfrak{d}_s = \alpha_s * \mathfrak{d}_c$, where the scaling parameter $\mathfrak{d}_c$ satisfies $0 < \mathfrak{d}_c < 1.5$, whereas exponential weight functions provide good results for the scaling parameter $1 < \mathfrak{d}_c < 2.0$. In overall comparison, the author found that the exponential weight functions provide much better results than the other weight functions (i.e. elliptical, cosine, and quadratic) for heat transfer problems.

- **Cubic spline**: The weight function of a cubic spline is defined by

$$w(s) = \begin{cases} \frac{2}{3} - 4s^2 + 4s^3, & s \leq 1/2 \\ \frac{4}{3} - 4s + 4s^2 - \frac{4}{3}s^3, & 1/2 < s \leq 1 \\ 0, & s > 1. \end{cases}$$

  Cubic spline weight functions were firstly proposed by Dolbow and Belytschko [60] in the study of EFG method. The authors constructed cubic spline weight functions to impose C^2-continuity requirements while solving linear elastostatic problems. Some of the frequently used weight functions widely adopted by many researchers while employing the EFG methodology. Park and Leap [171] utilized the EFG method with cubic spline weight functions for solving groundwater flow problems. Yang and He [230] utilized these weight functions in the EFG method for heat transfer problems. Juan et al. [98] used cubic spline weight functions to solve the topology optimization problem of the continuum structures. Zhang et al. [237] also applied the EFG method with cubic spline weight functions for two-dimensional elastodynamics problems. Sharma [194] also successfully applied these weight functions along with the EFG method to study the heat transfer fluid flow problems over a stretching sheet.

- **Quartic spline**: The quartic spline weight function is given by

$$w(s) = \begin{cases} 1 - 6s^2 + 8s^3 - 3s^4, & s \leq 1 \\ 0, & s > 1. \end{cases}$$

  Researchers widely use these weight functions as it provides C^2 continuity. Shibata and Murakami [197] presented a stability procedure for soil-water coupled problems using the EFG method with quartic spline weight function. He et al. [87] established a hybrid EFG method and scaled boundary method known as EFG scaled boundary method. The

authors further employed quartic spline weight function in EFG formulation to carry out numerical results. Jaberzadeh et al. [93] also considered quartic weight function in EFG methodology to study thermal buckling of trapezoidal plates. Cheng et al. demonstrated improved complex variable EFG method for advection-diffusion [42]. The impact of cubic and quartic spline weight functions on computational precision has been discussed in both articles. The proposed method has higher computational accuracy while employing quartic spline weight functions. The quartic spline weight functions in the EFG technique have been adopted by various researchers for solving different problems like non-linear shallow water equations [231], static and buckling analysis of thin plate [158] etc.

- **Gaussian exponential spline**: The Gaussian exponential spline weight function is defined as

$$w(s) = \begin{cases} \frac{e^{-(s/\alpha)^2} - e^{-(1/\alpha)^2}}{1 - e^{-(1/\alpha)^2}}, & s \leq 1 \\ 0, & s > 1. \end{cases}$$

Here, the parameter α is generally chosen from the interval $[0.3, 0.5]$. The Gaussian weighting function of exponential type is one of the most commonly used weight functions. These weight functions have been initially utilized by Belytschko and his co-authors to solve elasticity and heat conduction problems [23], crack propagation problems [24] and fracture problems [71]. Following these, many researchers employed Gaussian exponential weight functions for solving various types of other problems like fractional cable equation [55], quasi three-dimensional free vibration analysis of multilayered composite plates [228] and bi-material problems [169] etc. The performance of Gaussian weight functions has been analyzed by comparison with other weight functions in [157, 248].

- **Conical weight function**: Conical weight function is defined as

$$w(s) = \begin{cases} 1 - s^{2k}, & s \leq 1 \\ 0, & s > 1. \end{cases}$$

Liu et al. [142] performed EFG formulation with conical weight function to obtain the numerical solutions to 3D electromagnetic problems. The authors compared the performance of different weight functions(cubic spline, rational formula, conical formula, negative exponential, quartic spline) by correlating the results obtained by EFG method with the exact one. The graphical results indicate that error estimation of the conical formula increases by increasing the value of scaling parameter d_c. Zhuang et al. [248] highlighted issues and sources of errors for meshless methods. The control of errors has been shown by considering three types of weight functions, i.e. rational function, an exponential function, and a conical function in the element-free Galerkin methodology. Graphical results of curve fitting problems show that the conical weight function exhibits lower error in comparison to the exponential weight function. The steady heat transfer analysis for orthotropic structure has been carried out by Zhang et al. [234] based on the proposed EFG technique. Different weight functions like cubic spline, parabola function, conical function, triangle weight function and exponential weight function have been considered. The numerical results suggest preferring cubic spline and parabola weight functions compared to the conical weight function for the heat transfer problems.

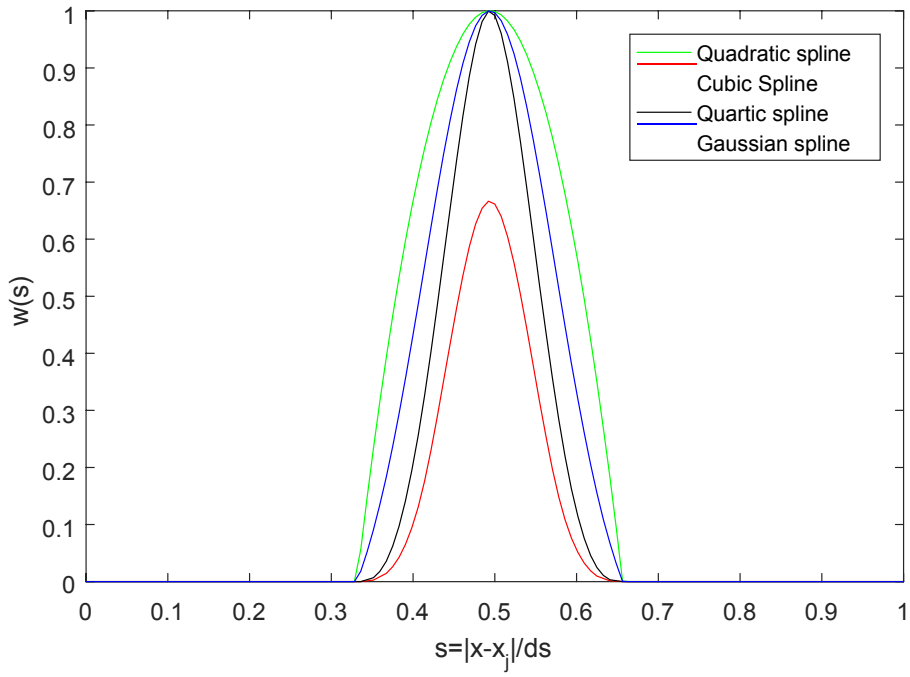

Figure 2.1: Graphical representation of different types of weight functions.

- **Cosine weight function**: The cosine weight function is defined as

$$w(s) = \begin{cases} \cos(\frac{\pi s}{2}), & 0 \leq \ s \leq 1 \\ 0, & s > 1. \end{cases}$$

Though only a few researchers have utilized the cosine weight functions in the EFG formulation, these weight functions provide C^1-continuous approximations. Bouillard and Suleau [28] successfully applied these weight functions for numerical assessment of the pollution effect governed by the Helmholtz model problem. After that, Singh [204] also mentioned the cosine weight function along with some other weight functions for the EFG formulation to solve three-dimensional heat transfer problems.

- **Hyperbolic and Elliptical weight functions** : Hyperbolic and el-

liptic weight functions are given by

$$w(s) = \begin{cases} \text{sech}(s+3), & 0 \leq \ s \leq 1 \\ 0, & s > 1, \end{cases}$$

and

$$w(s) = \begin{cases} 2\sqrt{1-s^2}, & 0 \leq \ s \leq 1 \\ 0, & s > 1, \end{cases}$$

respectively. Elliptical weight functions have been used by Singh in [204]. The author also considered exponential and cosine weight functions to carry out error and steady-state analysis for $3D$ heat transfer problems under the EFG framework.

The shapes of different weight functions at any point x in the domain have been presented in Fig. 2.1.

2.3.4 Weak formulation

Following MLS methodology, the EFG weak formulation, for the problem discussed in (2.2.1), is given by

$$\begin{aligned} \sum_j \Big[\epsilon \int_\Omega \phi_i' \phi_j' d\Omega - \int_\Omega a(x)\phi_i \phi_j' d\Omega - \int_\Omega b(x)\phi_i\phi_j d\Omega\Big] u_j \\ + \sum_l \sum_j \delta\lambda_j(-N_l\phi_j u_j)\Big|_{x=0} - \sum_l \delta\lambda_i(-N_l u_0)\Big|_{x=0} \\ + \sum_l \sum_j \delta u_l(-\phi_l N_j)\lambda_j\Big|_{x=0} + \sum_l \sum_j \delta\rho_j(-R_l\phi_j)u_j\Big|_{x=1} \\ - \sum_l^n \delta\rho_l(-R_i u_1)\Big|_{x=1} + \sum_l \sum_j \delta u_l(-\phi_l R_j)\rho_j\Big|_{x=1} \\ = \Big[\int_\Omega \phi_i f(x) d\Omega + \epsilon\phi_i(1)\frac{du}{dx}\Big|_{x=1} - \epsilon\phi_i(0)\frac{du}{dx}\Big|_{x=0}\Big]. \end{aligned} \tag{2.3.3}$$

Here, the test functions $\phi_i's$ are obtained using the moving least-square approach, as discussed in subsection 2.3.2. The last terms in Eq. (2.3.3) are due to the method of Lagrange multipliers for handling essential boundary conditions (2.2.2).
After solving and assembling nodal weak formulations, the resulting algebraic equations can be expressed in matrix form as follows:

$$\begin{bmatrix} K & G & H \\ G^T & 0 & 0 \\ H^T & 0 & 0 \end{bmatrix} \begin{bmatrix} U \\ \lambda \\ \rho \end{bmatrix} = \begin{bmatrix} F \\ q \\ q_c \end{bmatrix}$$

where

$$\begin{aligned} K_{ij} &= -\epsilon \int_\Omega \phi_i' \phi_j' d\Omega - \int_\Omega a(x)\phi_i \phi_j' d\Omega - \int_\Omega b(x)\phi_i \phi_j d\Omega, \\ F_i &= \int_\Omega \phi_i f(x) d\Omega, \\ G_{lj}^T &= -\delta\lambda_j (N_l \phi_j)\Big|_{x=0}, \quad H_{lj}^T = -\delta\rho_j (R_l \phi_j)\Big|_{x=1}, \\ q_l &= -\delta\lambda_l (N_l u_0)\Big|_{x=0}, \quad q_{c_l} = -\delta\rho_l (R_l u_1)\Big|_{x=1}, \end{aligned}$$

where $\lambda = \sum_{l=1}^{n} N_l \lambda_l$ and $\rho = \sum_{l=1}^{n} R_l \rho_l$ are Lagrange multipliers and N_I and R_I are shape functions for I^{th} node on the essential boundary.

2.4 Singularly perturbed non-linear elliptic problem

We have investigated the following non-linear singularly perturbed problem:

$$\epsilon u'' = f(u', u, x), \ x \in \Omega = (0, 1), \tag{2.4.1}$$

with essential boundary conditions defined by

$$u(0) = u_0,\ u(1) = u_1, \quad u_0, u_1 \in \mathbb{R}, \tag{2.4.2}$$

where ϵ is a small positive parameter known as singular perturbation parameter with $0 < \epsilon \ll 1$ and we suppose that $f(u', u, x)$ is non-linear term which is continuously differentiable function.

2.5 Quasilinearization technique

Quasilinearization is a standard technique that is widely used for approximating the non-linear problems by their linearized version for obtaining the approximate solutions. Since the problem under consideration is non-linear in nature, we will discuss the quasilinearization process and its convergence for such a problem in this Section.
Using the quasilinearization process by Bellman and Kalaba [20], Eq. (2.4.1) can be linearized as follows:

$$\begin{aligned}\epsilon u''^{(k+1)} =& f(u'^{(k)}, u^{(k)}, x) + (u'^{(k+1)} - u'^{(k)})\frac{\partial f}{\partial u'}(u'^{(k)}, u^{(k)}, x) \\ &+ (u^{(k+1)} - u^{(k)})\frac{\partial f}{\partial u}(u'^{(k)}, u^{(k)}, x),\end{aligned} \tag{2.5.1}$$

where $u^{(k+1)}$ stands for the approximate solution at $(k+1)$th iteration level.

2.5.1 Convergence of quasilinearization process

To establish the convergence of the quasilinearization process, Eq. (2.4.1) can be considered as

$$\begin{aligned}\epsilon u'' &= f(u), \quad 0 < x < 1, \\ u(0) &= u_0, \quad u(1) = u_1.\end{aligned}$$

By using quasilinearization process, the differential equation has been discretized in the form of given by

$$\begin{aligned} \epsilon u''^{(k+1)} &= f(u^{(k)}) + (u^{(k+1)} - u^{(k)})\frac{\partial f(u^{(k)})}{\partial u}, \quad 0 < x < 1, \\ u^{(k+1)}(0) &= u_0, \quad u^{(k+1)}(1) = u_1, \end{aligned} \tag{2.5.2}$$

where (k) denotes the iteration level. We assume $u^{(k=0)}$ be the initial guess which also incorporates the boundary conditions. Rewriting the above relation at the previous iteration step, we get

$$\epsilon u''^{(k)} = f(u^{(k-1)}) + (u^{(k)} - u^{(k-1)})\frac{\partial f(u^{(k-1)})}{\partial u}, \quad 0 < x < 1. \tag{2.5.3}$$

By subtracting Eq. (2.5.3) from Eq. (2.5.2), the following relation is obtained

$$\begin{aligned} \epsilon(u''^{(k+1)} - u''^{(k)}) =& f(u^{(k)}) - f(u^{(k-1)}) + (u^{(k+1)} - u^{(k)})\frac{\partial f(u^{(k)})}{\partial u} \\ & - (u^{(k)} - u^{(k-1)})\frac{\partial f(u^{(k-1)})}{\partial u}, \quad 0 < x < 1. \end{aligned} \tag{2.5.4}$$

The above differential equation is of second order in $(u^{(k+1)} - u^{(k)})$. Further, with the help of Green's function $G(x, r)$, the above Eq. (2.5.4) can be converted into the integral equation

$$\begin{aligned} \epsilon(u^{(k+1)} - u^{(k)}) = \int_a^b G(x, r)\Big[& f(u^{(k)}) - f(u^{(k-1)}) + (u^{(k+1)} - u^{(k)})\frac{\partial f(u^{(k)})}{\partial u} \\ & - (u^{(k)} - u^{(k-1)})\frac{\partial f(u^{(k-1)})}{\partial u}\Big] ds \quad 0 < x < 1, \end{aligned} \tag{2.5.5}$$

where $G(x, r)$ is defined as

$$G(x, r) = \begin{cases} x(r-1), & 0 \le x \le r \le 1 \\ (x-1)r, & 0 \le r \le x \le 1, \end{cases}$$

and

$$\max_{x,r} G(x,r) = \frac{1}{4}. \tag{2.5.6}$$

Now, by using mean value theorem, we get

$$f(u^{(k)}) - f(u^{(k-1)}) = (u^{(k)} - u^{(k-1)})\frac{\partial f(u^{(k-1)})}{\partial u} + \frac{(u^{(k)} - u^{(k-1)})^2}{2}\frac{\partial^2 f(\theta)}{\partial u^2}, \tag{2.5.7}$$

where $u^{(k-1)} < \theta < u^{(k)}$.

So, using Eq. (2.5.7) in Eq. (2.5.5), we get the following expression

$$\epsilon(u^{(k+1)} - u^{(k)}) = \int_a^b G(x,r)\Big[\frac{(u^{(k)} - u^{(k-1)})^2}{2}\frac{\partial^2 f(\theta)}{\partial u^2} + (u^{(k+1)} - u^{(k)})\frac{\partial f(u^{(k)})}{\partial u}\Big]ds, \quad 0 < x < 1. \tag{2.5.8}$$

Suppose

$$\max_{|u^{(k-1)}|\leq 1}\Big|\frac{\partial^2 f(\theta)}{\partial u^2}\Big| = L, \quad \max_{|u^{(k)}|\leq 1}\Big|\frac{\partial f(u^{(k)})}{\partial u}\Big| = R. \tag{2.5.9}$$

Using maximum norm over the spatial domain and using Eqs.(2.5.6) and (2.5.9) in Eq.(2.5.8), we get

$$\|(u^{(k+1)} - u^{(k)})\| \leq \frac{1}{4\epsilon}\int_a^b \Big[\frac{L}{2}(u^{(k)} - u^{(k-1)})^2 + R\|u^{(k+1)} - u^{(k)}\|\Big]ds.$$

The given inequality can be simplified to obtain

$$\begin{aligned}\|(u^{(k+1)} - u^{(k)})\|_\Omega \leq & \frac{L}{8\epsilon - 2R}\|(u^{(k)} - u^{(k-1)})\|_\Omega^2 \\ = & Q\|(u^{(k)} - u^{(k-1)})\|_\Omega^2,\end{aligned}$$

where $Q = L/(8\epsilon - 2R)$.

Thus, the quasilinearization process converges quadratically by choosing

the appropriate initial iterative approximation $u^{(k=0)}$. Therefore, in order to find the solution of the non-linear problem (2.4.1), it is sufficient to find the solution of its approximate linearized problem (2.5.1). Next, we will discuss the proposed numerical strategy to approximate the solution of the linearized problem (2.5.1).

2.5.2 Weak formulation

Following MLS, the EFG weak formulation for the linearized problem (2.5.1) is given by

$$\begin{aligned}
\sum_j \Big[& -\epsilon \int_\Omega \phi_i' \phi_j'^{(k+1)} d\Omega - \int_\Omega \frac{\partial f}{\partial u'}(u'^{(k)}, u^{(k)}, x)\phi_i \phi_j'^{(k+1)} d\Omega \\
& - \int_\Omega \frac{\partial f}{\partial u}(u'^{(k)}, u^{(k)}, x)\phi_i \phi_j^{(k+1)} d\Omega \Big] u_j^{(k+1)} + \sum_l \sum_j \delta\lambda_l(-N_l \phi_j u_j)\Big|_{x=0} \\
& - \sum_l \delta\lambda_l(-N_l u_0)\Big|_{x=0} + \sum_l \sum_j \delta u_j(-\phi_j N_l)\lambda_l\Big|_{x=0} \\
& + \sum_l \sum_j \delta\rho_l(-R_l\phi_j)u_j\Big|_{x=1} - \sum_l \delta\rho_l(-R_l u_1)\Big|_{x=1} \\
& + \sum_l \sum_j \delta u_j(-\phi_j R_l)\rho_l\Big|_{x=1} = \int_\Omega \phi_i f(x) d\Omega \\
& - \int_\Omega \frac{\partial f}{\partial u'}(u'^{(k)}, u^k, x)\phi_i \phi_j'^{(k)} d\Omega \\
& - \int_\Omega \frac{\partial f}{\partial u}((u'^{(k)}, u^k, x))u^{(k)}\phi_i \phi_j^{(k)} d\Omega \\
& + \epsilon\phi_i(1)u'\Big|_{x=1} - \epsilon\phi_i(0)u'\Big|_{x=0}.
\end{aligned}$$

On solving the above nodal weak formulations and assembling, the resulted algebraic linear equation thus obtained can be written in the matrix form

as

$$\begin{bmatrix} K & G & H \\ G^T & 0 & 0 \\ H^T & 0 & 0 \end{bmatrix} \begin{bmatrix} V \\ \lambda \\ \rho \end{bmatrix} = \begin{bmatrix} F \\ q \\ q_c \end{bmatrix},$$

where

$$\begin{aligned} K_{ij} =& -\epsilon \int_\Omega \phi_i' \phi_j'^{(k+1)} d\Omega - \int_\Omega \frac{\partial f}{\partial u'}(u'^{(k)}, u^{(k)}, x)\phi_i \phi_j'^{(k+1)} d\Omega \\ & - \int_\Omega \frac{\partial f}{\partial u}(u'^{(k)}, u^{(k)}, x)\phi_i \phi_j^{(k+1)} d\Omega, \\ G_{lj}^T =& -\delta\lambda_l (N_l \phi_j)\Big|_{x=0}, \quad H_{lj}^T = -\delta\rho_l (R_l \phi_j)\Big|_{x=1}, \\ F_i =& \int_\Omega \phi_i f(x) d\Omega \; - \int_\Omega \frac{\partial f}{\partial u'}(u'^{(k)}, u^k, x)\phi_i \phi_j'^{(k)} d\Omega \\ & - \int_\Omega \frac{\partial f}{\partial u}((u'^{(k)}, u^k, x))u^{(k)} \phi_i \phi_j^{(k)} d\Omega, \\ q_l =& -\delta\lambda_l (N_l u_0)\Big|_{x=0}, \quad q_{c_l} = -\delta\rho_l (R_l u_1)\Big|_{x=1}, \end{aligned}$$

where λ and ρ have same expressions as defined in subsection 2.3.4.

2.6 Numerical results and discussions

In the present Section, we, firstly formalize the algorithm of the proposed scheme to help the interested researchers and then illustrate it with numerical examples.

2.6.1 Algorithm for the element-free Galerkin scheme

We mention below the step-by-step algorithm for the proposed scheme:

1. Enter the given parameter values and material properties.
2. Set up the adaptive nodal coordinates in the domain of interest.

3. Set up the Gauss quadrature background points(to carry out numerical integrations), weights, and Jacobian.

4. Define the support domain of nodal points.

5. Set parameters for weight functions and calculate the weight functions for each node.

6. Define loop over Gauss integration points and do:

   (a) Construct shape functions and their derivatives at each node.

   (b) Assemble the contributions from each node to matrix K and the source vector F based on the weak formulation as defined in the last Section.

   (c) Incorporate the essential boundary conditions using the Lagrange multiplier method (G and H matrices defined above) or the penalty method.

7. Solve the global system using some efficient solver to get the nodal parameter values u_i.

Next, we will consider some linear and non-linear SPP to test the efficiency and robustness of the proposed scheme. The basis functions have been chosen as $c(x) = [1, x, x^2]$. Since the boundary layer appears in the solution of SPP, non-uniformly distributed nodes have been generated, wherein more nodes have been put in the boundary layer region as discussed in Section 2.3.1. The accuracy of the proposed method also depends upon the choice of the size of the support domain, which is taken as $2.8 \leq \alpha_s \leq 3.4$. Two-point Gauss quadrature rule has been implemented in order to approximate the resulted integrals arising due to the EFG weak formulation. The pointwise errors and maximum absolute errors have been presented for the considered

problems. These errors have been estimated by

$$e_i^N = |u(x_i) - U_h(x_i)| \quad \text{and} \quad E_\epsilon^N = \max_i e_i^N.$$

Herein, $u(x)$ and $U_h(x)$ are exact and computed EFG solutions respectively and N represent number of nodes.
To demonstrate the potential of the present approach, the numerical results obtained using the proposed numerical methodology have been compared with those cited in the literature. Computations have been performed on **MATLAB R2016a** software. Absolute errors have been presented for the numerical examples to depict the numerical efficiency and accuracy of the proposed scheme.

Example 2.6.1 *We considered the following non-homogeneous convection-diffusion singularly perturbed problem [122]*

$$\epsilon u'' + u' = 1 + 2x,$$

with Dirichlet boundary conditions

$$u(0) = 0, \ u(1) = 1.$$

Exact solution of the problem is given by

$$u(x) = x(x + 1 - 2\epsilon) + \frac{(2\epsilon - 1)(1 - e^{-x/\epsilon})}{(1 - e^{-1/\epsilon})}.$$

The problem has been solved using the proposed EFG method with exponential weight functions. Table 2.1 shows the maximum absolute errors for various values of the singular perturbation parameter ϵ and number of nodes N. The table also shows the numerical convergence of the proposed scheme.

Table 2.1: Maximum absolute errors for Example 2.6.1.

ϵ	$N = 16$	$N = 32$	$N = 64$	$N = 128$	$N = 256$
2^{-2}	5.00×10^{-3}	2.50×10^{-3}	1.20×10^{-3}	2.00×10^{-3}	1.97×10^{-3}
2^{-4}	2.45×10^{-2}	4.60×10^{-3}	2.90×10^{-3}	2.10×10^{-3}	1.96×10^{-3}
2^{-6}	5.66×10^{-2}	8.30×10^{-3}	3.80×10^{-3}	3.10×10^{-3}	2.90×10^{-3}
2^{-8}	9.05×10^{-2}	2.60×10^{-2}	9.10×10^{-3}	4.40×10^{-3}	2.50×10^{-3}
2^{-10}	7.74×10^{-2}	6.10×10^{-3}	8.50×10^{-3}	4.50×10^{-3}	2.21×10^{-3}
2^{-12}	8.22×10^{-2}	6.00×10^{-3}	4.90×10^{-3}	4.30×10^{-3}	3.40×10^{-3}
2^{-14}	8.34×10^{-2}	6.10×10^{-3}	5.40×10^{-3}	3.80×10^{-3}	2.90×10^{-3}
2^{-16}	8.37×10^{-2}	6.10×10^{-3}	5.55×10^{-3}	3.80×10^{-3}	2.90×10^{-3}
2^{-18}	8.37×10^{-2}	6.10×10^{-3}	5.55×10^{-3}	3.80×10^{-3}	2.90×10^{-3}

Table 2.2: Comparison of numerical results of Example 2.6.1 with the results of [122] with $\epsilon = 10^{-4}$.

x	Exact solution	$u(x)$ [122]	Present method	Absolute errors
0.0001	-0.653191	-0.632020	-0.653352	$1.61E-04$
0.0020	-0.997783	-0.997996	-0.996840	$9.43E-04$
0.1000	-0.887528	-0.890000	-0.887320	$2.08E-04$
0.3000	-0.607484	-0.610000	-0.607528	$4.40E-05$
0.5000	-0.247780	-0.250000	-0.248012	$2.32E-04$
0.7000	0.191586	0.190000	0.191220	$3.66E-04$
0.9000	0.710613	0.709000	0.710274	$3.39E-04$
1.0000	1.000000	1.000000	1.000000	0

It can be recognized that the proposed scheme approximates the solution very efficiently even for extremely small values of ϵ such as $\epsilon = 2^{-18}$ and for a very less number of nodal points $N = 32$ which clearly depicts the robustness of the scheme. A comparison of the solutions obtained using the proposed scheme has been made with those obtained by Kumar et al. [122] in Table 2.2 for $\epsilon = 10^{-4}$.

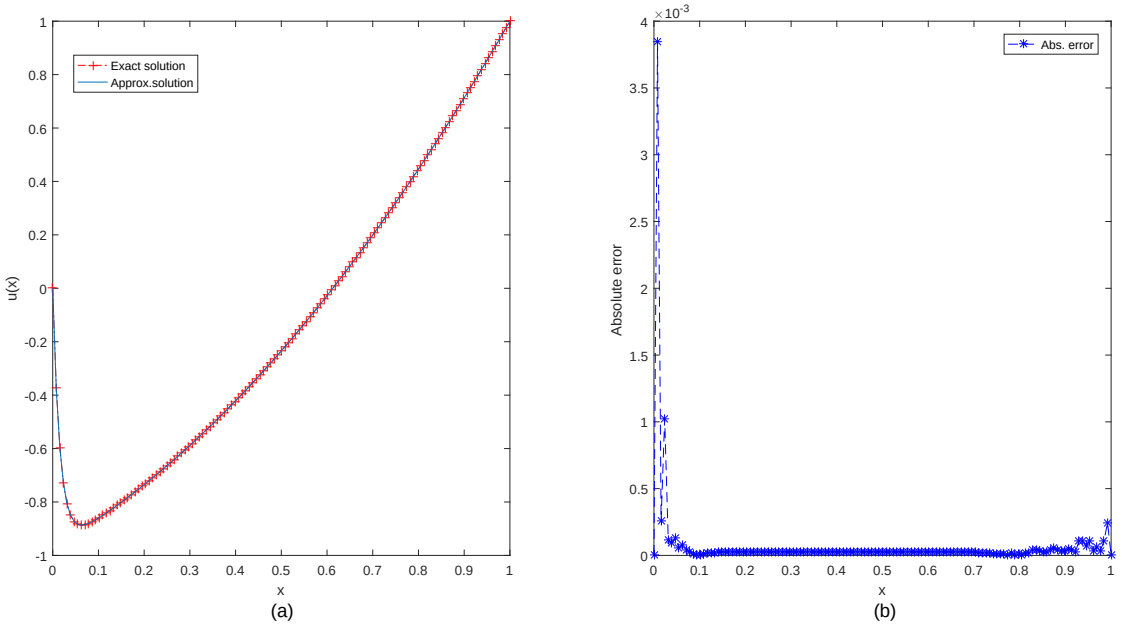

Figure 2.2: (a) Exact and EFG solution plot; (b) Pointwise absolute error plot for $\epsilon = 2^{-7},\ N = 128$ for Example 2.6.1.

It can clearly be observed that the proposed scheme provides a better solution for the considered problem. Fig. 2.2 illustrates the contrast of the numerical solution with exact solution along with the maximum absolute error for $\epsilon = 2^{-6}$, $N = 128$. One can easily see in the Figure that the EFG solution matches the exact one with great accuracy.

Example 2.6.2 *Consider the following homogeneous problem [122]*

$$\epsilon u'' + u' - u = 0,$$

with

$$u(0) = 1,\ \textit{and}\ u(1) = 1.$$

Its exact solution is given by

$$u(x) = \frac{(e^{m_2} - 1)e^{m_1 x} + (1 - e^{m_1})e^{m_2 x}}{e^{m_2} - e^{m_1}},$$

where

$$m_1 = \frac{-1+\sqrt{1+4\epsilon}}{2\epsilon}, \quad m_2 = \frac{-1-\sqrt{1+4\epsilon}}{2\epsilon}.$$

When the singular perturbation parameter ϵ approaches zero, the considered problem exhibits boundary layers at x=0. The considered problem has been examined by Kumar et al. [122] by using the boundary value technique. Table 2.3, which shows the maximum absolute errors obtained for various values of ϵ and N, testifies the good performance of the EFG method. Table 2.4 exhibits the contrast between absolute errors attained by the proposed scheme and the boundary value approach in [122]. Plot 2.3(a) illustrates the comparison of the exact and computed solutions for $\epsilon = 2^{-12}$ and $N = 128$. The plot clearly depicts that the proposed method is robust enough to capture even very sharp boundary layers. Maximum pointwise errors have been plotted in Plot 2.3(b) over the whole domain.

Table 2.3: Maximum absolute errors for Example 2.6.2.

ϵ	$N = 16$	$N = 32$	$N = 64$	$N = 128$	$N = 256$
2^{-2}	2.00×10^{-3}	1.50×10^{-3}	1.00×10^{-3}	2.00×10^{-3}	1.98×10^{-3}
2^{-4}	7.00×10^{-3}	3.40×10^{-3}	2.20×10^{-3}	1.90×10^{-3}	1.90×10^{-3}
2^{-6}	1.05×10^{-2}	4.00×10^{-3}	2.50×10^{-3}	2.00×10^{-3}	1.50×10^{-3}
2^{-8}	3.81×10^{-2}	4.60×10^{-3}	5.00×10^{-3}	2.30×10^{-3}	1.93×10^{-3}
2^{-10}	3.61×10^{-2}	3.70×10^{-3}	3.40×10^{-3}	2.30×10^{-3}	2.20×10^{-3}
2^{-12}	3.54×10^{-2}	3.50×10^{-3}	3.20×10^{-3}	2.70×10^{-3}	2.69×10^{-3}
2^{-14}	3.52×10^{-2}	3.50×10^{-3}	3.40×10^{-3}	2.50×10^{-3}	2.40×10^{-3}
2^{-16}	3.52×10^{-2}	3.50×10^{-3}	3.40×10^{-3}	2.54×10^{-3}	2.40×10^{-3}

Table 2.4: Comparison of pointwise absolute errors of the EFG method and boundary value method (BVM) [122] for Example 2.6.2 for $\epsilon = 10^{-4}$.

x	Exact solution	Present method	Abs.errors(EFGM)	Abs.errors(BVM)
0.0	1.000000	1.000000	0.000000	0.000000
0.1	0.404952	0.404784	0.000168	0.000365
0.3	0.495583	0.495747	0.000164	0.000347
0.5	0.607250	0.607150	0.000100	0.000302
0.7	0.745500	0.745398	0.000102	0.000222
0.9	0.954685	0.954679	0.000006	0.000090
1.0	1.000000	1.000000	0.000000	0.000000

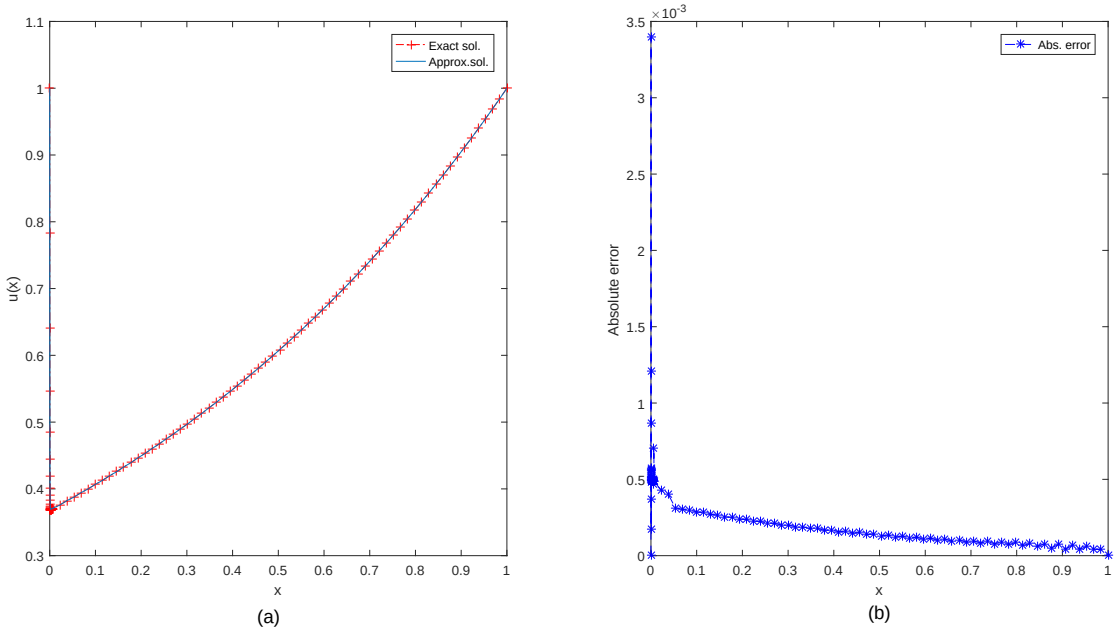

Figure 2.3: (a) Exact and EFG solution plot; (b) Pointwise absolute error plot for $\epsilon = 2^{-12}$, $N = 64$ for Example 2.6.2.

Example 2.6.3 *Consider the following variable coefficients singularly perturbed problem [104]*

$$\epsilon u'' + (1+x)^2 u' + 2(1+x)u = f(x),$$

with boundary conditions

$$u(a) = 0, \ u(b) = e^{-1/2} - e^{-7/3\epsilon},$$

where $f(x)$ is so chosen to satisfy the exact solution

$$u(x) = e^{-x/2} - e^{-x(x^2+3x+3)/3\epsilon}.$$

The proposed EFG scheme has been employed to solve the problem 2.6.3. The problem has been solved by considering different weight functions and using both the linear and the quadratic basis functions. Comparisons have been made for different weight functions in both the cases and the results have been tabulated in Tables 2.5 and 2.6 for 128 nodes and different values of singular perturbation parameter ϵ. One can easily observe that the present scheme provides more accurate results by utilizing the Gaussian exponential and cubic spline weight functions with shape parameter $\alpha = 0.3$ for both linear and quadratic basis functions. Also, as expected, the numerical results are more accurate in the case of quadratic basis functions in comparison to the linear basis functions.

Table 2.5: Maximum absolute errors for Example 2.6.3 for different values of ϵ with linear basis functions.

ϵ	Quadratic spline	Cubic spline	Quartic spline	Gaussian exp.spline	Cosine function	Conical function	Hyperbolic function	Elliptic function
2^{-2}	1.51×10^{-2}	1.60×10^{-4}	1.54×10^{-2}	3.57×10^{-5}	1.18×10^{-2}	2.01×10^{-2}	1.45×10^{-1}	7.10×10^{-3}
2^{-4}	$6.08\times10-2$	3.48×10^{-3}	5.32×10^{-2}	5.06×10^{-4}	4.10×10^{-2}	9.63×10^{-2}	5.60×10^{-1}	3.45×10^{-2}
2^{-6}	5.85×10^{-2}	5.62×10^{-3}	5.49×10^{-2}	8.49×10^{-4}	5.30×10^{-2}	9.58×10^{-2}	6.83×10^{-1}	4.51×10^{-2}
2^{-8}	9.08×10^{-2}	5.57×10^{-3}	5.23×10^{-2}	8.54×10^{-4}	5.86×10^{-2}	9.73×10^{-2}	6.91×10^{-1}	4.60×10^{-2}
2^{-10}	8.57×10^{-2}	5.58×10^{-3}	5.14×10^{-2}	8.80×10^{-4}	5.46×10^{-2}	9.83×10^{-2}	6.76×10^{-1}	4.57×10^{-2}
2^{-12}	7.41×10^{-2}	5.58×10^{-3}	5.07×10^{-2}	8.60×10^{-4}	5.36×10^{-2}	9.26×10^{-2}	6.74×10^{-1}	4.72×10^{-2}
2^{-14}	7.39×10^{-2}	5.59×10^{-3}	5.08×10^{-2}	8.08×10^{-4}	5.34×10^{-2}	9.18×10^{-2}	6.73×10^{-1}	4.69×10^{-2}
2^{-16}	7.44×10^{-2}	5.60×10^{-3}	5.47×10^{-2}	8.24×10^{-4}	5.33×10^{-2}	9.18×10^{-2}	6.73×10^{-1}	4.64×10^{-2}
2^{-18}	7.48×10^{-2}	5.60×10^{-3}	5.37×10^{-2}	8.33×10^{-4}	5.33×10^{-2}	9.18×10^{-2}	6.73×10^{-1}	4.64×10^{-2}
2^{-20}	7.49×10^{-2}	5.60×10^{-3}	5.34×10^{-2}	8.36×10^{-4}	5.33×10^{-2}	9.18×10^{-2}	6.73×10^{-1}	4.64×10^{-2}
2^{-22}	7.49×10^{-2}	5.60×10^{-3}	5.33×10^{-2}	8.36×10^{-4}	5.33×10^{-2}	9.18×10^{-2}	6.73×10^{-1}	4.64×10^{-2}
2^{-24}	7.49×10^{-2}	5.60×10^{-3}	5.33×10^{-2}	8.36×10^{-4}	5.33×10^{-2}	9.18×10^{-2}	6.73×10^{-1}	4.64×10^{-2}

Table 2.6: Maximum absolute errors for Example 2.6.3 for different values of ϵ with quadratic basis functions.

ϵ	Quadratic spline	Cubic spline	Quartic spline	Gaussian exp.spline	Cosine function	Conical function	Hyperbolic function	Elliptic function
2^{-2}	2.27×10^{-2}	1.78×10^{-3}	3.20×10^{-1}	3.35×10^{-4}	5.90×10^{-3}	4.50×10^{-3}	4.02×10^{-2}	1.98×10^{-2}
2^{-4}	9.69×10^{-2}	2.55×10^{-3}	1.47×10^{-1}	9.30×10^{-4}	2.10×10^{-2}	2.07×10^{-2}	1.24×10^{-1}	7.23×10^{-2}
2^{-6}	1.18×10^{-1}	2.83×10^{-3}	3.96×10^{-1}	7.66×10^{-4}	2.73×10^{-2}	2.72×10^{-2}	1.28×10^{-1}	8.28×10^{-2}
2^{-8}	1.18×10^{-1}	1.09×10^{-3}	7.82×10^{-1}	7.09×10^{-4}	2.60×10^{-2}	2.51×10^{-2}	1.27×10^{-1}	8.48×10^{-2}
2^{-10}	1.19×10^{-1}	6.78×10^{-4}	8.18×10^{-1}	7.36×10^{-4}	2.94×10^{-2}	2.48×10^{-2}	1.25×10^{-1}	8.52×10^{-2}
2^{-12}	1.19×10^{-1}	7.03×10^{-4}	8.01×10^{-1}	7.34×10^{-4}	2.32×10^{-2}	2.44×10^{-2}	1.27×10^{-1}	8.05×10^{-2}
2^{-14}	1.19×10^{-1}	7.06×10^{-4}	8.60×10^{-1}	7.34×10^{-4}	2.37×10^{-2}	2.44×10^{-2}	1.27×10^{-1}	8.05×10^{-2}
2^{-16}	1.19×10^{-1}	7.13×10^{-4}	8.00×10^{-1}	7.34×10^{-4}	2.37×10^{-2}	2.43×10^{-2}	1.27×10^{-1}	8.05×10^{-2}
2^{-18}	1.19×10^{-1}	7.22×10^{-4}	7.75×10^{-1}	7.35×10^{-4}	2.37×10^{-2}	2.43×10^{-2}	1.27×10^{-1}	8.05×10^{-2}
2^{-20}	1.19×10^{-1}	7.42×10^{-4}	7.62×10^{-1}	7.35×10^{-4}	2.37×10^{-2}	2.43×10^{-2}	1.27×10^{-1}	8.05×10^{-2}
2^{-22}	1.19×10^{-1}	7.48×10^{-4}	7.84×10^{-1}	7.35×10^{-4}	2.37×10^{-2}	2.43×10^{-2}	1.27×10^{-1}	8.05×10^{-2}
2^{-24}	1.19×10^{-1}	7.50×10^{-4}	7.41×10^{-1}	7.35×10^{-4}	2.37×10^{-2}	2.43×10^{-2}	1.27×10^{-1}	8.05×10^{-2}

Table 2.7: Maximum absolute errors for Example 2.6.3 for different values of ϵ.

ϵ	$N=16$	$N=32$	$N=64$	$N=128$	$N=256$
2^{-2}	4.40×10^{-3}	2.90×10^{-3}	5.00×10^{-4}	3.35×10^{-4}	1.35×10^{-3}
2^{-4}	7.90×10^{-3}	7.40×10^{-3}	8.00×10^{-4}	9.30×10^{-4}	1.54×10^{-3}
2^{-6}	1.18×10^{-2}	6.70×10^{-3}	1.00×10^{-3}	7.66×10^{-4}	4.87×10^{-4}
2^{-8}	1.76×10^{-2}	6.10×10^{-3}	1.10×10^{-3}	7.09×10^{-4}	2.14×10^{-4}
2^{-10}	2.17×10^{-2}	6.30×10^{-3}	1.10×10^{-3}	7.36×10^{-4}	2.20×10^{-4}
2^{-12}	2.20×10^{-2}	6.70×10^{-3}	1.10×10^{-3}	7.34×10^{-4}	2.22×10^{-4}
2^{-14}	2.20×10^{-2}	6.70×10^{-3}	1.10×10^{-3}	7.34×10^{-4}	2.24×10^{-4}
2^{-16}	2.20×10^{-2}	6.70×10^{-3}	1.10×10^{-3}	7.34×10^{-4}	2.27×10^{-4}

The problem has been solved again for different values of ϵ and the different number of nodes by considering quadratic basis and Gaussian exponential spline weight functions. The $L_\infty-$errors have been presented in Table 2.7. It can be observed that for each ϵ, the maximum pointwise absolute errors decrease as the number of nodes increases.

Table 2.8: Comparison of $L_\infty-$errors for fitted mesh finite difference method (FMFDM) [104] and EFG method for Example 2.6.3.

ϵ	$N=64$		$N=128$		$N=256$		$N=512$	
	FMFDM	EFGM	FMFDM	EFGM	FMFDM	EFGM	FMFDM	EFGM
2^{-4}	0.29×10^{-2}	0.81×10^{-3}	0.73×10^{-3}	0.93×10^{-3}	0.18×10^{-3}	0.15×10^{-3}	0.46×10^{-4}	0.30×10^{-3}
2^{-8}	0.39×10^{-1}	0.11×10^{-2}	0.12×10^{-1}	0.70×10^{-3}	0.38×10^{-2}	0.21×10^{-3}	0.12×10^{-2}	0.19×10^{-2}
10^{-4}	0.38×10^{-1}	0.10×10^{-2}	0.11×10^{-1}	0.73×10^{-3}	0.37×10^{-2}	0.21×10^{-3}	0.12×10^{-2}	0.19×10^{-2}
10^{-5}	0.38×10^{-1}	0.11×10^{-2}	0.11×10^{-1}	0.73×10^{-3}	0.37×10^{-2}	0.22×10^{-3}	0.12×10^{-2}	0.19×10^{-2}
10^{-6}	0.38×10^{-1}	0.11×10^{-2}	0.11×10^{-1}	0.73×10^{-3}	0.37×10^{-2}	0.22×10^{-3}	0.12×10^{-2}	0.19×10^{-2}

This clearly depicts that the proposed scheme converges numerically. The results thus obtained from the proposed scheme have also been compared with those cited in the literature in Table 2.8.

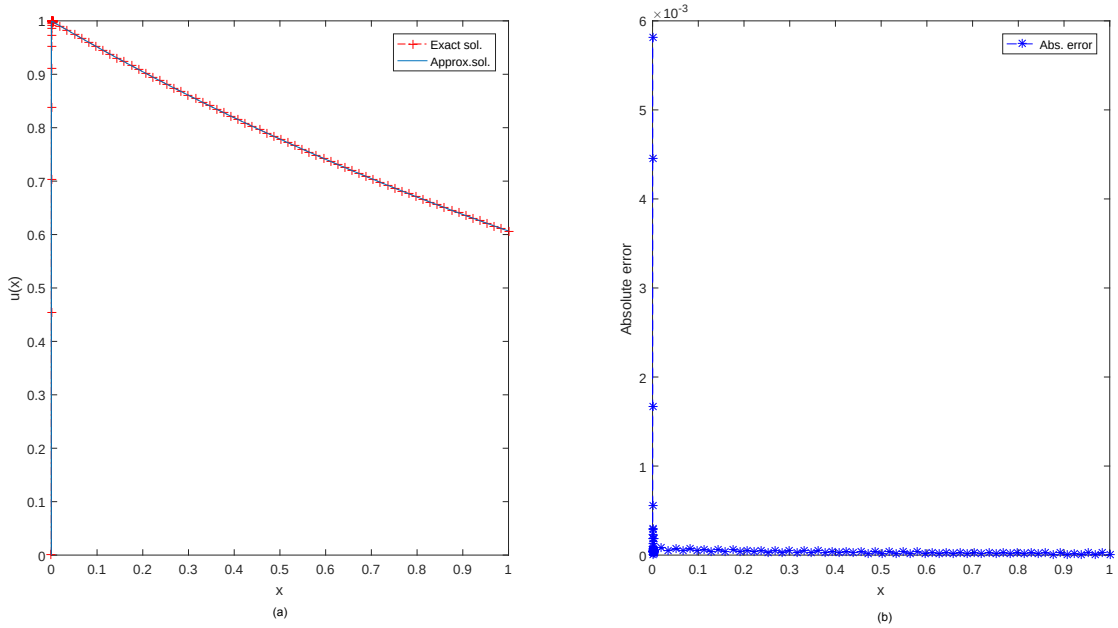

Figure 2.4: (a) Exact and EFG solution plot; (b) Pointwise absolute error plot for $\epsilon = 10^{-4},\ N = 128$ for Example 2.6.3 using linear basis and cubic spline weight functions

It can be noticed that the proposed scheme provides comparative and better accurate results. Fig. 2.4 also exhibits that the EFG scheme is very efficient in capturing the sharp boundary layers.

Example 2.6.4 *The following variable coefficients convection-diffusion sin-*

gularly perturbed problem [104] has been considered:

$$\epsilon u'' + (1+x)^3 u' = f(x),$$

with boundary conditions

$$u(0) = 2,\ u(1) = \frac{e^{-15/4\epsilon}}{8} + e^{-1/2}.$$

Its exact solution is given by

$$u(x) = \frac{e^{-[(x+1)^4-1]/4\epsilon}}{(x+1)^3} + e^{-x/2}.$$

Table 2.9: Maximum absolute errors for Example 2.6.4 for different values of ϵ with linear basis functions.

ϵ	Quadratic spline	Cubic spline	Quartic spline	Gaussian exp.spline	Cosine function	Conical function	Hyperbolic function	Elliptic function
2^{-2}	7.14×10^{-1}	4.36×10^{-2}	5.05×10^{-2}	4.37×10^{-2}	5.74×10^{-2}	3.55×10^{-2}	2.71×10^{-1}	3.72×10^{-2}
2^{-4}	2.60×10^{-1}	6.17×10^{-3}	5.55×10^{-2}	7.51×10^{-3}	4.90×10^{-2}	3.61×10^{-2}	4.98×10^{-1}	4.53×10^{-2}
2^{-6}	2.90×10^{-1}	4.38×10^{-3}	4.11×10^{-2}	5.10×10^{-4}	5.95×10^{-2}	3.80×10^{-2}	4.35×10^{-1}	3.55×10^{-2}
2^{-8}	4.41×10^{-1}	4.55×10^{-3}	4.24×10^{-2}	4.24×10^{-4}	4.90×10^{-2}	3.71×10^{-2}	4.18×10^{-1}	3.36×10^{-2}
2^{-10}	4.41×10^{-1}	4.55×10^{-3}	4.38×10^{-2}	5.88×10^{-4}	5.17×10^{-2}	3.86×10^{-2}	4.18×10^{-1}	3.29×10^{-2}
2^{-12}	4.40×10^{-1}	4.55×10^{-3}	4.11×10^{-2}	7.09×10^{-4}	5.31×10^{-2}	3.79×10^{-2}	4.73×10^{-1}	3.26×10^{-2}
2^{-14}	4.40×10^{-1}	4.56×10^{-3}	4.63×10^{-2}	8.13×10^{-4}	5.34×10^{-2}	3.78×10^{-2}	4.21×10^{-1}	3.27×10^{-2}
2^{-16}	4.40×10^{-1}	4.56×10^{-3}	5.85×10^{-2}	8.57×10^{-4}	5.35×10^{-2}	3.78×10^{-2}	4.21×10^{-1}	3.27×10^{-2}
2^{-18}	4.40×10^{-1}	4.56×10^{-3}	5.96×10^{-2}	8.70×10^{-4}	5.35×10^{-2}	3.78×10^{-2}	4.20×10^{-1}	3.27×10^{-2}
2^{-20}	4.40×10^{-1}	4.56×10^{-3}	5.35×10^{-2}	8.74×10^{-4}	5.35×10^{-2}	3.78×10^{-2}	4.20×10^{-1}	3.27×10^{-2}
2^{-22}	4.40×10^{-1}	4.56×10^{-3}	5.91×10^{-2}	8.74×10^{-4}	5.35×10^{-2}	3.78×10^{-2}	4.20×10^{-1}	3.27×10^{-2}
2^{-24}	4.40×10^{-1}	4.56×10^{-3}	5.99×10^{-2}	8.74×10^{-4}	5.35×10^{-2}	3.78×10^{-2}	4.20×10^{-1}	3.27×10^{-2}

The problem 2.6.4 has boundary layers at $x = 0$ for small values of the singular perturbation parameter ϵ. For this problem also, it can be easily noticed in both the cases, i.e. linear basis functions(Table 2.9) and quadratic basis functions(Table 2.10), that the Gaussian exponential spline weight functions provide better results in comparison to the other weight functions

for all values of the singular perturbation parameter ϵ.

Table 2.10: Maximum absolute errors for Example 2.6.4 for different values of ϵ with quadratic basis functions.

ϵ	Quadratic spline	Cubic spline	Quartic spline	Gaussian exp.spline	Cosine function	Conical function	Hyperbolic function	Elliptic function
2^{-2}	8.26×10^{-2}	4.33×10^{-2}	2.87×10^{-1}	4.36×10^{-2}	4.60×10^{-2}	4.28×10^{-2}	7.32×10^{-2}	4.41×10^{-2}
2^{-4}	1.88×10^{-1}	7.46×10^{-3}	4.21×10^{-1}	7.80×10^{-3}	2.91×10^{-2}	2.12×10^{-2}	1.73×10^{-1}	1.17×10^{-2}
2^{-6}	1.91×10^{-1}	2.71×10^{-3}	3.43×10^{-1}	8.78×10^{-4}	2.63×10^{-2}	2.32×10^{-2}	1.55×10^{-1}	7.60×10^{-3}
2^{-8}	1.77×10^{-1}	1.07×10^{-3}	6.67×10^{-1}	5.57×10^{-4}	2.37×10^{-2}	2.42×10^{-2}	1.51×10^{-1}	6.10×10^{-3}
2^{-10}	1.61×10^{-1}	7.09×10^{-4}	8.38×10^{-1}	2.74×10^{-4}	2.84×10^{-2}	2.46×10^{-2}	1.50×10^{-1}	5.90×10^{-3}
2^{-12}	1.86×10^{-1}	7.19×10^{-4}	8.37×10^{-1}	2.83×10^{-4}	2.41×10^{-2}	2.45×10^{-2}	1.54×10^{-1}	6.10×10^{-3}
2^{-14}	1.86×10^{-1}	7.23×10^{-4}	8.85×10^{-1}	3.05×10^{-4}	2.39×10^{-2}	2.47×10^{-2}	1.53×10^{-1}	5.90×10^{-3}
2^{-16}	1.86×10^{-1}	7.21×10^{-4}	8.21×10^{-1}	3.02×10^{-4}	2.38×10^{-2}	2.47×10^{-2}	1.53×10^{-1}	6.10×10^{-3}
2^{-18}	1.86×10^{-1}	7.19×10^{-4}	8.15×10^{-1}	3.01×10^{-4}	2.38×10^{-2}	2.47×10^{-2}	1.53×10^{-1}	6.20×10^{-3}
2^{-20}	1.86×10^{-1}	7.14×10^{-4}	8.17×10^{-1}	3.01×10^{-4}	2.38×10^{-2}	2.47×10^{-2}	1.53×10^{-1}	6.20×10^{-3}
2^{-22}	1.86×10^{-1}	7.14×10^{-4}	8.14×10^{-1}	3.01×10^{-4}	2.38×10^{-2}	2.47×10^{-2}	1.53×10^{-1}	6.20×10^{-3}
2^{-24}	1.86×10^{-1}	7.14×10^{-4}	8.20×10^{-1}	3.01×10^{-4}	2.38×10^{-2}	2.47×10^{-2}	1.53×10^{-1}	6.20×10^{-3}

The maximum absolute errors obtained by the proposed method for different values of ϵ and N have been presented in Table 2.11. From all these tables, one can easily conclude the numerical convergence of the proposed scheme.

Table 2.11: $L_\infty-$errors for Example 2.6.4 for different values of ϵ for quadratic basis and Gaussian weight functions.

ϵ	$N=16$	$N=32$	$N=64$	$N=128$	$N=256$
2^{-2}	4.25×10^{-2}	4.31×10^{-2}	4.37×10^{-2}	4.36×10^{-2}	4.22×10^{-2}
2^{-4}	1.45×10^{-2}	8.40×10^{-3}	7.70×10^{-3}	9.80×10^{-3}	6.40×10^{-3}
2^{-6}	1.37×10^{-2}	2.30×10^{-3}	1.40×10^{-3}	8.78×10^{-4}	1.43×10^{-4}
2^{-8}	1.81×10^{-2}	3.40×10^{-2}	7.00×10^{-4}	5.57×10^{-4}	1.30×10^{-4}
2^{-10}	1.92×10^{-2}	3.80×10^{-3}	7.00×10^{-4}	2.74×10^{-4}	2.10×10^{-4}
2^{-12}	1.95×10^{-2}	4.00×10^{-3}	7.00×10^{-4}	2.83×10^{-4}	3.00×10^{-4}
2^{-14}	1.96×10^{-2}	4.00×10^{-3}	7.00×10^{-4}	3.05×10^{-4}	3.00×10^{-4}
2^{-16}	1.96×10^{-2}	4.00×10^{-3}	8.00×10^{-4}	3.02×10^{-4}	3.00×10^{-4}

Table 2.12: Comparison of $L_\infty-$errors for FMFDM [104] and EFG method for Example 2.6.4.

ϵ	$N=64$		$N=128$		$N=256$		$N=512$	
	FMFDM	EFGM	FMFDM	EFGM	FMFDM	EFGM	FMFDM	EFGM
2^{-8}	0.39×10^{-1}	0.90×10^{-3}	0.12×10^{-1}	0.57×10^{-3}	0.39×10^{-2}	0.13×10^{-3}	0.12×10^{-2}	0.11×10^{-2}
10^{-4}	0.38×10^{-1}	0.80×10^{-3}	0.11×10^{-1}	0.21×10^{-3}	0.37×10^{-2}	0.46×10^{-3}	0.12×10^{-2}	0.42×10^{-3}
10^{-5}	0.38×10^{-1}	0.81×10^{-3}	0.11×10^{-1}	0.21×10^{-3}	0.37×10^{-2}	0.46×10^{-3}	0.12×10^{-2}	0.41×10^{-3}
10^{-6}	0.38×10^{-1}	0.82×10^{-3}	0.11×10^{-1}	0.20×10^{-3}	0.37×10^{-2}	0.47×10^{-3}	0.12×10^{-2}	0.41×10^{-3}
10^{-7}	0.38×10^{-1}	0.82×10^{-3}	0.11×10^{-1}	0.20×10^{-3}	0.37×10^{-2}	0.47×10^{-3}	0.12×10^{-2}	0.38×10^{-3}
10^{-8}	0.38×10^{-1}	0.82×10^{-3}	0.11×10^{-1}	0.20×10^{-3}	0.37×10^{-2}	0.47×10^{-3}	0.12×10^{-2}	0.38×10^{-3}

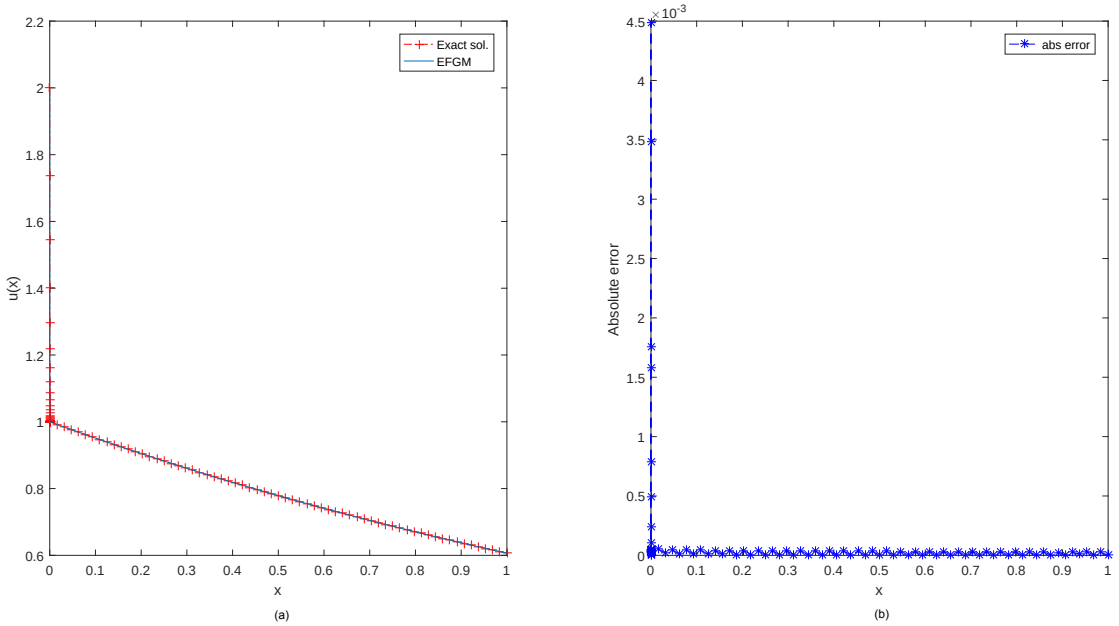

Figure 2.5: (a) Exact and EFG solution plot; (b) Pointwise absolute error plot for $\epsilon = 2^{-7}$, $N = 128$ for Example 2.6.4 using linear basis and cubic weight functions.

Comparison of the EFG method results in Table 2.12 with those cited in the literature for different values of ϵ also justifies the efficiency of the proposed EFG scheme. In plots (a) and (b) of Fig. 2.5, comparison of the EFG, the exact solutions and the L_∞-errors have been plotted. The Figure shows that very sharp boundary layers appear in the solution at $x = 0$ and the proposed EFG scheme is efficient enough to capture these layers efficiently even for very small values of ϵ. The L_∞-error plot also presents the stability

of the proposed scheme.

Example 2.6.5 *Consider the following non-linear singularly perturbed problem [144]*

$$\epsilon u'' + 2u' + e^u = 0,$$

with boundary conditions

$$u(0) = 0, \quad u(1) = 0.$$

The exact solution of the above problem is not available, however, a close approximation of the exact solution of the problem is considered to be

$$u(x) = -\ln\left(\frac{x+1}{2}\right) + \ln\left(\frac{1}{2}\right)e^{-2x/\epsilon}. \tag{2.6.1}$$

Table 2.13: Maximum absolute errors for Example 2.6.5 for different values of ϵ with linear basis functions.

ϵ	Quadratic spline	Cubic spline	Quartic spline	Gaussian exp.spline	Cosine function	Conical function	Hyperbolic function	Elliptic function
2^{-2}	3.40×10^{-2}	2.83×10^{-2}	8.09×10^{-2}	2.83×10^{-2}	3.35×10^{-2}	3.03×10^{-2}	1.14×10^{-1}	2.71×10^{-1}
2^{-4}	2.79×10^{-1}	1.88×10^{-2}	7.19×10^{-2}	1.55×10^{-2}	3.15×10^{-2}	1.18×10^{-1}	3.60×10^{-1}	5.40×10^{-1}
2^{-6}	1.03×10^{-1}	6.77×10^{-3}	6.01×10^{-2}	5.72×10^{-3}	8.49×10^{-2}	1.32×10^{-1}	4.14×10^{-1}	5.26×10^{-1}
2^{-8}	1.07×10^{-1}	3.38×10^{-3}	6.26×10^{-2}	1.78×10^{-3}	8.78×10^{-2}	1.35×10^{-1}	4.45×10^{-1}	5.09×10^{-1}
2^{-10}	1.08×10^{-1}	3.39×10^{-3}	6.33×10^{-2}	6.64×10^{-4}	8.87×10^{-2}	1.36×10^{-1}	4.28×10^{-1}	5.04×10^{-1}
2^{-12}	1.08×10^{-1}	3.39×10^{-3}	6.26×10^{-2}	5.53×10^{-4}	8.89×10^{-2}	1.36×10^{-1}	4.41×10^{-1}	5.06×10^{-1}
2^{-14}	1.08×10^{-1}	3.40×10^{-3}	6.29×10^{-2}	5.51×10^{-4}	8.86×10^{-2}	1.36×10^{-1}	3.91×10^{-1}	4.96×10^{-1}
2^{-16}	1.08×10^{-1}	3.41×10^{-3}	6.51×10^{-2}	5.63×10^{-4}	8.84×10^{-2}	1.36×10^{-1}	3.96×10^{-1}	4.99×10^{-1}
2^{-18}	1.08×10^{-1}	3.41×10^{-3}	6.42×10^{-2}	5.67×10^{-4}	8.83×10^{-2}	1.36×10^{-1}	3.97×10^{-1}	5.00×10^{-1}
2^{-20}	1.08×10^{-1}	3.41×10^{-3}	6.41×10^{-2}	5.68×10^{-4}	8.83×10^{-2}	1.36×10^{-1}	3.97×10^{-1}	5.00×10^{-1}
2^{-22}	1.08×10^{-1}	3.41×10^{-3}	6.41×10^{-2}	5.68×10^{-4}	8.83×10^{-2}	1.36×10^{-1}	3.97×10^{-1}	5.00×10^{-1}
2^{-24}	1.08×10^{-1}	3.41×10^{-3}	6.41×10^{-2}	5.68×10^{-4}	8.82×10^{-2}	1.36×10^{-1}	3.97×10^{-1}	5.00×10^{-1}

Alike the above test problems, comparisons of the EFG solutions obtained using different weight functions for both the linear and the quadratic basis

functions have been presented in Tables 2.13 and 2.14 respectively.

Table 2.14: Maximum absolute errors for Example 2.6.5 for different values of ϵ with quadratic basis functions.

ϵ	Quadratic spline	Cubic spline	Quartic spline	Gaussian exp.spline	Cosine function	Conical function	Hyperbolic function	Elliptic function
2^{-2}	2.88×10^{-2}	2.83×10^{-2}	2.87×10^{-2}	2.83×10^{-2}	2.86×10^{-2}	3.03×10^{-2}	3.02×10^{-2}	4.04×10^{-2}
2^{-4}	2.01×10^{-2}	1.61×10^{-2}	3.29×10^{-1}	1.53×10^{-2}	1.95×10^{-2}	6.08×10^{-2}	5.67×10^{-2}	6.63×10^{-2}
2^{-6}	2.31×10^{-2}	7.76×10^{-3}	3.15×10^{-1}	5.15×10^{-3}	1.99×10^{-2}	6.04×10^{-2}	6.18×10^{-2}	8.89×10^{-2}
2^{-8}	2.40×10^{-2}	2.15×10^{-3}	2.10×10^{-1}	1.88×10^{-3}	2.07×10^{-2}	6.04×10^{-2}	6.43×10^{-2}	7.18×10^{-2}
2^{-10}	2.40×10^{-2}	8.66×10^{-4}	2.58×10^{-1}	9.85×10^{-4}	2.09×10^{-2}	6.03×10^{-2}	6.43×10^{-2}	6.17×10^{-2}
2^{-12}	2.40×10^{-2}	8.25×10^{-4}	2.33×10^{-1}	9.23×10^{-4}	2.09×10^{-2}	5.96×10^{-2}	6.53×10^{-2}	5.79×10^{-2}
2^{-14}	2.40×10^{-2}	8.20×10^{-4}	2.36×10^{-1}	9.19×10^{-4}	2.75×10^{-2}	5.96×10^{-2}	6.64×10^{-2}	5.67×10^{-2}
2^{-16}	2.40×10^{-2}	8.21×10^{-4}	1.65×10^{-1}	9.16×10^{-4}	2.20×10^{-2}	5.96×10^{-2}	6.67×10^{-2}	5.66×10^{-2}
2^{-18}	2.40×10^{-2}	8.29×10^{-4}	1.19×10^{-1}	9.12×10^{-4}	2.00×10^{-2}	5.96×10^{-2}	6.68×10^{-2}	5.65×10^{-2}
2^{-20}	2.40×10^{-2}	8.25×10^{-4}	1.03×10^{-1}	9.14×10^{-4}	2.09×10^{-2}	5.96×10^{-2}	6.69×10^{-2}	5.64×10^{-2}
2^{-22}	2.40×10^{-2}	8.21×10^{-4}	1.03×10^{-1}	9.14×10^{-4}	2.09×10^{-2}	5.96×10^{-2}	6.69×10^{-2}	5.64×10^{-2}
2^{-24}	2.40×10^{-2}	8.21×10^{-4}	1.03×10^{-1}	9.14×10^{-4}	2.09×10^{-2}	5.96×10^{-2}	6.69×10^{-2}	5.64×10^{-2}

Table 2.15: $L_\infty-$errors for Example 2.6.5 for different values of ϵ.

ϵ	$N = 16$	$N = 32$	$N = 64$	$N = 128$	$N = 256$
2^{-2}	2.76×10^{-2}	2.81×10^{-2}	2.82×10^{-2}	2.82×10^{-2}	2.69×10^{-2}
2^{-4}	2.02×10^{-2}	1.76×10^{-2}	1.64×10^{-2}	1.53×10^{-2}	1.42×10^{-2}
2^{-6}	8.50×10^{-3}	5.60×10^{-3}	5.00×10^{-3}	5.15×10^{-3}	4.92×10^{-3}
2^{-8}	1.03×10^{-2}	4.80×10^{-3}	2.80×10^{-3}	1.88×10^{-3}	1.76×10^{-3}
2^{-10}	1.24×10^{-2}	5.20×10^{-3}	2.70×10^{-3}	9.85×10^{-4}	8.57×10^{-4}
2^{-12}	1.31×10^{-2}	5.40×10^{-3}	2.80×10^{-3}	9.23×10^{-4}	8.70×10^{-4}
2^{-14}	1.33×10^{-2}	5.50×10^{-3}	2.80×10^{-3}	9.19×10^{-4}	8.04×10^{-4}
2^{-16}	1.34×10^{-2}	5.50×10^{-3}	2.80×10^{-3}	9.16×10^{-4}	8.37×10^{-4}
2^{-18}	1.34×10^{-2}	5.60×10^{-3}	2.80×10^{-3}	9.12×10^{-4}	8.65×10^{-4}
2^{-20}	1.34×10^{-2}	5.60×10^{-3}	2.80×10^{-3}	9.14×10^{-4}	8.63×10^{-4}

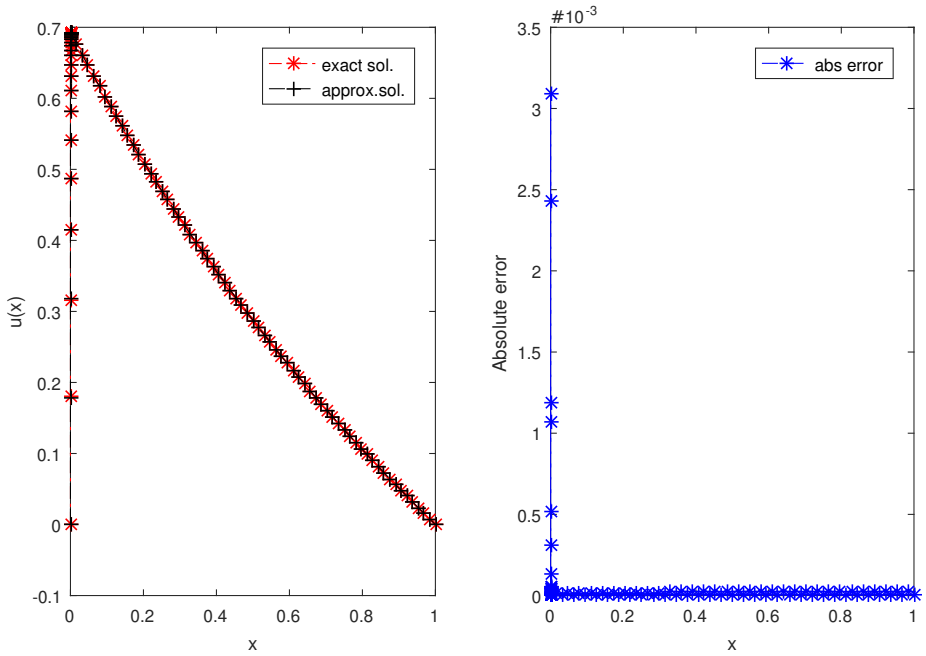

Figure 2.6: (a) Exact and EFG solution plot; (b) Pointwise absolute error plot for $\epsilon = 10^{-6}$, $N = 128$ for Example 2.6.5 using linear basis and cubic weight functions.

It can clearly be observed that for the non-linear SPP, Gaussian exponential spline weight functions perform much better than the other weight functions. The $L_\infty-$errors have been presented in Table 2.15 for distinct values of ϵ and the different number of nodes. The comparison of the EFG solution with that given by (2.6.1), depicting the sharp boundary layer, has been displayed in Fig. 2.6(a). The pointwise absolute error plot in Fig. 2.6(b) demonstrate the compatibility and robustness of the proposed scheme.

Example 2.6.6 *For the fourth example, we have considered the following non-linear singularly perturbed problem [110, 181]*

$$\epsilon u'' + uu' - u = 0, \quad x \in (0, 1),$$
$$u(0) = -1, \ u(1) = 3.9995,$$

with uniformly valid approximation

$$u(x) = x + c_1 \tanh\left(\frac{c_1}{2}\left(\frac{x}{\epsilon} + c_2\right)\right), \tag{2.6.2}$$

where $c_1 = 2.9995,\ c_2 = \frac{1}{c_1}\log_e\left[\frac{c_1-1}{c_1+1}\right]$.

Table 2.16: Comparison of the EFG solution with exact and other scheme solutions of Example 2.6.6 for $\epsilon = 10^{-3}$, $N = 10^3$.

x	Exact solution	EFG method	Kaushik [110]	Reddy [181]
0.00	−1.00000	−1.00000	−1.00000	−1.00000
0.01	3.009500	3.009567	3.009400	–
0.02	3.019500	3.019534	3.019500	3.019465
0.03	3.029500	3.029753	3.029500	–
0.04	3.039500	3.039727	3.039500	3.039476
0.05	3.049500	3.049770	3.049500	–
0.06	3.059500	3.059949	–	3.059494
0.08	3.079500	3.079712	–	3.079436
0.10	3.099500	3.099492	3.099500	3.099503
0.20	3.199500	3.199682	–	3.199500
0.30	3.299500	3.299199	3.299500	–
0.40	3.399500	3.399990	–	3.399476
0.50	3.499500	3.499973	3.499500	–
0.60	3.599500	3.599599	–	3.599431
0.70	3.699500	3.699656	3.699500	–
0.80	3.799500	3.799260	–	3.799473
0.90	3.899500	3.899348	3.899500	–
1.00	3.999500	3.999500	3.999500	3.999499

From Table 2.16, one can analyze the validity and accuracy of the proposed EFG scheme. The pointwise EFG solution of the considered problem 2.6.6 and the solutions obtained by different methods [110, 181] have also been presented in this Table. From the Table, it is clear that the EFG results are in good agreement with those cited in the literature. The comparison of the EFG solution and the approximate solution obtained by Eq. (2.6.2) has

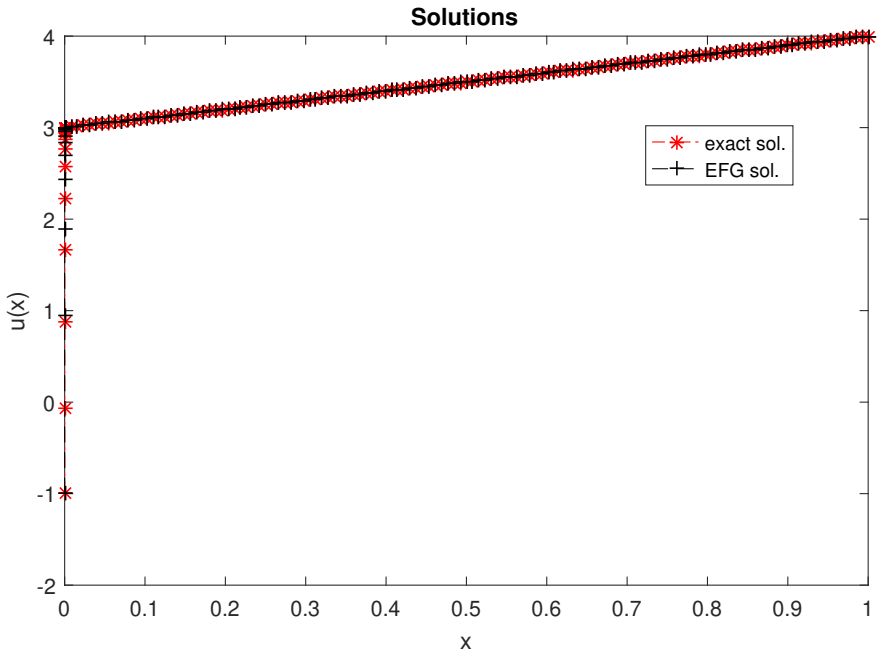

Figure 2.7: Exact and EFG solution plot for $\epsilon = 10^{-5}$, $N = 256$ for Example 2.6.6.

been made in Fig. 2.7. Clearly, the EFG solution approximates the close approximation of the exact one up to a reasonable precision of accuracy.

2.7 Conclusion

In the present work, an effort has been made to propose the appropriate weight functions in order to implement the EFG method for SPP. Since boundary layers appear in the solutions of SPP, non-uniform nodes have been generated, which condense in the boundary layer region and thus utilize the benefit of the proposed scheme. As for the choices of weight functions which affects the approximation in the EFG method, a variety of weight functions have been presented and tested in the EFG formulation for solving both linear and non-linear SPP. It has been concluded that the exponential weight functions are the most reliable and provides the most accurate results for SPP in comparison to other weight functions in presence of both the linear and quadratic basis functions. The MLS approxima-

tions and the Lagrange multiplier method have been utilized to generate the shape functions and implement the boundary conditions, respectively. For non-linear problems, the quasilinearization process has been used, and its convergence has been discussed. Since the radius of the support domain also affects more to the accuracy of the EFG solution, after a lot of numerical experiments, it has been concluded that for the range $\alpha_s \in (2.8, 3.2)$, the proposed method provides better approximate results. The convergence of the proposed method has been shown numerically in different examples. The EFG results have been compared with those available in the literature and are found in good agreement with both the linear and non-linear singularly perturbed problems.

Chapter 3

Element-free Galerkin method and its analysis for one-dimensional singularly perturbed parabolic problem

3.1 Introduction

In engineering and the applied sciences, singularly perturbed time-dependent problems are a relatively new and vigorous area of research. However, conventional numerical techniques developed so far, including finite difference methods, finite element methods, and finite volume methods etc., are unable to provide precise solutions for a suitable mesh length of the solution domain. Furthermore, these techniques do not possess parameter-independent convergent strategies. This dilemma occurs due to the presence of the perturbation parameter ϵ as well as the presence of boundary layers where the solutions fluctuate significantly [153].

In order to solve the singularly perturbed problems (SPP) with diverse physical behaviors, some of the effective numerical approaches have been presented in [31,38,39,50–52,118,119,123,124,172,193]. These techniques yield precise solutions for SPP. Comparative analysis of these methods demonstrate their incredibility for solving the SPP. Additionally, the techniques employed to solve various classes of singularly perturbed problems are uniformly convergent. Volterra Integro differential equations of fractional order has recently been studied for their approximation and convergence analysis [53, 180]. Also, a graded mesh refinement method for singularly perturbed time-delayed parabolic convection-diffusion problems has been pre-

sented in [121]. These techniques present a parameterized operator-based approach that approximates the solutions of considered problems.
Typically, nonlinearity in SPP can be managed by using quasilinearization techniques. In [13, 118–120, 123, 124], researchers focused on the analysis of singularly perturbed semi-linear spatial delay differential equations. The majority of these developed numerical algorithms produce reliable results only when the mesh length of the solution domain is less than the perturbation parameter value and hence most of these schemes are computationally expensive. Considering the literature reviews, since some of the mesh-free methods have been applied to the singularly perturbed parabolic problems, so far, thus in the present work, we have introduced a robust and efficient numerical approach known as the element-free Galerkin (EFG) technique to capture the solutions of these problems. The key feature of the proposed method includes the non-requirement of node connectivity, due to which node particles can be added or deleted without difficulty. As a result, a flexible refinement of domain discretization can be achieved efficiently and quickly. In the present Chapter, drive to this advantage, non-uniformly distributed nodes that condense in the boundary layer region have been constructed. The proposed scheme uses moving least-square (MLS) approximation to generate shape functions. The methodology is based on the global weak form. The numerical integrations are computed by employing the Gauss quadrature background cells. The time discretization has been carried out by using the implicit Crank-Nicolson method before spatial discretization. The Lagrange multipliers approach imposes the essential boundary constraints as the MLS shape functions do not satisfy the Kronecker delta function property. The Chapter is structured as follows:
The model problem has been discussed in the Section 3.2. The Crank-Nicolson scheme for temporal discretization has been discussed in the Section 3.3, where the stability of the time-discrete approach have also been investigated. The EFG methodology with the node generation procedure

has been explained in the Section 3.4. The Section 3.5 demonstrates the existence and uniqueness of the EFG solution. The convergence analysis of the full-discrete scheme has been carried out in the Section 3.6. Section 3.7 deals with the numerical experiments that depict the robustness and efficiency of the proposed strategy. Finally, the conclusion has been given at the end of Chapter in Section 3.8.

3.2 Model problem

In the current Chapter, we consider the time dependent singularly perturbed reaction-diffusion equation of the form

$$\begin{aligned} u_t(x,t) - \epsilon\nabla^2 u(x,t) + a(x,t)u(x,t) &= F(u(x,t)), \\ (x,t) \in \Omega \equiv \Omega_x \times \Omega_t &\equiv (0,1) \times (0,T], \end{aligned} \tag{3.2.1}$$

with initial condition

$$u(x,0) = u_0(x),\ x \in \bar{\Omega}_x, \tag{3.2.2}$$

and boundary conditions as

$$u(0,t) = f(t),\quad u(1,t) = g(t),\ t \in \bar{\Omega}_t, \tag{3.2.3}$$

where $a(x,t)$ is continuous function satisfying $\alpha \leq a(x,t) \leq \alpha^*$ and $F(u)$ is the continuous non-linear term. In Eq.(3.2.1), ϵ is known as singular perturbation parameter satisfying $0 < \epsilon \ll 1$. The problem (3.2.1) exhibits boundary layers in the solution when $\epsilon \to 0$.
We impose the compatibility conditions as

$$u(0,0) = u_0(0) = f(0),\quad \textit{and}\ \ u(1,0) = u_0(1) = g(1), \tag{3.2.4}$$

so that the data matches at the end points $(0,0)$ and $(1,0)$ of the domain $\overline{\Omega}$.

3.3 Time semi-discrete scheme

The weak form of the considered problem (3.2.1) is

$$< u_t, \upsilon > +\epsilon < \nabla u, \nabla \upsilon > + < au, \upsilon >=< F(u), \upsilon >, \quad \forall\ \upsilon \in H^1(\Omega).$$

We define $t_n = n\tau,\ n = 0, 1, ..., N$, where $\tau = T/N$ is the step-size of the time variable. We will discretize the time derivative term using implicit Crank-Nicolson scheme for the above equation as follows:

$$< \widehat{\delta}_t U^{(n+1)}, \upsilon > +\epsilon < \nabla \widehat{U}^{(n+1)}, \nabla \upsilon > + < \widehat{aU}^{(n+1)}, \upsilon > =< F(\widehat{U}^{(n+1)}), \upsilon >, \quad \forall\ \upsilon \in H^1(\Omega), \tag{3.3.1}$$

where we have used the notations

$$\widehat{\delta}_t U^{(n+1)} = \frac{U^{(n+1)} - U^{(n)}}{\tau}, \qquad \widehat{U}^{(n+1)} = \frac{U^{(n+1)} + U^{(n)}}{2},$$

and $U^{(n+1)}$ is the solution of semi-discrete scheme at $(n+1)^{th}$ time level. On simplification, we get

$$\begin{aligned} < U^{(n+1)}, \upsilon > + \frac{\tau\epsilon}{2} < \nabla U^{(n+1)}, \nabla \upsilon > + \frac{\tau}{2} < a^{(n+1)} U^{(n+1)}, \upsilon > \\ - \frac{\tau}{2} < F(U^{(n+1)}), \upsilon >=< U^{(n)}, \upsilon > - \frac{\tau\epsilon}{2} < \nabla U^{(n)}, \nabla \upsilon > \\ - \frac{\tau}{2} < a^{(n)} U^{(n)}, \upsilon > + \frac{\tau}{2} < F(U^{(n)}), \upsilon >, \quad \forall\ \upsilon \in H^1(\Omega). \end{aligned} \tag{3.3.2}$$

3.3.1 Stability of the time-discrete scheme

Before proving the stability of the method, we state below some Lemmas which will be used in the results to follow.

Lemma 3.3.1 *[190] Let* $0 < \epsilon \ll 1$. *Then under the compatibility conditions defined by* (3.2.4), *the solution* $u(x,t)$ *of the continuous problem* (3.2.1) *satisfies*

$$\begin{aligned} \Big|u(x,t) - u_0(x)\Big| &\leq Ct \quad \forall (x,t) \ \in \ \overline{\Omega} \\ \textit{and} \ \Big|u(x,t) - f(t)\Big| &\leq Cx \quad \forall (x,t) \ \in \ \overline{\Omega}. \end{aligned}$$

Lemma 3.3.2 *From Lemma 3.3.1, one can easily deduce that*

$$\Big|u(x,t)\Big| \leq C \quad \forall \ (x,t) \ \in \overline{\Omega}.$$

Lemma 3.3.3 *Let* $u \in C(\overline{\Omega})$ *and* $\overline{\Omega} \subset \mathbb{R}^2$ *be a bounded closed set. Then the non-linear term* $F(u)$ *satisfies the inequality*

$$|F(u)| \leq \overline{M}.$$

Proof From the given assumption, we have

$$\min\{u : u \in C(\overline{\Omega})\} \ \leq u \leq \ \max\{u : u \in C(\overline{\Omega})\},$$

and thus $\exists$ a positive integer M such that

$$\max_{u \in C(\overline{\Omega})} |u| \leq M. \tag{3.3.3}$$

The result follows from (3.3.3).

Proposition 3.3.4 *[179] Let* $\{\theta_n\}$, $\{\phi_n\}$ *and* $\{d_k\}$ *be non-negative sequences and* $v_0 > 0$ *be any real number. Suppose that the sequence* θ_n

satisfies

$$\begin{cases} \theta_0 \leq v_0, \\ \theta_n \leq v_0 + \sum_{k=0}^{n-1} d_k + \sum_{k=0}^{n-1} \phi_k \theta_k, \quad n \geq 1. \end{cases}$$

If $v_0 \geq 0$ *and* $d_0 \geq 0$, *then*

$$\theta_n \leq \Big(v_0 + \sum_{k=0}^{n-1} d_k\Big) \exp\Big(\sum_{k=0}^{n-1} \phi_k\Big), \quad n \geq 1.$$

Theorem 3.3.5 *Suppose* $U^{(n+1)} \in H^1(\overline{\Omega})$. *Then the time discrete scheme* (3.3.2) *is unconditionally stable.*

Proof Setting $\upsilon = U^{(n+1)}$ in the time-discrete variational weak formulation (3.3.2) provides

$$\begin{aligned} &< U^{(n+1)}, U^{(n+1)} > + \frac{\tau\epsilon}{2} < \nabla U^{(n+1)}, \nabla U^{(n+1)} > + \frac{\tau}{2} < a^{(n+1)} U^{(n+1)}, U^{(n+1)} > \\ &- \frac{\tau}{2} < F(U^{(n+1)}), U^{(n+1)} > = < U^n, U^{(n+1)} > - \frac{\tau\epsilon}{2} < \nabla U^{(n)}, \nabla U^{(n+1)} > \\ &- \frac{\tau}{2} < a^{(n)} U^{(n)}, U^{(n+1)} > + \frac{\tau}{2} < F(U^{(n)}), U^{(n+1)} > . \end{aligned}$$

Using the Cauchy-Schwarz inequality and simplifying, we get

$$\begin{aligned} \Big\|U^{(n+1)}\Big\|^2_{L^2(\Omega)} + \frac{\tau\epsilon}{2}\Big\|\nabla U^{(n+1)}\Big\|^2_{L^2(\Omega)} &\leq \Big\|U^{(n)}\Big\|_{L^2(\Omega)} . \Big\|U^{(n+1)}\Big\|_{L^2(\Omega)} \\ &+ \frac{\tau\epsilon}{2}\Big\|\nabla U^{(n)}\Big\|_{L^2(\Omega)} . \Big\|\nabla U^{(n+1)}\Big\|_{L^2(\Omega)} + \frac{\tau\alpha^*}{2}\Big\|U^{(n+1)}\Big\|^2_{L^2(\Omega)} \\ &+ \frac{\tau\alpha^*}{2}\Big\|U^{(n)}\Big\|_{L^2(\Omega)} . \Big\|U^{(n+1)}\Big\|_{L^2(\Omega)} + \frac{\tau}{2}\Big\|F(U^{(n+1)})\Big\|_{L^2(\Omega)} . \Big\|U^{(n+1)}\Big\|_{L^2(\Omega)} \\ &+ \frac{\tau}{2}\Big\|F(U^{(n)})\Big\|_{L^2(\Omega)} . \Big\|U^{(n+1)}\Big\|_{L^2(\Omega)} . \end{aligned}$$

The use of Young's inequality and Lemma 3.3.3 results in the following

relation

$$\frac{1}{2}\left\|U^{(n+1)}\right\|^2_{L^2(\Omega)}+\frac{\tau\epsilon}{4}\left\|\nabla U^{(n+1)}\right\|^2_{L^2(\Omega)}\leq\frac{1}{2}\left\|U^{(n)}\right\|^2_{L^2(\Omega)}+\frac{\tau\epsilon}{4}\left\|\nabla U^{(n)}\right\|^2_{L^2(\Omega)}+(3\alpha^*+2)\frac{\tau}{4}\left\|U^{(n+1)}\right\|^2_{L^2(\Omega)}+\frac{\tau\alpha^*}{4}\left\|U^{(n)}\right\|^2_{L^2(\Omega)}+\frac{\tau}{2}|\overline{M}|^2. \tag{3.3.4}$$

Next, we define the following weighted Hilbert norm

$$\left\|U^{(n+1)}\right\|^2_{H_w(\Omega)}=\frac{1}{2}\left\|U^{(n+1)}\right\|^2_{L^2(\Omega)}+\frac{\tau\epsilon}{4}\left\|\nabla U^{(n+1)}\right\|^2_{L^2(\Omega)}.$$

Then, Eq.(3.3.4) can be rewritten as

$$\left\|U^{(n+1)}\right\|^2_{H_w(\Omega)}\leq\left\|U^{(n)}\right\|^2_{H_w(\Omega)}+(3\alpha^*+2)\frac{\tau}{2}\left\|U^{(n+1)}\right\|^2_{H_w(\Omega)}+\frac{\tau\alpha^*}{2}\left\|U^{(n)}\right\|^2_{L^2(\Omega)}+\frac{\tau}{2}|\overline{M}|^2.$$

Considering the above relation at all time levels and summing them up leads to

$$\sum_{i=0}^{n}\left\|U^{(i+1)}\right\|^2_{H_w(\Omega)}\leq\sum_{i=0}^{n}\left\|U^{(i)}\right\|^2_{H_w(\Omega)}+(3\alpha^*+2)\frac{\tau}{2}\sum_{i=0}^{n}\left\|U^{(i+1)}\right\|^2_{H_w(\Omega)}+\frac{\tau\alpha^*}{2}\sum_{i=0}^{n}\left\|U^{(i)}\right\|^2_{H_w(\Omega)}+\frac{\tau}{2}\sum_{i=0}^{n}|\overline{M}|^2,$$

or equivalently

$$\left\|U^{(n+1)}\right\|^2_{H_w(\Omega)}\leq\left\|U^{(0)}\right\|^2_{H_w(\Omega)}+(2\alpha^*+1)\tau\sum_{i=0}^{n}\left\|U^{(i+1)}\right\|^2_{H_w(\Omega)}+\frac{\tau}{2}\sum_{i=0}^{n}|\overline{M}|^2.$$

Applying Proposition 3.3.4 to the above inequality, we arrive at

$$\left\|U^{(n+1)}\right\|^2_{H_w(\Omega)}\leq\left[\left\|U^{(0)}\right\|^2_{H_w(\Omega)}+\frac{n\tau}{2}|\overline{M}|^2\right]\exp\Big((2\alpha^*+1)n\tau\Big)$$

$$\leq \left[\left\|U^{(0)}\right\|^2_{H_w(\Omega)} + \frac{T}{2}|\overline{M}|^2\right]\exp\Big((2\alpha^* + 1)T\Big)$$
$$\leq \mathcal{C}\left\|U^{(0)}\right\|^2_{H_w(\Omega)}.$$

Thus, the semi-discrete scheme (3.3.2) is unconditionally stable.

3.4 Element-free Galerkin formulation

In order to elaborate the proposed EFG formulation, we start with the generation of nodes in the spatial domain Ω_x.

3.4.1 Domain discretization

The node generation process has been carried out by employing Shishkin's technique. The strategy has been designed to accommodate density of points in the boundary layer region. We will illustrate the node distribution by considering that the boundary layer occurs at both endpoints.
Let N be the total number of nodes in domain $\bar{\Omega} = [0, 1]$. Divide the spatial domain Ω into three subdomains $[0, \delta]$, $[\delta, 1-\delta]$ and $[1-\delta, 1]$, where the transition parameter is given by

$$\delta = \min\Big\{\frac{1}{4}, \kappa\epsilon \ln N\Big\},$$

where κ is a constant chosen appropriately. On each of these sub-domains, the nodes are generated as follows:

$$x_i = \begin{cases} i \times h_i, & 0 \leq i \leq \frac{N}{4} \\ \delta + (i - N/4) \times h_i, & \frac{N}{4} + 1 \leq i \leq \frac{3N}{4}, \\ (1-\delta) + (i - 3N/4) \times h_i, & \frac{3N}{4} + 1 \leq i \leq N, \end{cases}$$

where the step size $h_i's$ are given by

$$h_i = \begin{cases} \frac{4\delta}{N}, & 0 \leq i \leq \frac{N}{4};\ \frac{3N}{4}+1 \leq i \leq N \\ \frac{2(1-2\delta)}{N}, & \frac{N}{4}+1 \leq i \leq \frac{3N}{4}. \end{cases}$$

3.4.2 Moving least-square approximation

Let $\Omega_h = \{x_i\}_{i=1}^n$ be distribution of nodes in the spatial domain $\Omega_x = [0,1]$ as discussed above.
The domain of influence of any typical node x with radius $\mathfrak{d}_{\mathfrak{s}}$ is defined as

$$\mathfrak{d}(x) = \big\{x^* \in \Omega_h : |x - x^*| < \mathfrak{d}_{\mathfrak{s}}(x)\big\}.$$

We define

$$\mathfrak{c}(x) = \big[\mathfrak{c}_{\mathfrak{1}}(x), \mathfrak{c}_{\mathfrak{2}}(x), ..., \mathfrak{c}_{\mathfrak{m}}(x)\big]^T, x \in \Omega_x,$$

to be the set of polynomial basis functions. In the present Chapter, we use quadratic basis functions defined as

$$\mathfrak{c}(x) = [1, x, x^2].$$

Let the field function $u(x,t)$ is approximated by $u_h(x,t)$ using MLS approximation in the domain Ω and is defined as

$$u_h(x,t) = \sum_{j=1}^{m} \mathfrak{c}_{\mathfrak{j}}(x)\mathfrak{a}_{\mathfrak{j}}(x,t) = \mathfrak{c}^T(x)\mathfrak{a}, \tag{3.4.1}$$

where $\mathfrak{a}$ is an unknown vector of coefficients which depends on x and t, and is to be determined by minimizing the weighted residual functional

$$J = \sum_{i=1}^{n} w(x - x_i) \left[\mathfrak{c}^T(x_i)\mathfrak{a} - u_i \right]^T.$$

The minimization of J with respect to $\mathfrak{a}$ leads to $\frac{\partial J}{\partial \mathfrak{a}} = 0$.
This gives

$$\mathfrak{a} = \mathbf{P}^{-1}(x)\mathbf{S}(x)\mathbf{u}. \tag{3.4.2}$$

Furthermore, on solving this expression as in Section 2.3.2 of Chapter 2, the approximate EFG solution can be written as

$$u(x,t) \approx u_h(x,t) = \sum_{i=1}^{n} \Phi_i(x) u_i,$$

in which the MLS shape functions are given by

$$\Phi_i(x) = \begin{cases} \sum_{j=1}^{m} \mathfrak{c}_j(x) \left(\mathbf{P^{-1}}(x)\mathbf{S}(x) \right)_{ji}, & x \in \mathfrak{d}_\mathfrak{i}, \\ 0, & x \notin \mathfrak{d}_\mathfrak{i}, \end{cases} \tag{3.4.3}$$

and u_i are nodal approximants. Note that u_i are not nodal values of $u_h(x,t)$ because $u_h(x,t)$ is an approximant, not an interpolant. The derivatives of the MLS shape functions can be obtained by differentiating (3.4.3) with respect to the spatial coordinates.
The continuity of the shape functions $\phi_i(x)$ depend on the continuity of the weight function $w_i(x)$ and that of the basis functions $c(x)$. If $w_i(x) \in C^k$, then it follows that $\phi_i(x) \in C^k$ for a polynomial basis.
In the EFG method, every node is associated with a domain of influence, generally known as support of the weight functions $w(x)$ corresponding to the node x with $w(x) > 0$ in the domain of influence and $w(x) = 0$ outside it.

Though the cubic spline functions are commonly used in practice, whileas the appropriate selection of weight function exert impact on the accuracy of the solution as clearly shown in [109]. In the current Chapter, the following Gaussian exponential spline weight function, based on a normalized distance $s = \frac{\|x-x_i\|}{\mathfrak{d}_{\mathfrak{s}}}$, has been employed

$$w(s) = \begin{cases} \frac{e^{-(s/\alpha)^2} - e^{-(1/\alpha)^2}}{1-e^{-(1/\alpha)^2}}, & s \leq 1 \\ 0, & s > 1, \end{cases}$$

where the parameter α is mostly taken as $\alpha = 0.3$ and $\mathfrak{d}_{\mathfrak{s}} = \alpha_s \mathfrak{d}_{\mathfrak{c}}$ is the radius of the influence domain of the node x_j.

3.4.3 Element-free Galerkin discrete scheme

Let V_h be the finite dimensional subspace of $H^1(\Omega)$.
Then the full-discrete scheme is given by

$$\begin{aligned} < \widehat{\delta}_t U_h^{(n+1)}, \upsilon_h > + \epsilon < \nabla \widehat{U}_h^{(n+1)}, \nabla \upsilon_h > + < \widehat{a}^{(n+1)} \widehat{U}_h^{(n+1)}, \upsilon_h > \\ =< F(\widehat{U}_h^{(n+1)}), \upsilon_h >, \quad \forall \upsilon_h \in V_h. \end{aligned} \tag{3.4.4}$$

3.5 Existence and uniqueness of the element-free Galerkin solution

Theorem 3.5.1 *Suppose $U_h^{(n)}$, the solution at $(n)^{th}$ time level of the EFG scheme* (3.4.4) *is known. Then the solution $U_h^{(n+1)}$ of* (3.4.4) *at $(n+1)^{th}$ time level exists.*

Proof We can rewrite Eq. (3.4.4) as

$$\begin{aligned} \Big\langle U_h^{(n+1)}, \upsilon_h \Big\rangle - \Big\langle U_h^{(n)}, \upsilon_h \Big\rangle + \epsilon\tau \Big\langle \nabla \widehat{U}_h^{(n+1)}, \nabla \upsilon_h \Big\rangle + \tau \Big\langle \widehat{aU}_h^{(n+1)}, \upsilon_h \Big\rangle \\ = \tau \Big\langle F(\widehat{U}_h^{(n+1)}), \upsilon_h \Big\rangle. \end{aligned}$$

Define the operator ζ as follows:

$$\Big\langle \zeta(\omega), \upsilon_h \Big\rangle = \Big\langle \omega, \upsilon_h \Big\rangle + \epsilon\tau \Big\langle \nabla\omega, \nabla\upsilon_h \Big\rangle + \tau \Big\langle a\omega, \upsilon_h \Big\rangle - \Big\langle U_h^{(n)}, \upsilon_h \Big\rangle - \tau \Big\langle F(\omega), \upsilon_h \Big\rangle.$$

Thus, we will have

$$\begin{aligned}\Big\langle \zeta(\omega_1) - \zeta(\omega_2), \upsilon_h \Big\rangle =& \Big\langle \omega_1 - \omega_2, \upsilon_h \Big\rangle + \epsilon\tau \Big\langle \nabla(\omega_1 - \omega_2), \nabla\upsilon_h \Big\rangle \\ &+ \tau \Big\langle a(\omega_1 - \omega_2), \upsilon_h \Big\rangle - \tau \Big\langle F(\omega_1) - F(\omega_2), \upsilon_h \Big\rangle.\end{aligned}$$

By using Lipschitz condition on F i.e. $|F(u_1) - F(u_2)| \leq \mathfrak{L}|u_1 - u_2|$ and employing the Cauchy-Schwarz inequality, we get

$$\begin{aligned}\Big\langle \zeta(\omega_1) - \zeta(\omega_2), \upsilon_h \Big\rangle &\leq \Big\| (\omega_1 - \omega_2) \Big\|_{L^2(\Omega)} \Big\| \upsilon_h \Big\|_{L^2(\Omega)} \\ &+ \epsilon\tau \Big\| \nabla(\omega_1 - \omega_2) \Big\|_{L^2(\Omega)} \Big\| \nabla\upsilon_h \Big\|_{L^2(\Omega)} + (\alpha^* + \mathfrak{L})\tau \Big\| (\omega_1 - \omega_2) \Big\|_{L^2(\Omega)} \Big\| \upsilon_h \Big\|_{L^2(\Omega)} \\ &\leq \left[(1 + \sqrt{(\alpha^* + \mathfrak{L})\tau}) \Big\| (\omega_1 - \omega_2) \Big\|_{L^2(\Omega)} + \sqrt{\epsilon\tau} \Big\| \nabla(\omega_1 - \omega_2) \Big\|_{L^2(\Omega)} \right] \\ &\times \left[(1 + \sqrt{(\alpha^* + \mathfrak{L}\tau)}) \Big\| \upsilon_h \Big\|_{L^2(\Omega)} + \sqrt{\epsilon\tau} \Big\| \nabla\upsilon_h \Big\|_{L^2(\Omega)} \right].\end{aligned}$$

Using the weighted norm definition

$$\Big\| \vartheta_h \Big\|_{H_{\omega^*}(\Omega)} = \Big(1 + \sqrt{(\alpha^* + \mathfrak{L})\tau} \Big) \Big\| \vartheta_h \Big\|_{L^2(\Omega)} + \sqrt{\epsilon\tau} \Big\| \nabla\vartheta_h \Big\|_{L^2(\Omega)},$$

the above inequality can be written as

$$\Big\langle \zeta(\omega_1) - \zeta(\omega_2), \upsilon_h \Big\rangle \leq \Big\| (\omega_1 - \omega_2) \Big\|_{H_{\omega^*}(\Omega)} \Big\| \upsilon_h \Big\|_{H_{\omega^*}(\Omega)}.$$

Let $\upsilon_h = \omega$, then

$$\Big\langle \zeta(\omega), \omega \Big\rangle = \Big\langle \omega, \omega \Big\rangle + \epsilon\tau \Big\langle \nabla\omega, \nabla\omega \Big\rangle + \tau \Big\langle a\omega, \omega \Big\rangle - \Big\langle U_h^{(n)}, \omega \Big\rangle - \tau \Big\langle F(\omega), \omega \Big\rangle$$

$$
\begin{aligned}
&\geq \Big\|\omega\Big\|^2_{L^2(\Omega)} + \epsilon\tau\Big\|\nabla\omega\Big\|^2_{L^2(\Omega)} + \alpha^*\tau\Big\|\omega\Big\|^2_{L^2(\Omega)} \\
&- \Big\|U_h^{(n)}\Big\|_{L^2(\Omega)}\Big\|\omega\Big\|_{L^2(\Omega)} - \tau\Big\|F(\omega)\Big\|_{L^2(\Omega)}\Big\|\omega\Big\|_{L^2(\Omega)} \\
&\geq \Big\|\omega\Big\|^2_{H_\omega(\Omega)} + \alpha^*\tau\Big\|\omega\Big\|^2 - \Big\|U_h^{(n)}\Big\|_{H_\omega(\Omega)}\Big\|\omega\Big\|_{H_\omega(\Omega)} - \tau\Big\|F(\omega)\Big\|_{H_\omega(\Omega)}\Big\|\omega\Big\|_{H_\omega(\Omega)} \\
&= \Big\|\omega\Big\|_{H_\omega(\Omega)}\left[\Big\|\omega\Big\|_{H_\omega(\Omega)} + \alpha^*\tau\Big\|\omega\Big\| - \Big\|U_h^{(n)}\Big\|_{H_\omega(\Omega)} - \tau\Big\|F(\omega)\Big\|_{H_\omega(\Omega)}\right].
\end{aligned}
$$

By selecting

$$
\Big\|\omega\Big\|_{H_\omega(\Omega)} = \Big\|U_h^{(n)}\Big\|_{H_\omega(\Omega)} - \alpha^*\tau\Big\|\omega\Big\| + \tau\Big\|F(\omega)\Big\|_{H_\omega(\Omega)}.
$$

Now, the existence of the EFG solution of (3.4.4) can be concluded using Brouwer's fixed point theorem.

Theorem 3.5.2 *If the* $(n+1)^{th}$ *time-level EFG solution of* (3.4.4) *exists, then it is unique.*

Proof Assume $U_{1h}^{(n+1)}$ and $U_{2h}^{(n+1)}$ be two EFG solutions of (3.4.4). Define

$$
\chi_h^{(n+1)} = U_{1h}^{(n+1)} - U_{2h}^{(n+1)}.
$$

Then, Eq. (3.4.4) yields

$$
\begin{aligned}
&<\chi_h^{(n+1)}, \upsilon> + \frac{\tau\epsilon}{2} < \nabla\chi_h^{(n+1)}, \nabla\upsilon> + \frac{\tau}{2} < a^{(n+1)}\chi_h^{(n+1)}, \upsilon> \\
&\quad + \frac{\tau}{2} < F(U_{1h}^{(n+1)}) - F(U_{2h}^{(n+1)}), \upsilon> = < \chi_h^{(n)}, \upsilon> - \frac{\tau\epsilon}{2} < \nabla\chi_h^{(n)}, \nabla\upsilon> \\
&\quad - \frac{\tau}{2} < a^{(n)}\chi_h^{(n)}, \upsilon> - \frac{\tau}{2} < F(U_{1h}^{(n)}) - F(U_{2h}^{(n)}), \upsilon> .
\end{aligned}
$$

Setting $\upsilon = \chi_h^{(n+1)}$ in above relation gives

$$
<\chi_h^{(n+1)}, \chi_h^{(n+1)}> + \frac{\tau\epsilon}{2} < \nabla\chi_h^{(n+1)}, \nabla\chi_h^{(n+1)}> + \frac{\tau}{2} < a^{(n+1)}\chi_h^{(n+1)}, \chi_h^{(n+1)} >
$$

$$
\begin{aligned}
&=< \chi_h^{(n)}, \chi_h^{(n+1)} > -\frac{\tau\epsilon}{2} < \nabla\chi_h^{(n)}, \nabla\chi_h^{(n+1)} > \\
&-\frac{\tau}{2} < a^{(n)}\chi_h^{(n)}, \chi_h^{(n+1)} > +\frac{\tau}{2} < F(U_{1h}^{(n+1)}) - F(U_{2h}^{(n+1)}), \chi_h^{(n+1)} > \\
&+\frac{\tau}{2} < F(U_{1h}^{(n)}) - F(U_{2h}^{(n)}), \chi_h^{(n+1)} > .
\end{aligned}
$$

Proceeding further as in Theorem 3.3.5 results in

$$
\left\|\chi_h^{(n)}\right\|^2_{H_w(\Omega)} \leq \left[\left\|\chi_h^{(0)}\right\|^2_{H_w(\Omega)}\right]\exp\Big(MT\Big).
$$

As $\chi_h^{(0)} = 0$, we have

$$
\begin{aligned}
\left\|\chi^{(n)}\right\|_{H_w(\Omega)} &= 0 \\
\Rightarrow \chi_h^{(n)} &= 0.
\end{aligned}
$$

This completes the proof.

3.6 Convergence of full-discrete scheme

To estimate the error bounds of the EFG method, we present some preliminaries which will be used in the current Section.
We define the finite-dimensional solution space

$$
V_h = \text{span}\{\phi_1, \phi_2, ..., \phi_n\},
$$

and the Ritz-projection

$$
\Upsilon_r^d : H^1(\Omega) \to V_h
$$

such that for $u \in H^1(\Omega)$

$$
< \nabla\Upsilon_r^d u, \nabla v_r >=< \nabla u, \nabla v_r >, \qquad \forall v_r \in V_h.
$$

Lemma 3.6.1 *[212] Let $\varphi(x) \in C^{m,1}(\Omega)$. Then there exist constant C_κ independent of $\mathfrak{d}_\mathfrak{s}$ such that*

$$\left\| D^\kappa \varphi - D^\kappa \Upsilon_r^d \varphi \right\|_{L^2(\Omega)} \leq C_\kappa {\mathfrak{d}_\mathfrak{s}}^{m+1-|\kappa|} |\varphi|_{m,1}, \quad |\kappa| \leq 2.$$

Before proving the convergence of the EFG scheme, we discuss weak formulation as follows:
Find $U_h^{(n+1)} \in V_h$ such that

$$\begin{aligned} &< U_h^{(n+1)}, \upsilon_r > + \frac{\tau\epsilon}{2} < \nabla U_h^{(n+1)}, \nabla \upsilon_r > + \frac{\tau}{2} < a^{(n+1)} U_h^{(n+1)}, \upsilon_r > \\ &- \frac{\tau}{2} < F(U_h^{(n+1)}), \upsilon_r > = < U_h^{(n)}, \upsilon_r > - \frac{\tau\epsilon}{2} < \nabla U_h^{(n)}, \nabla \upsilon_r > \\ &- \frac{\tau}{2} < a^{(n)} U_h^{(n)}, \upsilon_r > + \frac{\tau}{2} < F(U_h^{(n)}), \upsilon_r > . \end{aligned} \tag{3.6.1}$$

Lemma 3.6.2 *Let*

$$\begin{aligned} <\mathfrak{F}_h^{(n+1)}, \upsilon_r > &= \frac{1}{\tau} < U_h^{(n+1)} - U^{(n+1)}, \upsilon_r > + \frac{\epsilon\tau}{2} < \nabla U^{(n+1)} - \nabla U^{(n+1)}, \upsilon_r > \\ &- \frac{1}{2} < (M - a^{(n+1)})(U_h^{(n+1)} - U^{(n+1)}), \upsilon_r > - \frac{1}{2} < (M - a^{(n)})(U_h^{(n)} - U^{(n)}), \upsilon_r > \\ &- \frac{1}{\tau} < U_h^{(n)} - U^{(n)}, \upsilon_r > + \frac{\epsilon\tau}{2} < \nabla U^{(n)} - \nabla U^{(n)}, \upsilon_r > . \end{aligned} \tag{3.6.2}$$

Then, we have

$$\| \mathfrak{F}_h^{(n+1)} \|_{L^2(\Omega)} \leq C {\mathfrak{d}_\mathfrak{s}}^m.$$

Proof Setting $\upsilon_r = \mathfrak{F}_h^{(n+1)}$ in Eq. (3.6.2) and using Cauchy-Schwarz inequality, we have

$$\begin{aligned} \left\| \mathfrak{F}_h^{(n+1)} \right\|_{L^2(\Omega)} \leq & \left\| U_h^{(n+1)} - U^{(n+1)} \right\|_{L^2(\Omega)} + \frac{\tau}{2} |M - \alpha| \Big[\left\| U_h^{(n+1)} - U^{(n+1)} \right\|_{L^2(\Omega)} \\ & + \left\| U_h^{(n)} - U^{(n)} \right\|_{L^2(\Omega)} \Big] + \left\| U_h^{(n)} - U^{(n)} \right\|_{L^2(\Omega)} \end{aligned}$$

$$
\begin{aligned}
&+\frac{\epsilon\tau}{2}\Big[\Big\|\nabla U^{(n+1)}-\nabla U^{(n+1)}\Big\|_{L^2(\Omega)}+\Big[\Big\|\nabla U^{(n)}-\nabla U^{(n)}\Big\|_{L^2(\Omega)}\Big]\\
&=\Big(1+\frac{\tau}{2}|M-\alpha|\Big)\Big[\Big\|U_h^{(n+1)}-U^{(n+1)}\Big\|_{L^2(\Omega)}+\Big\|U_h^{(n)}-U^{(n)}\Big\|_{L^2(\Omega)}\Big]\\
&+\frac{\epsilon\tau}{2}\Big[\Big\|\nabla U^{(n+1)}-\nabla U^{(n+1)}\Big\|_{L^2(\Omega)}+\Big[\Big\|\nabla U^{(n)}-\nabla U^{(n)}\Big\|_{L^2(\Omega)}\Big].
\end{aligned}
$$

Now, by using Lemma 3.6.1, the proof is clear.

Since $U^{(n+1)}(=U(x,t_{n+1}))$ is the temporal discrete approximation of the exact solution $u^{(n+1)}(=u(x,t_{n+1}))$, hence $u(x,t)$ satisfies

$$
\begin{aligned}
&<u^{(n+1)},\upsilon_r>+\frac{\tau\epsilon}{2}<\nabla u^{(n+1)},\nabla\upsilon_r>+\frac{\tau}{2}<a^{(n+1)}u^{(n+1)},\upsilon_r>-\frac{\tau}{2}<F(u^{(n+1)}),\upsilon_r>\\
&\quad=<u^{(n)},\upsilon_r>-\frac{\tau\epsilon}{2}<\nabla u^{(n)},\nabla\upsilon_r>-\frac{\tau}{2}<a^{(n)}u^{(n)},\upsilon_r>+\frac{\tau}{2}<F(u^{(n)}),\upsilon_r>\\
&\quad-\tau<\mathfrak{E},\upsilon_r>, \qquad (3.6.3)
\end{aligned}
$$

where $\mathfrak{E}$ is the residual term due to the temporal semi-discretization.

Theorem 3.6.3 *Let $U_h^{(n+1)}$ be the element-free Galerkin solution given by* (3.3.2) *and $u^{(n+1)}$ be solution of* (3.2.1). *Then the EFG scheme converges with*

$$
\Big\|U_h^{(n+1)}-u^{(n+1)}\Big\|_{H_w(\Omega)}\leq\mathcal{C}(\tau^2+{\mathfrak{d}_{\mathfrak{s}}}^m).
$$

Proof Since the time-discrete solution $U^{(n+1)}$ and $u^{(n+1)}$ satisfies Eqs. (3.6.1) and (3.6.3) respectively, subtracting these equations, we get

$$
\begin{aligned}
&<U^{(n+1)}-u^{(n+1)},\upsilon_r>+\frac{\tau\epsilon}{2}<\nabla U^{(n+1)}-\nabla u^{(n+1)},\nabla\upsilon_r>\\
&+\frac{\tau}{2}<a^{(n+1)}(U^{(n+1)}-u^{(n+1)}),\upsilon_r>-\frac{\tau}{2}<F(U^{(n+1)})-F(u^{(n+1)}),\upsilon_r>\\
&=<U^{(n)}-u^{(n)},\upsilon_r>-\frac{\tau\epsilon}{2}<\nabla U^{(n)}-\nabla u^{(n)},\nabla\upsilon_r>-\frac{\tau}{2}<a^{(n)}(U^{(n)}-u^{(n)}),\upsilon_r>\\
&+\frac{\tau}{2}<F(U^{(n)})-F(u^{(n)}),\upsilon_r>+\tau<\mathfrak{E},\upsilon_r>,\quad \upsilon_r\in V_h.
\end{aligned}
$$

Then using mean value theorem, we have

$$
\begin{aligned}
&<U^{(n+1)}-u^{(n+1)},\upsilon_r>+\frac{\tau\epsilon}{2}<\nabla U^{(n+1)}-\nabla u^{(n+1)},\nabla\upsilon_r>\leq<U^{(n)}-u^{(n)},\upsilon_r>\\
&-\frac{\tau\epsilon}{2}<\nabla U^{(n)}-\nabla u^{(n)},\nabla\upsilon_r>+\frac{\tau}{2}<(M-a^{(n+1)})(U^{(n+1)}-u^{(n+1)}),\upsilon_r>\\
&+\frac{\tau}{2}<(M-a^{(n)})(U^{(n)}-u^{(n)}),\upsilon_r>+\tau<\mathfrak{E},\upsilon_r>,
\end{aligned}
$$

where $\max|F^{'}(x)|=M$.
Now, we can write

$$U^{(n+1)}-u^{(n+1)}=(U^{(n+1)}-U_h^{(n+1)})+(U_h^{(n+1)}-u^{(n+1)}),$$

we get

$$
\begin{aligned}
&<U_h^{(n+1)}-u^{(n+1)},\upsilon_r>+\frac{\tau\epsilon}{2}<\nabla U_h^{(n+1)}-\nabla u^{(n+1)},\nabla\upsilon_r>\leq<U_h^{(n)}-u^{(n)},\upsilon_r>\\
&-\frac{\tau\epsilon}{2}<\nabla U_h^{(n)}-\nabla u^{(n)},\nabla\upsilon_r>+\frac{\tau}{2}<(M-a^{(n+1)})(U_h^{(n+1)}-u^{(n+1)}),\upsilon_r>\\
&+\frac{\tau}{2}<(M-a^{(n)})(U_h^{(n)}-u^{(n)}),\upsilon_r>-<U_h^{(n)}-U^{(n)},\upsilon_r>\\
&+\frac{\tau\epsilon}{2}<\nabla U_h^{(n)}-\nabla U^{(n)},\nabla\upsilon_r>+<U_h^{(n+1)}-U^{(n+1)},\upsilon_r>\\
&+\frac{\tau\epsilon}{2}<\nabla U_h^{(n+1)}-\nabla U^{(n+1)},\nabla\upsilon_r>-\frac{\tau}{2}<(M-a^{(n+1)})(U_h^{(n+1)}-U^{(n+1)}),\upsilon_r>\\
&-\frac{\tau}{2}<(M-a^{(n)})(U_h^{(n)}-U^{(n)}),\upsilon_r>+\tau<\mathfrak{E},\upsilon_r>. \qquad (3.6.4)
\end{aligned}
$$

Taking

$$\mathfrak{X}_h^{(n+1)}=U_h^{(n+1)}-u^{(n+1)},\quad \mathfrak{T}_h^{(n+1)}=U_h^{(n+1)}-U^{(n+1)},$$

Eq.(3.6.4) can be rewritten as

$$
\begin{aligned}
&<\mathfrak{X}_h^{(n+1)},\upsilon_r>+\frac{\tau\epsilon}{2}<\nabla\mathfrak{X}_h^{(n+1)},\nabla\upsilon_r>\leq<\mathfrak{X}_h^{(n)},\upsilon_r>-\frac{\tau\epsilon}{2}<\nabla\mathfrak{X}_h^{(n)},\nabla\upsilon_r>\\
&+\frac{\tau}{2}<(M-a^{(n+1)})\mathfrak{X}_h^{(n+1)},\upsilon_r>+\frac{\tau}{2}<(M-a^{(n)})\mathfrak{X}_h^{(n)},\upsilon_r>+<\mathfrak{T}_h^{(n+1)},\upsilon_r>
\end{aligned}
$$

$$
\begin{aligned}
&+\frac{\tau\epsilon}{2}<\nabla\mathfrak{T}_h^{(n+1)},\nabla\upsilon_r>-\frac{\tau}{2}<(M-a^{(n+1)})\mathfrak{T}_h^{(n+1)},\upsilon_r>\\
&-<\mathfrak{T}_h^{(n)},\upsilon_r>+\frac{\tau\epsilon}{2}<\nabla\mathfrak{T}_h^{(n)},\nabla\upsilon_r>-\frac{\tau}{2}<(M-a^{(n)})\mathfrak{T}_h^{(n)},\upsilon_r>\\
&+\tau<\mathfrak{E},\upsilon_r>.
\end{aligned}
$$

Thus, using the definition (3.6.2), we have

$$
\begin{aligned}
&<\mathfrak{X}_h^{(n+1)},\upsilon_r>+\frac{\tau\epsilon}{2}<\nabla\mathfrak{X}_h^{(n+1)},\nabla\upsilon_r>\leq<\mathfrak{X}_h^{(n)},\upsilon_r>-\frac{\tau\epsilon}{2}<\nabla\mathfrak{X}_h^{(n)},\nabla\upsilon_r>\\
&\quad+\frac{\tau}{2}<(M-a^{(n+1)})\mathfrak{X}_h^{(n+1)},\upsilon_r>+\frac{\tau}{2}<(M-a^{(n)})\mathfrak{X}_h^{(n)},\upsilon_r>\\
&\quad+\tau<\mathfrak{F}_h^{(n+1)},\upsilon_r>+\tau<\mathfrak{E},\upsilon_r>.
\end{aligned}
$$

Setting $\upsilon_r=\mathfrak{X}_h^{(n+1)}$ in above relation, we obtain

$$
\begin{aligned}
&<\mathfrak{X}_h^{(n+1)},\mathfrak{X}_h^{(n+1)}>+\frac{\tau\epsilon}{2}<\nabla\mathfrak{X}_h^{(n+1)},\nabla\mathfrak{X}_h^{(n+1)}>\leq<\mathfrak{X}_h^{(n)},\mathfrak{X}_h^{(n+1)}>\\
&\quad-\frac{\tau\epsilon}{2}<\nabla\mathfrak{X}_h^{(n)},\nabla\mathfrak{X}_h^{(n+1)}>+\frac{\tau}{2}<(M-a^{(n+1)})\mathfrak{X}_h^{(n+1)},\mathfrak{X}_h^{(n+1)}>\\
&\quad+\frac{\tau}{2}<(M-a^{(n)})\mathfrak{X}_h^{(n)},\mathfrak{X}_h^{(n+1)}>+\tau<\mathfrak{F}_h^{(n+1)},\mathfrak{X}_h^{(n+1)}>+\tau<\mathfrak{E},\mathfrak{X}_h^{(n+1)}>.
\end{aligned}
$$

By employing Cauchy-Schwarz and Young's inequalities, yields

$$
\begin{aligned}
&\frac{1}{2}\Big\|\mathfrak{X}_h^{(n+1)}\Big\|^2_{L^2(\Omega)}+\frac{\tau\epsilon}{4}\Big\|\nabla\mathfrak{X}_h^{(n+1)}\Big\|^2_{L^2(\Omega)}\leq\frac{1}{2}\Big\|\mathfrak{X}_h^{(n)}\Big\|^2_{L^2(\Omega)}+\frac{\tau\epsilon}{4}\Big\|\nabla\mathfrak{X}_h^{(n)}\Big\|^2_{L^2(\Omega)}\\
&\quad+\Big(\frac{3}{4}|M-\alpha|+1\Big)\tau\Big\|\mathfrak{X}_h^{(n+1)}\Big\|^2_{L^2(\Omega)}+|M-\alpha|\frac{\tau}{4}\Big\|\mathfrak{X}_h^{(n)}\Big\|^2_{L^2(\Omega)}\\
&\quad+\frac{\tau}{2}\Big\|\mathfrak{F}_h^{(n+1)}\Big\|^2_{L^2(\Omega)}+\frac{\tau}{2}\Big\|\mathfrak{E}\Big\|^2_{L^2(\Omega)}.
\end{aligned}
$$

By defining weighted norm,

$$
\Big\|\mathfrak{X}_h^{(n+1)}\Big\|^2_{H_w(\Omega)}=\frac{1}{2}\Big\|\mathfrak{X}_h^{(n+1)}\Big\|^2_{L^2(\Omega)}+\frac{\tau\epsilon}{4}\Big\|\nabla\mathfrak{X}_h^{(n+1)}\Big\|^2_{L^2(\Omega)},
$$

we get

$$\Big\|\mathfrak{X}_h^{(n+1)}\Big\|^2_{H_w(\Omega)} \le \Big\|\mathfrak{X}_h^{(n)}\Big\|^2_{H_w(\Omega)} + \Big(3|M-\alpha|+4\Big)\frac{\tau}{2}\Big\|\mathfrak{X}_h^{(n+1)}\Big\|^2_{H_w(\Omega)} + |M-\alpha|\frac{\tau}{2}\Big\|\mathfrak{X}_h^{(n)}\Big\|^2_{H_w(\Omega)} + \frac{\tau}{2}\Big\|\mathfrak{F}_h^{(n+1)}\Big\|^2_{L^2(\Omega)} + \frac{\tau}{2}\Big\|\mathfrak{E}\Big\|^2_{L^2(\Omega)}. \tag{3.6.5}$$

Summing Eq. (3.6.5) over j from 0 to n,

$$\sum_{j=0}^{n}\Big\|\mathfrak{X}_h^{(j+1)}\Big\|^2_{H_w(\Omega)} \le \sum_{j=0}^{n}\Big\|\mathfrak{X}_h^{(j)}\Big\|^2_{H_w(\Omega)} + \Big(3|M-\alpha|+4\Big)\frac{\tau}{2}\sum_{j=0}^{n}\Big\|\mathfrak{X}_h^{(j+1)}\Big\|^2_{H_w(\Omega)} + |M-\alpha|\frac{\tau}{2}\sum_{j=0}^{n}\Big\|\mathfrak{X}_h^{(j)}\Big\|^2_{H_w(\Omega)} + \frac{\tau}{2}\sum_{j=0}^{n}\Big\|\mathfrak{F}_h^{(j+1)}\Big\|^2_{L^2(\Omega)} + \frac{\tau}{2}\sum_{j=0}^{n}\Big\|\mathfrak{E}\Big\|^2_{L^2(\Omega)}.$$

$$\Rightarrow \quad \Big\|\mathfrak{X}_h^{(n+1)}\Big\|^2_{H_w(\Omega)} \le \underbrace{\Big\|\mathfrak{X}_h^{(0)}\Big\|^2_{H_w(\Omega)}}_{=0} + (4|M-\alpha|+1)\frac{\tau}{2}\sum_{j=0}^{n}\Big\|\mathfrak{X}_h^{(j+1)}\Big\|^2_{H_w(\Omega)} + \frac{\tau}{2}\sum_{j=0}^{n}\Big\|\mathfrak{F}_h^{(j+1)}\Big\|^2_{L^2(\Omega)} + \frac{n\tau}{2}\Big\|\mathfrak{E}\Big\|^2_{L^2(\Omega)}.$$

Applying Proposition 3.3.4, the above relation can be written as

$$\begin{aligned}\Big\|\mathfrak{X}_h^{(n+1)}\Big\|^2_{H_w(\Omega)} &\le \Big[\frac{\tau}{2}\Big(\sum_{j=0}^{n}\Big\|\mathfrak{F}_h^{(j+1)}\Big\|^2_{L^2(\Omega)} + n\Big\|\mathfrak{E}\Big\|^2_{L^2(\Omega)}\Big)\Big]\exp\Big((4|M-\alpha|+1)\frac{n\tau}{2}\Big)\\ &\le \Big[\frac{T}{2}(\mathfrak{d}_{\mathfrak{s}}{}^m+\tau^2)^2\Big]\exp\Big((4|M-\alpha|+1)T\Big) \qquad [\text{since } T=n\tau]\\ &\le \mathcal{C}(\mathfrak{d}_{\mathfrak{s}}{}^m+\tau^2)^2.\end{aligned}$$

Thus we have

$$\Big\|\mathfrak{X}_h^{(n+1)}\Big\|_{H_w(\Omega)} \le \mathcal{C}(\tau^2+\mathfrak{d}_{\mathfrak{s}}{}^m),$$

which completes the proof.

3.7 Numerical results and discussions

In the current Section, we will numerically examine the convergence and stability of the proposed EFG scheme by considering some examples. It has been observed that the computational efficiency of the proposed scheme is significantly influenced by the size of the nodal influence domain. In this study, we choose scaling parameter $\mathfrak{d}_{\mathfrak{c}} \in [2.7, 3.2]$. Moreover, as discussed in the previous Chapter, the Lagrange multiplier technique is employed to impose the essential boundary conditions. The Gauss quadrature formula has been implemented for background integral cells in which the nodes align nicely with the background cell vertices, minimizing overlapping in nodal influence domains. The $L_\infty-$errors for the considered problems have been estimated by

$$e_\epsilon^{N,\tau} = |u(x_i, t_j) - U_h(x_i, t_j)| \text{ and } E_\epsilon^{N,\tau} = \max_{i,j} e_\epsilon^{N,\tau}, \tag{3.7.1}$$

where N represents the number of nodes in the spatial direction, $t_j = j\tau$. Herein, $u(x,t)$ and $U_h(x,t)$ refer to the exact and computed EFG solutions respectively.

Example 3.7.1 *Consider the following non-linear singularly perturbed time-dependent problem*

$$u_t - \epsilon\nabla^2 u + (1 + x\exp(-t))u = F(x,t),$$

where $F(x,t)$ is chosen to satisfy the exact solution

$$u(x,t) = t\Big[\frac{\exp\left(-x/\sqrt{\epsilon}\right) + \exp\left(-(1-x)/\sqrt{\epsilon}\right)}{1 + \exp\left(-1/\sqrt{\epsilon}\right)} - \cos^2(\pi x)\Big].$$

Table 3.1: Maximum absolute errors for Example 3.7.1 for different values of ϵ at $t = 1.0$.

ϵ	$N = 32$	$N = 64$	$N = 128$
2^{-2}	9.864×10^{-5}	5.527×10^{-5}	1.384×10^{-5}
2^{-4}	9.718×10^{-5}	9.333×10^{-5}	2.334×10^{-5}
2^{-6}	9.513×10^{-4}	2.969×10^{-4}	7.432×10^{-5}
2^{-8}	6.151×10^{-3}	9.854×10^{-4}	3.197×10^{-4}
2^{-10}	5.140×10^{-3}	7.183×10^{-3}	6.053×10^{-4}
2^{-12}	6.432×10^{-3}	6.678×10^{-3}	5.690×10^{-4}
2^{-14}	1.466×10^{-2}	6.546×10^{-3}	6.276×10^{-4}
2^{-16}	3.093×10^{-2}	6.510×10^{-3}	8.711×10^{-4}
2^{-18}	3.441×10^{-2}	6.507×10^{-3}	8.727×10^{-4}
2^{-20}	3.441×10^{-2}	6.491×10^{-3}	8.727×10^{-4}

Table 3.1 displays the maximum absolute errors to demonstrate the $\epsilon-$uniform convergence of the proposed method. Since the exact solution is known, the maximum absolute errors have been calculated by using (3.7.1).

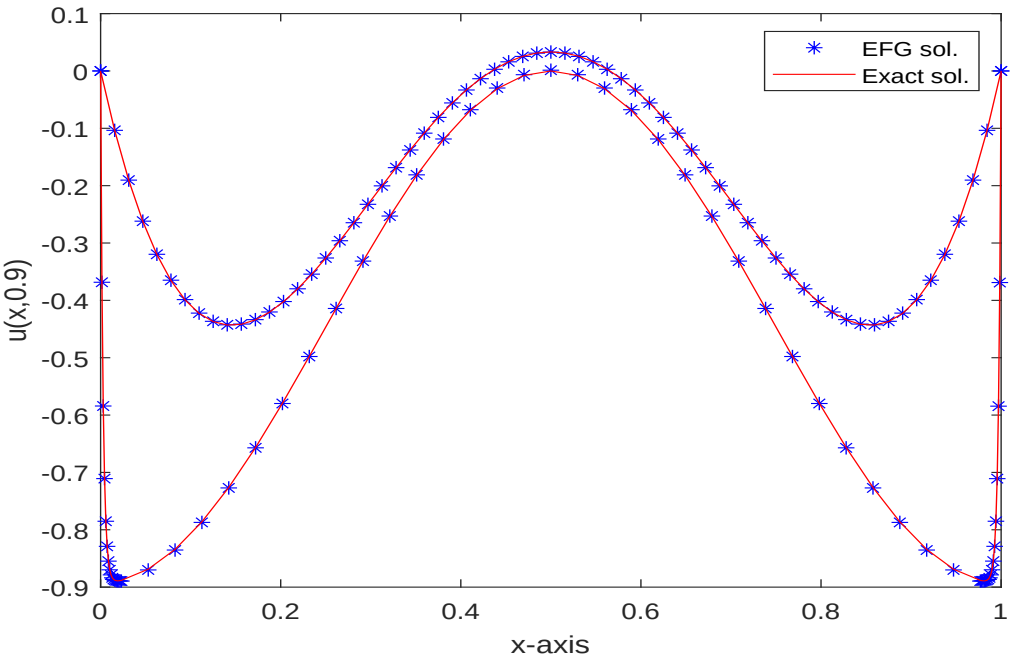

Figure 3.1: Comparison of EFG solution with exact solution for $N = 64,\ \epsilon = 2^{-7},\ 2^{-18}$.

Fig. 3.1 displays the element-free Galerkin solutions together with the exact ones for $N = 64$ and $\epsilon = 2^{-7}, 2^{-18}$ at time level $t = 0.9$. The boundary

layers are clearly visible near both the end points i.e. $x = 0$ and $x = 1$ of spatial domain. The plot clearly signifies the efficiency of the proposed scheme.

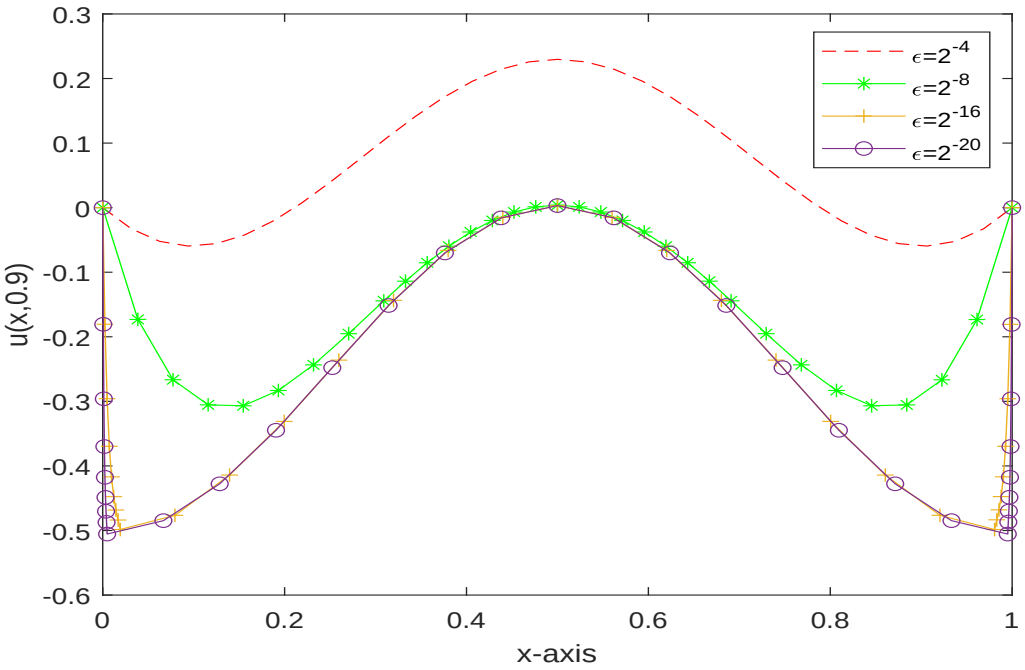

Figure 3.2: Epsilon-effect for $N = 64$ and $t = 0.5$.

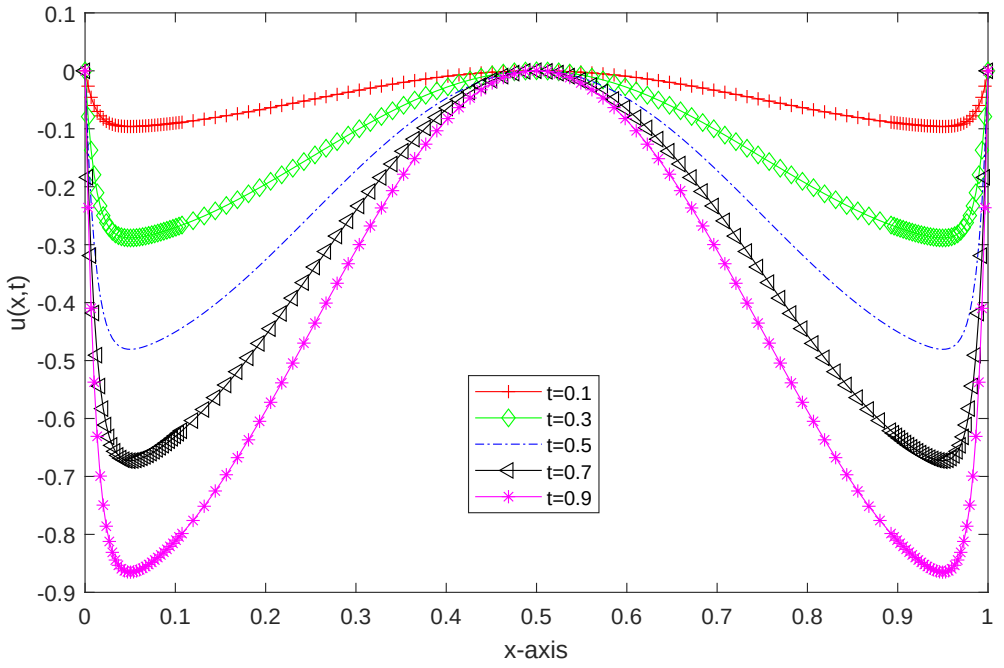

Figure 3.3: Time-effect on EFG solution for $N = 128$ and $\epsilon = 2^{-14}$.

In the next two Figures i.e. 3.2 and 3.3, we show the effect of the singularly perturbation parameter ϵ and the time t which exhibit the consistency and flexibility of the EFG method. The behavior of the EFG solution corresponding to small values of ϵ has been shown in Fig. 3.2. The sharpness of the boundary layers at the end points increases as $\epsilon \to 0$. Nodal refinement has been carried out in the steep boundary layer region by using Shiskhin's approach. Fig. 3.3 displays EFG solution plot at different time levels i.e. $t = 0.1,\ 0.3,\ 0.5,\ 0.7,\ 0.9$ with $N = 128$ and $\epsilon = 2^{-14}$. These solution plots easily verify the ability of the proposed EFG scheme in capturing very sharp boundary layers. The evolution of the EFG solution profile with respect to the continuous space-time domain has been displayed in Fig. 3.4.

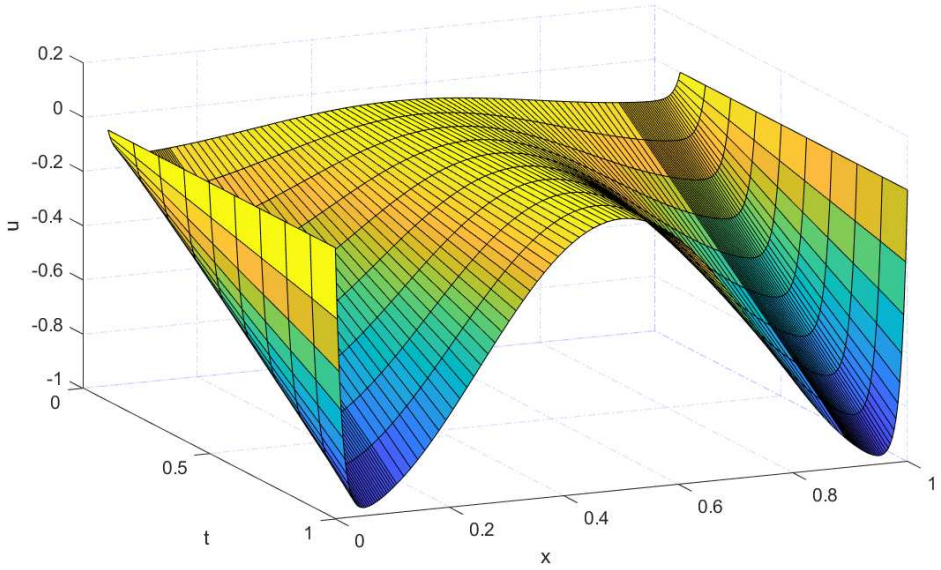

Figure 3.4: The numerical solution profile w.r.t. space-time domain for $\epsilon = 2^{-14}$.

Example 3.7.2 *For the second example, we have considered the following*

time-dependent singularly perturbed reaction-diffusion problem

$$u_t - \epsilon\nabla^2 u + \frac{1+x^2}{2}u = \exp(t) - 1 + \sin(\pi x),$$
$$u(x,0) = 0,$$
$$u(0,t) = u(1,t) = 0.$$

The exact solution of the considered problem is not known.
The boundary layers for this problem also occur on both sides of the solution, i.e., at $x = 0$ and $x = 1$. Table 3.2 presents the EFG solution at different spatial and temporal values and for different values of ϵ for future comparisons.

Table 3.2: EFG solution for Example 3.7.2 for different values of ϵ, x and t with $N = 128$.

t	x	$\epsilon = 2^{-5}$	$\epsilon = 2^{-10}$	$\epsilon = 2^{-15}$	$\epsilon = 2^{-20}$
0.1	0.007	0.00303	0.00476	0.00726	0.00611
	0.015	0.00598	0.00658	0.00819	0.01086
	0.25	0.07185	0.07477	0.07608	0.07428
	0.50	0.09909	0.10178	0.10217	0.10197
	0.75	0.08150	0.07123	0.07196	0.07339
	0.95	0.01670	0.01899	0.01968	0.01990
0.5	0.007	0.01880	0.05000	0.13349	0.14220
	0.015	0.03701	0.07056	0.14690	0.16377
	0.25	0.39344	0.45005	0.45636	0.44905
	0.50	0.50581	0.56217	0.56448	0.56446
	0.75	0.37818	0.41551	0.41908	0.42621
	0.95	0.09899	0.17874	0.18962	0.19068
1.0	0.007	0.04033	0.13289	0.41972	0.49704
	0.015	0.07929	0.18892	0.47368	0.53307
	0.25	0.80396	0.99474	1.00586	0.99459
	0.50	0.99904	1.15783	1.16629	1.16320
	0.75	0.76318	0.89813	0.90433	0.91653
	0.95	0.20851	0.47535	0.53075	0.53263

In Fig. 3.5, the grid validation test has been performed for $\epsilon = 2^{-16}$ at $t = 0.8$. Shishkin's approach has been utilized to generate more nodes in both boundary layer regions. It can be seen that a grid of 64 or more nodes is sufficient enough to capture very sharp boundary layers for very small values of the singular perturbation parameter like $\epsilon = 2^{-16}$. The impact of the singular perturbation parameter on the EFG solution for different values of $\epsilon = 2^{-3},\ 2^{-9},\ 2^{-15}$ and 2^{-18} at final time $t = 1.0$ has been illustrated in Fig. 3.6. The evolution of sharp boundary layers at both the end points of the domain can be noticed in the EFG solutions as ϵ approaches to zero.

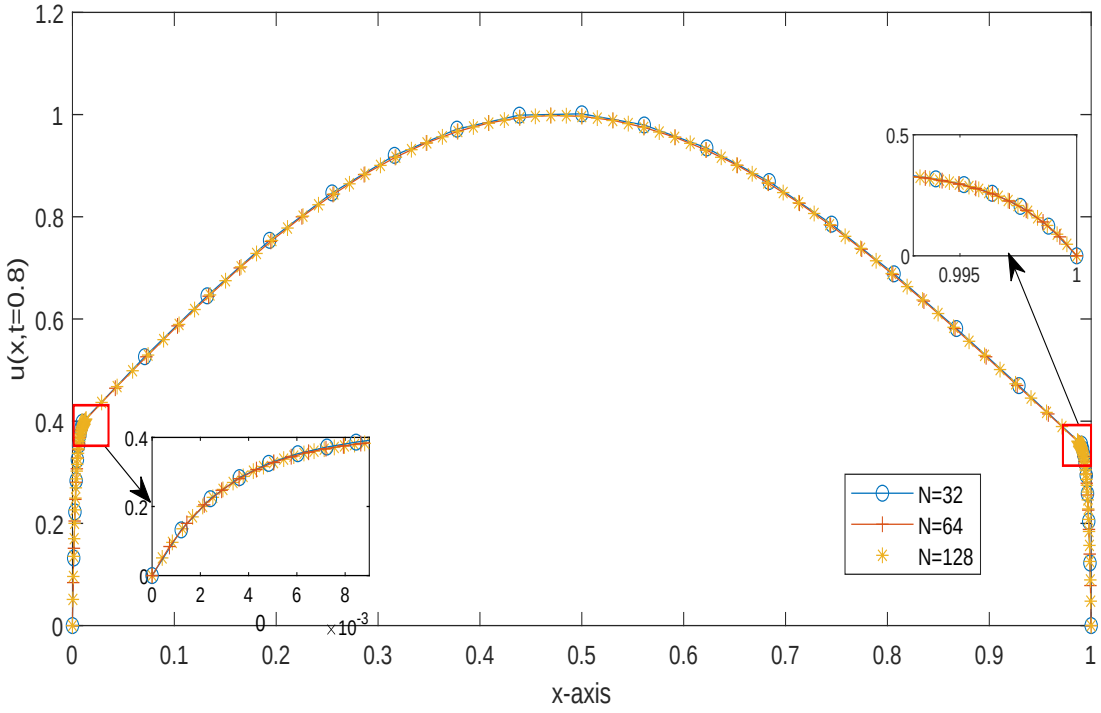

Figure 3.5: Grid validation test for $\epsilon = 2^{-16}$ at $t = 0.8$.

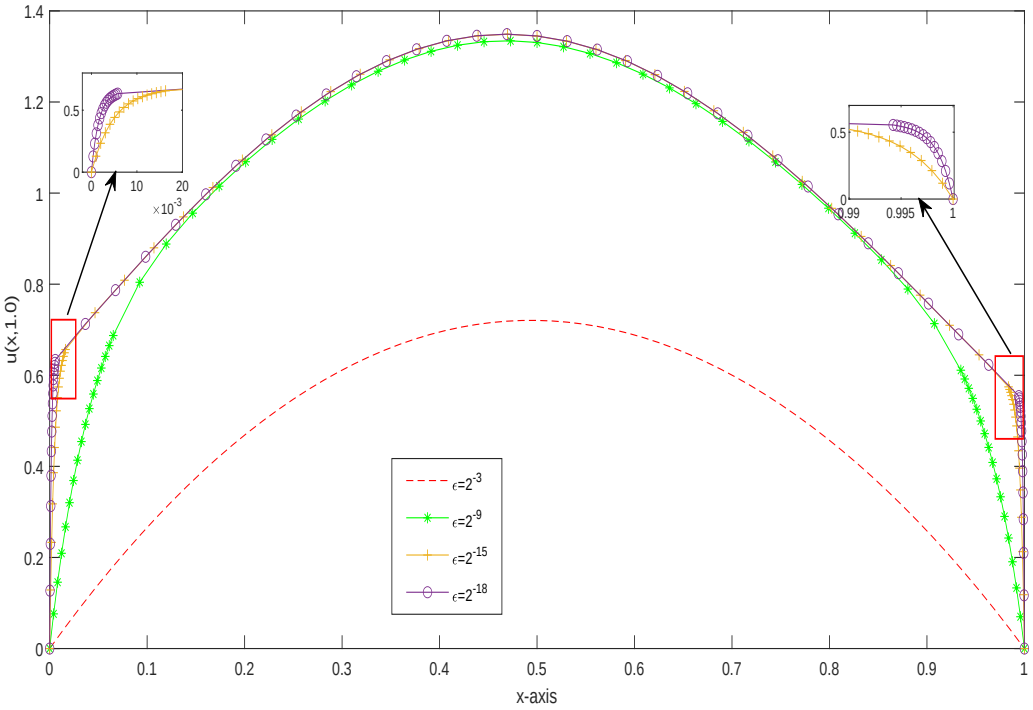

Figure 3.6: $\epsilon-$effect for $t = 1.0$ and $N = 64$ on EFG solution.

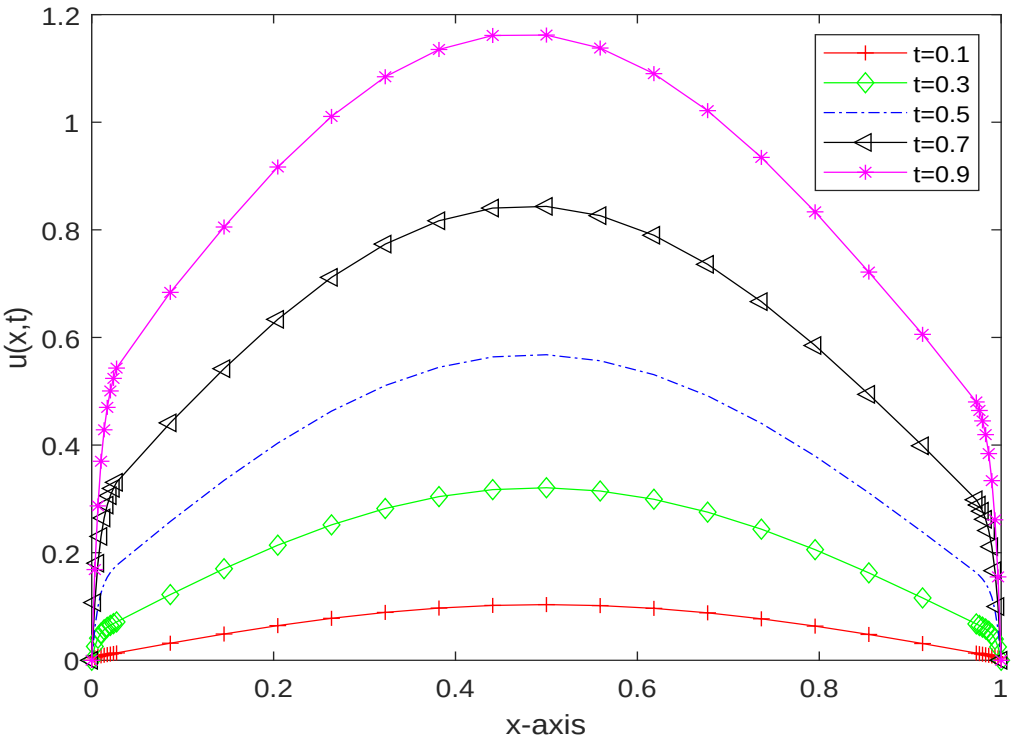

Figure 3.7: Time-effect on the numerical solution for $\epsilon = 2^{-13}$ and $N = 32$.

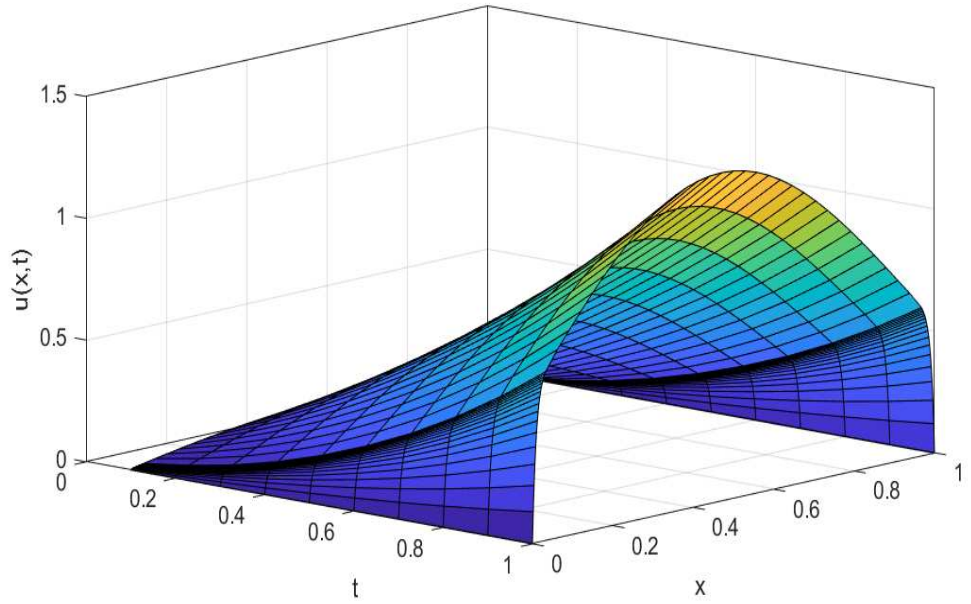

Figure 3.8: The EFG solution profile for Example 3.7.2 w.r.t. space-time domain for $\epsilon = 2^{-13}$ and $N = 64$.

In Fig. 3.7, the numerical solution has been plotted for $\epsilon = 2^{-13}$ at time levels $t = 0.1,\ 0.3,\ 0.5,\ 0.7$ and 0.9. All these solution plots easily verify the ability of the EFG method to capture very sharp boundary layers present in the solution. The three-dimensional solution plot for the space-time domain has been displayed in Fig. 3.8.

3.8 Conclusion

In the present Chapter, we have proposed element-free Galerkin technique to investigate the solution of the non-linear time-dependent singularly perturbed reaction-diffusion problem (3.2.1). The method combines the EFG scheme for spatial discretization with an implicit Crank-Nicolson method for temporal discretization. The stability of the time-discrete scheme for the considered non-linear problem has been analyzed. The existence and uniqueness of the EFG solution have been proved. It has been demonstrated

that the proposed approach converges uniformly with order $(\tau^2 + \mathfrak{d}_{\mathfrak{s}}{}^m)$. Numerical tests have been performed to validate the efficiency and robustness of the proposed scheme. The numerical outcomes confirm the theoretical findings addressed in the present work and the capabilities of the algorithm. Moreover, the presented technique is quite capable of capturing sharp boundary layers occurring in the solution when $\epsilon \to 0$. In order to test the ability and robustness of the proposed EFG technique for singularly perturbed problems, in the next two Chapters, we will propose the EFG approach for solving two model problems governing real-life phenomenon.

Chapter 4

Application of the element-free Galerkin method and its analysis for Fisher's problem

4.1 Introduction

In 1937, Fisher [69] examined the contrast of linear diffusion and non-linear reaction terms and proposed the Fisher's equation as a model for the propagation of genes in a habitat with an advantageous selection intensity. The present Chapter deals with one such kind of model problem known as time-dependent singularly perturbed Fisher's problem and is given by

$$\frac{\partial u(x,t)}{\partial t} = \epsilon \nabla^2 u(x,t) + \beta u(x,t)(1-u(x,t)),$$
$$(x,t) \in \Omega = \Omega_x \times \Omega_t = (0,1) \times (0,T], \qquad (4.1.1)$$

with initial condition

$$u(x,0) = u_0(x),\ x \in \bar{\Omega}_x, \qquad (4.1.2)$$

and boundary conditions as

$$u(0,t) = f(t),\quad u(1,t) = g(t),\ t \in \bar{\Omega}_t, \qquad (4.1.3)$$

where $u(x,t)$ symbolizes the occurrence of traveling waves, the parameter β is non-negative and $\partial\Omega = \bar{\Omega}\backslash\Omega$ is the boundary of the domain. In Eq. (4.1.1), ϵ is known as singular perturbation parameter satisfying $0 < \epsilon \ll 1$. The problem (4.1.1) becomes singularly perturbed in the case $\epsilon \to 0$.

The considered Fisher's problem is widely encountered in chemical kinet-

ics [83] and population dynamics [91] which include problems such as non-linear evolution of a population in habitat, flame propagation in nuclear reactor theory, the branching Brownian motion process [35] etc. Due to the extensive range of applications, researchers have been interested in solutions of Fisher's problem. Various numerical approaches have been developed to solve Fisher's equation.

Wazwaz and Gorguis [224] developed an analytical solution of generalized Fisher's equation by using the Adomian decomposition methodology. Rosa et al. [185] presented an application of Lie point symmetries for generalized Fisher's equation modeling the tumor progression in biological interests. A numerical analysis of the reaction-diffusion problem has been carried out by Al-Khaled [2] by employing the sinc collection approach. Ablowitz and Zeppetella [1] derived an explicit solution of the traveling wave equation and determined the exact solution for a particular value of wave speed $c = 5/\sqrt{6}$. Thenceforth, Wang [220] obtained exact and explicit solitary wave solutions of generalized Fisher's equation by introducing a mathematical method based on the non-linear transformation. Analytical representations of various traveling wave solutions for Fisher's equation have been derived by Brazhnik and Tyson [217] in two spatial dimensions. Feng and Li [67] obtained complex traveling wave solutions by reducing Fisher's equation to a first-order integrable ordinary differential equation using the first integral method. Mittal and Jiwari [154] adopted the differential quadrature method to study the numerical solutions of Fisher's problem. A pseudo-spectral technique was presented by Olmos and Shizgal [164], later by Balyan et al. [12]. Carey and Shen [36] developed a least-squares finite-element formulation for solving Fisher's equation. Petrov-Galerkin finite element method has been presented by Tang and Weber [214] to deal with Fisher's problem. Khader and Saad [112] developed a numerical technique for solving the fractional Fisher's equation, which represents the problem of biological invasion. The spectral collocation technique based upon Cheby-

shev approximations was employed to reduce the considered problem into a system of ordinary differential equations, which were further solved by the finite difference method. Radial basis functions based mesh-free approach for solving extended Fisher-Kolmogorov model was studied by Kumar et al. [121]. Atangana [5] applied fractional derivatives, introduced by Caputo and Fabrizio, to the non-linear Fisher's equation and derived a unique solution using the Sumudu decomposition iterative method.

Even though Fisher's problem has vast applications in diverse areas of science and engineering, only a few researchers have paid attention to the solution strategies for the singularly perturbed version of the Fisher's problem i.e. for $\epsilon \ll 1$, only a few researchers have proposed any numerical scheme so far. Dag and Ersoy [49] suggested a collocation scheme for solving Fisher's equation with a small value of the diffusion coefficient ϵ. Uzunca et al. [218] developed a discontinuous Galerkin approach with a moving mesh strategy for solving non-linear Fisher's equation with traveling wave solutions. Numerical results demonstrate different natures of traveling waves for $\epsilon \to 0$.
In the present Chapter, we will focus on the numerical analysis of the EFG scheme for singularly perturbed Fisher's model problem. To handel the nonlinearity present in the model problem, we have utilized the quasilinearization process proposed by Bellman and Kalaba [20]. The EFG technique has already been discussed in the previous Chapters. The work presented in this Chapter is organized as follows:
In Section 4.2, the Crank-Nicolson scheme is introduced as a method for temporal discretization. Section 4.3 deals with the quasilinearization process and its convergence. EFG formulation have been explained briefly in Section 4.4. In Section 4.5, the convergence of full-discrete scheme has been discussed. Section 4.6 presents numerical results which help to illustrate the effectiveness and accuracy of the EFG scheme. In the last, conclusion has been presented.

4.2 Temporal semi-discretization

In order to discretize the considered Fisher's model problem, first we discretize the time-derivative term by invoking the Crank-Nicolson scheme.

4.2.1 Semi-discrete scheme

To derive the weak formulation of Eq. (4.1.1), first we discretize the equation with respect to time. We employ the implicit Crank-Nicolson scheme with a uniform step size of τ for temporal semi-discretization. Performing temporal semi-discretization as discussed in Section 3.3, the considered problem reduces to

$$\frac{U^{(n+1)}-U^{(n)}}{\tau}=\epsilon\frac{\nabla^2U^{(n+1)}+\nabla^2U^{(n)}}{2}+\beta\frac{U^{(n+1)}+U^{(n)}}{2}-\beta\frac{(U^2)^{(n+1)}+(U^2)^{(n)}}{2}, \tag{4.2.1}$$

where $U^{(n+1)}$ denotes the solution of the temporal discrete scheme at $(n+1)^{th}$ time level. On simplifying, Eq. (4.2.1) results in

$$\begin{aligned} U^{(n+1)}-\frac{\tau\epsilon}{2}\nabla^2U^{(n+1)}-\frac{\tau\beta}{2}U^{(n+1)}+\frac{\tau\beta}{2}(U^2)^{n+1}& \\ =U^{(n)}+\frac{\tau\epsilon}{2}\nabla^2U^{(n)}+\frac{\tau\beta}{2}U^{(n)}-\frac{\tau\beta}{2}(U^2)^{(n)},& \end{aligned} \tag{4.2.2}$$

where $\nabla^2U^{(n+1)}=\frac{\partial^2U^{(n+1)}}{\partial x^2}$.
The stability of the above time semi-discrete scheme (4.2.2) is given by the following theorem:

Theorem 4.2.1 *Suppose $U^{(n+1)}\in H^1(\overline{\Omega})$. Then the time discrete scheme* (4.2.2) *is unconditionally stable.*

Proof The proof of the theorem can be derived on similar lines as in Theorem 3.3.5.

4.3 Quasilinearization technique

As the problem under consideration is non-linear in nature, and quasilinearization is a standard technique broadly used for approximating the non-linear problems by their linearized version for obtaining the approximate solutions, in this Section, we will linearize the considered problem using the quasilinearization process and will discuss its convergence.
By using the quasilinearization process proposed by Bellman and Kalaba [20], Eq. (4.2.2) can be transformed into the linear form

$$-\epsilon\frac{\tau}{2}\nabla^2 U^{(n+1),(k+1)} + \big[1-\beta\frac{\tau}{2}+\beta\tau U^{(n+1),(k)}\big]U^{(n+1),(k+1)} = \big(1+\beta\frac{\tau}{2}\big)U^{(n)} + \epsilon\frac{\tau}{2}\nabla^2 U^{(n)} - \beta\frac{\tau}{2}(U^2)^{(n)} + \beta\frac{\tau}{2}(U^2)^{(n+1),(k)}, \tag{4.3.1}$$

with initial condition $U^{(0),(k+1)} = U_0(x)$,
and boundary conditions

$$U^{(n+1),(k+1)}(0,t) = f(t^{(n+1)}) \;\; and \;\; U^{(n+1),(k+1)}(1,t) = g(t^{(n+1)}),$$

where $U^{(n+1),(k+1)}$ denotes the approximate solution at time level $(n+1)^{th}$ and $(k+1)^{th}$ iteration.

Theorem 4.3.1 (Convergence of quasilinearization technique) *Let* $\big\{U^{(n+1),(k)}\big\}_{k=0}^{\infty}$ *be the sequence produced by quasilinearization technique at* $(n+1)^{th}$ *time level and* $(k)^{th}$ *iteration. Then there exist a constant* $Q>0$, *independent of* n, *such that*

$$\|U^{(n+1),(k+1)} - U^{(n+1),(k)}\|_{\bar{\Omega}_x} \leq Q\|U^{(n+1),(k)} - U^{(n+1),(k-1)}\|^2_{\bar{\Omega}_x},$$

i.e. the quasilinearization process converges quadratically.

Proof In order to prove the convergence of the quasilinearization process,

we consider

$$\epsilon\nabla^2 U^{(n+1)} = F(U^{n+1}), \quad x \in \Omega_x, \quad n \geq 0,$$
$$U^{(n+1)}(0,t) = f(t^{n+1}), \quad U^{(n+1)}(1,t) = g(t^{n+1}), \quad n \geq 0.$$

We assume $U^{(n+1),(k=0)}$ be the initial guess which also incorporates the boundary conditions.
By applying quasilinearization process, we obtain a sequence $\left\{U^{(n+1),(k)}\right\}_{k=0}^{\infty}$ of linear differential equations determined by the following recurrence relation:

$$\epsilon\nabla^2 U^{(n+1),(k+1)} \approx F(U^{(n+1),(k)}) + (U^{(n+1),(k+1)} - U^{(n+1),(k)})\frac{\partial F(U^{(n+1),(k)})}{\partial U}, \tag{4.3.2}$$
$$U^{(n+1),(k+1)}(0,t) = f(t^{n+1}), \quad U^{(n+1),(k+1)}(1,t) = g(t^{n+1}), \quad x \in \Omega_x, \quad n \geq 0.$$

At $k-$th iteration step, the above Eq. (4.3.2) becomes

$$\epsilon\nabla^2 U^{(n+1),(k)} = F(U^{(n+1),(k-1)}) + (U^{(n+1),(k)} - U^{(n+1),(k-1)})\frac{\partial F(U^{(n+1),(k-1)})}{\partial U}, \quad x \in \Omega_x, \quad n \geq 0. \tag{4.3.3}$$

Subtracting Eq.(4.3.3) from (4.3.2), we have

$$\begin{aligned}\epsilon(\nabla^2 U^{(n+1),(k+1)} - \nabla^2 U^{(n+1),(k)}) = {} & F(U^{(n+1),(k)}) - F(U^{(n+1),(k-1)}) \\ & + (U^{(n+1),(k+1)} - U^{(n+1),(k)})\frac{\partial F(U^{(n+1),(k)})}{\partial U} \\ & - (U^{(n+1),(k)} - U^{(n+1),(k-1)})\frac{\partial F(U^{(n+1),(k-1)})}{\partial U}, \quad x \in \Omega_x, \quad n \geq 0,\end{aligned} \tag{4.3.4}$$

which is of second-order differential equation in $(U^{(n+1),(k+1)} - U^{(n+1),(k)})$. Utilizing Green's function, Eq. (4.3.4) can be converted into the integral

equation

$$\epsilon(U^{(n+1),(k+1)} - U^{(n+1),(k)}) = \int_0^1 G(x,s)\Big[F(U^{(n+1),(k)}) - F(U^{(n+1),(k-1)}) + (U^{(n+1),(k+1)} - U^{(n+1),(k)})\frac{\partial F(U^{(n+1),(k)})}{\partial U} - (U^{(n+1),(k)} - U^{(n+1),(k-1)})\frac{\partial F(U^{(n+1),(k-1)})}{\partial U}\Big]ds, \quad x \in \Omega_x, \quad n \geq 0, \tag{4.3.5}$$

where the Green's function $G(x,s)$ is defined by

$$G(x,s) = \begin{cases} x(s-1), & 0 \leq x \leq s \leq 1, \\ (x-1)s, & 0 \leq s \leq x \leq 1, \end{cases}$$

and

$$\max_{x,s} G(x,s) = \frac{1}{4}. \tag{4.3.6}$$

Using mean value theorem, we have

$$F(U^{(n+1),(k)}) - F(U^{(n+1),(k-1)}) = (U^{(n+1),(k)} - U^{(n+1),(k-1)})\frac{\partial F(U^{(n+1),(k-1)})}{\partial U} + \frac{(U^{(n+1),(k)} - U^{(n+1),(k-1)})^2}{2}\frac{\partial^2 F(\theta)}{\partial U^2}, \tag{4.3.7}$$

where $U^{(n+1),(k-1)} \leq \theta \leq U^{(n+1),(k)}$. Now substituting the value of $F(U^{(n+1),(k)}) - F(U^{(n+1),(k-1)})$ in Eq. (4.3.5), the resulting expression will become

$$\epsilon(U^{(n+1),(k+1)} - U^{(n+1),(k)}) = \int_0^1 G(x,s)\Big[\frac{(U^{(n+1),(k)} - U^{(n+1),(k-1)})^2}{2}\frac{\partial^2 F(\theta)}{\partial U^2} + (U^{(n+1),(k+1)} - U^{(n+1),(k)})\frac{\partial F(U^{(n+1),(k)})}{\partial U}\Big]ds, \quad x \in \Omega_x, \quad n \geq 0. \tag{4.3.8}$$

Assume that

$$\max_{|\theta|\leq 1}\Big|\frac{\partial^2 F(\theta)}{\partial U^2}\Big| = L, \quad \max_{|U^{(n+1),(k)}|\leq 1}\Big|\frac{\partial F(U^{(n+1),(k)})}{\partial U}\Big| = R. \tag{4.3.9}$$

Now using (4.3.6) and (4.3.9) in Eq. (4.3.8) and taking maximum norm, we get

$$\begin{aligned}\epsilon\big\|U^{(n+1),(k+1)} - U^{(n+1),(k)}\big\|_{\bar{\Omega}_x} \leq & \frac{1}{4}\int_0^1 \Big[\frac{L}{2}(U^{(n+1),(k)} - U^{(n+1),(k-1)})^2 \\ & + R\big\|U^{(n+1),(k+1)} - U^{(n+1),(k)}\big\|_{\bar{\Omega}_x}\Big]ds.\end{aligned}$$

On simplifying this inequality, we get

$$\begin{aligned}\big\|(U^{(n+1),(k+1)} - U^{(n+1),(k)})\big\|_{\bar{\Omega}_x} &\leq \frac{L}{8\epsilon - 2R}\big\|(U^{(n+1),(k)} - U^{(n+1),(k-1)})\big\|^2_{\bar{\Omega}_x}, \\ &= Q\|(U^{(n+1),(k)} - U^{(n+1),(k-1)})\|^2_{\bar{\Omega}_x},\end{aligned}$$

where $Q = L/(8\epsilon - 2R)$.
Hence, with the appropriate choice of initial iterative approximation $U^{(n+1),(k=0)}$, the quasilinearization technique converges quadratically.

4.4 Element-free Galerkin weak formulation

As discussed earlier in Section 4.3, in order to obtain the solution of the Fisher's problem, we consider its linear approximation (4.3.1), obtained by quasilinearization process.
The EFG weak formulation of the linearized Eq. (4.3.1) is given as follows:

$$\frac{\epsilon\tau}{2}\int_{\Omega_x}\nabla U^{(n+1),(k+1)}\nabla\phi_i dx + \big[1 - \frac{\beta\tau}{2} + \beta\tau U^{(n+1),(k)}\big]\int_{\Omega_x} U^{(n+1),(k+1)}\phi_i dx$$

$$
\begin{aligned}
&- \delta\lambda(U - f(t))\Big|_{x=0} - \delta U\lambda\Big|_{x=0} - \delta\rho(U - g(t))\Big|_{x=1} - \delta U\rho\Big|_{x=1} \\
&= \big(1 + \frac{\beta\tau}{2}\big) \int_{\Omega_x} U^{(n)}\phi_i dx - \frac{\epsilon\tau}{2} \int_{\Omega_x} \nabla U^{(n)} \nabla\phi_i dx \\
&- \frac{\beta\tau}{2} \int_{\Omega_x} (U^2)^{(n)}\phi_i dx + \frac{\beta\tau}{2} \int_{\Omega_x} (U^2)^{(n+1),(k)}\phi_i dx,
\end{aligned}
$$

where ϕ_i's are the test functions formulated by MLS approach as specified in Section 3.4.2. The last terms on the left-hand side of the above equation are introduced due to the method of Lagrange multipliers to enforce the essential boundary conditions (4.1.3). On solving and assembling, the above nodal weak formulations can be reformulated as

$$
\begin{bmatrix} K & G & H \\ G^T & 0 & 0 \\ H^T & 0 & 0 \end{bmatrix} \begin{bmatrix} U \\ \lambda \\ \rho \end{bmatrix} = \begin{bmatrix} F \\ q \\ q_c \end{bmatrix},
$$

where

$$
\begin{aligned}
K_{ij} &= \epsilon\frac{\tau}{2} \int_{\Omega_x} \nabla\phi_j \nabla\phi_i dx + \big[1 - \beta\frac{\tau}{2} + \beta\tau U^{(n+1),(k)}\big] \int_{\Omega_x} \phi_j\phi_i dx, \\
G^T_{lj} &= -\delta\lambda_l(N_l\phi_j)\Big|_{x=0}, \\
H^T_{lj} &= -\delta\rho_l(R_l\phi_j)\Big|_{x=1},
\end{aligned}
$$

$$
\begin{aligned}
F_i &= \big(1 + \beta\frac{\tau}{2}\big) \int_{\Omega_x} U^{(n)}\phi_i dx - \epsilon\frac{\tau}{2} \int_{\Omega_x} \nabla U^{(n)} \nabla\phi_i dx - \beta\frac{\tau}{2} \int_{\Omega_x} (U^2)^{(n)}\phi_i dx \\
&\quad + \beta\frac{\tau}{2} \int_{\Omega_x} (U^2)^{(n+1),(k)}\phi_i dx, \\
q_l &= -\delta\lambda_l(N_l f(t))\Big|_{x=0}, \\
q_{c_l} &= -\delta\rho_l(R_l g(t))\Big|_{x=1}.
\end{aligned}
$$

Here, λ and ρ are Lagrange multipliers.

4.5 Convergence of full-discrete scheme

The variational weak form of Eq. (4.2.2) is given as:
Find $u^{(n+1)} \in H^1(\Omega)$ such that

$$
\begin{aligned}
&<u^{(n+1)}, \upsilon_r> + \frac{\tau\epsilon}{2} < \nabla u^{(n+1)}, \nabla \upsilon_r> - \frac{\tau\beta}{2} < u^{(n+1)}, \upsilon_r> + \frac{\tau\beta}{2} < (u^2)^{(n)}, \upsilon_r> \\
&= < u^{(n+1)}, \upsilon_r> - \frac{\tau\epsilon}{2} < \nabla u^{(n+1)}, \nabla \upsilon_r> + \frac{\tau\beta}{2} < u^{(n+1)}, \upsilon_r> - \frac{\tau\beta}{2} < (u^2)^{(n)}, \upsilon_r> \\
&\quad + \tau < \mathfrak{E}^{(n+1)}, \upsilon_r>, \qquad (4.5.1)
\end{aligned}
$$

where the last term denotes the residual.

Theorem 4.5.1 *Let $u^{(n+1)}$ be solution of* (4.5.1) *and $U_h^{(n+1)}$ be solution of* (4.3.1). *Then*

$$\left\| U_h^{(n+1)} - u^{(n+1)} \right\|_{H_w(\Omega)} \leq \mathcal{C}(\tau^2 + \mathfrak{d}_{\mathfrak{s}}{}^m).$$

Proof of the theorem can be derived using the similar arguments as discussed in Theorem 3.6.3.

4.6 Numerical results

In this Section, we will numerically validate the theoretical findings and demonstrate the consistency and accuracy of the proposed method with the help of examples. The $L_\infty-$errors have been estimated by

$$e_{i,j}^{N,\tau} = |u(x_i, t_j) - U_h(x_i, t_j)| \quad \text{and} \quad E_\epsilon^{N,\tau} = \max_{i,j} e_{i,j}^{N,\tau},$$

where N symbolize number of nodes in the spatial direction and $t_j = j\tau$. Herein, $u(x,t)$ and $U_h(x,t)$ are exact and computed EFG solutions respectively.

The order of convergence has been calculated by employing double mesh principle defined by

$$p_\epsilon^{N,\tau} = \left| \frac{\ln\left(E_\epsilon^{N,\tau}\right) - \ln\left(E_\epsilon^{2N,\tau}\right)}{\ln(2)} \right|.$$

Example 4.6.1 *Consider the singularly perturbed non-linear Fisher's equation [154]*

$$\frac{\partial u}{\partial t} = \epsilon \frac{\partial^2 u}{\partial x^2} + u^2(1-u),$$

where the initial and boundary conditions are set to satisfy the exact solution

$$u(x,t) = \frac{1}{1 + exp(\sqrt{1/2\epsilon}x - t/2)}.$$

EFG method has been applied to the problem in order to check the efficiency of the method. Table 4.1 displays the maximum absolute errors for different number of nodes as $\epsilon \to 0$. Convergence order has also been presented in the Table. The numerical convergence of the proposed scheme can easily be observed from the Table. The robustness of the method in approximating the exact solution for very small values of the singular perturbation parameter can also be noticed clearly even for very less number of nodes.

In Table 4.2, the numerical results have been compared with those provided in [16, 154] for $\epsilon = 1$. It can clearly be observed that the present results obtained using proposed EFG method are quite better than those of differential quadrature method (DQM) and sixth-order compact finite difference method (CFD), presented in [16, 154] respectively.

The behavior of the solution has been plotted in Figs. $4.1 - 4.4$ for different parametric values. Grid validation of the code has been tested at time level $t = 1.0$ for the singular perturbation parameter values $\epsilon = 2^{-10}$ and 2^{-15} in Fig. 4.1. From these solution plots, it can clearly be seen that though a grid of 32 elements is sufficient enough to capture very sharp boundary layers for small values of ϵ like 2^{-15}, for the rest of the graphs, a grid of 64 elements has been considered for more accurate EFG solution plots.

Table 4.1: Maximum absolute errors and order of convergence for Example 4.6.1 for different values of ϵ.

ϵ	$N = 32$	$N = 64$	$N = 128$
2^{-2}	4.63×10^{-6}	1.16×10^{-6}	2.91×10^{-7}
	1.99	1.99	
2^{-4}	2.41×10^{-5}	6.04×10^{-6}	1.51×10^{-6}
	1.99	2	
2^{-6}	9.60×10^{-5}	2.40×10^{-5}	6.00×10^{-6}
	2	2	
2^{-8}	3.71×10^{-4}	9.60×10^{-5}	2.40×10^{-5}
	1.95	2	
2^{-10}	8.43×10^{-4}	3.16×10^{-4}	9.63×10^{-5}
	1.41	1.72	
2^{-12}	8.43×10^{-4}	3.16×10^{-4}	1.08×10^{-4}
	1.41	1.55	
2^{-14}	8.44×10^{-4}	3.16×10^{-4}	1.08×10^{-4}
	1.41	1.55	
2^{-16}	8.44×10^{-4}	3.16×10^{-4}	1.08×10^{-4}
	1.41	1.55	
2^{-18}	8.44×10^{-4}	3.16×10^{-4}	1.08×10^{-4}
	1.41	1.55	
2^{-20}	8.44×10^{-4}	3.16×10^{-4}	1.08×10^{-4}
	1.41	1.55	

Table 4.2: Comparison of results for Example 4.6.1 for $\epsilon = 1$ and $N = 13$.

t	x	DQM [154]	CFD	$EFGM$	$Exact$	$Absolute\ error$
0.5	0.25	0.51831	0.518298	0.518299	0.518297	1.69×10^{-6}
	0.75	0.43038	0.430373	0.430374	0.430372	1.60×10^{-6}
1.0	0.25	0.58012	0.580110	0.580111	0.580109	1.71×10^{-6}
	0.75	0.49243	0.492418	0.492419	0.492418	1.84×10^{-6}

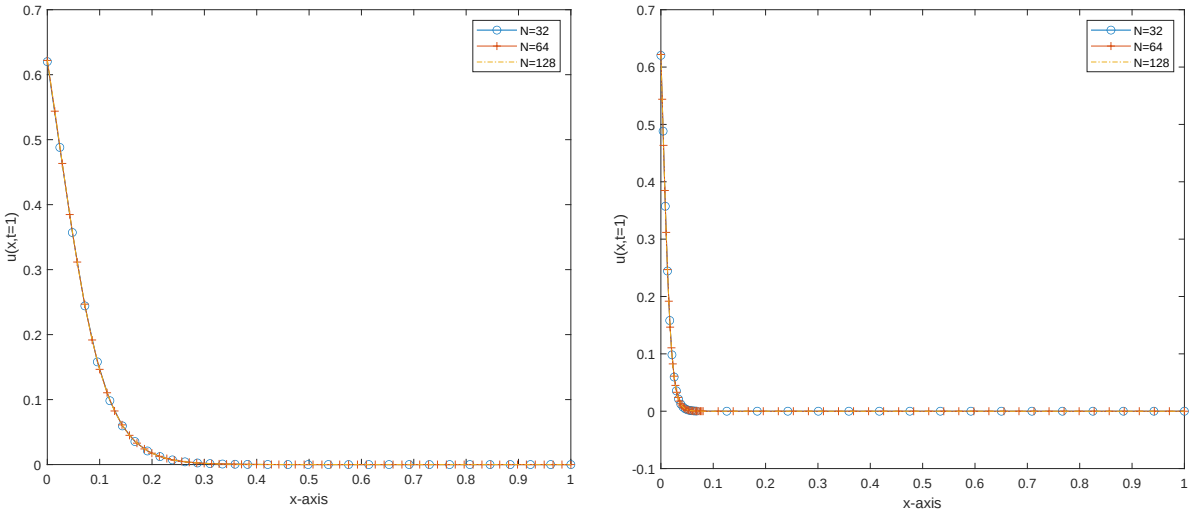

Figure 4.1: Grid validation test for $\epsilon = 2^{-10}, 2^{-15}$.

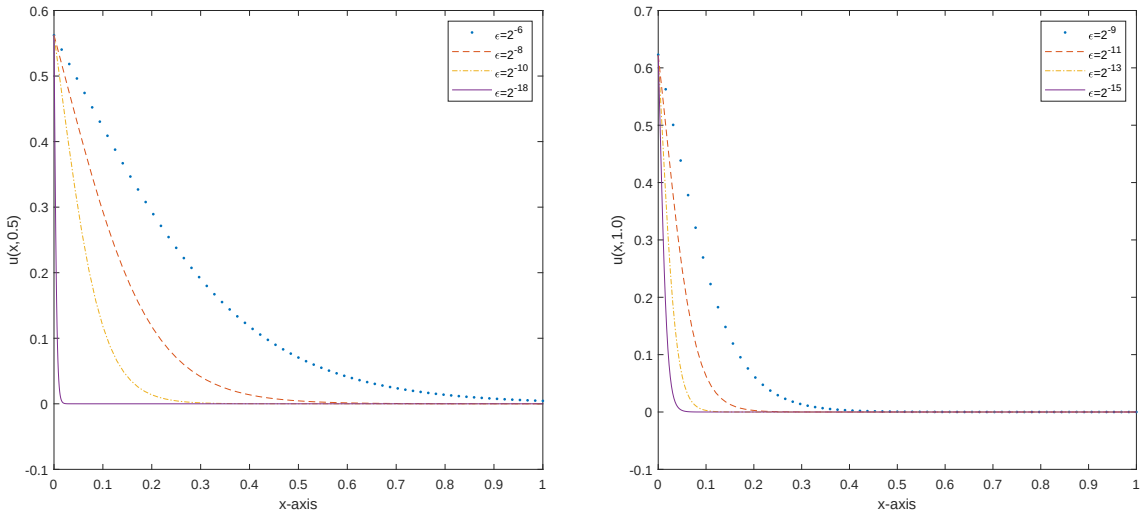

Figure 4.2: ϵ-effect at different time levels=0.5, 1.0.

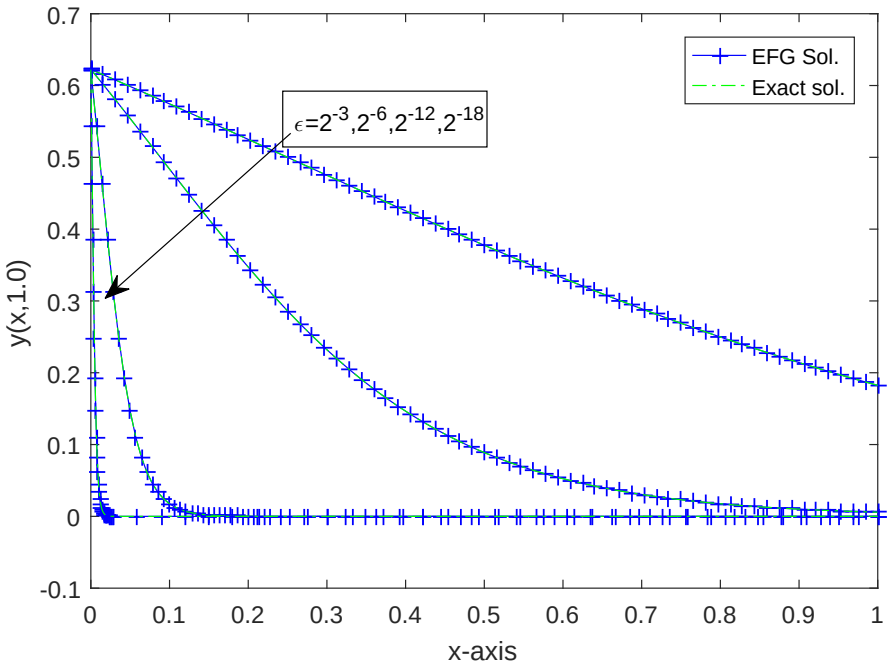

Figure 4.3: Comparison of EFG solution with exact for $N = 64,\ \epsilon = 2^{-3},\ 2^{-6},\ 2^{-12},\ 2^{-18}$.

The behavior of the singular perturbation parameter on the EFG solution has been illustrated in Fig. 4.2 as $\epsilon \to 0$. These solutions have been plotted for different values of ϵ at time levels $t = 0.5$ and $t = 1$. The more sharper boundary layers arise in the solution as the singular perturbation parameter tends to zero, as seen in both the graphs and the proposed numerical technique is efficient enough to capture these boundary layers.
In Fig. 4.3, the comparison of exact solutions with the computed ones is shown for different values of ϵ, which clearly depicts the efficiency and robustness of the proposed method in capturing very sharp boundary layers. One can easily observe that the EFG solutions overlap the exact solutions. The evolution of the EFG solution profile with respect to the space-time profile has been displayed in Fig. 4.4.

Example 4.6.2 *For the next example, consider the following singularly perturbed Fisher's equation [49]*

$$\frac{\partial u}{\partial t} = \epsilon \frac{\partial^2 u}{\partial x^2} + \beta u(1-u), \tag{4.6.1}$$

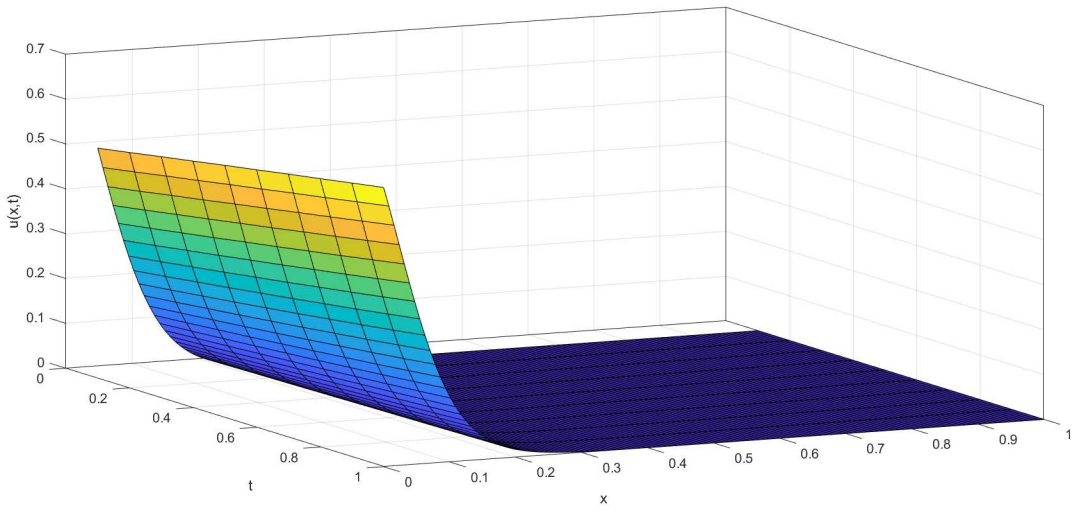

Figure 4.4: The space-time continuous solution profile of the EFG scheme for $\epsilon = 2^{-13}$.

with initial condition

$$u(x,0) = \frac{1}{(1+e^{\theta_1 x})^2} \ ,$$

and boundary conditions

$$u(0,t) = \frac{1}{(1+e^{-\theta_2 t})^2} \ , \quad u(1,t) = \frac{1}{(1+e^{\theta_1 - \theta_2 t})^2}.$$

The analytical solution is not available in the literature for the considered problem 4.6.2. The particular solution of the problem (4.6.1) for the case $\epsilon = 1$ has been found out by Ablowitz and Zepetella [1] and is given by

$$u(x,t) = \frac{1}{(1+e^{\theta_1 x - \theta_2 t})^2},$$

where $\theta_1 = \sqrt{\beta/6}$ and $\theta_2 = 5\beta/6$.
The boundary layers for the problem under consideration occur on both sides of the solution, i.e., at $x = 0$ and $x = 1$. This problem has not been solved in literature for small values of the singular perturbation parameter ϵ to the best of the our knowledge.
In Table 4.3, the EFG solution has been presented for different spatial and

temporal values and for different values of ϵ for future comparisons. The maximum absolute errors for different number of nodes and at different time levels are presented in Table 4.4 for $\epsilon = 1$. These tables clearly demonstrate the accuracy and reliability of the proposed technique.

Table 4.3: EFG solution for Example 4.6.2 for different values of ϵ with $N = 64$.

t	x	$\epsilon = 10^{-4}$	$\epsilon = 10^{-8}$	$\epsilon = 10^{-15}$
0.1	0.001	0.2696461	0.2688272	0.2576586
	0.02	0.2669727	0.2654958	0.2576586
	0.35	0.2653053	0.2333000	0.2417905
	0.50	0.2183068	0.2180167	0.2165156
	0.95	0.1768352	0.1757330	0.1757698
	1.00	0.1759522	0.1756538	0.1715217
0.5	0.001	0.3602343	0.3551286	0.3522459
	0.02	0.3521729	0.3512406	0.2576586
	0.35	0.3501394	0.3130705	0.3330882
	0.50	0.2941294	0.2945654	0.3019519
	0.95	0.2427267	0.2420207	0.2500889
	1.00	0.2521243	0.2524966	0.2445094
1.0	0.001	0.4838590	0.4751190	0.4605548
	0.02	0.4734536	0.4708751	0.2576586
	0.35	0.4704418	0.4282732	0.4394011
	0.50	0.4072134	0.4069866	0.4041880
	0.95	0.3435735	0.3441542	0.3431434
	1.00	0.3656529	0.3652396	0.3364854

Table 4.4: L_∞-errors at different time levels for $\epsilon = 1$ for Example 4.6.2.

Nodes	$t = 0.2$	$t = 0.4$	$t = 0.6$	$t = 0.8$	$t = 1.0$
$N = 32$	5.28×10^{-3}	1.08×10^{-2}	1.61×10^{-2}	2.13×10^{-2}	2.50×10^{-2}
$N = 64$	5.41×10^{-3}	1.09×10^{-2}	1.64×10^{-2}	2.14×10^{-2}	2.52×10^{-2}
$N = 128$	5.37×10^{-3}	1.10×10^{-2}	1.65×10^{-2}	2.14×10^{-2}	2.54×10^{-2}

In Fig. 4.5, the grid validation test has been performed for $\epsilon = 10^{-8}$ at $t = 1.0$. Shishkin's approach has been utilized to generate more nodes in both the boundary layer regions. It can be seen that a grid of 64 or

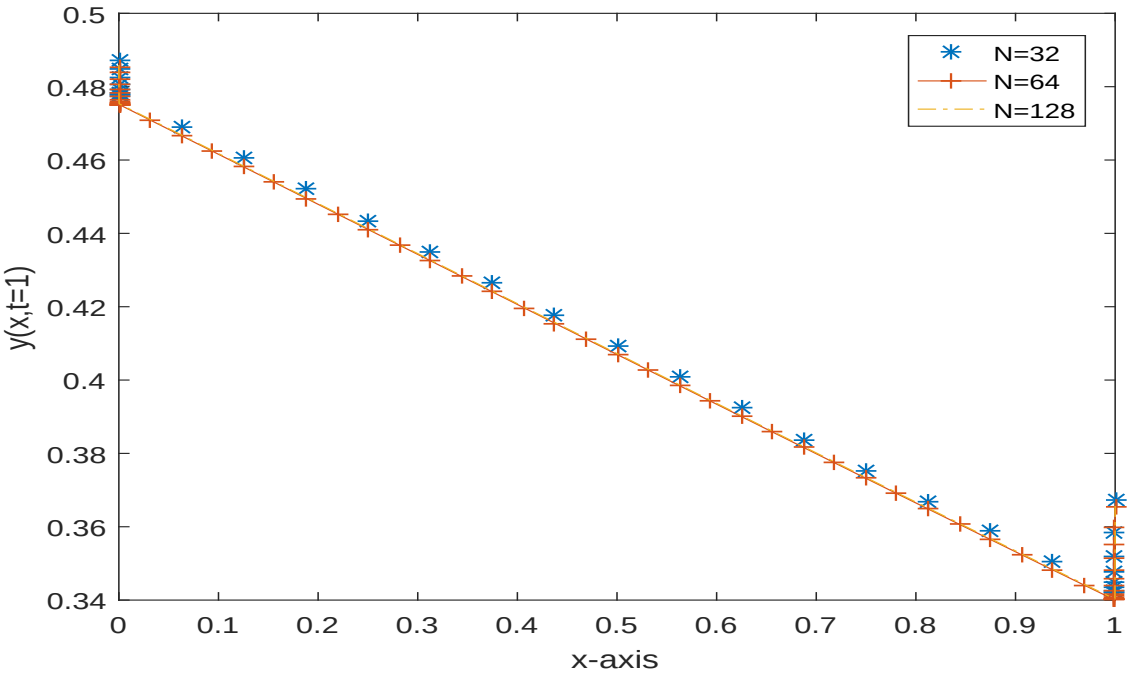

Figure 4.5: Grid validation test for $\epsilon = 10^{-8}$.

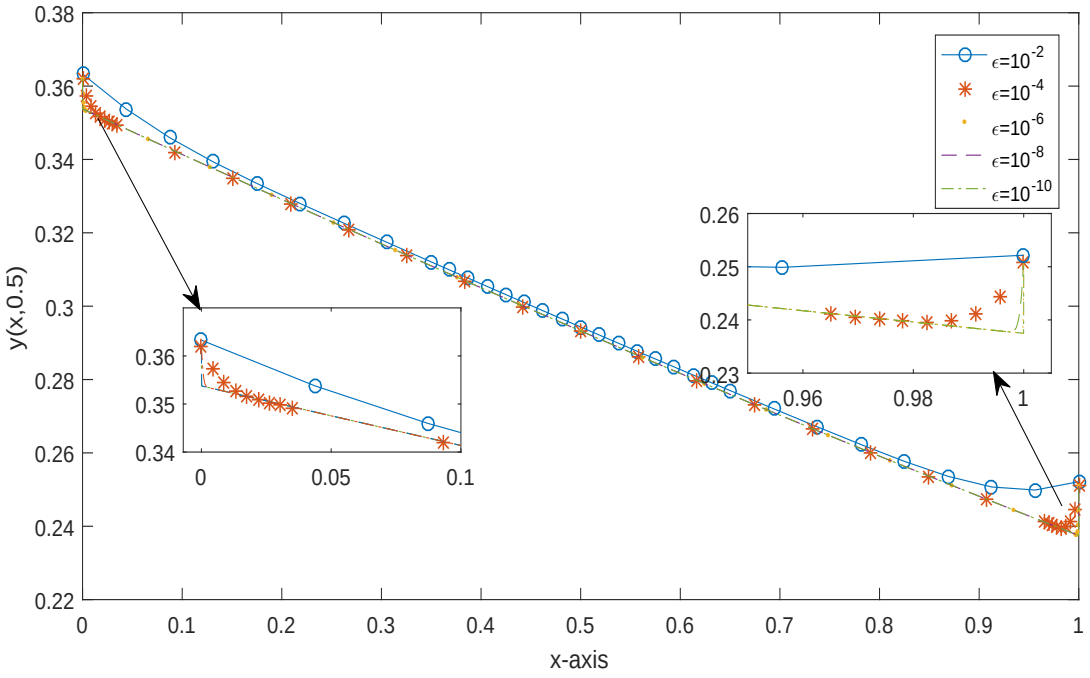

Figure 4.6: ϵ-effect on the EFG solution at time level $t = 0.5$.

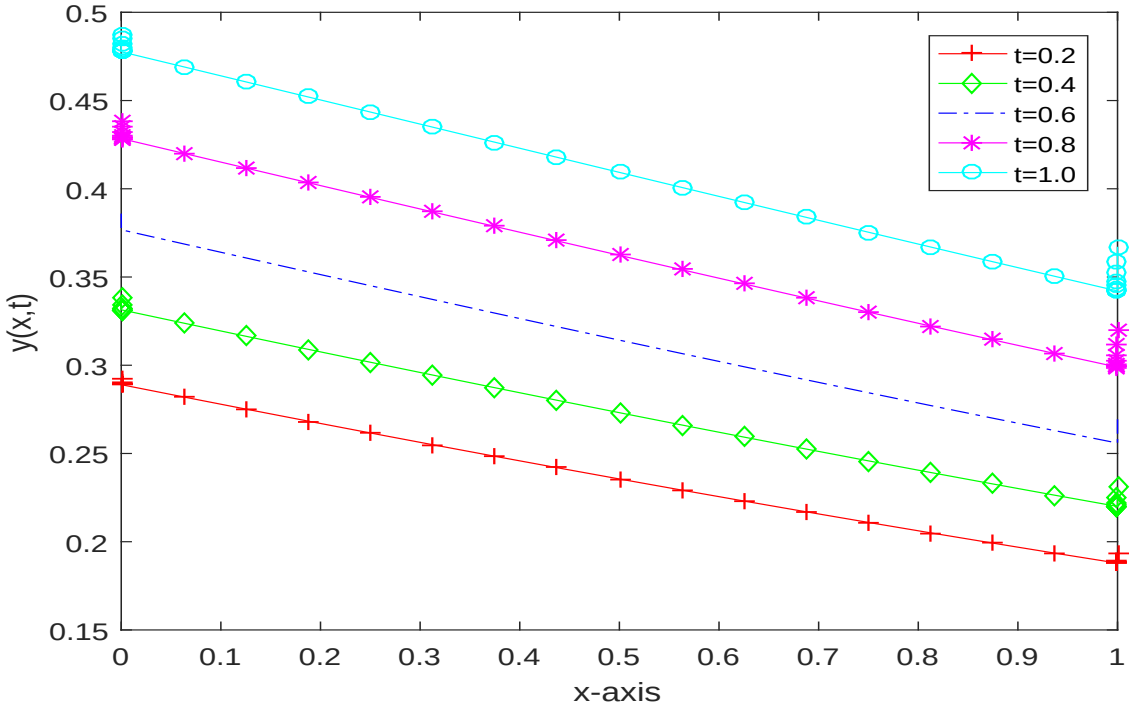

Figure 4.7: Time effect for N=32 and $\epsilon = 10^{-9}$.

more nodes is sufficient enough to capture very sharp boundary layers for very small values of the singular perturbation parameter like $\epsilon = 10^{-8}$. The impact of the singular perturbation parameter on the EFG solution for different values of $\epsilon = 10^{-2},\ 10^{-4},\ 10^{-6},\ 10^{-8}$ and 10^{-10} at time level $t = 0.5$ has been illustrated in Fig. 4.6. The evolution of sharp boundary layers at both the end points of the domain, i.e. at $x = 0$ and $x = 1$, can be noticed in the solutions as ϵ approaches to zero.

In Fig. 4.7, the solution has been plotted for $\epsilon = 10^{-9}$ at time levels $t = 0.2,\ 0.4,\ 0.6,\ 0.8$ and 1.0. These solution plots clearly depict the ability of the EFG method to capture such sharp boundary layers at various time levels. The three-dimensional solution plot for the whole space-time domain has been displayed in Fig. 4.8.

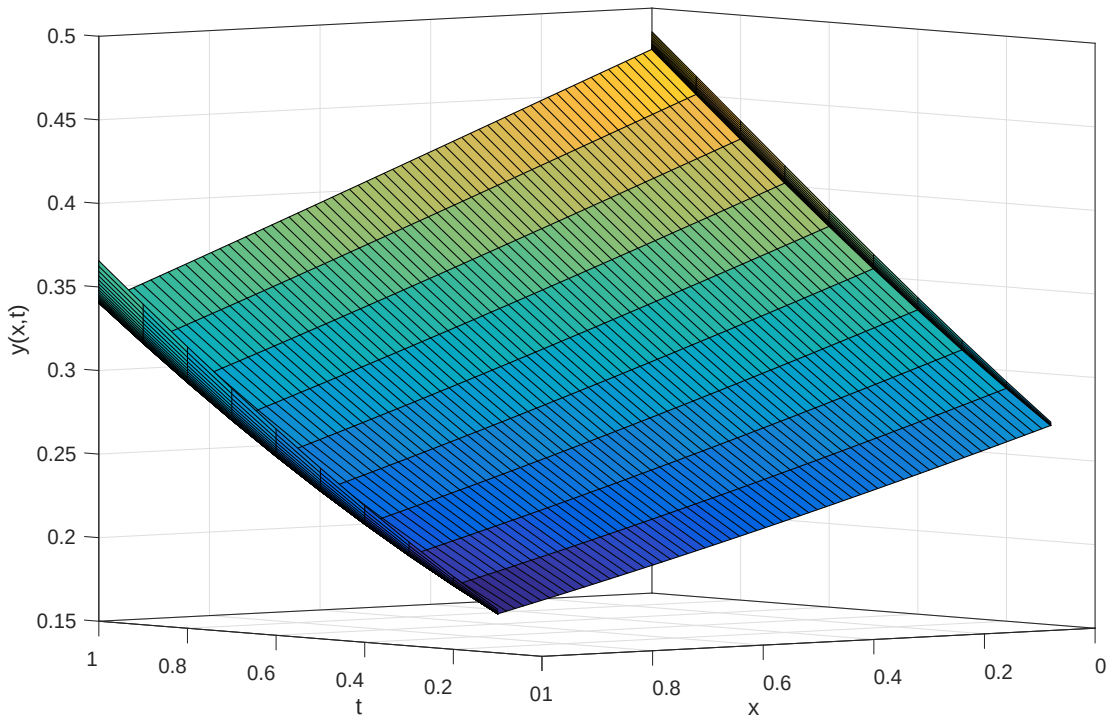

Figure 4.8: The numerical solution profile for $\epsilon = 10^{-5}$.

Example 4.6.3 *For the third example, we have considered the following singularly perturbed non-linear Fisher's equation*

$$\frac{\partial u}{\partial t} = \epsilon \frac{\partial^2 u}{\partial x^2} + u(1 - u^6),$$

with initial condition

$$u(x, 0) = \left[\frac{1}{2} + \frac{1}{2}\tanh\left(\frac{-3x}{4\epsilon}\right)\right]^{1/3},$$

and boundary conditions

$$u(0, t) = \left[\frac{1}{2} + \frac{1}{2}\tanh\left(\frac{15t}{8}\right)\right]^{1/3}, \quad u(1, t) = \left[\frac{1}{2} + \frac{1}{2}\tanh\left(\frac{-3}{4\epsilon} + \frac{15t}{8}\right)\right]^{1/3}.$$

The boundary layers for the problem under consideration occur at both boundary points, i.e., at $x = 0$ and $x = 1$. To the best of the our knowledge,

this problem has not yet been solved in literature for small values of the singular perturbation parameter ϵ. Here the problem has been solved by using the EFG method to check the convergence and robustness of the proposed method.

Table 4.5: Maximum absolute errors and order of convergence for Example 4.6.3 for different values of ϵ.

ϵ	$N = 32$	$N = 64$	$N = 128$	$N = 256$
2^{-2}	1.83×10^{-2}	1.51×10^{-2}	1.61×10^{-3}	1.29×10^{-3}
	0.277	3.229	0.319	
2^{-4}	2.88×10^{-2}	1.18×10^{-2}	4.06×10^{-3}	1.51×10^{-3}
	1.280	2.744	1.426	
2^{-6}	3.12×10^{-2}	4.07×10^{-3}	4.02×10^{-4}	4.56×10^{-5}
	2.938	3.339	3.140	
2^{-8}	3.17×10^{-2}	4.07×10^{-3}	3.60×10^{-4}	2.86×10^{-5}
	2.961	3.498	3.654	
2^{-10}	3.38×10^{-2}	4.03×10^{-3}	3.27×10^{-4}	3.34×10^{-5}
	3.068	3.623	3.291	
2^{-12}	3.37×10^{-2}	4.01×10^{-3}	3.26×10^{-4}	2.90×10^{-5}
	3.071	3.620	3.490	
2^{-14}	3.37×10^{-2}	4.04×10^{-3}	3.26×10^{-4}	2.91×10^{-5}
	3.061	3.631	3.486	
2^{-16}	3.36×10^{-2}	4.04×10^{-3}	3.26×10^{-4}	2.91×10^{-5}
	3.061	3.631	3.486	
2^{-18}	3.36×10^{-2}	4.04×10^{-3}	3.26×10^{-4}	2.91×10^{-5}
	3.061	3.631	3.486	
2^{-20}	3.36×10^{-2}	4.04×10^{-3}	3.26×10^{-4}	2.91×10^{-5}
	3.061	3.631	3.486	

Table 4.5 provides the maximum norm errors and order of convergence of the EFG scheme for Example 4.6.3. The outcomes clearly depict the parameter uniform numerical convergence of the proposed method as $\epsilon \to 0$.

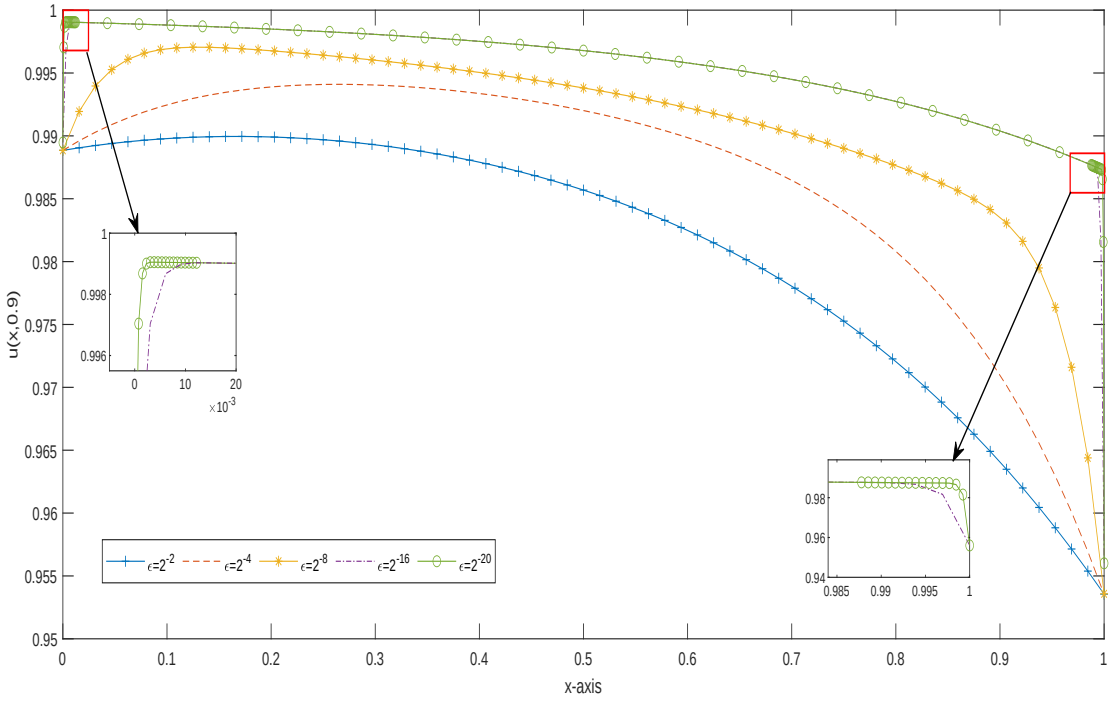

Figure 4.9: ϵ-effect for $N = 64$ at $t = 0.9$.

The physical behavior of the solution has been plotted in Figs. 4.9 - 4.12 for different values of the parameters.

Fig. 4.9 illustrates the singular perturbation parameter i.e. ϵ-effect on the EFG solution for various values of $\epsilon = 2^{-2},\ 2^{-4},\ 2^{-8},\ 2^{-16},\ 2^{-20}$ at $t = 0.9$ and for $N = 64$. For ϵ tends to zero, the evolution of sharp boundary layers at both the end points of the domain can clearly be observed and has been highlighted through the zoomed Figure.

The impact of time on the EFG solution has been presented in Fig. 4.10 at different time levels $t = 0.1,\ 0.3,\ 0.5,\ 0.7,\ 0.9$ for $N = 64$ and $\epsilon = 2^{-13}$. The proficiency of the proposed method in capturing edgy boundary layers at various time levels is easily verified through these plots. The continuous space-time profile of the EFG solution have been presented in Figs. 4.11 and 4.12 for $\epsilon = 2^{-2}$ and $\epsilon = 2^{-20}$ respectively.

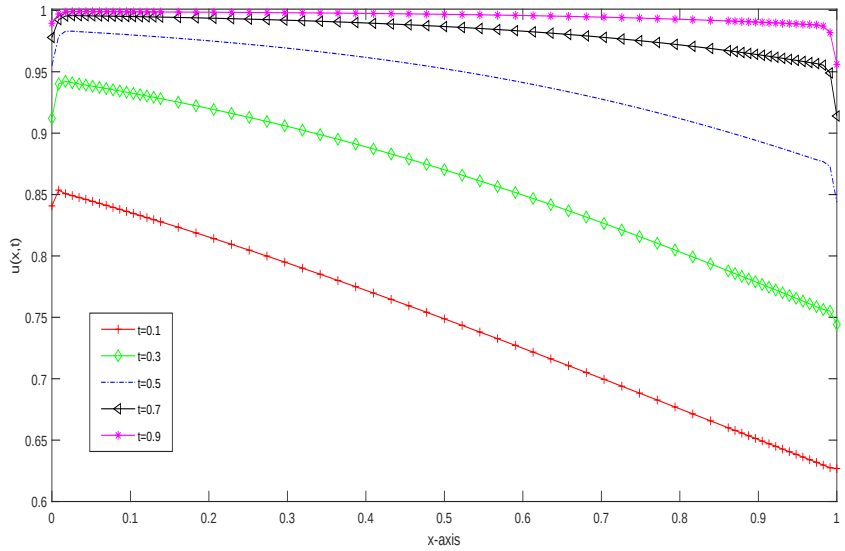

Figure 4.10: Time-effect on the EFG solution for $N = 64$ and $\epsilon = 2^{-13}$.

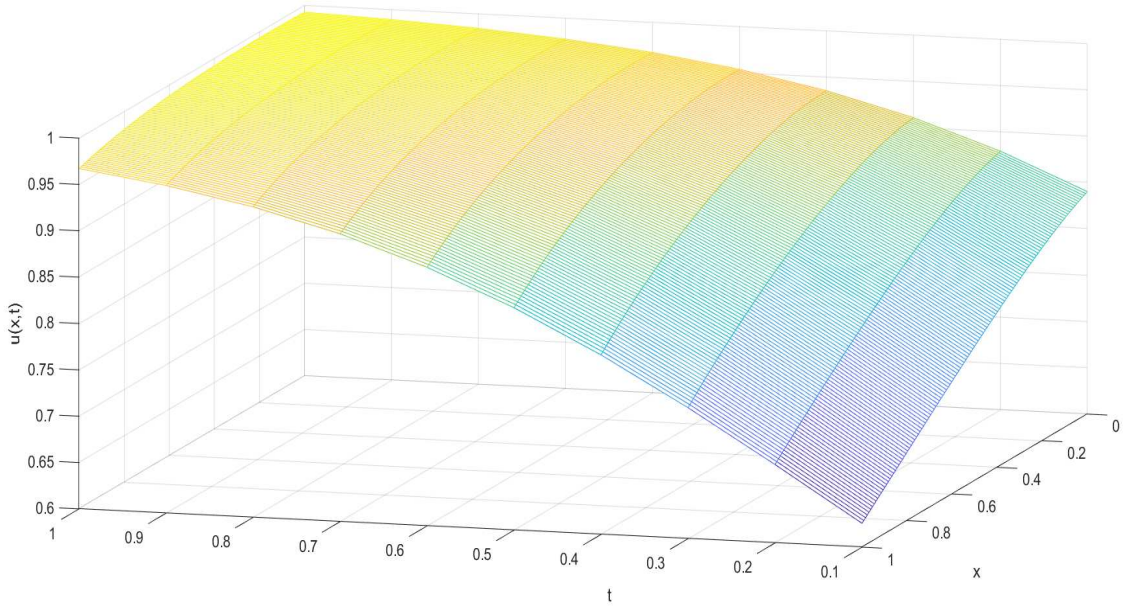

Figure 4.11: EFG solution profile w.r.t. continuous space and time for $\epsilon = 2^{-2}$.

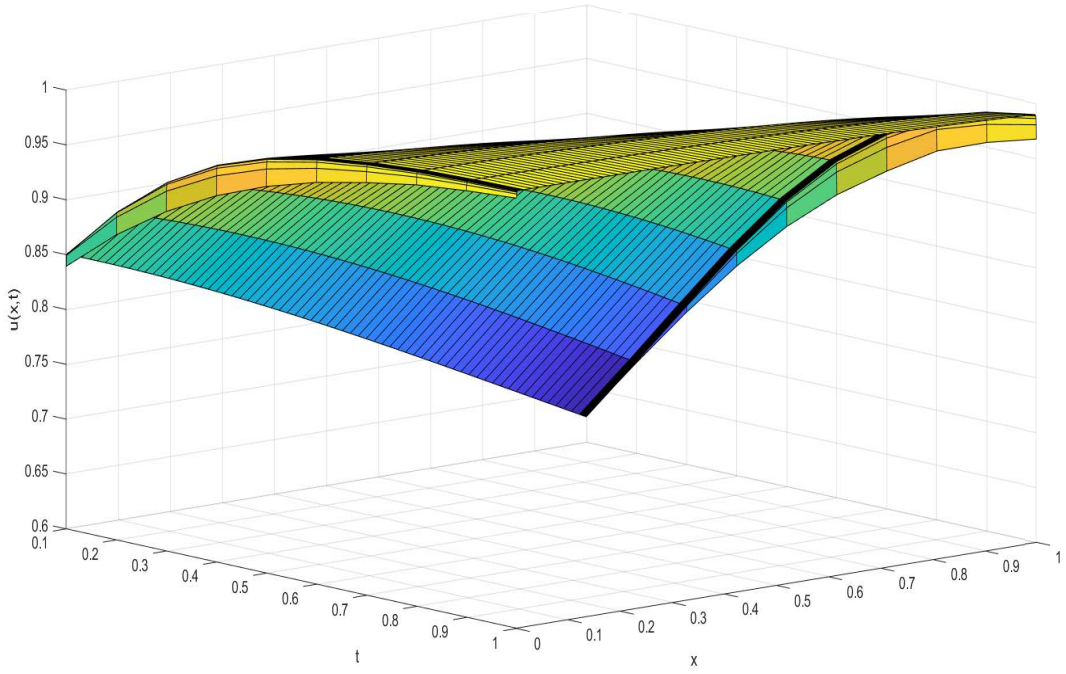

Figure 4.12: The solution profile w.r.t. time for $\epsilon = 2^{-20}$.

4.7 Conclusion

In the present Chapter, the element-free Galerkin method together with the Crank-Nicolson scheme have been proposed for the singularly perturbed Fisher's problem. The semi-discrete scheme is unconditionally stable in the weighted H^1-norm with second-order convergence. The nonlinearity present in the problem has been handled by utilizing the quasilinearization approach, and its convergence has also been studied. To capture the sharp boundary layers more precisely, non-uniformly distributed grid points condensing near the boundary layers have been generated. Some numerical examples have been considered to validate the theoretical results. The numerical results depict the robustness and efficiency of the proposed scheme in capturing very sharp boundary layers even for significantly less number of nodes, and hence proving the computational efficiency of the method. Overall, the proposed scheme provides satisfactory results for approximating the solution to the non-linear Fisher's problem.

Chapter 5

Numerical investigation of element-free Galerkin method for Burger-Fisher's model

5.1 Introduction

In the present Chapter, we have considered another real-life mathematical Burger-Fisher's model problem for the numerical analyzation using element-free Galerkin technique alongwith the Crank-Nicolson scheme. The Burger-Fisher's equation is a well-known non-linear partial differential equation that has numerous applications in various fields of science and engineering. In recent years, there has been a growing interest in the applications of the Burger-Fisher's equation in modeling complex phenomena in different domains. Its applications varied from fluid dynamics and traffic flow to chemical physics and non-linear optics. The equation describes the behavior of a wide range of physical systems, including turbulent fluids, chemical diffusion, and light propagation in non-linear media etc.
In this Chapter, we consider the generalized Burger-Fisher's model given by

$$\frac{\partial u}{\partial t} - \gamma \frac{\partial^2 u}{\partial x^2} + \alpha u^{\delta} \frac{\partial u}{\partial x} = \beta u(1 - u^{\delta}), \quad a \leq x \leq b, \ t \geq 0, \tag{5.1.1}$$

where γ is the diffusion coefficient, and $\alpha,\ \beta$ and δ are the parameters with $\alpha,\ \beta \geq 0$ and $\delta > 0$. For $\delta \geq 1$, Eq. (5.1.1) is known as generalized non-linear Burger-Fisher's problem.
Due to the wide range of applications, researchers have focused on developing numerical solutions for the Burger-Fisher's equations in the past years.

Ismail et al. [92] employed Adomain decomposition method to approximate the solution of the Burger-Fisher's and Burger-Huxley equations. Javidi [94] proposed another numerical scheme for solving the generalized Burger-Fisher's equation. The author used spectral collocation method to compute differentiation matrix and forth-order Runge-Kutta method for the numerical integration of the system. Bekir and Boz [19] studied Exp-function method to construct the solutions for non-linear evolution equations like Burger-Fisher's. The finite difference method of sixth-order along with Runge-Kutta method of third-order have been presented by Sari et al. [191] for solving the Burger-Fisher's equation. Behzadi [18] carried out the comparison between Adomain decomposition method, variational iteration method, homotopy method and their modified versions for solving Burger-Fisher's equation. An exponential spline approximation for second order derivative and finite difference approximation for time derivative term have been developed by Mohammadi [155] to solve the generalized Burger-Fisher's equation. The stability and convergence of the mentioned methods have also been discussed. Yadav and Jiwari [229] obtained the numerical solution of generalized Burger-Fisher's equation using finite element scheme. Wasim et al. [222] approximated the generalized Burger-Fisher's and Burger-Huxley equations by applying hybrid B-spline collocation method which was based on the finite difference scheme and Crank-Nicolson method.

From above literature review, we can see that several numerical approaches have been suggested so far to estimate the solution of the generalized Burger-Fisher's equation, including the finite element method [167], least squares quadratic B-spline finite element method [125], element-free characteristic Galerkin method [242], meshless method of lines [85], discontinuous Galerkin method [239], collocation of cubic B-spline scheme. But, hardly any researcher has demonstrated interest in mesh-less techniques for solving generalized Burger-Fisher's equations.

In the present Chapter, we have proposed the EFG technique for approximating the solution of generalized Burger-Fisher's problem. Moving least-square (MLS) approximation has been followed for generating shape functions and Lagrange multiplier strategy has been utilized for incorporating the boundary conditions. The methodology is based on the global weak form and Gauss quadrature background cells have been used for the computation of numerical integrations as has been discussed in the previous Chapters. The time discretization has been carried out by using the implicit Crank-Nicolson technique, before the spatial discretization.
The Chapter is organized as follows: In Section 5.2, the problem under consideration is presented with a brief description. In Section 5.3, semi-discrete scheme has been discussed. The numerical methodology has been presented in Section 5.4. Stability analysis of the semi-discrete scheme and existence and uniqueness of the full-discrete scheme have been carried out in Section 5.5. Section 5.6 deals with the convergence analysis of full-discrete scheme. Numerical results have been discussed in the Section 5.7 followed by conclusion.

5.2 Continuous generalized Burger-Fisher's problem

In the present study of the initial-boundary-value problem (5.1.1), we have taken $a = 0$ and $b = 1$. Therefore, the time dependent one-dimensional Burger-Fisher's equation will become

$$\frac{\partial u}{\partial t} - \gamma \frac{\partial u^2}{\partial^2 x} + \alpha u^{\delta} \frac{\partial u}{\partial x} = F(u),\ (x,t) \in \Omega \equiv \Omega_x \times \Omega_t \equiv (0,1) \times (0,T] \tag{5.2.1}$$

with initial condition

$$u(x,0) = u_0(x),\ x \in \bar{\Omega}_x, \tag{5.2.2}$$

and boundary conditions

$$u(0,t) = f(t), \quad u(1,t) = g(t), \ t \in \bar{\Omega}_t. \tag{5.2.3}$$

Here, we have taken $F(u) = \beta u(1-u^{\delta})$, and α, β and δ are the parameters satisfying $\alpha \geq 0, \ \beta \geq 0$ and $\delta \geq 1$.
We also assume that the compatibility conditions

$$u(0,0) = u_0(0) = f(0), \quad \textit{and} \ \ u(1,0) = u_0(1) = g(1) \tag{5.2.4}$$

are satisfied.

5.3 Time semi-discrete scheme

The weak form of Eq.(5.2.1) is given by

$$\Big\langle \frac{\partial u}{\partial t}, \upsilon \Big\rangle + \gamma \Big\langle \frac{\partial u}{\partial x}, \frac{\partial \upsilon}{\partial x} \Big\rangle + \Big\langle \alpha u^{\delta} \frac{\partial u}{\partial x}, \upsilon \Big\rangle = \Big\langle F(u), \upsilon \Big\rangle, \quad \forall \upsilon \in H^1(\Omega). \tag{5.3.1}$$

Define $t_n = n\tau$ for $n = 0, 1, ..., N$ where $\tau = T/N$.
Now, introducing the notations

$$\widehat{\delta}_t U^{(n+1)} = \frac{U^{(n+1)} - U^{(n)}}{\tau}, \quad \text{and} \ \ \widehat{U}^{(n+1)} = \frac{U^{(n+1)} + U^{(n)}}{2},$$

and employing the implicit Crank-Nicolson scheme, (5.3.1) results in

$$\Big\langle \widehat{\delta}_t U^{(n+1)}, \upsilon \Big\rangle + \gamma \Big\langle \frac{\partial \widehat{U}^{(n+1)}}{\partial x}, \frac{\partial \upsilon}{\partial x} \Big\rangle + \alpha U^{\delta(n)} \Big\langle \frac{\partial \widehat{U}^{(n+1)}}{\partial x}, \upsilon \Big\rangle = \Big\langle F(\widehat{U}^{(n+1)}), \upsilon \Big\rangle \quad \forall \upsilon \in H^1(\Omega). \tag{5.3.2}$$

$$\Rightarrow \Big\langle \frac{U^{(n+1)} - U^{(n)}}{\tau}, \upsilon \Big\rangle + \frac{\gamma}{2} \Big\langle \frac{\partial U^{(n+1)}}{\partial x} + \frac{\partial U^{(n)}}{\partial x}, \frac{\partial \upsilon}{\partial x} \Big\rangle + \frac{\alpha}{2} U^{\delta(n)} \Big\langle \frac{\partial U^{(n+1)}}{\partial x} + \frac{\partial U^{(n)}}{\partial x}, \upsilon \Big\rangle = \Big\langle \frac{F(U^{(n+1)}) + F(U^{(n)})}{2}, \upsilon \Big\rangle, \tag{5.3.3}$$

where $U^{(n+1)}$ denotes the solution of the semi-discrete scheme at $(n+1)^{th}$ time level.

5.4 Element-free Galerkin methodology

Utilizing the moving least-square approach for generating the basis functions and the node generation, as discussed in the earlier Chapters, the finite-dimensional discrete scheme can be written as

$$\Big\langle \widehat{\delta}_t U_h^{(n+1)}, \upsilon_h \Big\rangle + \gamma \Big\langle \frac{\partial \widehat{U}_h^{(n+1)}}{\partial x}, \frac{\partial \upsilon_h}{\partial x} \Big\rangle + \alpha U_h^{\delta(n)} \Big\langle \frac{\partial \widehat{U}_h^{(n+1)}}{\partial x}, \upsilon_h \Big\rangle = \Big\langle F(\widehat{U}_h^{(n+1)}), \upsilon_h \Big\rangle, \tag{5.4.1}$$

in which $U_h^{(n+1)}$ is an approximation of $U^{(n+1)}$ and $U_h^{(n+1)} \in V_h$ where V_h is the finite dimensional subspace of $H^1(\Omega)$. Since the basis functions used in the EFG technique do not follow the Kronecker delta property, therefore, in order to incorporate the boundary conditions (5.2.3), the application of the Lagrange multiplier methodology results in the following element-free Galerkin formulation for Eq. (5.4.1):

$$\begin{aligned}
&\frac{\gamma\tau}{2}\Big\langle \frac{\partial U_h^{(n+1)}}{\partial x}, \frac{\partial \upsilon_h}{\partial x} \Big\rangle + \frac{\alpha\tau}{2} U_h^{\delta(n)} \Big\langle \frac{\partial U_h^{(n+1)}}{\partial x}, \upsilon_h \Big\rangle + \Big\langle U_h^{(n+1)}, \upsilon_h \Big\rangle - \frac{\tau}{2}\Big\langle F(U_h^{(n+1)}), \upsilon_h \Big\rangle \\
&\quad - \delta\lambda(U - f(t))\Big|_{x=0} - \delta U\lambda\Big|_{x=0} - \delta\rho(U - g(t))\Big|_{x=1} - \delta U\rho\Big|_{x=1} = \Big\langle U_h^{(n)}, \upsilon_h \Big\rangle \\
&\quad - \frac{\alpha\tau}{2} U_h^{\delta(n)} \Big\langle \frac{\partial U_h^{(n)}}{\partial x}, \upsilon_h \Big\rangle - \frac{\gamma\tau}{2}\Big\langle \frac{\partial U_h^{(n)}}{\partial x}, \frac{\partial \upsilon_h}{\partial x} \Big\rangle + \frac{\tau}{2}\Big\langle F(U_h^{(n)}), \upsilon_h \Big\rangle.
\end{aligned}$$

Further, taking $\upsilon_h = \phi_i,\ i = 1, 2, 3, ..., N$ in the above equation and assembling, the resulted system of equations can be rewritten as

$$\begin{bmatrix} K & G & H \\ G^T & 0 & 0 \\ H^T & 0 & 0 \end{bmatrix} \begin{bmatrix} U \\ \lambda \\ \rho \end{bmatrix} = \begin{bmatrix} \tilde{F} \\ q \\ q_c \end{bmatrix},$$

where

$$K_{ij} = \frac{\gamma\tau}{2}\Big\langle \frac{\partial\phi_j}{\partial x}, \frac{\partial\phi_i}{\partial x}\Big\rangle + \frac{\alpha\tau U_h^{\delta(n)}}{2}\Big\langle \frac{\partial\phi_j}{\partial x}, \phi_i\Big\rangle + \Big\langle \phi_j, \phi_i\Big\rangle - \frac{\tau}{2}\Big\langle F(\phi_j), \phi_i\Big\rangle,$$

$$G_{lj}^T = -\delta\lambda_l(N_l\phi_j)\Big|_{x=0},$$

$$H_{lj}^T = -\delta\rho_l(R_l\phi_j)\Big|_{x=1},$$

$$\tilde{F}_i = \Big\langle U_h^{(n)}, \phi_i\Big\rangle - \frac{\alpha\tau U_h^{\delta(n)}}{2}\Big\langle \frac{\partial U_h^{(n)}}{\partial x}, \phi_i\Big\rangle - \frac{\gamma\tau}{2}\Big\langle \frac{\partial U_h^{(n)}}{\partial x}, \frac{\partial\phi_i}{\partial x}\Big\rangle + \frac{\tau}{2}\Big\langle F(U_h^{(n)}), \phi_i\Big\rangle,$$

$$q_l = -\delta\lambda_l(N_l f(t))\Big|_{x=0},$$

$$q_{c_l} = -\delta\rho_l(R_l g(t))\Big|_{x=1}.$$

Here, λ and ρ are Lagrange multipliers, $\phi_i's$ are shape functions computed using MLS approach as discussed in subsection 3.4.2 of Chapter 3.

5.5 Stability analysis

Theorem 5.5.1 *Assuming $U^{(n+1)} \in H^1(\overline{\Omega})$, the semi-discrete scheme given in Eq.* (5.3.3) *exhibits unconditional stability.*

Proof Setting $\upsilon_h = U^{(n+1)}$ in Eq.(5.3.3), we obtain

$$\Big\langle U^{(n+1)}, U^{(n+1)}\Big\rangle + \tau A_1\Big\langle \frac{\partial U^{(n+1)}}{\partial x}, \frac{\partial U^{(n+1)}}{\partial x}\Big\rangle - \tau A_2\Big\langle U^{(n+1)}, \frac{\partial U^{(n+1)}}{\partial x}\Big\rangle$$
$$- \frac{\tau}{2}\Big\langle F(U^{(n+1)}), U^{(n+1)}\Big\rangle = \Big\langle U^{(n)}, U^{(n+1)}\Big\rangle - \tau A_1\Big\langle \frac{\partial U^{(n)}}{\partial x}, \frac{\partial U^{(n+1)}}{\partial x}\Big\rangle$$
$$- \tau A_2\Big\langle \frac{\partial U^{(n)}}{\partial x}, U^{(n+1)}\Big\rangle + \frac{\tau}{2}\Big\langle F(U^{(n)}), U^{(n+1)}\Big\rangle,$$

where $A_1 = \gamma/2$, $A_2 = \alpha U^{\delta(n)}/2$.

Utilizing Cauchy-Schwarz inequality leads to

$$\begin{aligned}\Big\|U^{(n+1)}\Big\|^2_{L^2(\Omega)} + \tau A_1\Big\|\frac{\partial U^{(n+1)}}{\partial x}\Big\|^2_{L^2(\Omega)} &\leq \tau\|A_2\|\Big\langle U^{(n+1)}, \frac{\partial U^{(n+1)}}{\partial x}\Big\rangle \\ &+ \Big\|U^{(n)}\Big\|_{L^2(\Omega)}\Big\|U^{(n+1)}\Big\|_{L^2(\Omega)} + \tau A_1\Big\|\frac{\partial U^{(n)}}{\partial x}\Big\|_{L^2(\Omega)}\Big\|\frac{\partial U^{(n+1)}}{\partial x}\Big\|_{L^2(\Omega)} \\ &+ \tau\|A_2\|\Big\langle \frac{\partial U^{(n)}}{\partial x}, U^{(n+1)}\Big\rangle + \frac{\tau}{2}\Big\langle F(U^{(n+1)}) + F(U^{(n)}), U^{(n+1)}\Big\rangle.\end{aligned}$$

Now, Lemma 3.3.2 conclude

$$\|A_2\| \leq C.$$

On simplification, the above relation can be written as

$$\begin{aligned}\Big\|U^{(n+1)}\Big\|^2_{L^2(\Omega)} + \tau A_1\Big\|\frac{\partial U^{(n+1)}}{\partial x}\Big\|^2_{L^2(\Omega)} &\leq \tau C\Big\|U^{(n+1)}\Big\|_{L^2(\Omega)}\Big\|\frac{\partial U^{(n+1)}}{\partial x}\Big\|_{L^2(\Omega)} \\ &+ \Big\|U^{(n)}\Big\|_{L^2(\Omega)}\Big\|U^{(n+1)}\Big\|_{L^2(\Omega)} + \tau A_1\Big\|\frac{\partial U^{(n)}}{\partial x}\Big\|_{L^2(\Omega)}\Big\|\frac{\partial U^{(n+1)}}{\partial x}\Big\|_{L^2(\Omega)} \\ &+ \tau C\Big\|\frac{\partial U^{(n)}}{\partial x}\Big\|_{L^2(\Omega)}\Big\|U^{(n+1)}\Big\|_{L^2(\Omega)} + \frac{\tau}{2}\Big\|F(U^{(n+1)}) + F(U^{(n)})\Big\|_{L^2(\Omega)}\Big\|U^{(n+1)}\Big\|_{L^2(\Omega)}.\end{aligned}$$

By using the Lemma 3.3.3 for F-terms and simplifying, the above relation outputs as

$$\begin{aligned}\frac{1}{2}\Big\|U^{(n+1)}\Big\|^2_{L^2(\Omega)} + \frac{1}{4}\tau A_1\Big\|\frac{\partial U^{(n+1)}}{\partial x}\Big\|^2_{L^2(\Omega)} &\leq \frac{1}{2}\Big\|U^{(n)}\Big\|^2_{L^2(\Omega)} + \frac{1}{2}\tau A_1\Big\|\frac{\partial U^{(n)}}{\partial x}\Big\|^2_{L^2(\Omega)} \\ &+ \frac{5\tau C^2}{2A_1}\Big\|U^{(n+1)}\Big\|^2_{L^2(\Omega)} + \tau\frac{2C^2}{A_1}\Big\|U^{(n)}\Big\|^2_{L^2(\Omega)} + \tau\frac{A_1}{C^2}|\overline{M}|^2. \qquad (5.5.1)\end{aligned}$$

Defining

$$\Big\|U^{(n+1)}\Big\|^2_{H_w(\Omega)} = \frac{1}{2}\Big\|U^{(n+1)}\Big\|^2_{L^2(\Omega)} + \frac{1}{2}\tau A_1\Big\|\frac{\partial U^{(n+1)}}{\partial x}\Big\|^2_{L^2(\Omega)},$$

Eq. (5.5.1) can be expressed as

$$\left\|U^{(n+1)}\right\|^2_{H_w(\Omega)} \leq \left\|U^{(n)}\right\|^2_{H_w(\Omega)} + \frac{5\tau C^2}{2A_1}\left\|U^{(n+1)}\right\|^2_{H_w(\Omega)} + \tau\frac{2C^2}{A_1}\left\|U^{(n)}\right\|^2_{H_w(\Omega)} + \tau\frac{A_1}{C^2}|\overline{M}|^2.$$

$$\Rightarrow \sum_{i=0}^{n}\left\|U^{(i+1)}\right\|^2_{H_w(\Omega)} \leq \sum_{i=0}^{n}\left\|U^{(i)}\right\|^2_{H_w(\Omega)} + \frac{5\tau C^2}{A_1}\sum_{i=0}^{n}\left\|U^{(i+1)}\right\|^2_{H_w(\Omega)} + \tau\frac{4C^2}{A_1}\sum_{i=0}^{n}\left\|U^{(i)}\right\|^2_{H_w(\Omega)} + \tau\frac{A_1}{C^2}\sum_{i=0}^{n}\left|\overline{M}\right|^2.$$

On simplyfing, we get

$$\left\|U^{(i+1)}\right\|^2_{H_w(\Omega)} \leq \left\|U^{(0)}\right\|^2_{H_w(\Omega)} + \frac{9\tau C^2}{A_1}\sum_{i=0}^{n}\left\|U^{(i+1)}\right\|^2_{H_w(\Omega)} + \tau n\frac{A_1}{C^2}\left|\overline{M}\right|^2.$$

Applying generalized Gronwall inequality on previous relation, we have

$$\begin{aligned}\left\|U^{(n+1)}\right\|^2_{H_w(\Omega)} &\leq \left[\left\|U^{(0)}\right\|^2_{H_w(\Omega)} + n\tau\frac{A_1}{C^2}\left|\overline{M}\right|^2\right]\exp\left(\frac{9n\tau C^2}{A_1}\right)\\ &\leq \left[\left\|U^{(0)}\right\|^2_{H_w(\Omega)} + T\frac{A_1}{C^2}\left|\overline{M}\right|^2\right]\exp\left(\frac{9TC^2}{A_1}\right) \quad [\because T = n\tau]\\ &\leq \mathcal{C}\left\|U^{(0)}\right\|^2_{H_w(\Omega)}.\end{aligned}$$

Thus, the time discrete scheme is unconditionally stable.

5.5.1 Existence and uniqueness of the element-free Galerkin solution

In this subsection, we will prove the existence and uniqueness of the element-free Galerkin scheme for the considered Burger-Fisher's mathematical model.

Theorem 5.5.2 *Suppose $U_h^{(n)}$, the EFG solution of the full discrete EFG*

scheme (5.4.1) *at* $(n)^{th}$ *time level, exists. Then* $U_h^{(n+1)}$ *also exists.*

Proof Eq.(5.4.1) can be rewritten as

$$\Big\langle U_h^{(n+1)}, \upsilon_h \Big\rangle - \Big\langle U_h^{(n)}, \upsilon_h \Big\rangle + \gamma\tau \Big\langle \frac{\partial \widehat{U}_h^{(n+1)}}{\partial x}, \frac{\partial \upsilon_h}{\partial x} \Big\rangle + \alpha\tau U_h^{\delta(n)} \Big\langle \frac{\partial \widehat{U}_h^{(n+1)}}{\partial x}, \upsilon_h \Big\rangle = \tau \Big\langle F(\widehat{U}_h^{(n+1)}), \upsilon_h \Big\rangle.$$

Define the operator ζ with the help of weak formulation as

$$\Big\langle \zeta(\omega), \upsilon_h \Big\rangle = \Big\langle \omega, \upsilon_h \Big\rangle + \gamma\tau \Big\langle \frac{\partial \omega}{\partial x}, \frac{\partial \upsilon_h}{\partial x} \Big\rangle + \alpha\tau U_h^{\delta(n)} \Big\langle \frac{\partial \omega}{\partial x}, \upsilon_h \Big\rangle - \Big\langle U_h^{(n)}, \upsilon_h \Big\rangle - \tau \Big\langle F(\omega), \upsilon_h \Big\rangle.$$

Then,

$$\Big\langle \zeta(\omega_1) - \zeta(\omega_2), \upsilon_h \Big\rangle = \Big\langle \omega_1 - \omega_2, \upsilon_h \Big\rangle + \gamma\tau \Big\langle \frac{\partial}{\partial x}(\omega_1 - \omega_2), \frac{\partial \upsilon_h}{\partial x} \Big\rangle + \alpha\tau U_h^{\delta n} \Big\langle \frac{\partial}{\partial x}(\omega_1 - \omega_2), \upsilon_h \Big\rangle - \tau \Big\langle F(\omega_1 - \omega_2), \upsilon_h \Big\rangle.$$

Next, invoking the Lipschitz condition on F and simplifying the above equation results in

$$\begin{aligned}
\Big\langle \zeta(\omega_1) - \zeta(\omega_2), \upsilon_h \Big\rangle &\leq \Big\| (\omega_1 - \omega_2) \Big\|_{L^2(\Omega)} \Big\| \upsilon_h \Big\|_{L^2(\Omega)} \\
&+ \alpha\tau U_h^{\delta(n)} \Big\| \frac{\partial}{\partial x}(\omega_1 - \omega_2) \Big\|_{L^2(\Omega)} \Big\| \upsilon_h \Big\|_{L^2(\Omega)} \\
&+ \gamma\tau \Big\| \frac{\partial}{\partial x}(\omega_1 - \omega_2) \Big\|_{L^2(\Omega)} \Big\| \frac{\partial \upsilon_h}{\partial x} \Big\|_{L^2(\Omega)} + \mathfrak{L}\tau \Big\| (\omega_1 - \omega_2) \Big\|_{L^2(\Omega)} \Big\| \upsilon_h \Big\|_{L^2(\Omega)} \\
&\leq \Bigg[\Big\| (\omega_1 - \omega_2) \Big\|_{L^2(\Omega)} + \sqrt{\alpha\tau U_h^{\delta(n)}} \Big\| \frac{\partial}{\partial x}(\omega_1 - \omega_2) \Big\|_{L^2(\Omega)} \\
&+ \sqrt{\gamma\tau} \Big\| \frac{\partial}{\partial x}(\omega_1 - \omega_2) \Big\|_{L^2(\Omega)} \Bigg] \times \Bigg[\Big\| \upsilon_h \Big\|_{L^2(\Omega)}
\end{aligned}$$

$$
\begin{aligned}
&+\sqrt{\alpha\tau U_h^{\delta(n)}}\Big\|\upsilon_h\Big\|_{L^2(\Omega)}+\sqrt{\gamma\tau}\Big\|\frac{\partial\upsilon_h}{\partial x}\Big\|_{L^2(\Omega)}\Big]\\
&+\mathfrak{L}\tau\Big\|(\omega_1-\omega_2)\Big\|_{L^2(\Omega)}\Big\|\upsilon_h\Big\|_{L^2(\Omega)}\\
&\leq\Big[(1+\sqrt{\mathfrak{L}\tau})\Big\|(\omega_1-\omega_2)\Big\|_{L^2(\Omega)}+\Big(\sqrt{\alpha\tau U_h^{\delta(n)}}+\sqrt{\gamma\tau}\Big)\Big\|\frac{\partial}{\partial x}(\omega_1-\omega_2)\Big\|_{L^2(\Omega)}\Big]\\
&\times\Big[\Big(1+\sqrt{\mathfrak{L}\tau}+\sqrt{\alpha\tau U_h^{\delta(n)}}\Big)\Big\|\upsilon_h\Big\|_{L^2(\Omega)}+\sqrt{\gamma\tau}\Big\|\frac{\partial\upsilon_h}{\partial x}\Big\|_{L^2(\Omega)}\Big].
\end{aligned}
$$

Define

$$
\begin{aligned}
\Big\|\vartheta_h\Big\|_{H_{\omega^*}(\Omega)}=&\Big(1+\sqrt{\mathfrak{L}\tau}+\sqrt{\alpha\tau U_h^{\delta(n)}}\Big)\Big\|\vartheta_h\Big\|_{L_2(\Omega)}\\
&+\Big(\sqrt{\alpha\tau U_h^{\delta(n)}}+\sqrt{\gamma\tau}\Big)\Big\|\frac{\partial\vartheta_h}{\partial x}\Big\|_{L_2(\Omega)}.
\end{aligned}
$$

Therefore, the above inequality simplifies to

$$
\Big\langle\zeta(\omega_1)-\zeta(\omega_2),\upsilon_h\Big\rangle\leq\Big\|(\omega_1-\omega_2)\Big\|_{H_{\omega^*}(\Omega)}\Big\|\upsilon_h\Big\|_{H_{\omega^*}(\Omega)}.
$$

Taking $\upsilon_h=\omega$, we obtain

$$
\begin{aligned}
\Big\langle\zeta(\omega),\omega\Big\rangle&=\Big\langle\omega,\omega\Big\rangle-\alpha\tau U_h^{\delta(n)}\Big\langle\omega,\frac{\partial\omega}{\partial x}\Big\rangle+\gamma\tau\Big\langle\frac{\partial\omega}{\partial x},\frac{\partial\omega}{\partial x}\Big\rangle-\Big\langle U_h^{(n)},\omega\Big\rangle-\tau\Big\langle F(\omega),\omega\Big\rangle\\
&\geq\Big\|\omega\Big\|_{L^2(\Omega)}^2+\gamma\tau\Big\|\frac{\partial\omega}{\partial x}\Big\|_{L^2(\Omega)}^2-\alpha\tau U_h^{\delta(n)}\Big\|\frac{\partial\omega}{\partial x}\Big\|_{L^2(\Omega)}\Big\|\omega\Big\|_{L^2(\Omega)}\\
&-\Big\|U_h^{(n)}\Big\|_{L^2(\Omega)}\Big\|\omega\Big\|_{L^2(\Omega)}-\tau\Big\|F(\omega)\Big\|_{L^2(\Omega)}\Big\|\omega\Big\|_{L^2(\Omega)}
\end{aligned}
$$

$$
\begin{aligned}
&\geq\Big\|\omega\Big\|_{H_\omega(\Omega)}^2-\alpha\tau U_h^{\delta(n)}\Big\|\frac{\partial\omega}{\partial x}\Big\|.\Big\|\omega\Big\|-\Big\|U_h^{(n)}\Big\|_{H_\omega(\Omega)}\Big\|\omega\Big\|_{H_\omega(\Omega)}\\
&-\tau\Big\|F(\omega)\Big\|_{H_\omega(\Omega)}\Big\|\omega\Big\|_{H_\omega(\Omega)}\\
&=\Big\|\omega\Big\|_{H_\omega(\Omega)}\Big[\Big\|\omega\Big\|_{H_\omega(\Omega)}-\alpha\tau U_h^{\delta(n)}\Big\|\frac{\partial\omega}{\partial x}\Big\|-\Big\|U_h^{(n)}\Big\|_{H_\omega(\Omega)}-\tau\Big\|F(\omega)\Big\|_{H_\omega(\Omega)}\Big].
\end{aligned}
$$

By choosing

$$\Big\|\omega\Big\|_{H_\omega(\Omega)} \geq \Big\|U_h^{(n)}\Big\|_{H_\omega(\Omega)} + \alpha\tau u_h^{\delta\,(n)}\Big\|\frac{\partial\omega}{\partial x}\Big\| + \tau\Big\|F(\omega)\Big\|_{H_\omega(\Omega)},$$

the above relation yields $\Big\langle \zeta(\omega), \omega \Big\rangle \geq 0$.
Now, using the Brouwer's fixed point theorem, the existence of (5.4.1) can be concluded.

Theorem 5.5.3 *The EFG solution $U_h^{(n)}$ of Eq.* (5.4.1)*, if exists, is unique.*

Proof Let $U_{1h}^{(n+1)}$ and $U_{2h}^{(n+1)}$ be two EFG solutions of Eq. (5.4.1).
Take $\chi_h^{(n+1)} = U_{1h}^{(n+1)} - U_{2h}^{(n+1)}$.
Then, from Eq. (5.4.1), we get

$$\begin{aligned}\Big\langle \widehat{\delta}_t\chi_h^{(n+1)}, \upsilon_h \Big\rangle + \gamma\Big\langle \frac{\partial\widehat{\chi}_h^{(n+1)}}{\partial x}, \frac{\partial\upsilon_h}{\partial x} \Big\rangle + \alpha U_h^{\delta(n)}\Big\langle \frac{\partial\widehat{\chi}_h^{(n+1)}}{\partial x}, \upsilon_h \Big\rangle \\ = \Big\langle F(\widehat{U}_{1h}^{(n+1)}) - F(\widehat{U}_{2h}^{(n+1)}), \upsilon_h \Big\rangle, \quad \forall\ \upsilon_h \in V_h.\end{aligned}$$

By following the similar steps as in Theorem 5.5.1, we can obtain

$$\Big\|\chi_h^{(n+1)}\Big\|^2_{H_w(\Omega)} \leq \mathcal{C}\Big\|\chi_h^0\Big\|^2_{H_w(\Omega)}.$$

As $\chi_h^0 = 0$, we have

$$\begin{aligned}\|\chi_h^{(n+1)}\|^2_{H_w(\Omega)} &= 0. \\ \Rightarrow \quad \chi_h^{(n+1)} &= 0,\end{aligned}$$

which completes the proof.

5.6 Convergence of full-discrete scheme

Next, we will prove the convergence of the proposed scheme (5.4.1) for the considered Burger-Fisher's model.

Theorem 5.6.1 *Let $u^{(n+1)}$ and $U_h^{(n+1)}$ be the exact and the element-free Galerkin solutions of* (5.3.1) *and* (5.4.1) *respectively. Then, the following error estimates for the full discrete scheme hold:*

$$\left\| u^{(n+1)} - U_h^{(n+1)} \right\|_{H_w(\Omega)} \leq \mathcal{C}\big(\tau^2 + \mathfrak{d}_{\mathfrak{s}}{}^m\big),$$

where $\mathcal{C}$ is independent of τ and $\mathfrak{d}_{\mathfrak{s}}$.

Proof We can write

$$u(t_{n+1}) - U_h^{(n+1)} = u(t_{n+1}) - U^{(n+1)} + U^{(n+1)} - U_h^{(n+1)}. \tag{5.6.1}$$

Take

$$e_h^{(n+1)} = U^{(n+1)} - u^{(n+1)}.$$

Now, using the main weak form, we get

$$\left\langle \widehat{\delta}_t e_h^{(n+1)}, \upsilon_h \right\rangle + \gamma \left\langle \frac{\partial \widehat{e}_h^{(n+1)}}{\partial x}, \frac{\partial \upsilon_h}{\partial x} \right\rangle + \alpha u_h^{\delta\,(n)} \left\langle \frac{\partial \widehat{e}_h^{(n+1)}}{\partial x}, \upsilon_h \right\rangle = \left\langle \mathfrak{X}_h^{(n+1)}, \upsilon_h \right\rangle + \mathfrak{K}(\upsilon_h), \tag{5.6.2}$$

where $\mathfrak{K}(\upsilon_h) = \left\langle F(\widehat{U}^{(n+1)}), \upsilon_h \right\rangle - \left\langle F(\widehat{u}^{(n+1)}), \upsilon_h \right\rangle$
and

$$\mathfrak{X}_h^{(n+1)} = \widehat{u}_t^{(n+1)} - \widehat{\delta}_t u^{(n+1)}.$$

Taking $\upsilon_h = \widehat{e}_h^{(n+1)}$ in Eq. (5.6.2), we obtain

$$\Big\langle \overline{\delta}_t e_h^{(n+1)}, \widehat{e}_h^{(n+1)} \Big\rangle + \gamma \Big\langle \frac{\partial \widehat{e}_h^{(n+1)}}{\partial x}, \frac{\partial \widehat{e}_h^{(n+1)}}{\partial x} \Big\rangle + \alpha u_h^{\delta\,(n)} \Big\langle \widehat{e}_h^{(n+1)}, \frac{\partial \widehat{e}_h^{(n+1)}}{\partial x} \Big\rangle = \Big\langle \mathfrak{X}_h^{(n+1)}, \widehat{e}_h^{(n+1)} \Big\rangle + \mathfrak{K}(\widehat{e}_h^{(n+1)}).$$

By summing the above relation from $j = 0$ to n and simpliying, we have

$$\sum_{j=0}^{n} \left[\left\| e_h^{(j+1)} \right\|^2 - \left\| e_h^{(j)} \right\|^2 \right] + 2|\gamma|\tau \sum_{j=0}^{n} \left\| \frac{\partial \widehat{e}_h^{(j+1)}}{\partial x} \right\|^2 \leq 2\tau \sum_{j=0}^{n} \Big\langle \mathfrak{X}_h^{(j+1)}, \widehat{e}_h^{(j+1)} \Big\rangle + B_2 \tau \sum_{j=0}^{n} \Big\langle \widehat{e}_h^{(j+1)}, \frac{\partial \widehat{e}_h^{(j+1)}}{\partial x} \Big\rangle + 2\tau \sum_{j=0}^{n} \mathfrak{K}(\widehat{e}_h^{(j+1)}), \tag{5.6.3}$$

where $B_2 = 2|\alpha| \|u_h^{\delta\,(n)}\|$.
Utilizing the Cauchy-Schwarz inequality and $\widehat{e}_h^0 = 0$, relation (5.6.3) becomes

$$\left\| \widehat{e}_h^{(n+1)} \right\|_{L^2(\Omega)}^2 + 2|\gamma|\tau \left\| \frac{\partial \widehat{e}_h^{(n+1)}}{\partial x} \right\|_{L^2(\Omega)}^2 \leq 2\tau \sum_{j=0}^{n} \left\| \mathfrak{X}_h^{(j+1)} \right\|_{L^2(\Omega)} \left\| \widehat{e}_h^{(j+1)} \right\|_{L^2(\Omega)} + B_2 \tau \sum_{j=0}^{n} \left\| \widehat{e}_h^{(j+1)} \right\|_{L^2(\Omega)} \left\| \frac{\partial \widehat{e}_h^{(j+1)}}{\partial x} \right\|_{L^2(\Omega)} + 2\tau \sum_{j=0}^{n} \mathfrak{K}(\widehat{e}_h^{(j+1)}).$$

Using Lipschitz condition on last term, we get

$$\left\| \widehat{e}_h^{(n+1)} \right\|_{L^2(\Omega)}^2 + 2|\gamma|\tau \left\| \frac{\partial \widehat{e}_h^{(n+1)}}{\partial x} \right\|_{L^2(\Omega)}^2 \leq \tau \sum_{j=0}^{n} \left\| \mathfrak{X}_h^{(j+1)} \right\|_{L^2(\Omega)}^2 + \tau \sum_{j=0}^{n} \left\| \widehat{e}_h^{(j+1)} \right\|_{L^2(\Omega)}^2 + \frac{\tau C^{*2}}{4|\gamma|} \sum_{j=0}^{n} \left\| \widehat{e}_h^{(j+1)} \right\|_{L^2(\Omega)}^2 + \tau|\gamma| \left\| \frac{\partial \widehat{e}_h^{(j+1)}}{\partial x} \right\|_{L^2(\Omega)}^2 + 2\tau \mathfrak{L} \sum_{j=0}^{n} \left\| \widehat{e}_h^{(j+1)} \right\|_{L^2(\Omega)}^2, \tag{5.6.4}$$

where C^* is generic constant.

Now,

$$\begin{aligned}\mathfrak{X}_h^{(j+1)} &= \widehat{u}_t^{(j+1)} - \widehat{\delta}_t u^{(j+1)} \\ &= \widehat{u}_t^{(j+1)} - \frac{1}{\tau}\int_{t_j}^{t_{j+1}} u_t(t)dt \\ &= \frac{1}{2\tau}\int_{t_j}^{t_{j+1}} \lambda_{j+1}(t)u_{ttt}(t)dt,\end{aligned}$$

where $\lambda_{j+1}(t) = (t_{j+1} - t)(t - t_j)$.
Thus,

$$\begin{aligned}\left\|\mathfrak{X}_h^{(j+1)}\right\|_{L^2(\Omega)} &\leq \frac{1}{2\tau}\left(\int_{t_j}^{t_{j+1}} \left(t_{j+1} - t\right)^2 dt\right)^{1/2}\left(\int_{t_j}^{t_{j+1}} \left(t - t_j\right)^2 \left\|u_{ttt}(t)\right\|_{L^2(\Omega)}^2 dt\right)^{1/2} \\ &\leq \mathfrak{C}\tau^{1/2}\left(\int_{t_j}^{t_{j+1}} \left(t - t_j\right)^2 \left\|u_{ttt}(t)\right\|_{L^2(\Omega)}^2 dt\right)^{1/2}\end{aligned}$$

$$\begin{aligned}\Rightarrow \tau\sum_{j=0}^{n}\left\|\mathfrak{X}_h^{(j+1)}\right\|_{L^2(\Omega)}^2 &\leq \mathfrak{C}\tau^2\sum_{j=0}^{n}\left(\int_{t_j}^{t_{j+1}} \left(t - t_j\right)^2 \left\|u_{ttt}(t)\right\|_{L^2(\Omega)}^2 dt\right) \\ &\leq \mathfrak{C}\tau^4\sum_{j=0}^{n}\left(\int_{t_j}^{t_{j+1}} \left\|u_{ttt}(t)\right\|_{L^2(\Omega)}^2 dt\right) \leq \mathfrak{C}\tau^4.\end{aligned}$$

By simplification, the inequality (5.6.4) yields

$$\left\|\widehat{e}_h^{(n+1)}\right\|_{L^2(\Omega)}^2 + \tau|\gamma|\left\|\frac{\partial\widehat{e}_h^{(n+1)}}{\partial x}\right\|_{L^2(\Omega)}^2 \leq \mathfrak{C}\tau^4 + \tau\Big(1 + \frac{C^{*2}}{4|\gamma|} + 2\mathfrak{L}\Big)\sum_{j=0}^{n}\left\|\widehat{e}_h^{(j+1)}\right\|_{L^2(\Omega)}^2. \tag{5.6.5}$$

Using the definition of weighted norm,

$$\left\|\widehat{e}_h^{(n+1)}\right\|_{H_w(\Omega)}^2 = \left\|\widehat{e}_h^{(n+1)}\right\|_{L^2(\Omega)}^2 + \tau|\gamma|\left\|\frac{\partial\widehat{e}_h^{(n+1)}}{\partial x}\right\|_{L^2(\Omega)}^2,$$

the inequality (5.6.5) can be written as

$$\left\|\widehat{e}_h^{(n+1)}\right\|^2_{H_w(\Omega)} \leq \mathfrak{C}\tau^4 + \mathcal{M}\tau \sum_{j=0}^{n} \left\|\widehat{e}_h^{(j+1)}\right\|^2_{H_w(\Omega)},$$

where $\mathcal{M} = \left(1 + \frac{C^{*2}}{4|\gamma|} + 2\mathfrak{L}\right)$.
Utilizating the Proposition 3.3.4 results in

$$\begin{aligned}\left\|\widehat{e}_h^{(n+1)}\right\|^2_{H_w(\Omega)} &\leq \mathfrak{C}\tau^4 exp(\mathcal{M}n\tau) \\ &\leq \mathfrak{C}_*\tau^4\end{aligned}$$

$$\Rightarrow \quad \left\|\widehat{e}_h^{(n+1)}\right\|_{H_w(\Omega)} \leq \mathfrak{C}_*\tau^2. \tag{5.6.6}$$

From Eq. (5.6.1), we have

$$\left\|u^{(n+1)} - U_h^{(n+1)}\right\|_{H_w(\Omega)} \leq \left\|u^{(n+1)} - U^{(n+1)}\right\|_{H_w(\Omega)} + \left\|U^{(n+1)} - U_h^{(n+1)}\right\|_{H_w(\Omega)}.$$

The inequality (5.6.6) and the Lemma 3.6.1 yields

$$\left\|u^{(n+1)} - U_h^{(n+1)}\right\|_{H_w(\Omega)} \leq \mathfrak{C}_*(\tau^2 + \mathfrak{d}_{\mathfrak{s}}{}^m),$$

which completes the proof.

5.7 Numerical experiments

To test the efficiency and accuracy of the proposed scheme numerically, we have considered the generalized Burger-Fisher's problem (5.2.1) with initial condition

$$u(x,0) = \left[0.5 + 0.5\tanh\left(\phi_1 x\right)\right]^{1/\delta}, \tag{5.7.1}$$

and boundary conditions as

$$u(0,t) = \Big[0.5 + 0.5\tanh\big(-\phi_1\phi_2 t\big)\Big]^{1/\delta}, \tag{5.7.2}$$

$$u(1,t) = \Big[0.5 + 0.5\tanh\big(\phi_1(1-\phi_2 t)\big)\Big]^{1/\delta}, \tag{5.7.3}$$

where $\phi_1 = \frac{-\alpha\delta}{2\gamma(1+\delta)}$ and $\phi_2 = \frac{\alpha}{\delta+1} + \frac{\beta\gamma(\delta+1)}{\alpha}$.
The exact solution of problem (5.2.1) is given by [189]

$$u(x,t) = \Big[0.5 + 0.5\tanh\big(\phi_1(x-\phi_2 t)\big)\Big]^{1/\delta}.$$

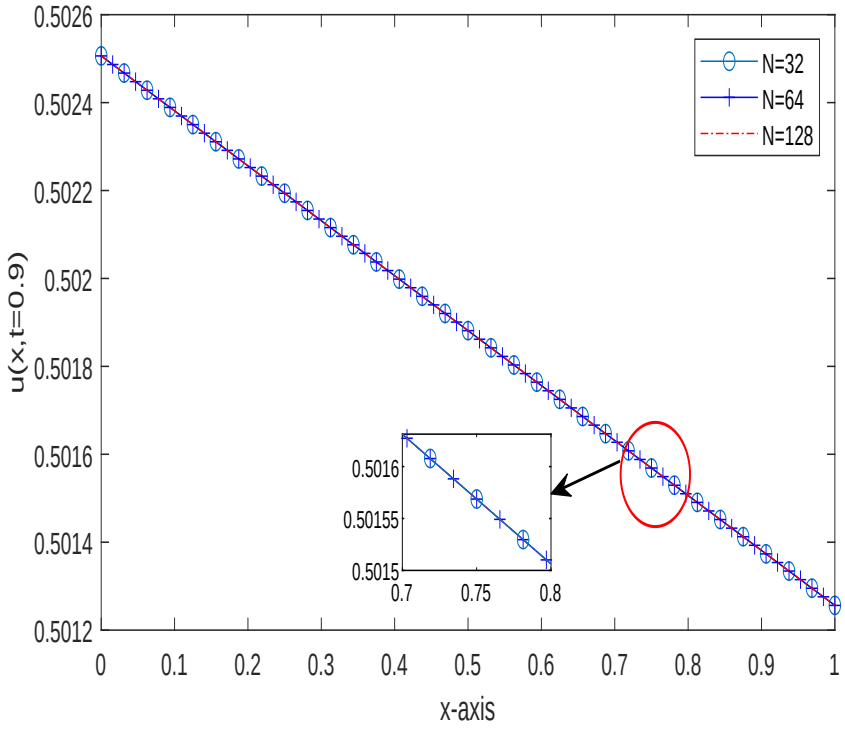

Figure 5.1: Grid-validation test for $N = 32, 64, 128$ at $t = 0.9$.

$L_\infty-$errors have been calculated using the formula as discussed in Section 4.6 of Chapter 4. The grid validity test for various number of nodes has been plotted in Fig. 5.1. It is clear that the proposed EFG scheme provides good accurate results even for 32 number of nodes.

Example 5.7.1 *For this example, we took the following values of the coef-*

ficients of problem (5.2.1)*:*

$\gamma = 1,\ \alpha = 0.1,\ \beta = -0.0025$ *and* $\tau = 0.0001$.

Table 5.1: Comparison of $L_\infty-$errors for BSQI [246] and EFG method for $\alpha = 0.1$, $\beta = -0.0025$ and for different values of δ.

t	$\delta = 1$		$\delta = 2$		$\delta = 4$	
	BSQI	EFGM	BSQI	EFGM	BSQI	EFGM
0.1	1.32×10^{-11}	1.14×10^{-12}	2.84×10^{-10}	1.66×10^{-12}	3.99×10^{-10}	5.35×10^{-14}
0.2	1.78×10^{-11}	1.58×10^{-12}	3.87×10^{-10}	2.31×10^{-12}	5.43×10^{-10}	7.40×10^{-14}
0.3	1.94×10^{-11}	1.74×10^{-12}	4.24×10^{-10}	2.55×10^{-12}	5.95×10^{-10}	8.02×10^{-14}
0.4	2.00×10^{-11}	1.80×10^{-12}	4.37×10^{-10}	2.64×10^{-12}	6.13×10^{-10}	8.24×10^{-14}
0.5	2.02×10^{-11}	1.82×10^{-12}	4.02×10^{-10}	2.67×10^{-12}	6.19×10^{-10}	8.31×10^{-14}

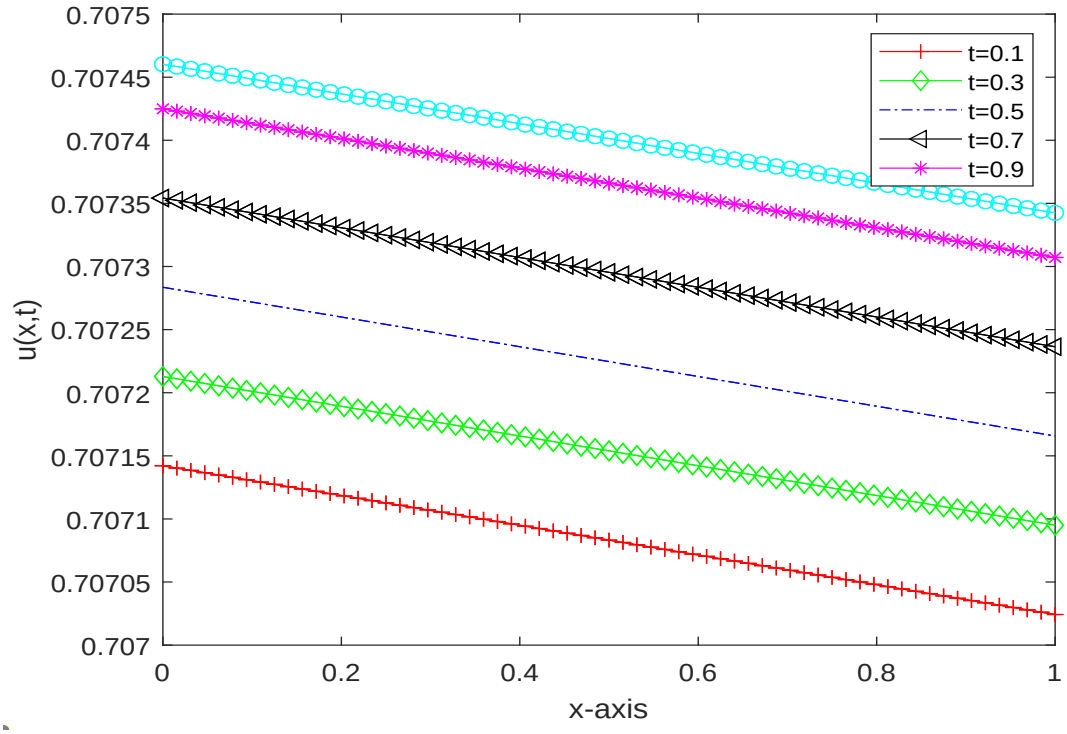

Figure 5.2: Time-effect for $\alpha = 0.1$, $\beta = -0.0025$.

For these values, the L_∞-errors in the EFG solution have been presented in Table 5.1 for different values of δ and t. These errors have been compared with those cited in [246], obtained by using B-spline quasi-interpolation (BSQI) technique. From the Table, it is evident that the proposed EFG

scheme provides much better results than the existing ones. The scheme provides an accuracy of 10^{-14} with only very less number of nodes like 64. Also one can clearly observe the numerical convergence of the proposed EFG scheme.

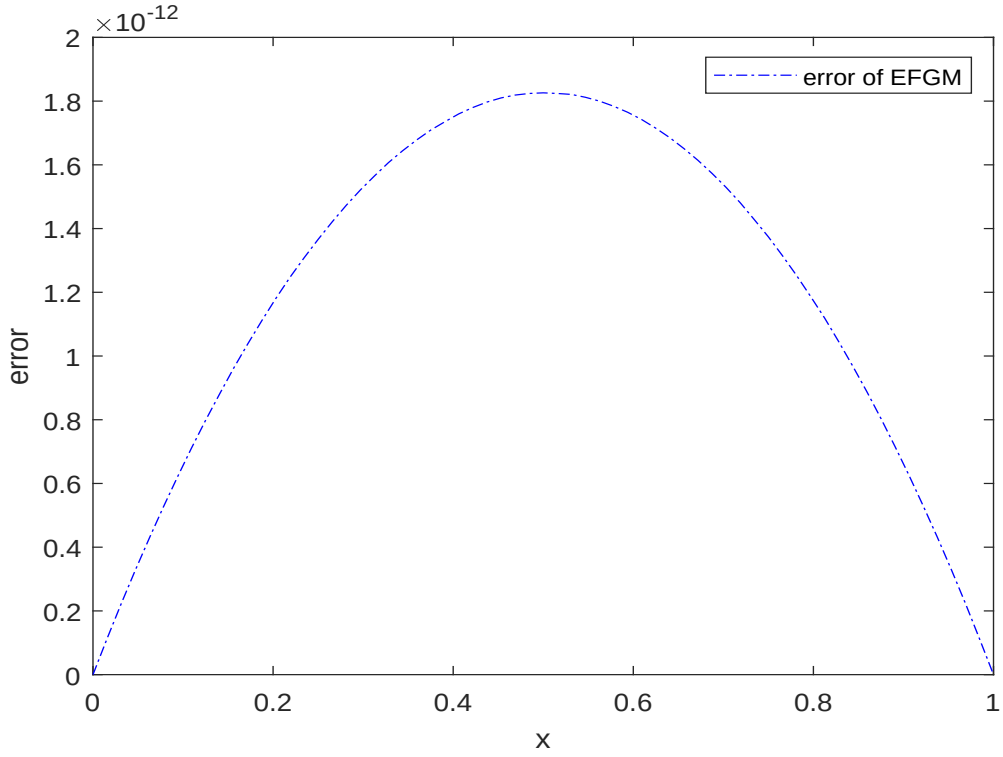

Figure 5.3: Error plot for $\alpha = 0.1$, $\beta = -0.0025$ and $\tau = 0.0001$.

In Fig. 5.2, time effect on the EFG solution has been displaced at various time levels. The EFG solution errors have been plotted for the considered model in Fig. 5.3.

Example 5.7.2 *For the second example, we have considered the following values of the coefficients:*
$\gamma = 1$, $\alpha = 1$, $\beta = 1$ *and* $\tau = 0.0001$.

The L_∞-errors in the EFG solution have been compared with those of the BSQI method for distinct values of δ and t in Table 5.2. In this case also, it can be seen that the proposed scheme provides more accurate and reliable

results than those cited in the literature. The table clearly depicts the numerical convergence of the EFG scheme.

Table 5.2: Comparison of $L_\infty-$errors of BSQI [246] and EFG methods for $\alpha = 1$, $\beta = 1$.

t	$\delta = 1$		$\delta = 2$		$\delta = 4$	
	BSQI	EFGM	BSQI	EFGM	BSQI	EFGM
0.2	5.55×10^{-7}	1.82×10^{-7}	2.56×10^{-6}	4.29×10^{-7}	1.76×10^{-6}	8.53×10^{-7}
0.4	9.05×10^{-7}	2.20×10^{-7}	4.24×10^{-6}	4.84×10^{-7}	4.17×10^{-6}	8.71×10^{-7}
0.6	2.18×10^{-6}	2.30×10^{-7}	3.56×10^{-6}	4.84×10^{-7}	2.42×10^{-6}	8.71×10^{-7}
0.8	2.93×10^{-6}	2.31×10^{-7}	1.46×10^{-6}	4.84×10^{-7}	2.35×10^{-6}	8.71×10^{-7}
1.0	3.01×10^{-6}	2.31×10^{-7}	5.54×10^{-6}	4.84×10^{-7}	1.44×10^{-6}	8.71×10^{-7}

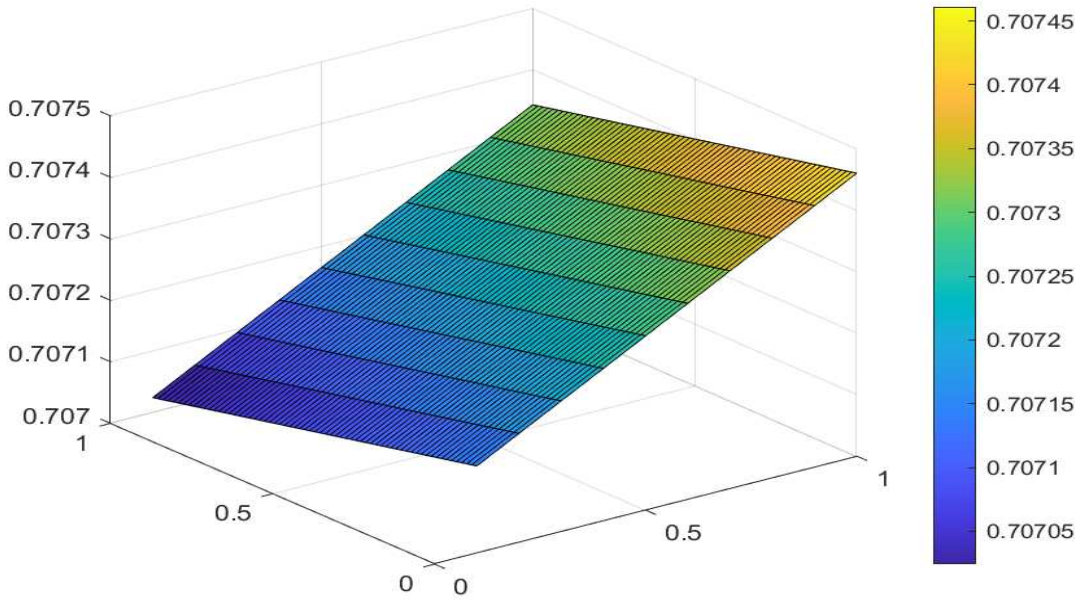

Figure 5.4: The EFG solution profile for $\alpha = 1$, $\beta = 1$.

The continuous space-time evolution of the EFG solution profile has been shown in Fig. 5.4.

Example 5.7.3 *For the third example, in Table 5.3, we have demonstrated the maximum absolute errors for different values of* δ *at different time levels with* $\gamma = 1$, $\alpha = \beta = 0.001$ *and* $\tau = 0.0001$.

Table 5.3: Maximum absolute errors for Example 5.7.3 for different values of δ and t with $N = 64$.

t	$\delta = 1$	$\delta = 2$	$\delta = 4$	$\delta = 8$
0.1	1.45×10^{-13}	3.38×10^{-13}	7.07×10^{-13}	1.44×10^{-12}
0.3	2.14×10^{-13}	5.19×10^{-13}	1.08×10^{-12}	2.21×10^{-12}
0.5	2.42×10^{-13}	5.44×10^{-13}	1.13×10^{-12}	2.32×10^{-12}
0.7	2.46×10^{-13}	5.47×10^{-13}	1.14×10^{-12}	2.34×10^{-12}
0.9	2.46×10^{-13}	5.49×10^{-13}	1.14×10^{-12}	2.34×10^{-12}

Table 5.4: Absolute error comparison of EFG solution with FEM and Exp-Function method at $t = 0.1$ for $\alpha = 0.001$, $\beta = 0.001$.

x	$EFGM$	FEM	$Exp - Fun$
0.00	1.03×10^{-14}	1.40×10^{-13}	2.23×10^{-8}
0.20	9.53×10^{-13}	6.97×10^{-10}	1.70×10^{-8}
0.40	1.38×10^{-13}	1.12×10^{-9}	1.04×10^{-8}
0.60	1.40×10^{-13}	1.12×10^{-9}	2.35×10^{-9}
0.80	9.71×10^{-13}	6.97×10^{-10}	7.06×10^{-9}
1.00	1.01×10^{-14}	1.40×10^{-14}	1.78×10^{-8}

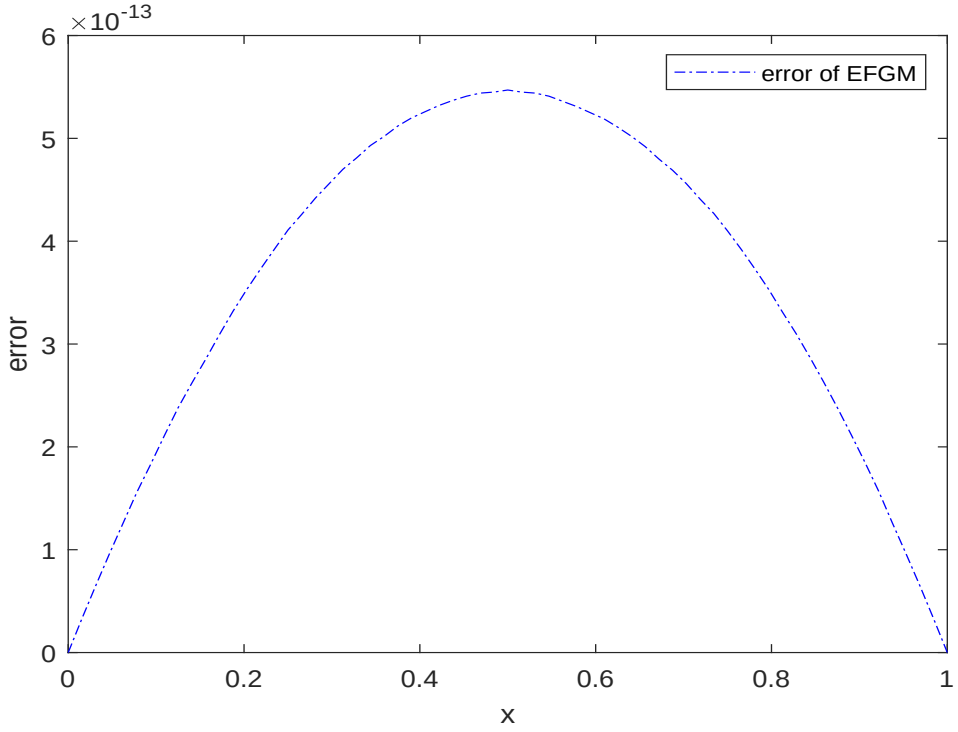

Figure 5.5: Error plot for $\alpha = 0.001$, $\beta = 0.001$ and $\tau = 0.0001$.

Table 5.4 shows the comparison of L_∞-errors in the EFG solution and in the finite element method (FEM) and Exp-Function solutions [229]. Here also, one can notice that the EFG scheme provides more accurate results than the other numerical schemes cited in the literature.

Table 5.5: Comparison of exact solution with EFG method for $\alpha = 0.001$, $\beta = 0.001$ and $t = 1$.

x	*Exact*	*EFGM*	*Error*
0.10	0.5002383415	0.5002383415	3.79×10^{-13}
0.20	0.5002246696	0.5002246696	1.54×10^{-13}
0.30	0.5002109977	0.5002100997	2.01×10^{-13}
0.40	0.5001973258	0.5001973258	2.37×10^{-13}
0.50	0.5001875602	0.5001875602	2.38×10^{-13}
0.60	0.5001738884	0.5001738884	2.26×10^{-13}
0.70	0.5001621696	0.5001621696	2.18×10^{-13}
0.80	0.5001484977	0.5001484977	1.41×10^{-13}
0.90	0.5001367790	0.5001367790	7.80×10^{-14}

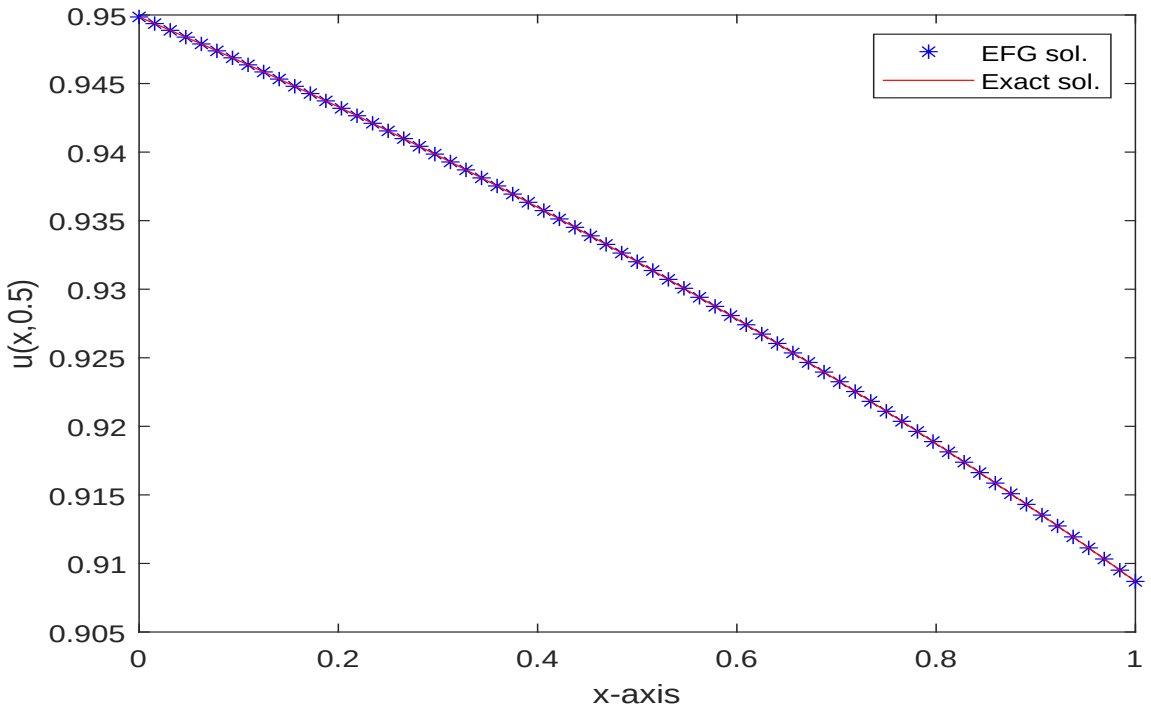

Figure 5.6: Comparison of EFG solution with exact solution at $t = 0.5$ for $\alpha = 0.001$, $\beta = 0.001$.

Fig. 5.5 displays the error plot. The comparison of exact solution with the EFG solution is presented in Table 5.5 and has been plotted in Fig. 5.6. All these tables clearly depict the robustness of the EFG method. The method provides an accuracy upto 10^{-13} which is very small even with very less number of nodes. We can notice that the EFG solutions are in very good agreement with the exact ones.

5.8 Conclusion

In this Chapter, we have established the element-free Galerkin approach to deal with the generalized non-linear Burger-Fisher's equation. Initially, the time derivative term has been discretized by employing the Crank-Nicolson strategy. The semi-discrete scheme is shown to be unconditional stable. Furthermore, the existence and uniqueness of the solution of the suggested technique have been analyzed in detail. In the second step, the error estimates of the full-discrete EFG formulation have been examined and it has been derived that the scheme converges with $\mathcal{O}(\tau^2 + \mathfrak{d}_{\mathfrak{s}}{}^m)$, where τ is the time-step and $\mathfrak{d}_{\mathfrak{s}}$ is the size of influence domain, respectively. Here, it is to be noted that the diffusion coefficient γ is not singular perturbation parameter. The EFG scheme does not converges uniformly in principle if we let $\gamma \to 0$. The full discrete scheme converges with the condition that the diffusion coefficient should be bounded below. The test problem have been studied for different values of the parameters and the numerical results have been presented. The L_∞-errors proves the robustness and efficiency of the proposed EFG scheme. It can be clearly observed that the EFG technique provides much better results than those cited in the literature.

Chapter 6

Element-free Galerkin method and its convergence analysis for two-dimensional singularly perturbed parabolic problem

6.1 Introduction

In the present Chapter, we consider the following two-dimensional non-linear time-dependent singularly perturbed reaction-diffusion initial-boundary-value problem (IBVP):

$$\frac{\partial u}{\partial t}(\mathbf{x},t) - \epsilon_1 \frac{\partial^2 u}{\partial x^2}(\mathbf{x},t) - \epsilon_2 \frac{\partial^2 u}{\partial y^2}(\mathbf{x},t) + a(\mathbf{x},t)u(\mathbf{x},t) = F(u(\mathbf{x},t)), \quad (\mathbf{x},t) \in \Omega, \tag{6.1.1}$$

$$u(\mathbf{x},0) = u_0(\mathbf{x}), \quad \mathbf{x} \in \overline{\Omega}_{\mathbf{x}},$$
$$u(\mathbf{x},t) = f(\mathbf{x},t), \quad (\mathbf{x},t) \in \partial\Omega \times [0,T],$$

where, $\mathbf{x} = (x,y)$, $\Omega = (0,1)^2 \times (0,T]$, and $0 < \epsilon_1, \epsilon_2 \ll 1$ are small singular perturbation parameters. $a(\mathbf{x},t)$ is sufficiently smooth function satisfies $\alpha \leq a(\mathbf{x},t) \leq \alpha^*$ and $F(u,\mathbf{x},t)$ is non-linear. We also assume that the compatibility conditions are satisfied on the boundary of the domain, i.e.

$$u(\mathbf{x},0) = u_0(\mathbf{x}) = f(\mathbf{x},0);\ \mathbf{x} \in \partial\Omega. \tag{6.1.2}$$

Parameter-dependent differential equations, specifically singularly perturbed differential equations, describe numerous realistic problems in the field of science and engineering. When the singular perturbation parameter ap-

proaches zero, the solutions to the problems may possess a multi-scale character, with abrupt fluctuations in some narrow regions adjacent to both the left and right lateral boundaries [153]. Classical numerical techniques fail to portray this sharpness in solutions since these schemes are inefficient in capturing the behavior of exact solutions, especially in the boundary layer regions. This causes a higher errors unless very small step sizes are used and also produces a negative impact on the computational efficiency of the method. Particularly, traditional finite difference or finite element methods on uniform meshes are insufficient to provide appropriate numerical results. Over the last few decades, many researchers have developed reliable numerical approaches to approximate the solutions. Linß and Stynes [139] carried out a survey on $\epsilon-$uniform numerical techniques for $2D$ singularly perturbed parabolic PDE. In [207], traditional finite difference approaches are applied to construct effective numerical methods for a $2D$ singularly perturbed parabolic system with reaction-diffusion type equations. The time derivative has been approximated using the implicit-Euler approach and demonstrated that the proposed technique is first- and second-order uniformly convergent in the temporal and spatial variables, respectively. Clavero and Jorge [46] recently presented a full-discrete finite difference scheme together with the fractional implicit Euler method for a $2D$ singularly perturbed parabolic problem. First-order accuracy and pointwise error estimation have been accomplished using Shishkin mesh.

For a system of coupled reaction-diffusion equations with parameters of various magnitudes, Linß and Madden [140] developed a finite element discretization on Shishkin and the Bakhvalov mesh. A finite element scheme for a system of singularly perturbed reaction-diffusion BVP have been discussed in [139], and accuracy of $\mathcal{O}(N^{-1}\ln N)$ has been described in some balanced norm. For a huge system of SPP in one dimension, the convergence theory of conforming linear finite elements is provided in [136] on arbitrary meshes, based on piecewise quadratic splines. Maneesh et al. [208] estab-

lished the superconvergence property of the Galerkin FEM for a system of singularly perturbed reaction-diffusion and convection-diffusion BVP. Error estimates have been improved using Gauss-Lobatto interpolation in the layer regions and for achieving second-order superconvergence results. Furthermore, Li et al. [130–132] demonstrated several strategies for obtaining uniformly convergent FEM in the L^2-norm for the singularly perturbed elliptic problem. Jorge and Bujanda [97] developed a new strategy by combining the alternating direction method with the Runge-Kutta scheme to deal with parabolic two-dimensional reaction-diffusion problems with nonlinear reaction terms.

To the best of the our knowledge, the two-dimensional singularly perturbed parabolic reaction-diffusion problem has still not been studied under the framework of the mesh-free approach which is parameter uniform convergent. Therefore, the primary purpose of this research is to establish a robust EFG approach for problem (6.1.1) and to examine the error estimates for the proposed scheme. The key benefit of the EFG method is the non-requirement of nodal connectivity which makes it easy to add and remove nodes as per necessity. This feature makes the mesh-free methods popular for problems involving moving boundaries, cracks or discontinuity in domains etc. In the case of SPP, where the solution contains sharp boundary layers, the EFG scheme exhibits more accurate and reliable results than any other traditional numerical method. The element connectivity-free feature of the proposed method benefits in the sense of inclusion of more nodes in the region of steep boundary layers arising in the solution profile and aids in capturing them. Consequently, a flexible refinement of domain discretization can be achieved efficiently and quickly, emphasizing the accuracy of the approximate solution. There are minor drawbacks of the EFG scheme, as it takes more computational time than FEM. Moreover, the imposition of essential boundary conditions is not straightforward, as the EFG method is based on the MLS approximation. The shape functions generated by using

MLS approximation lacks in satisfying the Kronecker delta property. In literature, the Lagrange multiplier, penalty, and coupled EFG-FEM methods have been adopted to conquer this issue. The methodology is based on the global weak form, and background cells have been generated using the Gaussian quadrature to compute numerical integrations. The choice of weight functions plays a crucial role in the formulation of the method and directly influences the efficiency and robustness of the EFG method.
The Chapter has been organized in the following way: The EFG methodology and discretization of time derivative by using implicit Crank-Nicolson scheme have been discussed in Section 6.2. Stability analysis of the semi-discrete scheme has been demonstrated in Section 6.3. Section 6.4 deals with the convergence of the full-discrete scheme. Some numerical experiments have been carried out in Section 6.5 to validate the theoretical results. Section 6.6 provides the summary of the findings discussed in the Chapter.

6.2 Element-free Galerkin formulation

6.2.1 Domain discretization

In case of SPP, very dense and fine nodal points are required inside the boundary layer regions which benefits in approximating the solution specially in the boundary layer regions. For the same, in the present work, we have employed Shishkin's approach in order to generate more number of nodes in the boundary layer regions. Let $N \in \mathbb{Z}^+$ be the number of elements in each $x-$ and y-direction. The transition parameter δ_x will be used to determine the boundary layer width along x-direction and is defined as

$$\delta_x = \min\left\{\frac{1}{4}, \kappa\epsilon \ln N\right\}.$$

Similarly, we can define the boundary layer width Ω_y along y-direction. We assume that the boundary layers arise in all the four corners of the spatial domain Ω. Now, the spatial domain Ω can be partitioned into four sub-domains using these transition parameters as follows:

$$\Omega = \Omega_{11} \cup \Omega_{21} \cup \Omega_{12} \cup \Omega_{22},$$

where

$$\begin{aligned}
\Omega_{11} &= [\delta_x, 1-\delta_x] \times [\delta_y, 1-\delta_y], \\
\Omega_{21} &= \big([0, \delta_x] \cup [1-\delta_x, 1]\big) \times [\delta_y, 1-\delta_y], \\
\Omega_{12} &= [\delta_x, 1-\delta_x] \times \big([0, \delta_y] \cup [1-\delta_y, 1]\big), \\
\Omega_{22} &= [0, \delta_x] \times \big([0, \delta_y] \cup [1-\delta_y, 1]\big) \cup \big[[1-\delta_x, 1] \times \big([0, \delta_y] \cup [1-\delta_y, 1]\big)\big].
\end{aligned}$$

In the $x-$intervals $[0, \delta_x]$ and $[1-\delta_x, 1]$, and $y-$intervals $[0, \delta_y]$ and $[1-\delta_y, 1]$, we generate $N/4$ equidistant nodes, while as in $[\delta_x, 1-\delta_x]$ and $[\delta_y, 1-\delta_y]$, we generate $N/2$ equidistant nodes. This results in a coarse nodal distribution on $[\delta_x, 1-\delta_x] \times [\delta_y, 1-\delta_y]$ and a fine nodal distribution elsewhere.

The set of nodal points $0 = x_0 < x_1 < x_2 < ... < x_N = 1$ and $0 = y_0 < y_1 < ... < y_N = 1$ are generated as follows:

$$x_i = \begin{cases} i \times h_i & for\ i = 1, ..., N/4, \\ \delta_x + (i - N/4) \times h_i & for\ i = (N/4) + 1, ..., 3N/4, \\ (1 - \delta_x) + i \times h_i & for\ i = (3N/4) + 1, ..., N. \end{cases}$$

$$y_j = \begin{cases} j \times k_j & for\ j = 1, ..., N/4, \\ \delta_y + (j - N/4) \times k_j & for\ j = (N/4) + 1, ..., 3N/4, \\ (1 - \delta_y) + j \times k_j & for\ j = (3N/4) + 1, ..., N. \end{cases}$$

with step sizes h_i and k_j for $i, j = 1, 2, ..., N$, defined by

$$h_i = \begin{cases} h_1 = 4\delta_x/N \quad for\ i = 1, ..., N/4; (3N/4) + 1, ..., N \\ h_2 = 2(1 - 2\delta_x)/N \quad for\ i = (N/4) + 1, ..., 3N/4, \end{cases}$$

and

$$k_j = \begin{cases} k_1 = 4\delta_y/N \quad for\ j = 1, ..., N/4; (3N/4) + 1, ..., N \\ k_2 = 2(1 - 2\delta_y)/N \quad for\ j = (N/4) + 1, ..., 3N/4. \end{cases}$$

6.2.2 Moving least-square approximation

As discussed in one-dimensional case, in the EFG technique, the trial and test functions for the variational weak form are constructed by utilizing the MLS approximation [127]. The MLS approximation $u_h(\mathfrak{x}, t)$ of the field variable $u(\mathfrak{x}, t)$ defined in the domain $\Omega = (0, 1)^2 \times (0, T]$ is given by

$$u_h(\mathfrak{x}, t) = \sum_{i=1}^{m} p_i(\mathfrak{x})\lambda_i(\mathfrak{x}, t) = \mathbf{p}^T(\mathfrak{x})\boldsymbol{\lambda}, \tag{6.2.1}$$

where $\mathbf{p}(\mathfrak{x})$ is the polynomial basis in the two-dimensional space coordinate $\mathfrak{x} = [x, y]^T$, m is the number of terms in the basis and $\boldsymbol{\lambda}^T = (\lambda_1, \lambda_2, ..., \lambda_m)$ is unknown coefficient vector of $p^T(\mathfrak{x})$, needed to be determined and which depends upon $\mathfrak{x}$ and t.

The coefficients $\lambda_i(\mathfrak{x}, t)$ in Eq. (6.2.1) are to be determined by performing a weighted least square fit locally. This results in the quadratic form

$$\begin{aligned} J(\mathfrak{x}) &= \sum_{j=1}^{n} w(\mathfrak{x} - \mathfrak{x}_j)[u_h(\mathfrak{x} - \mathfrak{x}_j, t) - u_j]^2 \\ &= \sum_{j=1}^{n} w(\mathfrak{x} - \mathfrak{x}_j)\Big[\sum_{i=1}^{m} p_i(\mathfrak{x})\lambda_i - u_j\Big]^2, \end{aligned} \tag{6.2.2}$$

where u_j are the nodal approximants of the unknown function $u(\mathfrak{x}, t)$ at the node $\mathfrak{x}_j$.
In order to derive the parameters λ_j, we compute the extremum of J from

$$\frac{\partial J}{\partial \lambda_j} = \mathbf{\Lambda}(\mathfrak{x})\boldsymbol{\lambda} - \mathbf{B}(\mathfrak{x})\mathbf{u} = 0, \tag{6.2.3}$$

where

$$\begin{aligned} \mathbf{u} &= [u_1, u_2, ..., u_n]^T, \\ \mathbf{\Lambda}(\mathfrak{x}) &= \sum_{j=1}^{n} w(\mathfrak{x} - \mathfrak{x}_j) p(\mathfrak{x}_j) p^T(\mathfrak{x}_j), \\ \text{and} \qquad \mathbf{B}(\mathfrak{x}) &= [w(\mathfrak{x} - \mathfrak{x}_1)p(\mathfrak{x}_1), w(\mathfrak{x} - \mathfrak{x}_2)p(\mathfrak{x}_2), ..., w(\mathfrak{x} - \mathfrak{x}_n)p(\mathfrak{x}_n)]. \end{aligned}$$

If $\mathbf{\Lambda}$ is invertible, the vector λ can be expressed as

$$\lambda = \mathbf{\Lambda}^{-1}(\mathfrak{x})\mathbf{B}(\mathfrak{x})\mathbf{u}.$$

Substituting the above value in Eq. (6.2.1), we obtain

$$\begin{aligned} u_h(\mathfrak{x}, t) &= \sum_{j=1}^{n} \sum_{i=1}^{m} p_i(\mathfrak{x}) [\Lambda^{-1}(\mathfrak{x}) B(\mathfrak{x})]_{ij} u_j \\ &= \sum_{j=1}^{n} \phi_j(\mathfrak{x}) \mathbf{u}, \end{aligned}$$

where the EFG shape functions are given by

$$\phi_j(\mathfrak{x}) = \sum_{i=1}^{m} p_i(\mathfrak{x}) [\Lambda^{-1}(\mathfrak{x}) B(\mathfrak{x})]_{ij}.$$

Similar to one-dimensional case, here also in the EFG method every node is associated with a domain of influence, generally known as ball or support of the weight function $w_j(\mathfrak{x})$. The most commonly used domains of influence are in the rectangle form or are circles.

For the two-dimensional case, we have chosen the Gaussian exponential spline weight functions, with rectangular nodal support domains, of the form

$$\begin{aligned} w(s) &= w(s_x).w(s_y) \\ &= w\Big(\frac{\|x-x_j\|}{\mathfrak{d}_s^x}\Big).w\Big(\frac{\|y-y_j\|}{\mathfrak{d}_s^y}\Big), \end{aligned}$$

where $\mathfrak{d}_s^x$ and $\mathfrak{d}_s^y$ are radii of influence domain along $x-$ and $y-$axis respectively.
The weight function $w(s_x)$ is defined as

$$w(s_x) = \begin{cases} \frac{e^{-(s_x/\alpha)^2}-e^{-(1/\alpha)^2}}{1-e^{-(1/\alpha)^2}}, & s_x \leq 1 \\ 0, & s_x > 1, \end{cases}$$

$s_x = \frac{\|x-x_j\|}{\mathfrak{d}_s^x}$, $\|x-x_j\|$ is normalized distance, and $\mathfrak{d}_s = \alpha\mathfrak{d}_c$ is the radius of the influence domain of the node $\mathfrak{x}_j$ along x-axis while the scaling parameter α is mostly taken as $\alpha = 0.3$ and $\mathfrak{d}_c^x$ is the average nodal spacing. The derivative of the weight functions can be computed using the chain rule.

6.2.3 Time semi-discrete scheme

The weak form of the considered problem (6.1.1) is given by

$$\Big\langle \frac{\partial u}{\partial t}, \upsilon \Big\rangle + \epsilon_1 \Big\langle \frac{\partial u}{\partial x}, \frac{\partial \upsilon}{\partial x} \Big\rangle + \epsilon_2 \Big\langle \frac{\partial u}{\partial y}, \frac{\partial \upsilon}{\partial y} \Big\rangle + \Big\langle au, \upsilon \Big\rangle = \Big\langle F(u), \upsilon \Big\rangle, \quad \upsilon \in H^1(\Omega). \tag{6.2.4}$$

Define $t_n = n\tau$ for $n = 0, 1, ..., N$ where $\tau = T/N$.
Further, as discussed in Chapters 3 and 5, with the use of Crank-Nicolson scheme and the notations

$$\widehat{\delta}_t U^{(n)} = \frac{U^{(n)} - U^{(n-1)}}{\tau}, \qquad \widehat{U}^{(n)} = \frac{U^{(n)} + U^{(n-1)}}{2}, \tag{6.2.5}$$

the temporal semi-discrete scheme for Eq. (6.2.4) becomes

$$\Big\langle \widehat{\delta}_t U^{(n)}, \upsilon \Big\rangle + \epsilon_1 \Big\langle \frac{\partial \widehat{U}^{(n)}}{\partial x}, \frac{\partial \upsilon}{\partial x} \Big\rangle + \epsilon_2 \Big\langle \frac{\partial \widehat{U}^{(n)}}{\partial y}, \frac{\partial \upsilon}{\partial y} \Big\rangle + \Big\langle \widehat{aU}^{(n)}, \upsilon \Big\rangle = \Big\langle \widehat{F}(U^{(n)}), \upsilon \Big\rangle, \quad \upsilon \in H^1(\Omega). \tag{6.2.6}$$

Simplifying, we get

$$\begin{aligned} &\Big\langle U^{(n)}, \upsilon \Big\rangle + \frac{\epsilon_1}{2}\tau \Big\langle \frac{\partial U^{(n)}}{\partial x}, \frac{\partial \upsilon}{\partial x} \Big\rangle + \frac{\epsilon_2}{2}\tau \Big\langle \frac{\partial U^{(n)}}{\partial y}, \frac{\partial \upsilon}{\partial y} \Big\rangle + \frac{\tau}{2} \Big\langle a^{(n)} U^{(n)}, \upsilon \Big\rangle \\ &- \frac{\tau}{2} \Big\langle F(U^{(n)}), \upsilon \Big\rangle = \Big\langle U^{(n-1)}, \upsilon \Big\rangle - \frac{\epsilon_1}{2}\tau \Big\langle \frac{\partial U^{(n-1)}}{\partial x}, \frac{\partial \upsilon}{\partial x} \Big\rangle - \frac{\epsilon_2}{2}\tau \Big\langle \frac{\partial U^{(n-1)}}{\partial y}, \frac{\partial \upsilon}{\partial y} \Big\rangle \\ &- \frac{\tau}{2} \Big\langle a^{(n-1)} U^{(n-1)}, \upsilon \Big\rangle + \frac{\tau}{2} \Big\langle F(U^{(n-1)}), \upsilon \Big\rangle. \end{aligned} \tag{6.2.7}$$

Let V_h be the finite dimensional subspace of $H^1(\Omega)$. Then the full-discrete EFG scheme can be written as

$$\begin{aligned} &\Big\langle U_h^{(n)}, \upsilon_h \Big\rangle + \frac{\epsilon_1}{2}\tau \Big\langle \frac{\partial U_h^{(n)}}{\partial x}, \frac{\partial \upsilon_h}{\partial x} \Big\rangle + \frac{\epsilon_2}{2}\tau \Big\langle \frac{\partial U_h^{(n)}}{\partial y}, \frac{\partial \upsilon_h}{\partial y} \Big\rangle + \frac{\tau}{2} \Big\langle a^{(n)} U_h^{(n)}, \upsilon_h \Big\rangle \\ &- \frac{\tau}{2} \Big\langle F(U_h^{(n)}), \upsilon_h \Big\rangle = \Big\langle U_h^{(n-1)}, \upsilon_h \Big\rangle - \frac{\epsilon_1}{2}\tau \Big\langle \frac{\partial U_h^{(n-1)}}{\partial x}, \frac{\partial \upsilon_h}{\partial x} \Big\rangle - \frac{\epsilon_2}{2}\tau \Big\langle \frac{\partial U_h^{(n-1)}}{\partial y}, \frac{\partial \upsilon_h}{\partial y} \Big\rangle \\ &- \frac{\tau}{2} \Big\langle a^{(n-1)} U_h^{(n-1)}, \upsilon_h \Big\rangle + \frac{\tau}{2} \Big\langle F(U_h^{(n-1)}), \upsilon_h \Big\rangle, \quad \forall \upsilon_h \in V_h \end{aligned} \tag{6.2.8}$$

where $U_h^{(n)}$ is finite-dimensional approximation of $U^{(n)}$.

6.3 Stability analysis of temporal-discrete scheme

Before proving the stability of the semi-discrete scheme (6.2.7), we state the following Lemmas which will be used in our analysis:

Lemma 6.3.1 *[190] Let $0 < \epsilon_1, \epsilon_2 \ll 1$. If the compatibility conditions defined by* (6.1.2) *hold, then the solution $u(\mathbf{x}, t)$ to the continuous problem*

(6.1.1) *will fulfill the conditions*

$$\Big|u(\mathbf{x},t)-u_0(\mathbf{x})\Big| \le Ct \quad \forall\ (\mathbf{x},t)\ \in \overline{\Omega}$$
$$\textit{and}\ \ \Big|u(\mathbf{x},t)-f(\mathbf{x},t)\Big| \le Cx \quad \forall\ (\mathbf{x},t)\ \in \overline{\Omega}.$$

Lemma 6.3.2 *It is straightforward to derive from Lemma 6.3.1 that*

$$\Big|u(\mathbf{x},t)\Big| \le C \quad \forall\ (\mathbf{x},t) \in \overline{\Omega}.$$

Lemma 6.3.3 *Assuming $u \in C(\overline{\Omega})$ and $\overline{\Omega} \subset \mathbb{R}^d$ (d=3) to be a bounded and closed set, the non-linear function $F(u)$ satisfies the inequality*

$$|F(u)| \le \overline{M}.$$

Next, we will comprehensively analyze the stability of the time-discrete scheme given by (6.2.7).

Theorem 6.3.4 *The temporal discrete scheme given by* (6.2.7) *is stable.*

Proof Putting $\upsilon = U^{(n)}$ in Eq. (6.2.7) yields

$$\Big\langle U^{(n)},U^{(n)}\Big\rangle + \frac{\epsilon_1}{2}\tau\Big\langle\frac{\partial U^{(n)}}{\partial x},\frac{\partial U^{(n)}}{\partial x}\Big\rangle + \frac{\epsilon_2}{2}\tau\Big\langle\frac{\partial U^{(n)}}{\partial y},\frac{\partial U^{(n)}}{\partial y}\Big\rangle + \frac{\tau}{2}\Big\langle a^{(n)}U^{(n)},U^{(n)}\Big\rangle$$
$$-\frac{\tau}{2}\Big\langle F(U^{(n)}),U^{(n)}\Big\rangle = \Big\langle U^{(n-1)},U^{(n)}\Big\rangle - \frac{\epsilon_1}{2}\tau\Big\langle\frac{\partial U^{(n-1)}}{\partial x},\frac{\partial U^{(n)}}{\partial x}\Big\rangle$$
$$-\frac{\epsilon_2}{2}\tau\Big\langle\frac{\partial U^{(n-1)}}{\partial y},\frac{\partial U^{(n)}}{\partial y}\Big\rangle - \frac{\tau}{2}\Big\langle a^{(n-1)}U^{(n-1)},U^{(n)}\Big\rangle + \frac{\tau}{2}\Big\langle F(U^{(n-1)}),U^{(n)}\Big\rangle.$$

$$
\begin{aligned}
\Rightarrow \quad & \frac{1}{2}\left\|U^{(n)}\right\|^2_{L^2(\Omega)} + \frac{\epsilon_1}{4}\tau\left\|\frac{\partial U^{(n)}}{\partial x}\right\|^2_{L^2(\Omega)} + \frac{\epsilon_2}{4}\tau\left\|\frac{\partial U^{(n)}}{\partial y}\right\|^2_{L^2(\Omega)} \leq \frac{1}{2}\left\|U^{(n-1)}\right\|^2_{L^2(\Omega)} \\
& + \frac{\epsilon_1}{4}\tau\left\|\frac{\partial U^{(n-1)}}{\partial x}\right\|^2_{L^2(\Omega)} + \frac{\epsilon_2}{4}\tau\left\|\frac{\partial U^{(n-1)}}{\partial y}\right\|^2_{L^2(\Omega)} + \frac{\tau\alpha^*}{4}\left\|U^{(n-1)}\right\|^2_{L^2(\Omega)} \\
& + \frac{3\alpha^*\tau}{4}\left\|U^{(n)}\right\|^2_{L^2(\Omega)} + \frac{\tau}{4}\Big[\left\|F(U^{(n)})\right\|^2_{L^2(\Omega)} + \left\|U^{(n)}\right\|^2_{L^2(\Omega)}\Big] \\
& + \frac{\tau}{4}\Big[\left\|F(U^{(n-1)})\right\|^2_{L^2(\Omega)} + \left\|U^{(n)}\right\|^2_{L^2(\Omega)}\Big].
\end{aligned}
$$

(Using Young's inequality)

$$
\begin{aligned}
& \leq \frac{1}{2}\left\|U^{(n-1)}\right\|^2_{L^2(\Omega)} + \frac{\epsilon_1}{4}\tau\left\|\frac{\partial U^{(n-1)}}{\partial x}\right\|^2_{L^2(\Omega)} + \frac{\epsilon_2}{4}\tau\left\|\frac{\partial U^{(n-1)}}{\partial y}\right\|^2_{L^2(\Omega)} \\
& + \frac{\alpha^*\tau}{4}\left\|U^{(n-1)}\right\|^2_{L^2(\Omega)} + \Big(\frac{3\alpha^*}{2}+1\Big)\frac{\tau}{2}\left\|U^{(n)}\right\|^2_{L^2(\Omega)} + \frac{\tau}{2}|\overline{M}|^2. \qquad (6.3.1)
\end{aligned}
$$

Define the weighted norm $\|.\|_{H_w(\Omega)}$ as

$$
\left\|U^{(n)}\right\|^2_{H_w(\Omega)} = \frac{1}{2}\left\|U^{(n)}\right\|^2_{L^2(\Omega)} + \frac{\epsilon_1}{4}\tau\left\|\frac{\partial U^{(n)}}{\partial x}\right\|^2_{L^2(\Omega)} + \frac{\epsilon_2}{4}\tau\left\|\frac{\partial U^{(n)}}{\partial y}\right\|^2_{L^2(\Omega)}.
$$

Eq. (6.3.1) can be expressed as

$$
\begin{aligned}
\left\|U^{(n)}\right\|^2_{H_w(\Omega)} \leq \left\|U^{(n-1)}\right\|^2_{H_w(\Omega)} + \frac{\alpha^*\tau}{2}\left\|U^{(n-1)}\right\|^2_{H_w(\Omega)} + \left(\frac{3\alpha^*}{2}+1\right)\tau\left\|U^{(n)}\right\|^2_{H_w(\Omega)} \\
+ \frac{\tau}{2}|\overline{M}|^2.
\end{aligned}
$$

Taking summation for i from 1 to n leads to

$$
\begin{aligned}
\sum_{i=1}^{n}\left\|U^{(i)}\right\|^2_{H_w(\Omega)} \leq \sum_{i=1}^{n}\left\|U^{(i-1)}\right\|^2_{H_w(\Omega)} + \frac{\alpha^*\tau}{2}\sum_{i=1}^{n}\left\|U^{(i-1)}\right\|^2_{H_w(\Omega)} \\
+ \left(\frac{3\alpha^*}{2}+1\right)\tau\sum_{i=1}^{n}\left\|U^{(i)}\right\|^2_{H_w(\Omega)} + \frac{\tau}{2}\sum_{i=1}^{n}|\overline{M}|^2.
\end{aligned}
$$

$$
\Rightarrow \quad \left\|U^{(n)}\right\|^2_{H_w(\Omega)} \leq \left\|U^{(0)}\right\|^2_{H_w(\Omega)} + (2\alpha^*+1)\tau\sum_{i=0}^{n}\left\|U^{(i)}\right\|^2_{H_w(\Omega)} + \frac{\tau}{2}\sum_{i=1}^{n}|\overline{M}|^2.
$$

Using Gronwall-Bellman inequality, we get

$$\begin{aligned}\left\|U^{(n)}\right\|^2_{H_w(\Omega)} &\leq \left[\left\|U^{(0)}\right\|^2_{H_w(\Omega)} + \frac{\tau}{2}n|\overline{M}|^2\right]\exp\Big((2\alpha^*+1)\tau n\Big)\\ &\leq \left[\left\|U^{(0)}\right\|^2_{H_w(\Omega)} + \frac{T}{2}|\overline{M}|^2\right]\exp\Big((2\alpha^*+1)T\Big)\\ &\leq \mathcal{C}*\left\|U^{(0)}\right\|^2_{H_w(\Omega)},\end{aligned}$$

which shows that the time discrete scheme is unconditionally stable.

6.4 Convergence of full-discrete scheme

The results provide the convergence of the full discrete EFG scheme (6.2.8).

Lemma 6.4.1 *[212] Let $\varphi(x) \in C^{m,1}(\Omega)$. Then there exist constant C_κ independent of $\mathfrak{d}_\mathfrak{s}$ such that*

$$\left\|D^\kappa\varphi - D^\kappa\Upsilon^d_r\varphi\right\|_{L^2(\Omega)} \leq C_\kappa {\mathfrak{d}_\mathfrak{s}}^{m+1-|\kappa|}|\varphi|_{m,1}, \quad |\kappa| \leq 2.$$

Lemma 6.4.2 *Define $\Xi^{(n)}_h$ as*

$$\begin{aligned}\Big\langle \Xi^{(n)}_h, \upsilon\Big\rangle &= \frac{1}{\tau}\Big\langle U^{(n)}_h - U^{(n)}, \upsilon\Big\rangle + \frac{\epsilon_1}{2}\Big\langle\frac{\partial}{\partial x}(U^{(n)}_h - U^{(n)}), \frac{\partial\upsilon}{\partial x}\Big\rangle\\ &+ \frac{\epsilon_2}{2}\Big\langle\frac{\partial}{\partial y}(U^{(n)}_h - U^{(n)}), \frac{\partial\upsilon}{\partial y}\Big\rangle - \frac{1}{\tau}\Big\langle U^{(n-1)}_h - U^{(n-1)}, \upsilon\Big\rangle\\ &+ \frac{\epsilon_1}{2}\Big\langle\frac{\partial}{\partial x}(U^{(n-1)}_h - U^{(n-1)}), \frac{\partial\upsilon}{\partial x}\Big\rangle + \frac{\epsilon_2}{2}\Big\langle\frac{\partial}{\partial y}(U^{(n-1)}_h - U^{(n-1)}), \frac{\partial\upsilon}{\partial y}\Big\rangle\\ &- \frac{1}{2}\Big\langle(M - a^{(n)})(U^{(n)}_h - U^{(n)}), \upsilon\Big\rangle - \frac{1}{2}\Big\langle(M - a^{(n-1)})(U^{(n-1)}_h - U^{(n-1)}), \upsilon\Big\rangle.\end{aligned} \tag{6.4.1}$$

Then,

$$\| \Xi_h^{(n)} \|_{L^2(\Omega)} \leq C \mathfrak{d}_{\mathfrak{s}}{}^m.$$

Since $U^{(n)}$ is the temporal discrete approximation of the exact solution $u^{(n)}$, hence $u(x,t)$ satisfies

$$\begin{aligned}
&\Big\langle u^{(n)}, \upsilon \Big\rangle + \frac{\tau\epsilon_1}{2}\Big\langle \frac{\partial u^{(n)}}{\partial x}, \frac{\partial \upsilon}{\partial x} \Big\rangle + \frac{\tau\epsilon_2}{2}\Big\langle \frac{\partial u^{(n)}}{\partial y}, \frac{\partial \upsilon}{\partial y} \Big\rangle + \frac{\tau}{2}\Big\langle a^{(n)}u^{(n)}, \upsilon \Big\rangle \\
&- \frac{\tau}{2}\Big\langle F(u^{(n)}), \upsilon \Big\rangle = \Big\langle u^{(n-1)}, \upsilon \Big\rangle - \frac{\tau\epsilon_1}{2}\Big\langle \frac{\partial u^{(n-1)}}{\partial x}, \frac{\partial \upsilon}{\partial x} \Big\rangle \\
&- \frac{\tau\epsilon_2}{2}\Big\langle \frac{\partial u^{(n-1)}}{\partial y}, \frac{\partial \upsilon}{\partial y} \Big\rangle - \frac{\tau}{2}\Big\langle a^{(n-1)}u^{(n-1)}, \upsilon \Big\rangle + \frac{\tau}{2}\Big\langle F(u^{(n-1)}), \upsilon \Big\rangle - \tau\Big\langle \mathfrak{R}, \upsilon \Big\rangle,
\end{aligned} \tag{6.4.2}$$

where $\mathfrak{R}$ is the residual.

Theorem 6.4.3 *Let $u(x,t_n) = u^{(n)}$ be the exact solution of Eq.* (6.1.1) *and $U_h^{(n)}$ be the solution of the full discrete scheme* (6.2.8)*. Assume that $u(x,t) \in H^1(\Omega), \forall\ t \in\ [0,T]$, then the element-free Galerkin scheme converges with*

$$\Big\| e_h^{(n)} \Big\|_{H_w(\Omega)} \leq \mathcal{C}\big(\tau^2 + \mathfrak{d}_{\mathfrak{s}}^{\mathfrak{m}}\big),$$

in which $e_h^{(n)} = U_h^{(n)} - u^{(n)}$.

Proof Since the time-discrete solution $U^{(n)}$ and $u^{(n)}$ satisfies Eqs. (6.2.7) and (6.4.2) respectively, subtracting these equations, arrives at

$$\begin{aligned}
&\Big\langle U^{(n)} - u^{(n)}, \upsilon \Big\rangle + \frac{\tau\epsilon_1}{2}\Big\langle \frac{\partial}{\partial x}(U^{(n)} - u^{(n)}), \frac{\partial \upsilon}{\partial x} \Big\rangle + \frac{\tau\epsilon_2}{2}\Big\langle \frac{\partial}{\partial y}(U^{(n)} - u^{(n)}), \frac{\partial \upsilon}{\partial y} \Big\rangle \\
&+ \frac{\tau}{2}\Big\langle a^{(n)}(U^{(n)} - u^{(n)}), \upsilon \Big\rangle - \frac{\tau}{2}\Big\langle F(U^{(n)}) - F(u^{(n)}), \upsilon \Big\rangle = \Big\langle U^{(n-1)} - u^{(n-1)}, \upsilon \Big\rangle \\
&- \frac{\tau\epsilon_1}{2}\Big\langle \frac{\partial}{\partial x}(U^{(n-1)} - u^{(n-1)}), \frac{\partial \upsilon}{\partial x} \Big\rangle - \frac{\tau\epsilon_2}{2}\Big\langle \frac{\partial}{\partial y}(U^{(n-1)} - u^{(n-1)}), \frac{\partial \upsilon}{\partial y} \Big\rangle \\
&- \frac{\tau}{2}\Big\langle a^{(n-1)}(U^{(n-1)} - u^{(n-1)}), \upsilon \Big\rangle + \frac{\tau}{2}\Big\langle F(U^{(n-1)}) - F(u^{(n-1)}), \upsilon \Big\rangle + \tau\Big\langle \mathfrak{R}, \upsilon \Big\rangle, \\
&\upsilon \in V_h.
\end{aligned}$$

Then using mean value theorem, we have

$$\Big\langle U^{(n)}-u^{(n)},\upsilon\Big\rangle+\frac{\tau\epsilon_1}{2}\Big\langle\frac{\partial}{\partial x}(U^{(n)}-u^{(n)}),\frac{\partial\upsilon}{\partial x}\Big\rangle+\frac{\tau\epsilon_2}{2}\Big\langle\frac{\partial}{\partial y}(U^{(n)}-u^{(n)}),\frac{\partial\upsilon}{\partial y}\Big\rangle$$
$$\leq\Big\langle U^{(n-1)}-u^{(n-1)},\upsilon\Big\rangle-\frac{\tau\epsilon_1}{2}\Big\langle\frac{\partial}{\partial x}(U^{(n-1)}-u^{(n-1)}),\frac{\partial\upsilon}{\partial x}\Big\rangle$$
$$+\frac{\tau\epsilon_2}{2}\Big\langle\frac{\partial}{\partial y}(U^{(n-1)}-u^{(n-1)}),\frac{\partial\upsilon}{\partial y}\Big\rangle+\frac{\tau}{2}\Big\langle(M-a^{(n)})(U^{(n)}-u^{(n)}),\upsilon\Big\rangle$$
$$+\frac{\tau}{2}\Big\langle(M-a^{(n-1)})(U^{(n-1)}-u^{(n-1)}),\upsilon\Big\rangle+\tau\Big\langle\mathfrak{R},\upsilon\Big\rangle,$$

where $\max|F^{'}(x)|=M$.
Now, we can write

$$U^{(n)}-u^{(n)}=(U^{(n)}-U_h^{(n)})+(U_h^{(n)}-u^{(n)}),$$

we get

$$\Big\langle U_h^{(n)}-u^{(n)},\upsilon\Big\rangle+\frac{\tau\epsilon_1}{2}\Big\langle\frac{\partial}{\partial x}(U_h^{(n)}-u^{(n)}),\frac{\partial\upsilon}{\partial x}\Big\rangle+\frac{\tau\epsilon_2}{2}\Big\langle\frac{\partial}{\partial y}(U_h^{(n)}-u^{(n)}),\frac{\partial\upsilon}{\partial y}\Big\rangle$$
$$\leq\Big\langle U_h^{(n-1)}-u^{(n-1)},\upsilon\Big\rangle-\frac{\tau\epsilon_1}{2}\Big\langle\frac{\partial}{\partial x}(U_h^{(n-1)}-u^{(n-1)}),\frac{\partial\upsilon}{\partial x}\Big\rangle$$
$$+\frac{\tau\epsilon_2}{2}\Big\langle\frac{\partial}{\partial y}(U_h^{(n-1)}-u^{(n-1)}),\frac{\partial\upsilon}{\partial y}\Big\rangle+\frac{\tau}{2}\Big\langle(M-a^{(n)})(U_h^{(n)}-u^{(n)}),\upsilon\Big\rangle$$
$$+\frac{\tau}{2}\Big\langle(M-a^{(n-1)})(U_h^{(n-1)}-u^{(n-1)}),\upsilon\Big\rangle+\Big\langle U_h^{(n)}-U^{(n)},\upsilon\Big\rangle$$
$$+\frac{\tau\epsilon_1}{2}\Big\langle\frac{\partial}{\partial x}(U_h^{(n)}-U^{(n)}),\frac{\partial\upsilon}{\partial x}\Big\rangle+\frac{\tau\epsilon_2}{2}\Big\langle\frac{\partial}{\partial y}(U_h^{(n)}-U^{(n)}),\frac{\partial\upsilon}{\partial y}\Big\rangle$$
$$-\Big\langle U_h^{(n-1)}-U^{(n-1)},\upsilon\Big\rangle+\frac{\tau\epsilon_1}{2}\Big\langle\frac{\partial}{\partial x}(U_h^{(n-1)}-U^{(n-1)}),\frac{\partial\upsilon}{\partial x}\Big\rangle$$
$$+\frac{\tau\epsilon_2}{2}\Big\langle\frac{\partial}{\partial y}(U_h^{(n-1)}-U^{(n-1)}),\frac{\partial\upsilon}{\partial y}\Big\rangle-\frac{\tau}{2}\Big\langle(M-a^{(n)})(U_h^{(n)}-U^{(n)}),\upsilon\Big\rangle$$
$$-\frac{\tau}{2}\Big\langle(M-a^{(n-1)})(U_h^{(n-1)}-U^{(n-1)}),\upsilon\Big\rangle+\tau\Big\langle\mathfrak{R},\upsilon\Big\rangle. \tag{6.4.3}$$

Assuming

$$e_h^{(n)}=U_h^{(n)}-u^{(n)},\quad \rho_h^{(n)}=U_h^{(n)}-U^{(n)},$$

then, relation (6.4.3) can be rewritten as

$$\begin{aligned}
&\Big\langle e_h^{(n)}, \upsilon \Big\rangle + \frac{\tau\epsilon_1}{2}\Big\langle \frac{\partial e_h^{(n)}}{\partial x}, \frac{\partial \upsilon}{\partial x}\Big\rangle + \frac{\tau\epsilon_2}{2}\Big\langle \frac{\partial e_h^{(n)}}{\partial y}, \frac{\partial \upsilon}{\partial y}\Big\rangle \leq \Big\langle e_h^{(n-1)}, \upsilon \Big\rangle \\
&\quad - \frac{\tau\epsilon_1}{2}\Big\langle \frac{\partial e_h^{(n-1)}}{\partial x}, \frac{\partial \upsilon}{\partial x}\Big\rangle + \frac{\tau\epsilon_2}{2}\Big\langle \frac{\partial e_h^{(n-1)}}{\partial y}, \frac{\partial \upsilon}{\partial y}\Big\rangle + \frac{\tau}{2}\Big\langle (M - a^{(n)})e_h^{(n)}, \upsilon\Big\rangle \\
&\quad + \frac{\tau}{2}\Big\langle (M - a^{(n-1)})e_h^{(n-1)}, \upsilon\Big\rangle + \Big\langle \rho_h^{(n)}, \upsilon\Big\rangle + \frac{\tau\epsilon_1}{2}\Big\langle \frac{\partial}{\partial x}\rho_h^{(n)}, \frac{\partial \upsilon}{\partial x}\Big\rangle \\
&\quad + \frac{\tau\epsilon_2}{2}\Big\langle \frac{\partial}{\partial y}\rho_h^{(n)}, \frac{\partial \upsilon}{\partial y}\Big\rangle - \Big\langle \rho_h^{(n-1)}, \upsilon\Big\rangle \\
&\quad + \frac{\tau\epsilon_1}{2}\Big\langle \frac{\partial}{\partial x}\rho_h^{(n-1)}, \frac{\partial \upsilon}{\partial x}\Big\rangle + \frac{\tau\epsilon_2}{2}\Big\langle \frac{\partial}{\partial x}\rho_h^{(n-1)}, \frac{\partial \upsilon}{\partial y}\Big\rangle \\
&\quad - \frac{\tau}{2}\Big\langle (M - a^{(n)})\rho_h^{(n)}, \upsilon\Big\rangle - \frac{\tau}{2}\Big\langle (M - a^{(n-1)})\rho_h^{(n-1)}, \upsilon\Big\rangle + \tau\Big\langle \mathfrak{R}, \upsilon\Big\rangle.
\end{aligned}$$

Thus, using the definition (6.4.1), we have

$$\begin{aligned}
&\Big\langle e_h^{(n)}, \upsilon \Big\rangle + \frac{\tau\epsilon_1}{2}\Big\langle \frac{\partial (e_h^{(n)})}{\partial x}, \frac{\partial \upsilon}{\partial x}\Big\rangle + \frac{\tau\epsilon_2}{2}\Big\langle \frac{\partial (e_h^{(n)})}{\partial y}, \frac{\partial \upsilon}{\partial y}\Big\rangle \leq \Big\langle U_h^{(n-1)} - u^{(n-1)}, \upsilon \Big\rangle \\
&\quad - \frac{\tau\epsilon_1}{2}\Big\langle \frac{\partial (e_h^{(n-1)})}{\partial x}, \frac{\partial \upsilon}{\partial x}\Big\rangle + \frac{\tau\epsilon_2}{2}\Big\langle \frac{\partial (e_h^{(n-1)})}{\partial y}, \frac{\partial \upsilon}{\partial y}\Big\rangle + \frac{\tau}{2}\Big\langle (M - a^{(n)})e_h^{(n)}, \upsilon\Big\rangle \\
&\quad + \frac{\tau}{2}\Big\langle (M - a^{(n-1)})e_h^{(n-1)}, \upsilon\Big\rangle + \tau\Big\langle \Xi_h^{(n)}, \upsilon\Big\rangle + \tau\Big\langle \mathfrak{R}, \upsilon\Big\rangle.
\end{aligned}$$

Now we set $\upsilon = e_h^{(n)}$ which gives

$$\begin{aligned}
&\Big\langle e_h^{(n)}, e_h^{(n)} \Big\rangle + \frac{\tau\epsilon_1}{2}\Big\langle \frac{\partial e_h^{(n)}}{\partial x}, \frac{\partial e_h^{(n)}}{\partial x}\Big\rangle + \frac{\tau\epsilon_2}{2}\Big\langle \frac{\partial e_h^{(n)}}{\partial y}, \frac{\partial e_h^{(n)}}{\partial y}\Big\rangle \leq \Big\langle e_h^{(n-1)}, e_h^{(n)} \Big\rangle \\
&\quad - \frac{\tau\epsilon_1}{2}\Big\langle \frac{\partial e_h^{(n-1)}}{\partial x}, \frac{\partial e_h^{(n)}}{\partial x}\Big\rangle + \frac{\tau\epsilon_2}{2}\Big\langle \frac{\partial e_h^{(n-1)}}{\partial y}, \frac{\partial e_h^{(n)}}{\partial y}\Big\rangle + \frac{\tau}{2}\Big\langle (M - a^{(n)})e_h^{(n)}, e_h^{(n)}\Big\rangle \\
&\quad + \frac{\tau}{2}\Big\langle (M - a^{(n-1)})e_h^{(n-1)}, e_h^{(n)}\Big\rangle + \tau\Big\langle \Xi_h^{(n)}, e_h^{(n)}\Big\rangle + \tau\Big\langle \mathfrak{R}, e_h^{(n)}\Big\rangle.
\end{aligned}$$

By employing Cauchy-Schwarz inequality, we obtain

$$\frac{1}{2}\Big\|e_h^{(n)}\Big\|^2_{L^2(\Omega)}+\frac{\tau\epsilon_1}{4}\Big\|\frac{\partial e_h^{(n)}}{\partial x}\Big\|^2_{L^2(\Omega)}+\frac{\tau\epsilon_2}{4}\Big\|\frac{\partial e_h^{(n)}}{\partial y}\Big\|^2_{L^2(\Omega)}\leq\frac{1}{2}\Big\|e_h^{(n-1)}\Big\|^2_{L^2(\Omega)}$$
$$+\frac{\tau\epsilon_1}{4}\Big\|\frac{\partial e_h^{(n-1)}}{\partial x}\Big\|^2_{L^2(\Omega)}+\frac{\tau\epsilon_2}{4}\Big\|\frac{\partial e_h^{(n-1)}}{\partial y}\Big\|^2_{L^2(\Omega)}+\Big(\frac{3}{2}|M-\alpha|+4\Big)\frac{\tau}{2}\Big\|e_h^{(n)}\Big\|^2_{L^2(\Omega)}$$
$$+|M-\alpha|\frac{\tau}{4}\Big\|e_h^{(n-1)}\Big\|^2_{L^2(\Omega)}+\frac{\tau}{2}\Big\|\Xi_h^{(n)}\Big\|^2_{L^2(\Omega)}+\frac{\tau}{2}\Big\|\mathfrak{R}\Big\|^2_{L^2(\Omega)}.$$

Define

$$\Big\|e_h^{(n)}\Big\|^2_{H_w(\Omega)}=\frac{1}{2}\Big\|e_h^{(n)}\Big\|^2_{L^2(\Omega)}+\frac{\tau\epsilon_1}{4}\Big\|\frac{\partial e_h^{(n)}}{\partial x}\Big\|^2_{L^2(\Omega)}+\frac{\tau\epsilon_2}{4}\Big\|\frac{\partial e_h^{(n)}}{\partial y}\Big\|^2_{L^2(\Omega)},$$

we get

$$\Big\|e_h^{(n)}\Big\|^2_{H_w(\Omega)}\leq\Big\|e_h^{(n-1)}\Big\|^2_{H_w(\Omega)}+\Big(3|M-\alpha|+8\Big)\frac{\tau}{2}\Big\|e_h^{(n)}\Big\|^2_{H_w(\Omega)}+|M-\alpha|\frac{\tau}{2}\Big\|e_h^{(n-1)}\Big\|^2_{H_w(\Omega)}$$
$$+\frac{\tau}{2}\Big\|\Xi_h^{(n)}\Big\|^2_{L^2(\Omega)}+\frac{\tau}{2}\Big\|\mathfrak{R}\Big\|^2_{L^2(\Omega)}.$$

Writing the above relation at all time-levels and summing up, we get

$$\sum_{i=1}^{n}\Big\|e_h^{(i)}\Big\|^2_{H_w(\Omega)}\leq\sum_{i=1}^{n}\Big\|e_h^{(i-1)}\Big\|^2_{H_w(\Omega)}+\Big(3|M-\alpha|+8\Big)\frac{\tau}{2}\sum_{i=1}^{n}\Big\|e_h^{(i)}\Big\|^2_{H_w(\Omega)}$$
$$+|M-\alpha|\frac{\tau}{2}\sum_{i=1}^{n}\Big\|e_h^{(i-1)}\Big\|^2_{H_w(\Omega)}+\frac{\tau}{2}\sum_{i=1}^{n}\Big\|\Xi_h^{(i)}\Big\|^2_{L^2(\Omega)}+\frac{\tau}{2}\sum_{i=1}^{n}\Big\|\mathfrak{R}\Big\|^2_{L^2(\Omega)}.$$

Simplifying furthermore, we can get

$$\Big\|e_h^{(n)}\Big\|^2_{H_w(\Omega)}\leq\underbrace{\Big\|e_h^{(0)}\Big\|^2_{H_w(\Omega)}}_{=0}+\Big(|M-\alpha|+2\Big)2\tau\sum_{i=1}^{n}\Big\|e_h^{(i)}\Big\|^2_{H_w(\Omega)}+\frac{\tau}{2}\sum_{i=1}^{n}\Big\|\Xi_h^{(i)}\Big\|^2_{L^2(\Omega)}$$
$$+\frac{\tau n}{2}\Big\|\mathfrak{R}\Big\|^2_{L^2(\Omega)}.$$

Employing Gronwall's Lemma, we achieve

$$\begin{aligned}\left\|e_h^{(n)}\right\|^2_{H_w(\Omega)} &\leq \Big[\frac{\tau}{2}\Big(\sum_{i=1}^{n}\left\|\Xi_h^{(i)}\right\|^2_{L^2(\Omega)} + n\left\|\mathfrak{R}\right\|^2_{L^2(\Omega)}\Big)\Big]\exp\Big(2n\tau(|M-\alpha|+2)\Big)\\ &\leq \Big[\frac{T}{2}({\mathfrak{d}_{\mathfrak{s}}}^m+\tau^2)^2\Big]\exp\Big(2T(|M-\alpha|+2)\Big)\\ &\leq \mathcal{C}({\mathfrak{d}_{\mathfrak{s}}}^m+\tau^2)^2.\end{aligned}$$

This completes the proof.

6.5 Numerical results and discussions

In this Section, numerical studies have been carried out for two examples to check the robustness and efficiency of the proposed scheme. The errors are presented, and the accuracy of the proposed method has been demonstrated. Maximum relative errors have been estimated using

$$e_{i,j}^{N,\tau} = \Big|\frac{u(\mathbf{x}_i,t_j)-U_h(\mathbf{x}_i,t_j)}{u(\mathbf{x}_i,t_j)}\Big| \text{ and } E_{\epsilon}^{N,\tau} = \max_{i,j} e_{i,j}^{N,\tau},$$

where $u(\mathbf{x},t)$ and $U_h(\mathbf{x},t)$ denote the exact and the computed EFG solutions respectively.

Example 6.5.1 *For the first example, we have considered the following singularly perturbed time-dependent problem:*

$$\begin{aligned}\frac{\partial u}{\partial t} - \epsilon_1\frac{\partial^2 u}{\partial x^2} - \epsilon_2\frac{\partial^2 u}{\partial y^2} &= F(u), \qquad (6.5.1)\\ u(x,y,0) &= \exp(x/\sqrt{\epsilon_1}+y/\sqrt{\epsilon_2}).\end{aligned}$$

The function $F(u)$ is taken so that the exact solution of Eq. (6.5.1) *becomes*

$$u(x,y,t) = \exp(x/\sqrt{\epsilon_1}+y/\sqrt{\epsilon_2}+2t).$$

Example 6.5.2 *For the second example, we examine the following non-*

linear parabolic equation:

$$\frac{\partial u}{\partial t} = \frac{\epsilon_1}{2}\frac{\partial^2 u}{\partial x^2} + \frac{\epsilon_2}{2}\frac{\partial^2 u}{\partial y^2} + 6u(1-u),$$

with initial condition

$$u(x, y, 0) = \frac{1}{(1 + \exp(x/\sqrt{\epsilon_1} + y/\sqrt{\epsilon_2}))^2}.$$

The exact solution of this problem is not known.

For Example 6.5.1, the maximum relative errors have been tabulated in Table 6.1. Since the exact solution is not known for Example 6.5.2, the L_∞ errors, given in Table 6.2, have been calculated using the double mesh principle. From these Tables, we can clearly conclude that the proposed EFG scheme produces very good accurate results and the scheme is reliable and efficient enough to capture the solution nicely. The numerical convergence of the EFG technique can also be clearly observed from these Tables.

Table 6.1: Maximum relative errors for Example 6.5.1 for different values of ϵ at $t = 1.0$.

ϵ	$N = 4$ $M = 4$	$N = 16$ $M = 4$	$N = 16$ $M = 16$	$N = 32$ $M = 8$	$N = 64$ $M = 16$	$N = 64$ $M = 64$
2^{-2}	1.92×10^{-3}	9.26×10^{-4}	1.38×10^{-4}	2.20×10^{-4}	5.65×10^{-5}	6.51×10^{-6}
2^{-4}	6.17×10^{-3}	2.75×10^{-3}	4.41×10^{-4}	9.52×10^{-4}	2.32×10^{-4}	2.72×10^{-5}
2^{-6}	4.50×10^{-2}	3.27×10^{-2}	9.45×10^{-3}	3.33×10^{-3}	6.25×10^{-4}	4.38×10^{-5}
2^{-8}	5.35×10^{-2}	3.35×10^{-2}	1.22×10^{-2}	3.38×10^{-3}	1.81×10^{-3}	4.38×10^{-4}
2^{-10}	5.31×10^{-2}	3.37×10^{-2}	1.28×10^{-2}	3.38×10^{-3}	1.88×10^{-3}	4.38×10^{-4}

Table 6.2: Maximum absolute errors for Example 6.5.2 for different values of ϵ at $t = 1.0$.

ϵ	$N = 16$ $M = 4$	$N = 32$ $M = 8$	$N = 64$ $M = 16$	$N = 32$ $M = 16$	$N = 64$ $M = 32$	$N = 64$ $M = 64$
2^{-2}	3.32×10^{-3}	8.17×10^{-4}	2.08×10^{-4}	2.45×10^{-4}	6.11×10^{-5}	7.82×10^{-6}
2^{-4}	8.19×10^{-2}	9.39×10^{-3}	2.30×10^{-3}	2.71×10^{-4}	6.76×10^{-4}	8.96×10^{-5}
2^{-6}	8.14×10^{-2}	4.09×10^{-2}	9.38×10^{-3}	1.10×10^{-3}	3.27×10^{-3}	3.89×10^{-4}
2^{-8}	8.14×10^{-2}	4.08×10^{-2}	8.22×10^{-2}	2.28×10^{-2}	3.85×10^{-3}	1.80×10^{-3}
2^{-10}	8.14×10^{-2}	4.08×10^{-2}	8.22×10^{-2}	2.38×10^{-2}	3.85×10^{-3}	1.80×10^{-3}

To observe the effect of the singular perturbation parameter ϵ on the solution computed using EFG technique, the EFG solutions have been plotted in Figs. 6.1 and 6.4 by fixing the variable $y = 0.5$ in the solution. One can easily notice how the boundary layers arise in the solution as $\epsilon \to 0$. In order to depict the clear effect, in other plots also y has been fixed as 0.5.

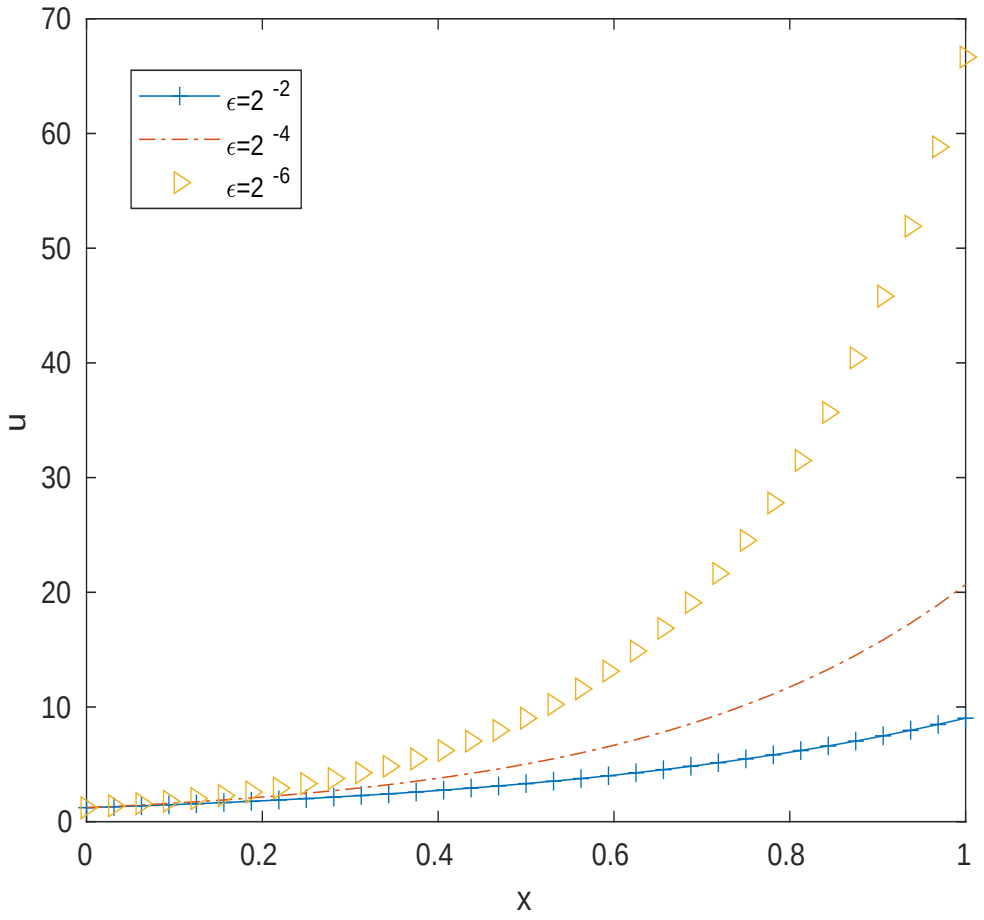

Figure 6.1: Epsilon-effect for Example 6.5.1 for $y = 0.5$, $N = 32$ and $t = 0.1$.

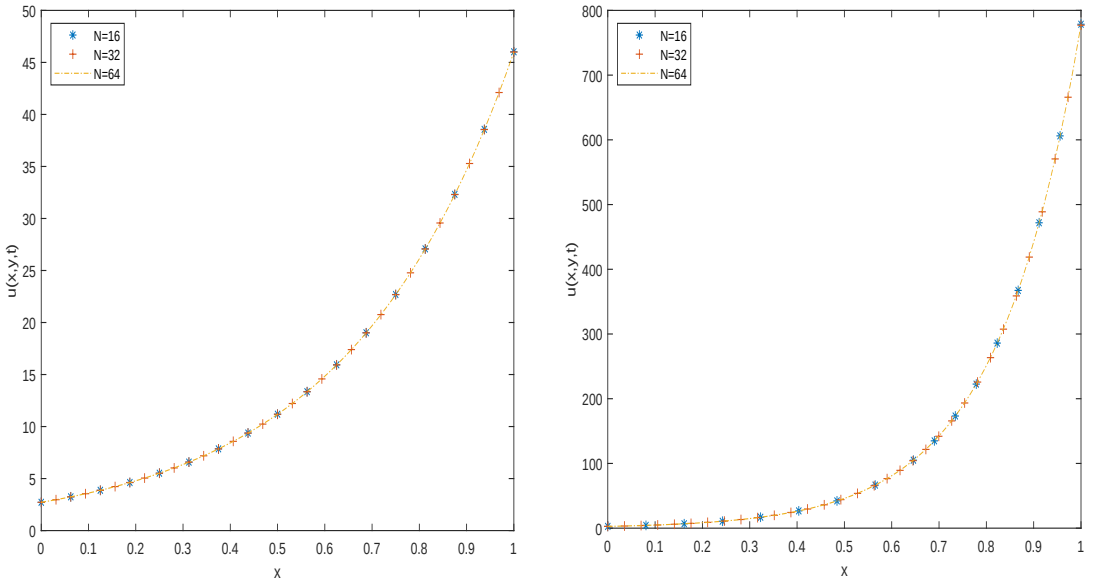

Figure 6.2: Grid validation for Example 6.5.1 for $\epsilon = 2^{-3}$ and $\epsilon = 2^{-5}$ at $t = 0.5$.

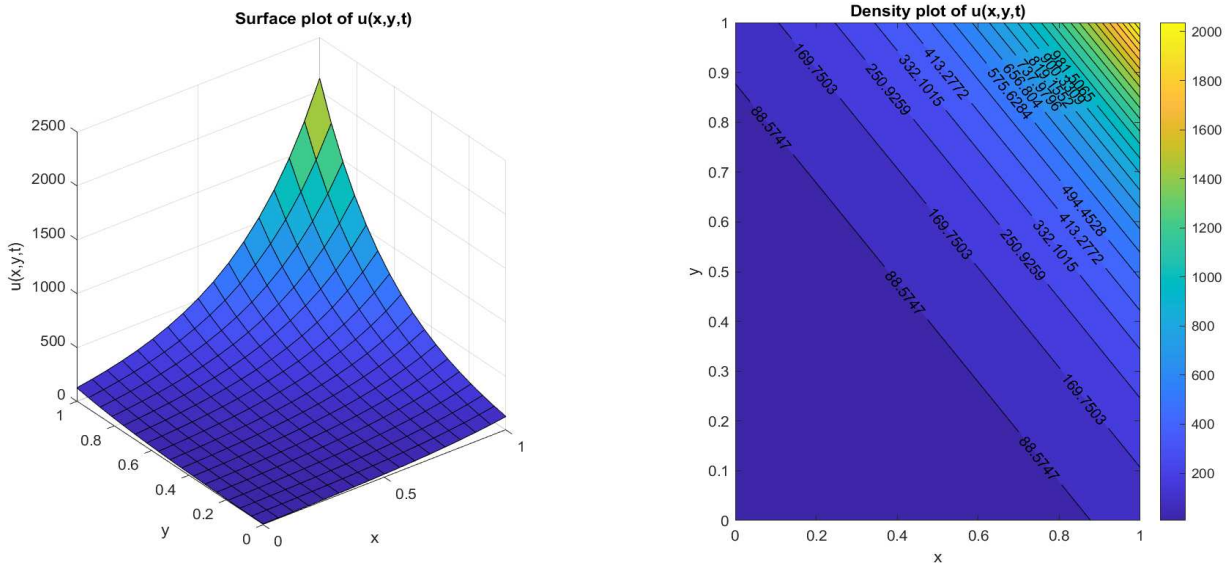

Figure 6.3: Numerical results for Example 6.5.1 for $\epsilon = 2^{-2}$, $N = M = 16$, at time level $t = 1.0$.

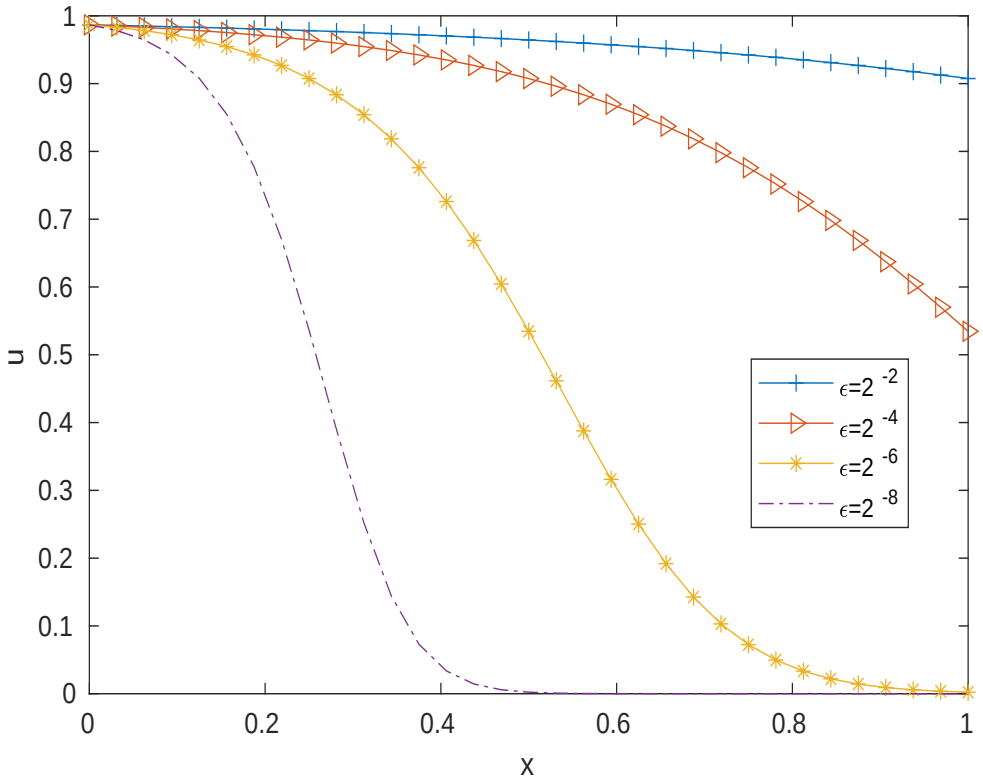

Figure 6.4: Epsilon-effect for Example 6.5.2 for $y = 0.5$, $N = 32$ and $t = 1.0$.

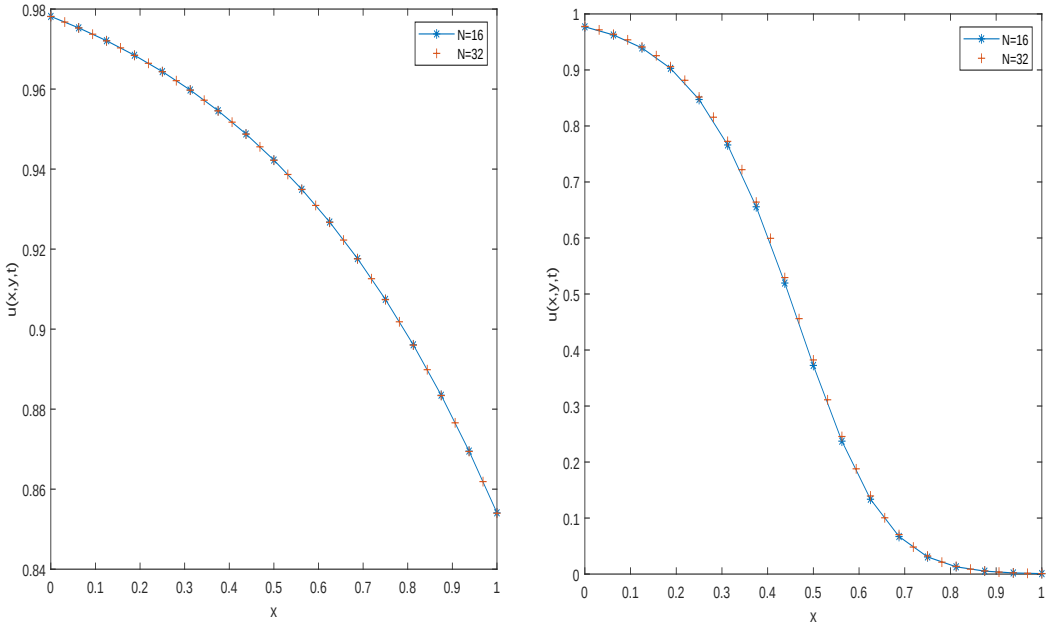

Figure 6.5: Grid validation for Example 6.5.2 for $\epsilon = 2^{-2}$ and $\epsilon = 2^{-8}$ at $t = 0.9$.

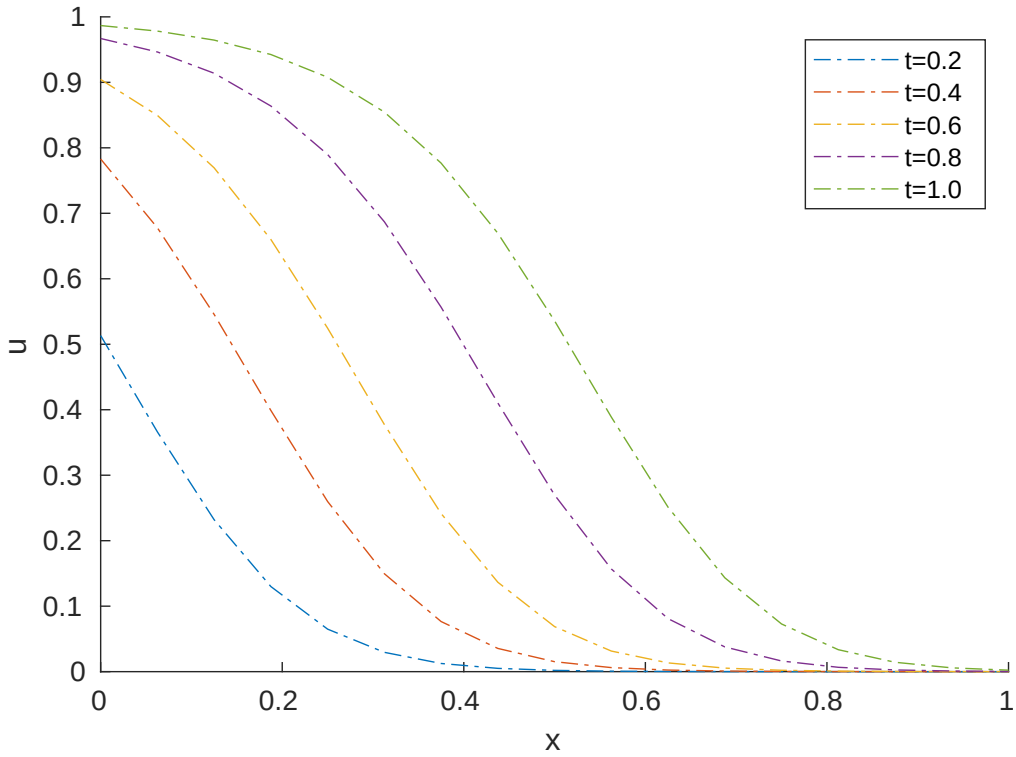

Figure 6.6: Time effect on EFG solution of Example 6.5.2 for $y = 0.5$, $N = 16$ and $\epsilon = 2^{-6}$.

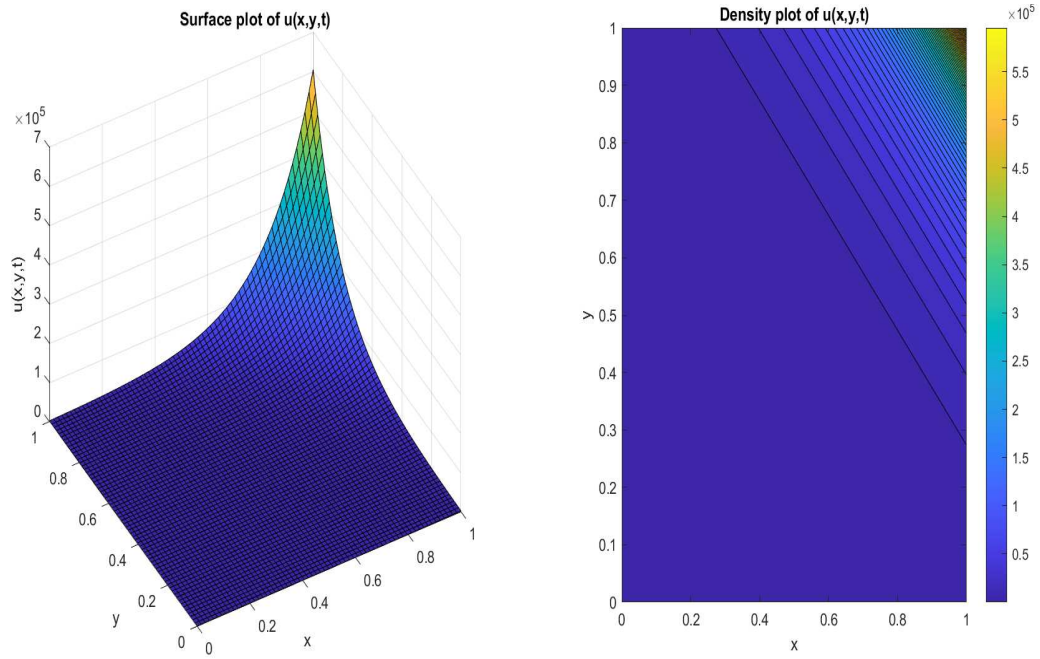

Figure 6.7: Numerical results for Example 6.5.1 for $\epsilon = 2^{-6}$, $N = M = 64$, at time level $t = 1.0$.

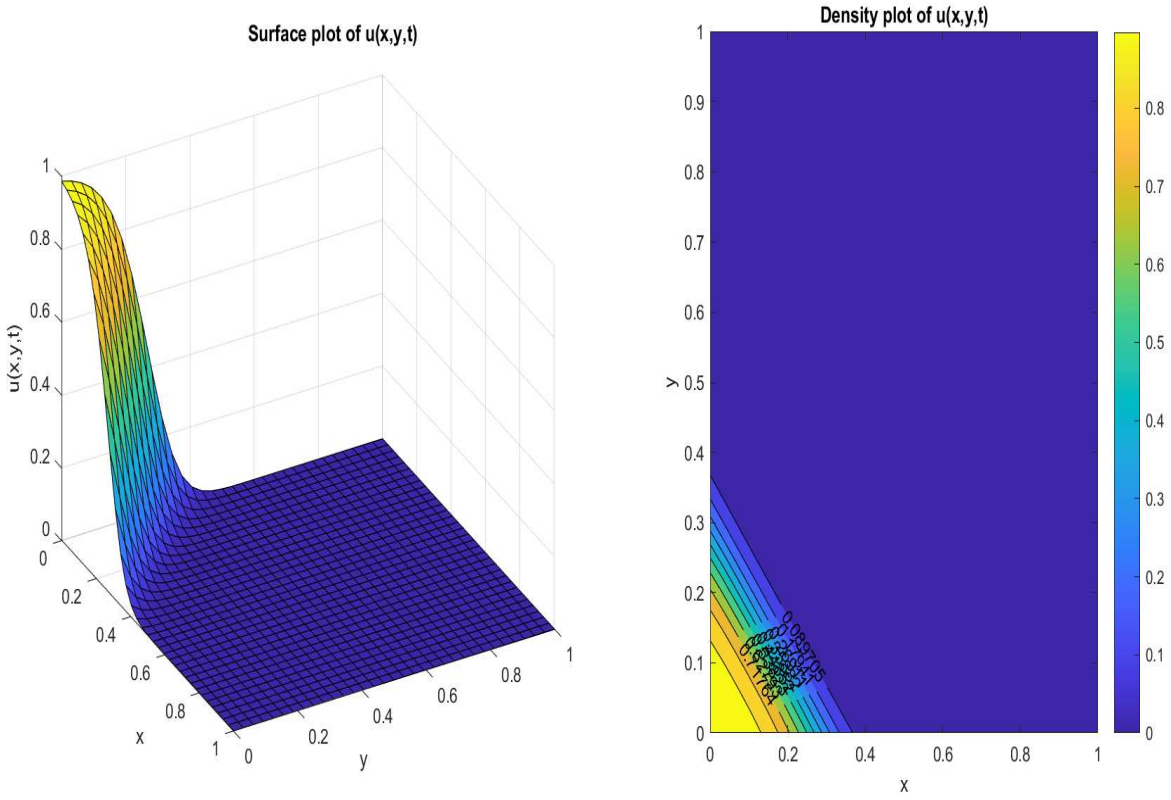

Figure 6.8: Numerical results for Example 6.5.2 for $\epsilon = 2^{-8}$, $N = 32$, at time level $t = 1.0$.

Grid validity has been shown via Figs. 6.2 and 6.5. One can see that even with very less number of nodes, the proposed EFG scheme provides very nice solution and no instability is present in the EFG solutions. The temporal effect on the solution have been presented in Fig. 6.6. The capability of the proposed EFG method to capture the sharp boundary layers with different number of nodes can clearly be observed from these Figures. Figs. 6.3-6.8 demonstrate the graphs of numerical solutions at the final time level $t = 1$. Figs. 6.3-6.7 clearly shows how the EFG scheme is capable of capturing even very large solutions with values like 6×10^5 by considering very small grid size of 64 nodes in each $x-$ and y-directions. From the results given in Tables 6.1-6.2 and Figs. 6.1-6.8, the applicability and accuracy of the proposed scheme can clearly be verified.

6.6 Conclusion

In this Chapter, the proposed EFG scheme has been extended to approximate the solution of two-dimensional singularly perturbed time-dependent reaction−diffusion problems. The algorithm uses the EFG scheme to discretize the spatial terms and an implicit Crank-Nicolson method to discretize the temporal derivative. The stability of the semi-discrete scheme has been discussed. The full-discrete scheme is shown to be ϵ-uniform convergent with order of convergence $\mathcal{O}(\tau^2 + \mathfrak{d}_{\mathfrak{s}}{}^m)$, where τ is the time-step and $\mathfrak{d}_{\mathfrak{s}}$ is the size of the influence domain. The numerical results validate the robustness and efficiency of the proposed EFG scheme. The scheme is capable of capturing the solutions with very large sudden changes in very small regions. The error tables clearly depict the numerical convergence of the proposed scheme. To conclude, the EFG technique is uniformly convergent with respect to the singular perturbation parameter and is efficient enough in capturing the sharp boundary layers arising in the solutions of the two-dimensional reaction-diffusion problems. In the next Chapter, the proposed EFG scheme has been tested on mathematical models arising in the field of mathematical finance.

Chapter 7

Numerical investigation of two-dimensional singularly perturbed Black-Scholes model using element-free Galerkin technique

7.1 Introduction

Mathematical modeling [73–75, 90, 96, 114, 209, 227] of financial market instruments has become a rapidly increasing study subject for both the mathematicians and the people with financial domain. Across major economies, financial derivatives are heavily used for transactional and investment purposes. Financial markets can be broadly classified into three categories: equity, debt and derivatives market. Among derivative instruments, options are the most commonly used derivative securities. An option gives the right to the holder to buy or sell the underlying asset at a contractually agreed price (called the exercise price or strike price) within a prescribed time period. While the seller of the option has the contractual obligation to fulfil this demand of the buyer.

Options are divided into call option(right to buy)and put option(right to sell). Among options, the European and American options are the widely used. Under the European options, the holder of the option can exercise his right only on the prescribed expiration date. In contrast, under the American options, the holder of the option can exercise his right at any time before the expiration date.

The Black-Scholes (B-S) equation is the well-known method to estimate the option pricing in the financial world. As a result, it has become an extensive

elementary subject for studying financial engineering and financial theory. In 1973, Black and Scholes [26] published the B-S model and option pricing formula in their paper to analyze the behavior of financial derivatives in the market. Their methodology is based on hedging and minimizing option pricing risk while buying or selling underlying assets. The European call option value of this model fluctuates with time and stock price. Moreover, the price of assets is modeled by a geometric Brownian motion with a constant drift and volatility term.

Various approaches have been explored for financial derivatives in the past few years. It is well known that there are some analytical techniques to obtain the solutions of many significant derivatives; and hence, the approximation procedures have been followed to find their estimation. To achieve this objective, various numerical approximation methods have been developed in the literature [3, 27, 29, 37, 64, 95, 182, 226].

In many situations, obtaining an explicit analytical solution to the generalized B-S equation is absurd. Thus, efficient and reliable numerical techniques are required to provide a wide variety of derivative securities. The lattice approach [48] has been suggested as the first numerical approach for the B-S equations. After that some other approximation techniques have been developed in the financial literature which are extensively used by researchers and option traders such as finite-difference technique [14, 47, 89, 192, 215, 219, 226], finite volume method, cubic B-spline collocation method [106, 107], homotopy perturbation method [216] etc.

In the present work, we are more interested in the European call option because of the benefits of European option pricing regarding trade at a discount. We have considered the two-dimensional B-S equation, known as the singularly perturbed B-S problem, in a dimensionless variable with two small parameters multiplying with the highest order space derivative terms. Thin layer phenomena arises in SPP, known as boundary layers, forming an essential subclass of mathematical problems with nonsmooth

solutions. Very few mathematicians and scientists have put efforts toward the singularly perturbed B-S model. For instance, Fouque et al. [75] presented a singular perturbation analysis of stochastic volatility pricing PDE and dealt with the non-smoothness of the payoff function inherent to option pricing. Li et al. [133,134] employed a parameter-uniform method for singularly perturbed parabolic equation modeling B-S equation with boundary layers. Therefore, we need to adopt some superior numerical techniques to capture these boundary layers when $\epsilon \to 0$.

So far, none of the mesh-free methods has been applied to solve the two-dimensional singularly perturbed B-S equation. The main motive of the present study is to introduce a robust and efficient numerical approach known as the element-free Galerkin (EFG) method to capture the non-smooth solutions of the singularly perturbed B-S equation. Due to absence of nodal connectivity, domain discretization can be achieved efficiently and quickly. The shape functions has been constructed by using moving least-square (MLS) approximation. The temporal discretization has been carried out by using the implicit Crank-Nicolson method before spatial discretization. Stability and convergence analysis of semi- and full-discrete schemes for the two-dimensional problem have been analyzed in L^2 and H^1 spaces.

The Chapter is organized as follows:
In Section 7.2, the formulation of singularly perturbed B-S equation in one and two dimensions has been explained. The EFG scheme and its convergence analysis has been addressed in Section 7.3. The effectiveness and robustness of the proposed method have been exhibited through numerical results in Section 7.4. Certain conclusions based on the present study are finally discussed in Section 7.5

7.2 Modeling of singularly perturbed Black-Scholes equation

In this Section, we will present the formulation of one-dimensional Black-Scholes (B-S) model followed by the formulation of the model in two-dimensions.

7.2.1 Formulation of one-dimensional Black-Scholes model

In this subsection, we will discuss the Black-Scholes (B-S) model in one-dimension which is based on the principle of hedging, and focus on eliminating risks associated with the volatility of underlying assets and stock option. The generalized B-S equation governing European call option $C(S,t)$ for asset price S at time t is given as

$$\frac{\partial C(S,t)}{\partial t}+\frac{1}{2}\sigma^2(S,t)S^2\frac{\partial^2 C(S,t)}{\partial S^2}+r(S,t)S\frac{\partial C(S,t)}{\partial S}-r(S,t)C(S,t)=0, \quad (S,t)\in\mathbb{R}^+\times(0,T), \tag{7.2.1}$$

equipped with the terminal and boundary conditions

$$C(S,0)=\max(S-E,0), \quad S\in\mathbb{R}^+, \tag{7.2.2}$$

$$C(0,t)=0; \quad C(S,t)\sim S \; for \; S\to\infty^+, \quad t\in[0,T]. \tag{7.2.3}$$

In the above expression, $\sigma(S,t)>0$ denotes the volatility rate of the underlying asset; T, the maturity time; E symbolizes the exercise price and $r(S,t)>0$ is the risk-free interest rate.
Eq. (7.2.1)-(7.2.3) represents an option pricing formula for European call option together with the following assumptions

- 'S' supports stochastic differential equation named as geometric Brownian motion i.e. $dS=\mu S d\tau+\sigma S dw$, in where μ is known as trend or

drift rate and w is increment of standard Brownian motion.

- The trend μ, used to compute the average rate of growth of the asset price, the volatility σ of underlying asset, and the risk-free interest rate r, used to evaluate the standard deviation of the returns, are known and constants for $0 \leq \tau \leq T$. No dividends are paid in that time period.

- The frictionless market.

- No arbitrage: There are no arbitrage opportunities of making a risk-less profit.

The market is complete under these hypothesis.
Here, we assume that $\sigma(S,t)$ and $r(S,t)$ are sufficiently smooth and bounded on the domain. If we consider σ and r as constants, Eqs. (7.2.1)-(7.2.3) becomes the classical B-S model whose existence and uniqueness are given by [77, 126].
The present B-S model is de-generated when $S \to 0$ and is also backward-in-time. To transform Eqs. (7.2.1)-(7.2.3) into non-degenerate and forward-in-time, we employ the transformations $S = \exp(x)$ and $t = T - \tau$, i.e.

$$x = \ln(S), \quad \tau = T - t.$$

Then the transformed equation becomes

$$\frac{\partial \widetilde{C}}{\partial \tau} = \frac{1}{2}\widehat{\sigma}^2(x,\tau)\frac{\partial^2 \widetilde{C}}{\partial x^2} + (\widehat{r}(x,\tau) - \frac{1}{2}\widehat{\sigma}^2(x,\tau))\frac{\partial \widetilde{C}}{\partial x} - \widehat{r}(x,\tau)\widetilde{C}; \quad (x,\tau) \in \mathbb{R} \times (0,T), \tag{7.2.4}$$

together with the initial and boundary conditions

$$\widetilde{C}(x,0) = \max(e^x - E, 0), \quad x \in \mathbb{R}$$
$$\widetilde{C}(x,\tau) = 0 \; as \; x \to -\infty, t \in [0,T],$$

where

$$\widetilde{C}(x,\tau) = C(S,t) = C(e^x,\tau),$$
$$\widetilde{\sigma}(x,\tau) = \sigma(S,t) = \sigma(e^x,\tau),$$
$$\widetilde{r}(x,\tau) = r(S,t) = r(e^x,\tau).$$

In order to remove the complexity during numerical analysis, we need to define (7.2.4) on truncated domain $\Omega = (x_{\min}, x_{\max})\times(0,T)$ where $x_{\min},\ x_{\max}$ are suitably chosen real numbers so that they do not effect the option price. Therefore, we consider the problem as

$$\frac{\partial U}{\partial \tau} = \frac{1}{2}\widehat{\sigma^2}(x,\tau)\frac{\partial^2 U(x,\tau)}{\partial x^2} + (\widehat{r}(x,\tau) - \frac{1}{2}\widehat{\sigma}^2(x,\tau))\frac{\partial U(x,\tau)}{\partial x} - \widehat{r}(x,\tau)U(x,\tau), \quad (x,\tau)\in\Omega, \tag{7.2.5}$$

with initial and boundary conditions

$$U(x,0) = \max(e^x - E, 0), \quad x \in (x_{\min}, x_{\max}), \tag{7.2.6}$$
$$U(x_{\min},\tau) = 0, \quad \tau \in [0,T], \tag{7.2.7}$$
$$U(x_{\max},\tau) = e^{\max} - Ee^{-\int_0^\tau \widehat{r}(x_{\max},s)ds}, \quad \tau\in[0,T]. \tag{7.2.8}$$

The boundary conditions are chosen according to [219]. The existence and uniqueness of classical solution of Eqs. (7.2.5)-(7.2.8) are given in [77, 126]. Thus, the final one-dimensional B-S model is given by rewriting Eqs. (7.2.5)-(7.2.8) on the truncated region $\Omega = \Omega_x \times \Omega_t = (x_{\min}, x_{\max}) \times (0,T)$ as:

$$LU(x,\tau) \equiv \left\{\frac{\partial}{\partial\tau} - \epsilon\frac{\partial^2}{\partial x^2} - \alpha\frac{\partial}{\partial x} - r\right\}U(x,\tau) = 0, \quad (x,\tau)\in\Omega,$$

with initial and boundary conditions

$$\begin{aligned} U(x,0) &= \max(e^x - E, 0), \quad x \in \overline{\Omega}_x, \\ U(x_{\min},\tau) &= 0, \quad \tau \in \overline{\Omega}_t, \\ U(x_{\max},\tau) &= e^{\max} - Ee^{-\int_0^\tau \widehat{r}(x_{\max},s)ds}, \quad \tau \in \overline{\Omega}_t, \end{aligned}$$

where $\epsilon = \frac{\widehat{\sigma^2}}{2}$, $\alpha = \widehat{r} - \epsilon$ and $r = \widehat{r}$.

7.2.2 Formulation of two-dimensional Black-Scholes model

The two-dimensional B-S model is formed by extending the model problem (7.2.1) as follows:
In general, B-S model with two assets for option pricing is given by

$$\begin{aligned} &\frac{\partial C}{\partial t}(S_1,S_2,t) + \frac{1}{2}\sigma_1^2 S_1^2 \frac{\partial^2 C}{\partial S_1^2}(S_1,S_2,t) + 2\rho\sigma_1\sigma_2 S_1 S_2 \frac{\partial^2 C}{\partial S_1 \partial S_2}(S_1,S_2,t) \\ &+ \frac{1}{2}\sigma_2^2 S_2^2 \frac{\partial^2 C}{\partial S_2^2}(S_1,S_2,t) + r\Big[S_1 \frac{\partial C}{\partial S_1}(S_1,S_2,t) + S_2 \frac{\partial C}{\partial S_2}(S_1,S_2,t)\Big] \\ &- rC(S_1,S_2,t) = 0, \qquad (S_1,S_2,t) \in (0,\infty)\times(0,\infty)\times(0,T), \end{aligned} \tag{7.2.9}$$

with the terminal condition

$$C(S_1,S_2,0) = \max\{\beta_1 S_1 + \beta_2 S_2 - E, 0\},$$

and the boundary conditions

$$C(S_1,S_2,t) = \begin{cases} \beta_1 S_1 + \beta_2 S_2 - Ee^{-r(T-\tau)} & \text{as } \ S_1,\ S_2 \to \infty \\ 0 & \text{as } \ S_1,\ S_2 \to 0, \end{cases}$$

where $C(S_1,S_2,t)$ denotes the value of a call option with underlying asset prices S_1 and S_2 at time $'t'$. Here, $'\sigma_1'$ and $'\sigma_2'$ are the volatilities of the underlying asset prices S_1 and S_2, respectively. $'r'$ is the risk-free interest rate, ρ is correlation value between S_1 and S_2, E is the strike or exercise

price, and β_1, β_2 are the coefficients so that all risky asset prices are at same level.

Now, to reformulate the above model into new problem where independent parameters appear in the coefficients of the equation, we use the following transformations

$$x = \ln(S_1) - \big(r - \frac{1}{2}\sigma_1^2\big)\tau, \quad y = \ln(S_2) - \big(r - \frac{1}{2}\sigma_2^2\big)\tau \text{ and } \tau = T - t. \tag{7.2.10}$$

The dependent variable $C(S_1, S_2, t)$ is transformed into new dependent variable $U(x, y, \tau)$ by using above transformations,

i.e.

$$C(S_1, S_2, t) = U(x, y, \tau).$$

Eq. (7.2.9) can be written as

$$-\frac{\partial U}{\partial \tau} + \frac{\sigma_1^2}{2}\frac{\partial^2 U}{\partial x^2} + \frac{\sigma_2^2}{2}\frac{\partial^2 U}{\partial y^2} + \rho\sigma_1\sigma_2\frac{\partial^2 U}{\partial x \partial y} - rU = 0, \quad (x, y, \tau) \in \mathbb{R} \times \mathbb{R} \times [0, T],$$

which satisfies the terminal condition

$$U(x, y, \tau) = \max\{\beta_1 e^{x+(r-\frac{\sigma_1^2}{2})T} + \beta_2 e^{y+(r-\frac{\sigma_2^2}{2})T} - E, 0\},$$

and boundary conditions

$$C(x, y, \tau) = \begin{cases} \beta_1 e^{x+(r-\frac{\sigma_1^2}{2})\tau} + \beta_2 e^{y+(r-\frac{\sigma_2^2}{2})\tau} - E & \text{as } x,\ y \to \infty \\ 0 & \text{as } x,\ y \to \infty. \end{cases}$$

In the present study, we assume that there is no correlation between the asset prices S_1 and S_2 and hence $\rho = 0$.

Thus, we obtain the following equation

$$LU(x,y,\tau) \equiv \left\{ -\frac{\partial}{\partial \tau} + \frac{\sigma_1^2}{2}\frac{\partial^2}{\partial x^2} + \frac{\sigma_2^2}{2}\frac{\partial^2}{\partial y^2} - r \right\} U(x,y,\tau) = 0,$$
$$(x,y,\tau) \in \mathbb{R} \times \mathbb{R} \times (0,T].$$

Under the conditions $r = \mathcal{O}(1)$ and for σ taking any value from the half-open interval $(0, \sqrt{2r})$, we come to the following initial-value problem which is of singularly perturbed type

$$LU(x,y,\tau) \equiv \left\{ -\frac{\partial}{\partial \tau} + \epsilon_1\frac{\partial^2}{\partial x^2} + \epsilon_2\frac{\partial^2}{\partial y^2} - r \right\} U(x,y,\tau) = 0, \qquad (7.2.11)$$

along with the above mentioned conditions.
Here, $\epsilon_1 = \frac{\sigma_1^2}{2}$, $\epsilon_2 = \frac{\sigma_2^2}{2}$ are dimensionless perturbation parameters and $\epsilon_1, \epsilon_2 \in (0,1]$.

7.3 Formulation and analysis of element-free Galerkin scheme

The weak form of the considered problem (7.2.11) is

$$\Big\langle \frac{\partial U}{\partial t}, \upsilon \Big\rangle + \epsilon_1 \Big\langle \frac{\partial U}{\partial x}, \frac{\partial \upsilon}{\partial x} \Big\rangle + \epsilon_2 \Big\langle \frac{\partial U}{\partial y}, \frac{\partial \upsilon}{\partial y} \Big\rangle + \Big\langle U, \upsilon \Big\rangle = 0, \quad \upsilon \in H^1(\Omega).$$

Now the semi-discrete temporal scheme is given by

$$\Big\langle U^n, \upsilon \Big\rangle + \frac{\epsilon_1}{2}\tau \Big\langle \frac{\partial U^n}{\partial x}, \frac{\partial \upsilon}{\partial x} \Big\rangle + \frac{\epsilon_2}{2}\tau \Big\langle \frac{\partial U^n}{\partial y}, \frac{\partial \upsilon}{\partial y} \Big\rangle + \frac{\tau}{2} \Big\langle U^n, \upsilon \Big\rangle = \Big\langle U^{n-1}, \upsilon \Big\rangle$$
$$- \frac{\epsilon_1}{2}\tau \Big\langle \frac{\partial U^{n-1}}{\partial x}, \frac{\partial \upsilon}{\partial x} \Big\rangle - \frac{\epsilon_2}{2}\tau \Big\langle \frac{\partial U^{n-1}}{\partial y}, \frac{\partial \upsilon}{\partial y} \Big\rangle - \frac{\tau}{2} \Big\langle U^{n-1}, \upsilon \Big\rangle, \qquad (7.3.1)$$

where U^n denote the numerical solution of (7.3.1) at the n^{th} time level.
Now, the stability of the above semi-discrete scheme (7.3.1) can be stated as:

Theorem 7.3.1 *Let $U^n \in H^1(\bar{\Omega})$. The temporal-discrete scheme given by Eq.* (7.3.1) *will be unconditionally stable.*

Proof The proof of the theorem follows on similar lines as outlined in 6.3.4 of Chapter 6.

7.3.1 Convergence of the full-discrete scheme

Let V_h be the finite dimensional subspace of $H^1(\Omega)$. Then the full-discrete scheme is given by

$$\Big\langle U_h^{(n)}, \upsilon_h \Big\rangle + \frac{\epsilon_1}{2}\tau\Big\langle \frac{\partial U_h^{(n)}}{\partial x}, \frac{\partial \upsilon_h}{\partial x} \Big\rangle + \frac{\epsilon_2}{2}\tau\Big\langle \frac{\partial U_h^{(n)}}{\partial y}, \frac{\partial \upsilon_h}{\partial y} \Big\rangle + \frac{\tau}{2}\Big\langle U_h^{(n)}, \upsilon_h \Big\rangle$$
$$= \Big\langle U_h^{(n-1)}, \upsilon_h \Big\rangle - \frac{\epsilon_1}{2}\tau\Big\langle \frac{\partial U_h^{(n-1)}}{\partial x}, \frac{\partial \upsilon_h}{\partial x} \Big\rangle - \frac{\epsilon_2}{2}\tau\Big\langle \frac{\partial U_h^{(n-1)}}{\partial y}, \frac{\partial \upsilon_h}{\partial y} \Big\rangle - \frac{\tau}{2}\Big\langle U_h^{(n-1)}, \upsilon_h \Big\rangle,$$
$$\forall \upsilon_h \in V_h, \tag{7.3.2}$$

where $U_h^{(n)}$ is finite dimensional approximation of $U^{(n)}$.

Theorem 7.3.2 *Let $u^n \in H^1(\Omega)$ be the solution of Eq.* (7.2.11) *and let $U_h^n \in V_h(\Omega)$ be the solution of Eq.* (7.3.2)*. Then, the error in the EFG method can be estimated as*

$$\Big\| u^n - U_h^n \Big\|_{H_w(\Omega)} \leq \mathcal{C}\big(\tau^2 + \mathfrak{d}_{\mathfrak{s}}{}^m\big),$$

where $\mathcal{C}$ is a constant independent of τ and $\mathfrak{d}_{\mathfrak{s}}$.

The theorem can be proved using the similar concepts as followed in Theorem 6.4.3.

7.4 Numerical results and discussions

Example 7.4.1 *To test the proposed EFG scheme, we have considered the following mathematical one-dimensional singularly perturbed B-S model*

problem

$$\begin{aligned} \frac{\partial u}{\partial t} &= \epsilon \frac{\partial^2 u}{\partial x^2} + \alpha \frac{\partial u}{\partial x} + ru + f(x,t), \qquad (7.4.1) \\ u(0,t) &= 0, \quad u(1,t) = 0, \\ u(x,0) &= x^2(1-x), \end{aligned}$$

where $f(x,t) = (2t+2)x^2(1-x) - (t+1)^2\left[\epsilon(2-6x) + \alpha(2x-3x^2) - rx^2(1-x)\right]$. The exact solution is not known in this case.

Numerical experiments have been carried out for the European call option

Table 7.1: Maximum absolute errors for Example 7.4.1 for different values of ϵ at $t = 1.0$.

ϵ	$N = 16$	$N = 32$	$N = 64$
2^{-2}	9.69×10^{-4}	2.40×10^{-4}	6.00×10^{-5}
2^{-4}	2.60×10^{-3}	6.49×10^{-4}	1.02×10^{-4}
2^{-6}	5.37×10^{-3}	1.14×10^{-3}	2.44×10^{-4}
2^{-8}	1.10×10^{-2}	2.56×10^{-3}	7.50×10^{-4}
2^{-10}	1.35×10^{-2}	3.80×10^{-3}	8.23×10^{-4}
2^{-12}	1.36×10^{-2}	3.87×10^{-3}	8.21×10^{-4}

for the parametric values of risk-free interest rate $r = 0.05$, volatility $\sigma = 25\%$, $\epsilon = \sigma^2/2$, $\alpha = (r - \epsilon)$ and time-period $T = 1$. Double mesh-principle has been used to calculate maximum absolute errors presented in Table 7.1. Numerical convergence of the proposed scheme is illustrated from the table. One can notice that the errors are decreasing with the increase in number of nodes. Fig. 7.1 shows the time effect on the solution of the problem for $\epsilon = 2^{-8}$. Fig. 7.2 displays the continuous time-space plot and density plot of the solution for a very small value $\epsilon = 2^{-12}$ of the singular perturbation parameter.

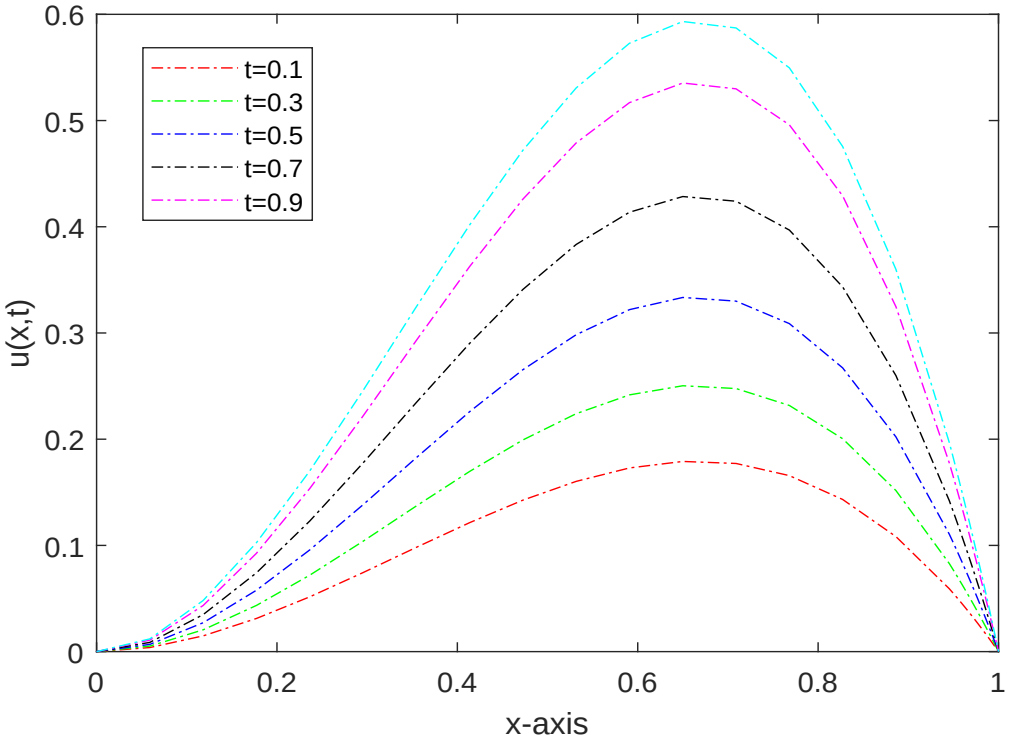

Figure 7.1: Time effect on the EFG solution for $\epsilon = 2^{-8}$, $N = 32$.

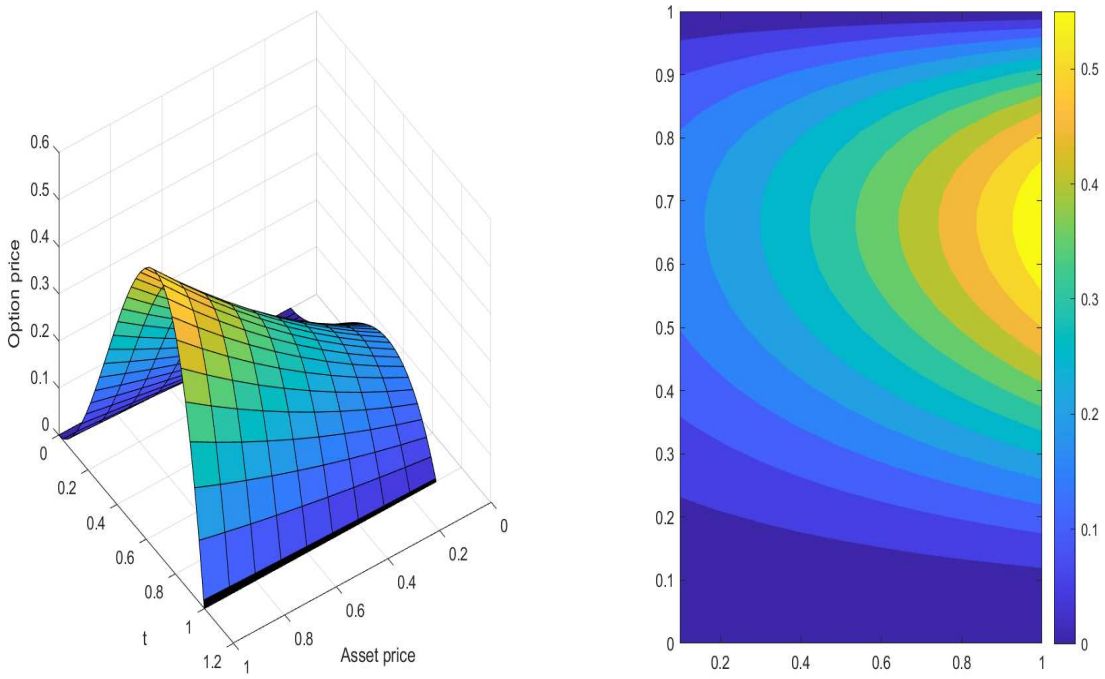

Figure 7.2: EFGM solution and density plot for $\epsilon = 2^{-12}$, $N = 64$ at $t = 0.5$.

Example 7.4.2 *For the second example, we have considered the two-dimensional*

Black-Scholes model given by Eq. (7.2.9) *based on European call option with two assets* S_1 *and* S_2 *over the range of* $0 \leq S_1 \leq 200$ *and* $0 \leq S_2 \leq 200$. *The numerical simulations have been carried out for the financial parameters* $\epsilon_1 = \frac{\sigma_1^2}{2}$, $\epsilon_2 = \frac{\sigma_2^2}{2}$, $T = 1$, $E = 70$, $\beta_1 = 2$, $\beta_2 = 1$ *and* $\rho = 0$. *The numerical tests have been performed for the following cases:*

Case 1. $\sigma_1 = 10\%$, $\sigma_2 = 20\%$, $r = 5\%$.

Case 2. $\sigma_1 = 5\%$, $\sigma_2 = 5\%$, $r = 5\%$.

Case 3. $\sigma_1 = 30\%$, $\sigma_2 = 10\%$, $r = 5\%$.

Where σ_1 *and* σ_2 *represent volatility rates for the assets* S_1 *and* S_2 *respectively.*

Using the transformations given by (7.2.10), the generalized Black-Scholes model is transformed into singularly perturbed Eq. (7.2.11) with the smooth initial condition

$$u(x, y, 0) = \max\{\beta_1 e^{(0.05-\epsilon_1+x)} + e^{(0.05-\epsilon_2+y)} - 70, 0\}.$$

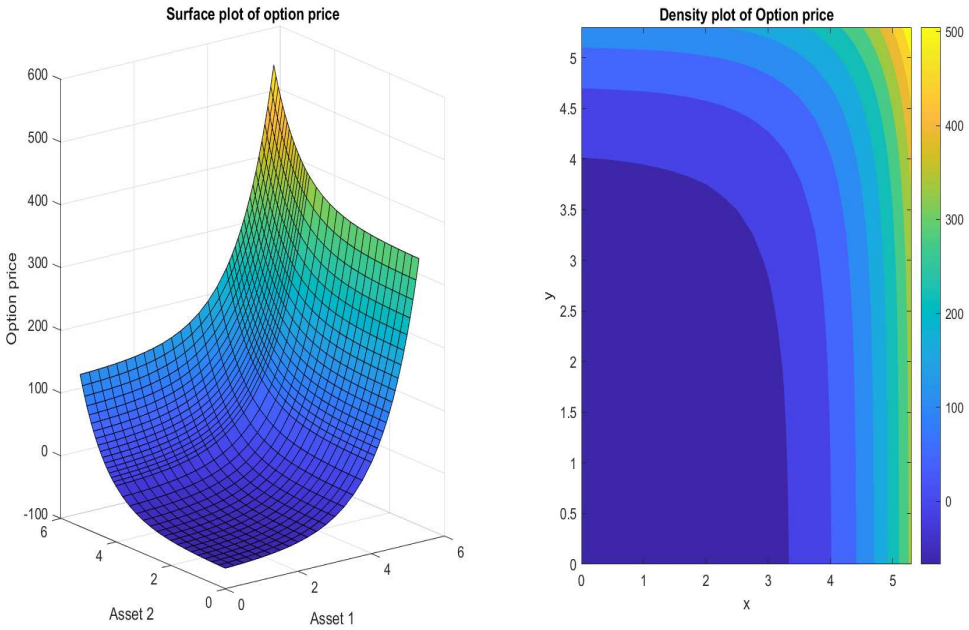

Figure 7.3: EFG solution profile for Example 7.4.2 at time level $t = 1.0$.

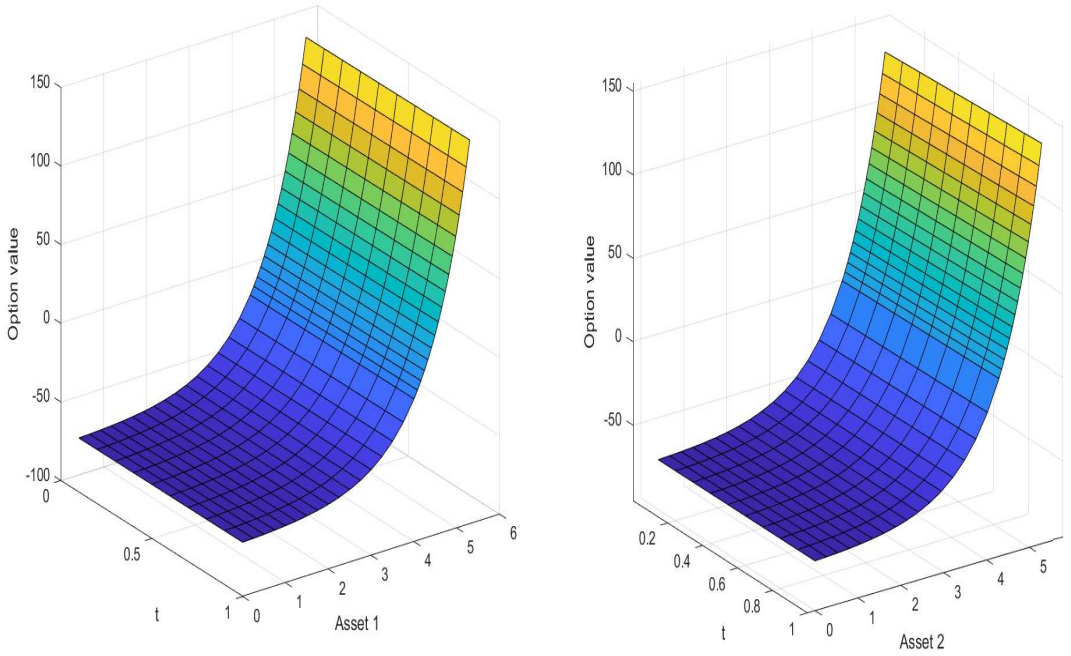

Figure 7.4: EFG solution profile w.r.t. time for asset 1 and asset 2 for Example 7.4.2.

The solution graphs for the problem under consideration are plotted in Figs. 7.3-7.5. In Fig. 7.3, for Case 1, the EFG solution and the density plots of the option price have been presented with respect to the asset prices over the range of $0 \leq x \leq 5.3$ and $0 \leq y \leq 5.3$ by taking 32 number of nodes in each direction. From the graph, we can easily analyze that more nodes have been generated in the region where the solution change is large. Also, we can notice that the option price is high for asset 1 in comparison to asset 2 which describes the physical phenomenon that in the case of low volatility rate, the option price should be high. For Case 2, we have considered the volatility rate to be 5% for both the assets, and hence the option price should increase in the same ratio for both the assets which is clearly describes by the EFG solution plot in Fig. 7.4. The solution has been plotted at time level $t = 0.1$ with $N = 32$ in both the directions.

For Case 3, the volatility rates have been taken as 30% and 10% for the assets S_1 and S_2 respectively. Since the volatility rate is less for asset S_2, the

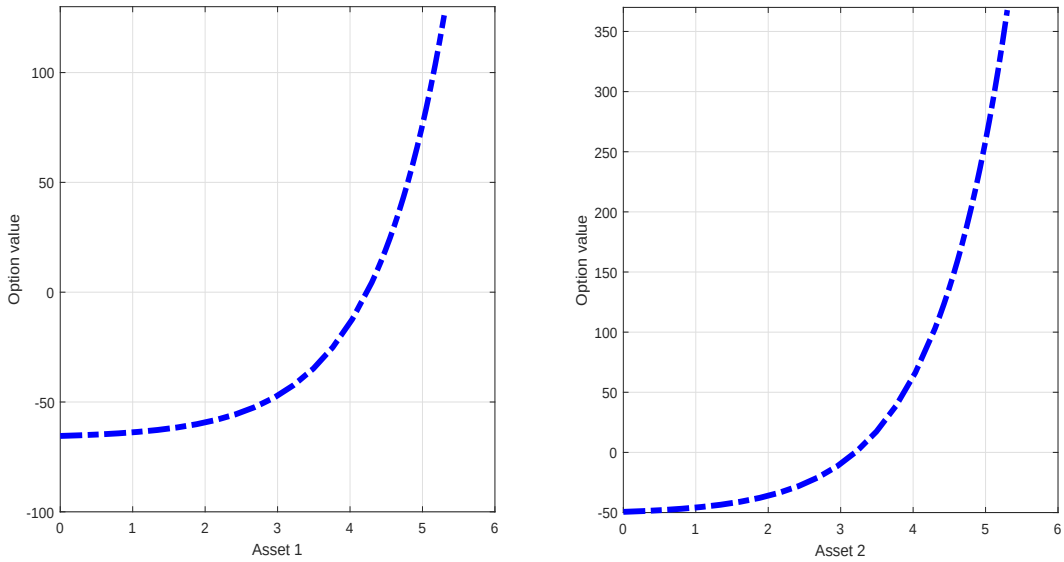

Figure 7.5: European call option value at time level $t = 0.5$ for case 3 of Example 7.4.2.

option price should be high for asset S_2 in comparison to asset S_1. This real phenomenon is clearly portrayed by the EFG solution in Fig. 7.5. In order to give the clear picture, the option price graphs i.e. the solution graphs have been plotted w.r.t. assets 1 and 2 separately by fixing the other one. These fix values have been taken as $y = 0.5$ and $x = 0.5$ respectively in the plots.

7.5 Conclusion

To test the element-free Galerkin method for mathematical models governing real-life phenomenon, very famous Black-Scholes model arising in the field of financial mathematics has been considered in both the one- and two-dimensions. The considered model represents European call option pricing phenomenon by considering the one and two assets for one- and two-dimensions respectively. Firstly the models have been rewritten by considering suitable transformations and then the EFG technique has been applied for spatial discretization together with Crank-Nicolson scheme for temporal discretization. The proposed scheme produces good accurate

results. The EFG results have been compared with the exact ones in one-dimensional case where the solution is known. The error analysis clearly depicts the theoretical and numerical convergence. Numerical results exhibit the expected results. The proposed scheme proves to be robust and reliable.

Conclusion and future scope

The present thesis focuses on proposing a mesh-free technique called element-free Galerkin (EFG) scheme for singularly perturbed problems (SPP). Singularly perturbed problems arise in almost all areas of science and engineering and hence plays an important role in the field of differential equations and are needed to be solved. Since these problems exhibit sharp changes, which are generally called boundary layers, in the solution in a very narrow region of the domain of the problem, standard numerical techniques fail to capture the solution of these problems nicely. Hence we need some special strategies to solve these problems. For the same purpose, EFG approach has been proposed for solving the SPP. The scheme has been applied on both the linear and non-linear SPP in one- and two-dimensions. To start with, the proposed scheme has been applied on one-dimensional time-independent SPP. Since various weight functions exist in the literature for mesh-free methods, a numerical study has been carried out for choosing the best weight function for SPP. It has been concluded that Gaussian exponential splines provide better results in comparison with other weight functions for singular perturbed problems. In order to capture the boundary layers in the solution nicely, density of nodes has been created using Shishkin's approach. Then the proposed EFG scheme has been applied to solve the one-dimensional time-dependent linear and non-linear reaction-diffusion SPP. Crank-Nicolson method has been used for temporal discretization while as for spatial discretization, EFG scheme has been provoked. The proposed EFG technique utilizes moving least-square method to generate basis functions. Since these basis functions do not satisfy the Kronecker delta property, Lagrange multiplier technique has been utilized to enforce the boundary conditions. The existence and uniqueness of the solution of the proposed scheme has also been shown. The stability and convergence of the

proposed scheme has been discussed. The scheme is shown to be second order accurate in time and $\mathfrak{d}_{\mathfrak{s}}{}^{m}$ accurate in space, where the $\mathfrak{d}_{\mathfrak{s}}$ represents the size of the support domain and m is the number of basis functions while representing the EFG solution in the support domain of some node point. The proposed EFG technique has also been applied to solve two real-life model problems. The first model, i.e. Fisher's model commonly occurs in the area of chemical reactions and bio-mathematical fields. In order to handle the non-linearity present in the model, quasilinearization process has been invoked. It comes out that the proposed quasilinearization process converges quadratically. Stability of the scheme has been analyzed and the scheme is shown to be stable. Convergence of the proposed scheme has also been shown. For the second real-life model problem, Burger-Fisher's problem has been considered which governs the wave propagation phenomenon. The stability of the proposed scheme has proven and the convergence of the proposed scheme is shown for the case where the singular perturbation parameter is bounded below. The proposed scheme has been applied to various numerical examples. The proposed EFG scheme provides solutions which are in good agreement with the exact ones and with those cited in the literature. The scheme is shown to be consistent and robust enough to capture even very sharp boundary layers.

The EFG approach has also been proposed for solving time-dependent two-dimensional non-linear SPP. The EFG scheme has been invoked for spatial discretization. The basis functions have been generated using the moving least-square approach and the Lagrange multiplier approach has been exploited to enforce the boundary conditions. Nodes have been created based on Shishkin's approach in order to put more nodes in the boundary layer region. The Crank-Nicolson scheme has been utilized for temporal discretization. The proposed scheme is again shown to be stable. The convergence of the proposed scheme has also been discussed and the scheme is shown to be uniformly convergent. To test the efficiency of the scheme,

the EFG scheme has been applied to solve the one- and two-dimensional Black-Scholes model problems which arise in the field of financial mathematics. The present considered model governs the European call option. The proposed scheme is shown to be stable and uniformly convergent for the considered model problems. Numerical results validate the efficiency and robustness of the EFG scheme.

To conclude, the element-free Galerkin scheme together with the Crank Nicolson scheme has been proposed to solve the one- and two-dimensional time-dependent singularly perturbed reaction-diffusion linear and non-linear problems. The proposed strategy has been applied on numerous one- and two-dimensional non-linear real-life model problems and examples. The proposed scheme turns out to be stable and uniformly convergent overall. The numerical scheme provides reliable and robust results for SPP. The scheme is efficient enough to capture even very sharp boundary layers in both one- and two-dimensions.

For the future work, we plan to extend the proposed scheme for time-dependent three-dimensional non-linear reaction-diffusion SPP. Further, the stability and convergence analysis need to be carried out for the three-dimensional problems. It has been analyzed that the proposed EFG scheme is computationally more expensive specially for higher dimensional problems and hence takes more time to provide the solutions. We plan to work on the parallelization of the proposed scheme so that it can be made time-efficient.

Bibliography

[1] M. J. Ablowitz and A. Zeppetella. Explicit solutions of Fisher's equation for a special wave speed. *Bulletin of Mathematical Biology*, 41(6):835–840, 1979.

[2] K. Al-Khaled. Numerical study of Fisher's reaction–diffusion equation by the sinc collocation method. *Journal of Computational and Applied Mathematics*, 137(2):245–255, 2001.

[3] K. Amin and A. Khanna. Convergence of american option values from discrete-to continuous-time financial models 1. *Mathematical Finance*, 4(4):289–304, 1994.

[4] V. Andreev and N. Kopteva. Pointwise approximation of corner singularities for a singularly perturbed reaction-diffusion equation in an L-shape domain. *Mathematics of computation*, 77(264):2125–2139, 2008.

[5] A. Atangana. On the new fractional derivative and application to nonlinear Fishers reaction–diffusion equation. *Applied Mathematics and Computation*, 273:948–956, 2016.

[6] S. N. Atluri and T. Zhu. A new meshless local Petrov-Galerkin (MLPG) approach in computational mechanics. *Computational mechanics*, 22(2):117–127, 1998.

[7] O. Axelsson and I. Gustafsson. A modified upwind scheme for convective transport equations and the use of a conjugate gradient method for the solution of non-symmetric systems of equations. *IMA Journal of Applied Mathematics*, 23(3):321–337, 1979.

[8] M. Azhari, M. M. Saadatpour, et al. A novel formulation for static and buckling analysis of plates using coupled element free Galerkin-finite strip (EFG-FS). *Applied Mathematical Modelling*, 2019.

[9] I. Babuška. The finite element method with lagrangian multipliers. *Numerische Mathematik*, 20(3):179–192, 1973.

[10] I. Babuška and J. M. Melenk. The partition of unity method. *International Journal for Numerical Methods in Engineering*, 40(4):727–758, 1997.

[11] E. Bahmyari, M. R. Khedmati, and C. G. Soares. Stochastic analysis of moderately thick plates using the generalized polynomial chaos and element free Galerkin method. *Engineering Analysis with Boundary Elements*, 79:23–37, 2017.

[12] L. Balyan, A. Mittal, M. Kumar, and M. Choube. Stability analysis and highly accurate numerical approximation of Fishers equations using pseudospectral method. *Mathematics and Computers in Simulation*, 177:86–104, 2020.

[13] K. Bansal, P. Rai, and K. K. Sharma. Numerical treatment for the class of time dependent singularly perturbed parabolic problems with general shift arguments. *Differential Equations and Dynamical Systems*, 25(2):327–346, 2017.

[14] G. Barles. Convergence of numerical schemes for degenerate parabolic equations arising in finance theory. *Numerical methods in finance*, 13(1):125–143, 1997.

[15] W. Barry and S. Saigal. A three-dimensional element-free Galerkin elastic and elastoplastic formulation. *International Journal for Numerical Methods in Engineering*, 46(5):671–693, 1999.

[16] M. Bastani and D. K. Salkuyeh. A highly accurate method to solve Fishers equation. *Pramana*, 78(3):335–346, 2012.

[17] J. Bear and A. Verruijt. *Modeling groundwater flow and pollution*, volume 2. Springer Science & Business Media, 1987.

[18] S. Behzadi, M. Araghi, et al. Numerical solution for solving Burger's-Fisher eguation by using iterative methods. *Mathematical and Computational Applications*, 16(2):443–455, 2011.

[19] A. Bekir and A. Boz. Exact solutions for nonlinear evolution equations using Exp-function method. *Physics Letters A*, 372(10):1619–1625, 2008.

[20] R. E. Bellman and R. K. Quasilinearization. *Nonlinear Boundary-Value Problems*. American Elsevier Publishing Co., Inc., New York, 1965.

[21] T. Belytschko, Y. Krongauz, D. Organ, M. Fleming, and P. Krysl. Meshless methods: an overview and recent developments. *Computer Methods in Applied Mechanics and Engineering*, 139(1-4):3–47, 1996.

[22] T. Belytschko, P. Krysl, and Y. Krongauz. A three-dimensional explicit element-free Galerkin method. *International Journal for Numerical Methods in Fluids*, 24(12):1253–1270, 1997.

[23] T. Belytschko, Y. Lu, and L. Gu. Element-free Galerkin methods. *International Journal for Numerical Methods in Engineering*, 37(2):229–256, 1994.

[24] T. Belytschko, Y. Lu, and L. Gu. Crack propagation by element-free Galerkin methods. *Engineering Fracture Mechanics*, 51(2):295–315, 1995.

[25] G. D. Birkhoff. On the asymptotic character of the solutions of certain linear differential equations containing a parameter. *Transactions of*

the American Mathematical Society, 9(2):219–231, 1908.

[26] F. Black and M. Scholes. The pricing of options and corporate liabilities. *Journal of Political Economy*, 81(3):637–654, 1973.

[27] M. Bohner and Y. Zheng. On analytical solutions of the black–scholes equation. *Applied Mathematics Letters*, 22(3):309–313, 2009.

[28] P. Bouillard and S. Suleaub. Element-free Galerkin solutions for helmholtz problems: fomulation and numerical assessment of the pollution effect. *Computer Methods in Applied Mechanics and Engineering*, 162(1-4):317–335, 1998.

[29] S. Boyarchenko and S. Z. Levendorskii. *Non-Gaussian Merton-Black-Scholes Theory*, volume 9. World scientific, 2002.

[30] I. Braianov and L. Vulkov. Numerical solution of a reaction-diffusion elliptic interface problem with strong anisotropy. *Computing*, 71(2):153–173, 2003.

[31] T. A. Bullo, G. F. Duressa, and G. A. Degla. Robust finite difference method for singularly perturbed two-parameter parabolic convection-diffusion problems. *International Journal of Computational Methods*, 18(02):2050034, 2021.

[32] V. F. Butuzov and N. N. Nefedov. Space-periodic contrast structures in singularly perturbed elliptic problems. In *Doklady Akademii Nauk*, volume 351, pages 731–734. Russian Academy of Sciences, 1996.

[33] V. F. Butuzov and A. V. Nesterov. Some singularly perturbed problems of hyperbolic type with transition layers. *Differentsial'nye Uravneniya*, 22(10):1739–1744, 1986.

[34] X. Cai, X. Sun, Z. Li, G. Ji, and J. Lu. The element-free Galerkin method for two-dimensional Schrödinger equation. *Procedia Engineering*, 31:1108–1114, 2012.

[35] J. Canosa. Diffusion in nonlinear multiplicative media. *Journal of Mathematical Physics*, 10(10):1862–1868, 1969.

[36] G. Carey and Y. Shen. Least-squares finite element approximation of Fisher's reaction–diffusion equation. *Numerical Methods for Partial Differential Equations*, 11(2):175–186, 1995.

[37] P. Carr and D. Faguet. Fast accurate valuation of american options. In *Journal of finance*, volume 51, pages 1030–1031. AMER FINANCE ASSN 44 WEST FOURTH ST, STE 9-190, NEW YORK, NY 10012, 1996.

[38] M. Chandru, P. Das, and H. Ramos. Numerical treatment of two-parameter singularly perturbed parabolic convection diffusion problems with non-smooth data. *Mathematical Methods in the Applied Sciences*, 41(14):5359–5387, 2018.

[39] M. Chandru, T. Prabha, P. Das, and V. Shanthi. A numerical method for solving boundary and interior layers dominated parabolic problems with discontinuous convection coefficient and source terms. *Differential Equations and Dynamical Systems*, 27(1):91–112, 2019.

[40] K. Chang and F. A. Howes. *Nonlinear singular perturbation phenomena: theory and applications*, volume 56. Springer Science & Business Media, 2012.

[41] H. Cheng, M. Peng, and Y. Cheng. A hybrid improved complex variable element-free Galerkin method for three-dimensional potential problems. *Engineering Analysis with Boundary Elements*, 84:52–62, 2017.

[42] H. Cheng, M. Peng, and Y. Cheng. A hybrid improved complex variable element-free Galerkin method for three-dimensional advection-diffusion problems. *Engineering Analysis with Boundary Elements*, 97:39–54, 2018.

[43] H. Cheng, M. Peng, and Y. Cheng. Analyzing wave propagation problems with the improved complex variable element-free Galerkin method. *Engineering Analysis with Boundary Elements*, 100:80–87, 2019.

[44] Y. Cheng. Meshless methods, 2015.

[45] Y. Cheng, J. Wang, and R. Li. The complex variable element-free Galerkin (CVEFG) method for two-dimensional elastodynamics problems. *International Journal of Applied Mechanics*, 4(04):1250042, 2012.

[46] C. Clavero and J. C. Jorge. An efficient numerical method for singularly perturbed time dependent parabolic 2d convection–diffusion systems. *Journal of Computational and Applied Mathematics*, 354:431–444, 2019.

[47] G. Courtadon. A more accurate finite difference approximation for the valuation of options. *Journal of Financial and Quantitative Analysis*, 17(5):697–703, 1982.

[48] J. C. Cox, S. A. Ross, and M. Rubinstein. Option pricing: A simplified approach. *Journal of financial Economics*, 7(3):229–263, 1979.

[49] I. Dag and O. Ersoy. The exponential cubic B-spline algorithm for Fisher equation. *Chaos, Solitons & Fractals*, 86:101–106, 2016.

[50] P. Das. Comparison of a priori and a posteriori meshes for singularly perturbed nonlinear parameterized problems. *Journal of Computational and Applied Mathematics*, 290:16–25, 2015.

[51] P. Das. A higher order difference method for singularly perturbed parabolic partial differential equations. *Journal of Difference Equations and Applications*, 24(3):452–477, 2018.

[52] P. Das and S. Natesan. Optimal error estimate using mesh equidistribution technique for singularly perturbed system of reaction–diffusion boundary-value problems. *Applied Mathematics and Computation*, 249:265–277, 2014.

[53] P. Das, S. Rana, and H. Ramos. On the approximate solutions of a class of fractional order nonlinear Volterra integro-differential initial value problems and boundary value problems of first kind and their convergence analysis. *Journal of Computational and Applied Mathematics*, 404:113–116, 2022.

[54] I. Debbabi, H. B. Salah, et al. Element-free and improved element-free Galerkin methods for one and two-dimensional potential problems. In *Design and Modeling of Mechanical Systems-II*, pages 201–212. Springer, 2015.

[55] M. Dehghan and M. Abbaszadeh. Analysis of the element free Galerkin (EFG) method for solving fractional cable equation with dirichlet boundary condition. *Applied Numerical Mathematics*, 109:208–234, 2016.

[56] M. Dehghan and M. Abbaszadeh. Error analysis and numerical simulation of magnetohydrodynamics (MHD) equation based on the interpolating element free Galerkin (IEFG) method. *Applied Numerical Mathematics*, 137:252–273, 2019.

[57] M. Dehghan and A. Shokri. A numerical method for solution of the two-dimensional sine-gordon equation using the radial basis functions. *Mathematics and Computers in Simulation*, 79(3):700–715, 2008.

[58] Y. Deng, C. Liu, M. Peng, and Y. Cheng. The interpolating complex variable element-free Galerkin method for temperature field problems. *International Journal of Applied Mechanics*, 7(02):1550017, 2015.

[59] P. Dinesh, M. Behera, P. Ranjith, and N. Muthu. An element-free Galerkin method using vertically integrated multiphase flow model for carbon sequestration. *Computers and Geotechnics*, 105:195–210, 2019.

[60] J. Dolbow and T. Belytschko. An introduction to programming the meshless element free Galerkin method. *Archives of Computational Methods in Engineering*, 5(3):207–241, 1998.

[61] J. Dolbow and T. Belytschko. Numerical integration of the Galerkin weak form in meshfree methods. *Computational Mechanics*, 23(3):219–230, 1999.

[62] C. A. Duarte and J. T. Oden. H-p cloudsan h-p meshless method. *Numerical Methods for Partial Differential Equations: An International Journal*, 12(6):673–705, 1996.

[63] S. R. Dunbar. Traveling waves in diffusive predator–prey equations: periodic orbits and point-to-periodic heteroclinic orbits. *SIAM Journal on Applied Mathematics*, 46(6):1057–1078, 1986.

[64] S. O. Edeki, O. O. Ugbebor, and E. A. Owoloko. Analytical solutions of the black–scholes pricing model for european option valuation via a projected differential transformation method. *Entropy*, 17(11):7510–7521, 2015.

[65] A. Erdélyi. *An expansion procedure for singular perturbations.* 1961.

[66] P. Farrell, A. Hegarty, J. M. Miller, E. O'Riordan, and G. I. Shishkin. *Robust computational techniques for boundary layers.* Chapman and hall/CRC, 2000.

[67] Z. Feng and Y. Li. Complex traveling wave solutions to the Fisher equation. *Physica A: Statistical Mechanics and its Applications*, 366:115–123, 2006.

[68] A. R. Firoozjaee and M. Sahebdel. Element-free Galerkin method for numerical simulation of sediment transport equations on regular and irregular distribution of nodes. *Engineering Analysis with Boundary Elements*, 84:108–116, 2017.

[69] R. A. Fisher. The wave of advance of advantageous genes. *Annals of Eugenics*, 7(4):355–369, 1937.

[70] J. E. Flaherty and W. Mathon. Collocation with polynomial and tension splines for singularly-perturbed boundary value problems. *SIAM Journal on Scientific and Statistical Computing*, 1(2):260–289, 1980.

[71] M. Fleming, Y. Chu, B. Moran, and T. Belytschko. Enriched element-free Galerkin methods for crack tip fields. *International Journal for Numerical Methods in Engineering*, 40(8):1483–1504, 1997.

[72] V. Flyud and V. Tsymbal. Asymptotics of the solution of a mixed problem for a singularly perturbed weakly constrained hyperbolic system. *Ukrainian Mathematical Journal*, 37(4):385–390, 1985.

[73] J. P. Fouque and C. H. Han. Pricing asian options with stochastic volatility. *Quantitative Finance*, 3(5):353–362, 2003.

[74] J. P. Fouque, G. Papanicolaou, R. Sircar, and K. Solna. Multiscale stochastic volatility asymptotics. *Multiscale Modeling & Simulation*, 2(1):22–42, 2003.

[75] J. P. Fouque, G. Papanicolaou, R. Sircar, and K. Solna. Singular perturbations in option pricing. *SIAM Journal on Applied Mathematics*, 63(5):1648–1665, 2003.

[76] L. Frank and W. Wendt. Coercive singular perturbations ii: reduction and convergence. *Journal of Mathematical Analysis and Applications*, 88(2):464–504, 1982.

[77] A. Friedman. *Partial differential equations of parabolic type*. Courier Dover Publications, 2008.

[78] K. O. Friedrichs and W. R. Wasow. Singular perturbations of nonlinear oscillations. *Duke Mathematical Journal*, 13(3):367–381, 1946.

[79] M. Garbey and W. Eckhaus. Quasilinear hyperbolic-hyperbolic singular perturbation problem: Study of shock layer. *Mathematical Methods in the Applied Sciences*, 11(2):237–252, 1989.

[80] F. Geng and S. Qian. Reproducing kernel method for singularly perturbed turning point problems having twin boundary layers. *Applied Mathematics Letters*, 26(10):998–1004, 2013.

[81] F. Geng and S. Qian. Modified reproducing kernel method for singularly perturbed boundary value problems with a delay. *Applied Mathematical Modelling*, 39(18):5592–5597, 2015.

[82] F. A. Ghassabzade, J. S. Nadjafi, and A. R. Soheili. A method based on the meshless approach for singularly perturbed differential-difference equations with boundary layers. *Computational Methods for Differential Equations*, 6(3):295–311, 2018.

[83] P. Gray and S. K. Scott. *Chemical oscillations and instabilities: nonlinear chemical kinetics*. 1990.

[84] S. Hagihara, M. Tsunori, T. Ikeda, and N. Miyazaki. Element-free Galerkin method using directed graph and its application to creep problems. *Computational Mechanics*, 31(6):489–495, 2003.

[85] S. Haq, A. Hussain, and M. Uddin. On the numerical solution of nonlinear Burgers-type equations using meshless method of lines. *Applied Mathematics and Computation*, 218(11):6280–6290, 2012.

[86] A. Hashemian and H. M. Shodja. A meshless approach for solution of Burgers equation. *Journal of Computational and Applied Mathemat-*

ics, 220(1-2):226–239, 2008.

[87] Y. He, H. Yang, and A. J. Deeks. An element-free Galerkin (EFG) scaled boundary method. *Finite Elements in Analysis and Design*, 62:28–36, 2012.

[88] A. F. Hegarty, E. O'Riordan, and M. Stynes. A comparison of uniformly convergent difference schemes for two-dimensional convection-diffusion problems. *Journal of Computational Physics*, 105(1):24–32, 1993.

[89] J. Hull and A. White. *Hull-White on derivatives: a compilation of articles*. Risk Publications, 1996.

[90] A. Ilhan, M. Jonsson, and R. Sircar. Singular perturbations for boundary value problems arising from exotic options. *SIAM Journal on Applied Mathematics*, 64(4):1268–1293, 2004.

[91] E. Infeld and G. Rowlands. *Nonlinear waves, solitons and chaos*. Cambridge university press, 2000.

[92] H. N. Ismail, K. Raslan, and A. A. Abd Rabboh. Adomian decomposition method for Burger's–Huxley and Burger's–Fisher equations. *Applied Mathematics and Computation*, 159(1):291–301, 2004.

[93] E. Jaberzadeh, M. Azhari, and B. Boroomand. Thermal buckling of functionally graded skew and trapezoidal plates with different boundary conditions using the element-free Galerkin method. *European Journal of Mechanics-A/Solids*, 42:18–26, 2013.

[94] M. Javidi. Spectral collocation method for the solution of the generalized Burger–Fisher equation. *Applied Mathematics and Computation*, 174(1):345–352, 2006.

[95] L. Jiang. *Mathematical modeling and methods of option pricing*. World Scientific Publishing Company, 2005.

[96] M. Jonsson and K. R. Sircar. Partial hedging in a stochastic volatility environment. *Mathematical Finance*, 12(4):375–409, 2002.

[97] J. Jorge and B. Bujanda. Numerical methods for evolutionary reaction–diffusion problems with nonlinear reaction terms. *Journal of Computational and Applied Mathematics*, 166(1):167–180, 2004.

[98] Z. Juan, L. Shuyao, and L. Guangyao. The topology optimization design for continuum structures based on the element free Galerkin method. *Engineering Analysis with Boundary Elements*, 34(7):666–672, 2010.

[99] M. K. Kadalbajoo and A. A. Appaji Rao. Parallel discrete invariant embedding algorithm for singular pertubation problems. *International Journal of Computer Mathematics*, 66(1-2):149–161, 1998.

[100] M. K. Kadalbajoo and V. Gupta. A brief survey on numerical methods for solving singularly perturbed problems. *Applied Mathematics and Computation*, 217(8):3641–3716, 2010.

[101] M. K. Kadalbajoo and K. C. Patidar. Numerical solution of singularly perturbed two-point boundary value problems by spline in tension. *Applied Mathematics and Computation*, 131(2-3):299–320, 2002.

[102] M. K. Kadalbajoo and K. C. Patidar. A survey of numerical techniques for solving singularly perturbed ordinary differential equations. *Applied Mathematics and Computation*, 130(2-3):457–510, 2002.

[103] M. K. Kadalbajoo and K. C. Patidar. Singularly perturbed problems in partial differential equations: a survey. *Applied Mathematics and Computation*, 134(2-3):371–429, 2003.

[104] M. K. Kadalbajoo and K. C. Patidar. ε-uniformly convergent fitted mesh finite difference methods for general singular perturbation problems. *Applied Mathematics and Computation*, 179(1):248–266, 2006.

[105] M. K. Kadalbajoo and Y. Reddy. Asymptotic and numerical analysis of singular perturbation problems: A survey. *Applied Mathematics and Computation*, 30(3):223–259, 1989.

[106] M. K. Kadalbajoo, L. P. Tripathi, and P. Arora. A robust nonuniform B-spline collocation method for solving the generalized black–scholes equation. *IMA Journal of Numerical Analysis*, 34(1):252–278, 2014.

[107] M. K. Kadalbajoo, L. P. Tripathi, and A. Kumar. A cubic B-spline collocation method for a numerical solution of the generalized black–scholes equation. *Mathematical and Computer Modelling*, 55(3-4):1483–1505, 2012.

[108] S. Kamin. On elliptic singular perturbation problems with turning points. *SIAM Journal on Mathematical Analysis*, 10(3):447–455, 1979.

[109] J. Kaur and V. Sangwan. Exponentially fitted element-free Galerkin approach for nonlinear singularly perturbed problems. *Journal of Mathematics*, 2021, 2021.

[110] A. Kaushik, V. Kumar, and A. K. Vashishth. An efficient mixed asymptotic-numerical scheme for singularly perturbed convection diffusion problems. *Applied Mathematics and Computation*, 218(17):8645–8658, 2012.

[111] W. G. Kelley. Boundary value problems for pairs of second order equations containing a small parameter. *The Rocky Mountain Journal of Mathematics*, 12(4):655–667, 1982.

[112] M. Khader and K. Saad. A numerical approach for solving the fractional Fisher equation using chebyshev spectral collocation method. *Chaos, Solitons & Fractals*, 110:169–177, 2018.

[113] R. Z. Khasminskii and G. Yin. Asymptotic series for singularly perturbed kolmogorov–fokker–planck equations. *SIAM Journal on Ap-*

plied Mathematics, 56(6):1766–1793, 1996.

[114] R. Z. Khasminskii and G. Yin. Uniform asymptotic expansions for pricing european options. *Applied Mathematics and Optimization*, 52(3):279–296, 2005.

[115] N. Kopteva. Maximum norm error analysis of a 2d singularly perturbed semilinear reaction-diffusion problem. *Mathematics of Computation*, 76(258):631–646, 2007.

[116] H. A. Kramers. Wellenmechanik und halbzahlige quantisierung. *Zeitschrift für Physik*, 39(10):828–840, 1926.

[117] Y. Krongauz and T. Belytschko. Enforcement of essential boundary conditions in meshless approximations using finite elements. *Computer Methods in Applied Mechanics and Engineering*, 131(1-2):133–145, 1996.

[118] B. R. Kumar and S. Kumar. Convergence of three-step Taylor Galerkin finite element scheme based monotone schwarz iterative method for singularly perturbed differential-difference equation. *Numerical Functional Analysis and Optimization*, 36(8):1029–1045, 2015.

[119] D. Kumar. An implicit scheme for singularly perturbed parabolic problem with retarded terms arising in computational neuroscience. *Numerical Methods for Partial Differential Equations*, 34(6):1933–1952, 2018.

[120] D. Kumar and M. K. Kadalbajoo. A parameter-uniform numerical method for time-dependent singularly perturbed differential-difference equations. *Applied Mathematical Modelling*, 35(6):2805–2819, 2011.

[121] K. Kumar, P. C. Podila, P. Das, and H. Ramos. A graded mesh refinement approach for boundary layer originated singularly perturbed

time-delayed parabolic convection diffusion problems. *Mathematical Methods in the Applied Sciences*, 44(16):12332–12350, 2021.

[122] M. Kumar, H. K. Mishra, and P. Singh. A boundary value approach for a class of linear singularly perturbed boundary value problems. *Advances in Engineering Software*, 40(4):298–304, 2009.

[123] S. Kumar and B. R. Kumar. A finite element domain decomposition approximation for a semilinear parabolic singularly perturbed differential equation. *International Journal of Nonlinear Sciences and Numerical Simulation*, 18(1):41–55, 2017.

[124] S. Kumar, B. R. Kumar, and J. T. T. Boonkkamp. Complete flux scheme for elliptic singularly perturbed differential–difference equations. *Mathematics and Computers in Simulation*, 165:255–270, 2019.

[125] S. Kutluay, A. Esen, and I. Dag. Numerical solutions of the Burgers equation by the least-squares quadratic B-spline finite element method. *Journal of Computational and Applied Mathematics*, 167(1):21–33, 2004.

[126] O. A. Ladyzhenskaya. Linear and quasilinear equations of parabolic type. *Translations of mathematical monographs*, 123, 1968.

[127] P. Lancaster and K. Salkauskas. Surfaces generated by moving least squares methods. *Mathematics of Computation*, 37(155):141–158, 1981.

[128] R. E. Langer. On the asymptotic solutions of ordinary differential equations, with an application to the Bessel functions of large order. *Transactions of the American Mathematical Society*, 33(1):23–64, 1931.

[129] N. Levinson. The first boundary value problem for ε δu+ a(x,y)ux+b(x,y)uy+c(x,y)u=d(x,y) for small ε. *Annals of Mathemat-*

ics, pages 428–445, 1950.

[130] J. Li. Quasioptimal uniformly convergent finite element methods for the elliptic boundary layer problem. *Computers & Mathematics with Applications*, 33(10):11–22, 1997.

[131] J. Li and I. M. Navon. Uniformly convergent finite element methods for singularly perturbed elliptic boundary value problems i: reaction-diffusion type. *Computers & Mathematics with Applications*, 35(3):57–70, 1998.

[132] J. Li and I. M. Navon. A global uniformly convergent finite element method for a quasi-linear singularly perturbed elliptic problem. *Computers & Mathematics with Applications*, 38(5-6):197–206, 1999.

[133] S. Li, G. I. Shishkin, and L. P. Shishkina. Approximation of the solution and its derivative for the singularly perturbed black-scholes equation with nonsmooth initial data. *Computational Mathematics and Mathematical Physics*, 47(3):442–462, 2007.

[134] S. Li, L. P. Shishkina, and G. I. Shishkin. Parameter–uniform method for a singularly perturbed parabolic equation modelling the black–scholes equation in the presence of interior and boundary layers, 2006.

[135] X. Li. Three-dimensional complex variable element-free Galerkin method. *Applied Mathematical Modelling*, 63:148–171, 2018.

[136] X. Li, H. Chen, and Y. Wang. Error analysis in sobolev spaces for the improved moving least-square approximation and the improved element-free Galerkin method. *Applied Mathematics and Computation*, 262:56–78, 2015.

[137] X. Li and S. Li. Analyzing the nonlinear p-laplacian problem with the improved element-free Galerkin method. *Engineering Analysis with Boundary Elements*, 2018.

[138] X. Li, S. Zhang, Y. Wang, and H. Chen. Analysis and application of the element-free Galerkin method for nonlinear sine-gordon and generalized sinh-gordon equations. *Computers & Mathematics with Applications*, 71(8):1655–1678, 2016.

[139] T. Linß. Analysis of a fem for a coupled system of singularly perturbed reaction–diffusion equations. *Numerical Algorithms*, 50(3):283–291, 2009.

[140] T. Linß and N. Madden. A finite element analysis of a coupled system of singularly perturbed reaction–diffusion equations. *Applied Mathematics and Computation*, 148(3):869–880, 2004.

[141] F. W. Liu and X. S. Zheng. A uniformly convergent difference scheme for the singular perturbation of a self adjoint elliptic partial differential equation. *Applied Mathematics and Mechanics*, 7(5):495–504, 1986.

[142] S. Liu, Q. Yang, H. Chen, W. Yang, and W. Yan. Application of element free Galerkin method to three dimensional electromagnetic computations. In *Electrical Machines and Systems, 2005. ICEMS 2005. Proceedings of the Eighth International Conference on*, volume 3, pages 2109–2111. IEEE, 2005.

[143] W. K. Liu, S. Jun, and Y. F. Zhang. Reproducing kernel particle methods. *International Journal for Numerical Methods in Fluids*, 20(8-9):1081–1106, 1995.

[144] R. K. Lodhi and H. K. Mishra. Quintic B-spline method for solving second order linear and nonlinear singularly perturbed two-point boundary value problems. *Journal of Computational and Applied Mathematics*, 319:170–187, 2017.

[145] Y. Lu, T. Belytschko, and L. Gu. A new implementation of the element free Galerkin method. *Computer Methods in Applied Mechanics and Engineering*, 113(3-4):397–414, 1994.

[146] Y. Lu, T. Belytschko, and M. Tabbara. Element-free Galerkin method for wave propagation and dynamic fracture. *Computer Methods in Applied Mechanics and Engineering*, 126(1-2):131–153, 1995.

[147] P. K. Maini, D. S. McElwain, and D. Leavesley. Travelling waves in a wound healing assay. *Applied Mathematics Letters*, 17(5):575–580, 2004.

[148] K. A. Makarov. Eigenfunctions of an operator of small diffusion in a boundary layer approximation. In *Doklady Akademii Nauk*, volume 280, pages 337–342. Russian Academy of Sciences, 1985.

[149] P. Mayer and J. Mandel. *The finite ray element method for the Helmholtz equation of scattering: first numerical experiments*. University of Colorado at Denver, Center for Computational Mathematics Denver, 1997.

[150] J. M. Melenk and I. Babuška. The partition of unity finite element method: basic theory and applications. *Computer Methods in Applied Mechanics and Engineering*, 139(1-4):289–314, 1996.

[151] J. M. Melenk and C. Schwab. A numerical approach to the testing of the fission hypothesis. *The Astronomical Journal*, 82:1013–1024, 1977.

[152] J. M. Melenk and C. Schwab. Analytic regularity for a singularly perturbed problem. *SIAM Journal on Mathematical Analysis*, 30(2):379–400, 1999.

[153] J. J. Miller, E. O'riordan, and G. I. Shishkin. *Fitted numerical methods for singular perturbation problems: error estimates in the maximum norm for linear problems in one and two dimensions*. World scientific, 1996.

[154] R. Mittal and R. Jiwari. Numerical study of Fishers equation by using

differential quadrature method. *International Journal of Information and Systems Science*, 5(1):143–160, 2009.

[155] R. Mohammadi. Spline solution of the generalized Burgers'-Fisher equation. *Applicable Analysis*, 91(12):2189–2215, 2012.

[156] V. Mohammadi and M. Dehghan. Simulation of the phase field cahn–hilliard and tumor growth models via a numerical scheme: Element-free Galerkin method. *Computer Methods in Applied Mechanics and Engineering*, 345:919–950, 2019.

[157] T. Most. A natural neighbour-based moving least-squares approach for the element-free Galerkin method. *International Journal for Numerical Methods in Engineering*, 71(2):224–252, 2007.

[158] H. Mousavi, M. Azhari, and M. M. Saadatpour. A novel formulation for static and buckling analysis of plates using coupled element free Galerkin-finite strip (EFG-FS). *Applied Mathematical Modelling*, 70:264–284, 2019.

[159] N. Muthu, S. Maiti, W. Yan, and B. Falzon. Modelling interacting cracks through a level set using the element-free Galerkin method. *International Journal of Mechanical Sciences*, 134:203–215, 2017.

[160] J. S. Nadjafi and F. A. Ghassabzade. The numerical solution of the singularly perturbed differential-difference equations based on the meshless method. *International Journal of Applied Mathematics Research*, 3(2):116–121, 2014.

[161] A. H. Nayfeh. *Introduction to perturbation techniques*. John Wiley & Sons, 2011.

[162] B. Nayroles, G. Touzot, and P. Villon. Generalizing the finite element method: diffuse approximation and diffuse elements. *Computational Mechanics*, 10(5):307–318, 1992.

[163] K. Niijima. On a difference scheme of exponential type for a nonlinear singular perturbation problem. *Numerische Mathematik*, 46(4):521–539, 1985.

[164] D. Olmos and B. D. Shizgal. A pseudospectral method of solution of Fisher's equation. *Journal of Computational and Applied Mathematics*, 193(1):219–242, 2006.

[165] S. Orszag and C. M. Bender. *Advanced mathematical methods for scientists and engineers*. McGraw-Hill New York, 1978.

[166] E. Ortiz, A. Pham-Ngoc-Dinh, and W. Törnig. An error analysis of the tau method for a class of singularly perturbed problems for differential equations. *Mathematical Methods in the Applied Sciences*, 6(1):457–466, 1984.

[167] T. Öziş, E. Aksan, and A. Özdeş. A finite element approach for solution of Burgers equation. *Applied Mathematics and Computation*, 139(2-3):417–428, 2003.

[168] X. Pan and H. Yuan. Computational algorithms and applications of element-free Galerkin methods for nonlocal damage models. *Engineering Fracture Mechanics*, 77(14):2640–2653, 2010.

[169] T. Pannachet, S. Triyotee, and M. Boonpichetvong. Numerical instability in the element-free Galerkin method for bi-material modeling. *Applied and Computational Mechanics*, 12(2):159–174, 2018.

[170] M. Pant, I. Singh, and B. Mishra. A novel enrichment criterion for modeling kinked cracks using element free Galerkin method. *International Journal of Mechanical Sciences*, 68:140–149, 2013.

[171] Y. C. Park and D. I. Leap. Modeling groundwater flow by the element-free Galerkin (EFG) method. *Geosciences Journal*, 4(3):231–241, 2000.

[172] S. Parthiban, S. Valarmathi, and V. Franklin. A numerical method to solve singularly perturbed linear parabolic second order delay differential equation of reaction-diffusion type. *Malaya Journal of Matematik*, 2:412–420, 2015.

[173] C. E. Pearson. On a differential equation of boundary layer type. *Journal of Mathematics and Physics*, 47(1-4):134–154, 1968.

[174] C. E. Pearson. On non-linear ordinary differential equations of boundary layer type. *Journal of Mathematics and Physics*, 47(1-4):351–358, 1968.

[175] M. Peng, D. Li, and Y. Cheng. The complex variable element-free Galerkin (CVEFG) method for elasto-plasticity problems. *Engineering Structures*, 33(1):127–135, 2011.

[176] L. Prandtl. Über flüssigkeitsbewegung bei sehr kleiner reibung. iii internationalen mathematiker-kongresses. *Heidelberg, Germany*, 1904.

[177] M. H. Protter and H. F. Weinberger. *Maximum principles in differential equations*. Springer Science & Business Media, 2012.

[178] J. Pudykiewicz. Simulation of the chernobyl dispersion with a 3-d hemispheric tracer model. *Tellus B*, 41(4):391–412, 1989.

[179] A. Quarteroni and A. Valli. *Numerical approximation of partial differential equations*, volume 23. Springer Science & Business Media, 2008.

[180] S. Rana and P. Das. Theoretical prospects of the solutions of fractional order weakly singular Volterra integro differential equations and their approximations with convergence analysis. *Authorea Preprints*, 2020.

[181] Y. Reddy and P. P. Chakravarthy. Method of reduction of order for solving singularly perturbed two-point boundary value problems. *Applied Mathematics and Computation*, 136(1):27–45, 2003.

[182] R. J. Rendleman. Two-state option pricing. *The Journal of Finance*, 34(5):1093–1110, 1979.

[183] H. G. Roos, M. Stynes, and L. Tobiska. *Robust numerical methods for singularly perturbed differential equations: convection-diffusion-reaction and flow problems*, volume 24. Springer Science & Business Media, 2008.

[184] W. V. Roosbroeck. Theory of flow of electrons and holes in germanium and other semiconductors. *Bell Systems Technical Journal*, 29:560–607, 1950.

[185] M. Rosa, S. Chulián, M. Gandarias, and R. Traciná. Application of lie point symmetries to the resolution of an interface problem in a generalized fisher equation. *Physica D: Nonlinear Phenomena*, 405:132411, 2020.

[186] M. Sakai and R. A. Usmani. On exponential splines. *Journal of Approximation Theory*, 47(2):122–131, 1986.

[187] A. A. Samarskii. *The theory of difference schemes*. CRC Press, 2001.

[188] S. Samimi and A. Pak. Three-dimensional simulation of fully coupled hydro-mechanical behavior of saturated porous media using element free Galerkin (EFG) method. *Computers and Geotechnics*, 46:75–83, 2012.

[189] V. Sangwan and B. Kaur. An exponentially fitted numerical technique for singularly perturbed Burgers-Fisher equation on a layer adapted mesh. *International Journal of Computer Mathematics*, 96(7):1502–1513, 2019.

[190] V. Sangwan and B. V. R. Kumar. Finite element analysis for mass-lumped three-step Taylor Galerkin method for time dependent singu-

larly perturbed problems with exponentially fitted splines. *Numerical Functional Analysis and Optimization*, 33(6):638–660, 2012.

[191] M. Sari, G. Gürarslan, and İ. Dağ. A compact finite difference method for the solution of the generalized Burgers–Fisher equation. *Numerical Methods for Partial Differential Equations: An International Journal*, 26(1):125–134, 2010.

[192] R. Seydel. Finite differences and standard options. In *Tools for Computational Finance*, pages 109–150. Springer, 2004.

[193] D. Shakti, J. Mohapatra, P. Das, and J. Vigo-Aguiar. A moving mesh refinement based optimal accurate uniformly convergent computational method for a parabolic system of boundary layer originated reaction–diffusion problems with arbitrary small diffusion terms. *Journal of Computational and Applied Mathematics*, 404:113167, 2022.

[194] R. Sharma. Effect of viscous dissipation and heat source on unsteady boundary layer flow and heat transfer past a stretching surface embedded in a porous medium using element free Galerkin method. *Applied Mathematics and Computation*, 219(3):976–987, 2012.

[195] R. Sharma. Element free Galerkin modeling of radiative hydromagnetic micropolar flow saturated darcy medium with heat transfer over a stretching sheet with Joule heating. *Asia-Pacific Journal of Chemical Engineering*, 9(1):50–62, 2014.

[196] R. Sharma, R. Bhargava, and I. Singh. Combined effect of magnetic field and heat absorption on unsteady free convection and heat transfer flow in a micropolar fluid past a semi-infinite moving plate with viscous dissipation using element free Galerkin method. *Applied Mathematics and Computation*, 217(1):308–321, 2010.

[197] T. Shibata and A. Murakami. A stabilization procedure for soil-water coupled problems using the element-free Galerkin method. *Computers and Geotechnics*, 38(5):585–597, 2011.

[198] G. I. Shishkin. A method of improving the accuracy of the solution of difference schemes for parabolic equations with a small parameter in the highest derivative. *USSR Computational Mathematics and Mathematical Physics*, 24(3):150–157, 1984.

[199] G. I. Shishkin. Solution of a boundary value problem for an elliptic equation with small parameter multiplying the highest derivatives. *Zhurnal Vychislitel'noi Matematiki i Matematicheskoi Fiziki*, 26(7):1019–1031, 1986.

[200] G. I. Shishkin. A difference scheme for a singularly perturbed equation of parabolic type with discontinuous boundary conditions. *USSR Computational Mathematics and Mathematical Physics*, 28(6):32–41, 1988.

[201] G. I. Shishkin. Approximation of the solutions of singularly perturbed boundary-value problems with a parabolic boundary layer. *USSR Computational Mathematics and Mathematical Physics*, 29(4):1–10, 1989.

[202] G. I. Shishkin. Grid approximations of singularly perturbed systems for parabolic convection-diffusion equations with counterflow. 1(3):281–297, 1998.

[203] A. Singh, I. V. Singh, and R. Prakash. Meshless element free Galerkin method for unsteady nonlinear heat transfer problems. *International Journal of Heat and Mass Transfer*, 50(5-6):1212–1219, 2007.

[204] I. Singh. Meshless EFG method in three-dimensional heat transfer problems: a numerical comparison, cost and error analysis. *Numerical Heat Transfer, Part A*, 46(2):199–220, 2004.

[205] I. Singh. Heat transfer analysis of composite slabs using meshless element free Galerkin method. *Computational Mechanics*, 38(6):521–532, 2006.

[206] I. Singh, M. Tanaka, and M. Endo. Thermal analysis of cnt-based nano-composites by element free Galerkin method. *Computational Mechanics*, 39(6):719–728, 2007.

[207] M. K. Singh and S. Natesan. Numerical solution of 2d singularly perturbed reaction–diffusion system with multiple scales. *Computers & Mathematics with Applications*, 80(4):36–53, 2020.

[208] M. K. Singh, G. Singh, and S. Natesan. A unified study on superconvergence analysis of Glerkin FEM for singularly perturbed systems of multiscale nature. *Journal of Applied Mathematics and Computing*, 66(1):221–243, 2021.

[209] R. Sircar and T. Zariphopoulou. Bounds and asymptotic approximations for utility prices when volatility is random. *SIAM Journal on Control and Optimization*, 43(4):1328–1353, 2004.

[210] F. Sun and J. Wang. Interpolating element-free Galerkin method for the regularized long wave equation and its error analysis. *Applied Mathematics and Computation*, 315:54–69, 2017.

[211] F. Sun, J. Wang, and Y. Cheng. An improved interpolating element-free Galerkin method for elastoplasticity via nonsingular weight functions. *International Journal of Applied Mechanics*, 8(08):1650096, 2016.

[212] F. Sun, J. Wang, Y. Cheng, and A. Huang. Error estimates for the interpolating moving least-squares method in n-dimensional space. *Applied Numerical Mathematics*, 98:79–105, 2015.

[213] H. Talebi, M. Froend, and B. Klusemann. Application of adaptive

element-free Galerkin method to simulate friction stir welding of aluminum. *Procedia Engineering*, 207:580–585, 2017.

[214] S. Tang and R. Weber. Numerical study of Fisher's equation by a Petrov-Galerkin finite element method. *The ANZIAM Journal*, 33(1):27–38, 1991.

[215] D. Tavella and C. Randall. *Pricing financial instruments: The finite difference method*, volume 13. John Wiley & Sons, 2000.

[216] K. Trachoo, W. Sawangtong, and P. Sawangtong. Laplace transform homotopy perturbation method for the two dimensional Black-Scholes model with European call option. *Mathematical and Computational Applications*, 22(1):23, 2017.

[217] J. J. Tyson and P. K. Brazhnik. On traveling wave solutions of Fisher's equation in two spatial dimensions. *SIAM Journal on Applied Mathematics*, 60(2):371–391, 2000.

[218] M. Uzunca, B. Karasözen, and T. Küçükseyhan. Moving mesh discontinuous Galerkin methods for pdes with traveling waves. *Applied Mathematics and Computation*, 292:9–18, 2017.

[219] C. Vázquez. An upwind numerical approach for an american and european option pricing model. *Applied Mathematics and Computation*, 97(2-3):273–286, 1998.

[220] X. Wang. Exact and explicit solitary wave solutions for the generalised Fisher equation. *Physics letters A*, 131(4-5):277–279, 1988.

[221] X. Wang, J. Ouyang, B. Yang, J. Ren, and T. Jiang. Simulating free surface flow problems using hybrid particle element free Galerkin method. *Engineering Analysis with Boundary Elements*, 36(3):372–384, 2012.

[222] I. Wasim, M. Abbas, and M. Amin. Hybrid -spline collocation method for solving the generalized Burgers-Fisher and Burgers-huxley equations. *Mathematical Problems in Engineering*, 2018, 2018.

[223] W. Wasow. *Asymptotic expansions for ordinary differential equations*. Courier Dover Publications, 1965.

[224] A. M. Wazwaz and A. Gorguis. An analytic study of Fisher's equation by using adomian decomposition method. *Applied Mathematics and Computation*, 154(3):609–620, 2004.

[225] G. Wentzel. Eine verallgemeinerung der quantenbedingungen für die zwecke der wellenmechanik. *Zeitschrift für Physik*, 38(6):518–529, 1926.

[226] P. Wilmott, J. Dewynne, and S. Howison. Option pricing: mathematical models and computation, 1993.

[227] H. Y. Wong and Y. L. Cheung. Geometric asian options: valuation and calibration with stochastic volatility. *Quantitative Finance*, 4(3):301–314, 2004.

[228] C. P. Wu, K. H. Chiu, and Y. M. Wang. RMVT-based meshless collocation and element-free Galerkin methods for the quasi-3D analysis of multilayered composite and FGM plates. *Composite Structures*, 93(2):923–943, 2011.

[229] O. P. Yadav and R. Jiwari. Finite element analysis and approximation of Burgers-Fisher equation. *Numerical Methods for Partial Differential Equations*, 33(5):1652–1677, 2017.

[230] H. Yang and Y. He. Solving heat transfer problems with phase change via smoothed effective heat capacity and element-free Galerkin methods. *International Communications in Heat and Mass Transfer*, 37(4):385–392, 2010.

[231] X. h. Yuan. A well-balanced element-free Galerkin method for the nonlinear shallow water equations. *Applied Mathematics and Computation*, 331:46–53, 2018.

[232] J. P. Zhang, S. S. Wang, S. G. Gong, Q. S. Zuo, and H. Y. Hu. Thermo-mechanical coupling analysis of the orthotropic structures by using element-free Galerkin method. *Engineering Analysis with Boundary Elements*, 101:198–213, 2019.

[233] J. P. Zhang, G. Q. Zhou, S. G. Gong, and S. S. Wang. Transient heat transfer analysis of anisotropic material by using element-free Galerkin method. *International Communications in Heat and Mass Transfer*, 84:134–143, 2017.

[234] J. P. Zhang, G. Q. Zhou, S. G. Gong, S. S. Wang, and S. Hu. Steady heat transfer analysis of orthotropic structure based on element-free Galerkin method. *International Journal of Thermal Sciences*, 121:163–181, 2017.

[235] L. W. Zhang, Y. J. Deng, and K. M. Liew. An improved element-free Galerkin method for numerical modeling of the biological population problems. *Engineering Analysis with Boundary Elements*, 40:181–188, 2014.

[236] L. W. Zhang, Y. J. Deng, K. M. Liew, and Y. M. Cheng. The improved complex variable element-free Galerkin method for two-dimensional Schrödinger equation. *Computers & Mathematics with Applications*, 68(10):1093–1106, 2014.

[237] L. W. Zhang, D. M. Li, and K. M. Liew. An element-free computational framework for elastodynamic problems based on the IMLS-Ritz method. *Engineering Analysis with Boundary Elements*, 54:39–46, 2015.

[238] P. Zhang, X. Zhang, J. Deng, and L. Song. A numerical study of natural convection in an inclined square enclosure with an elliptic cylinder using variational multiscale element free Galerkin method. *International Journal of Heat and Mass Transfer*, 99:721–737, 2016.

[239] R. P. Zhang, X. J. Yu, and G. Z. Zhao. A direct discontinuous Galerkin method for nonlinear Schrödinger equation. *Chinese Journal of Computational Physics*, 29, 2012.

[240] T. Zhang and X. Li. Meshless analysis of darcy flow with a variational multiscale interpolating element-free Galerkin method. *Engineering Analysis with Boundary Elements*, 2017.

[241] T. Zhang and X. Li. A generalized element-free Galerkin method for stokes problem. *Computers & Mathematics with Applications*, 75(9):3127–3138, 2018.

[242] X. H. Zhang, J. Ouyang, and L. Zhang. Element-free characteristic Galerkin method for Burgers equation. *Engineering Analysis with Boundary Elements*, 33(3):356–362, 2009.

[243] Z. Zhang, S. Y. Hao, K. M. Liew, and Y. M. Cheng. The improved element-free Galerkin method for two-dimensional elastodynamics problems. *Engineering Analysis with Boundary Elements*, 37(12):1576–1584, 2013.

[244] Z. Zhang, K. M. Liew, Y. Cheng, and Y. Y. Lee. Analyzing 2D fracture problems with the improved element-free Galerkin method. *Engineering Analysis with Boundary Elements*, 32(3):241–250, 2008.

[245] T. Zhou and Y. Song. Three-dimensional nonlinear bending analysis of FG-CNTs reinforced composite plates using the element-free Galerkin method based on the SR decomposition theorem. *Composite Structures*, 207:519–530, 2019.

[246] C. G. Zhu and W. S. Kang. Numerical solution of Burgers–Fisher equation by cubic B-spline quasi-interpolation. *Applied Mathematics and Computation*, 216(9):2679–2686, 2010.

[247] T. Zhu and S. Atluri. A modified collocation method and a penalty formulation for enforcing the essential boundary conditions in the element free Galerkin method. *Computational Mechanics*, 21(3):211–222, 1998.

[248] X. Zhuang, C. Heaney, and C. Augarde. On error control in the element-free Galerkin method. *Engineering Analysis with Boundary Elements*, 36(3):351–360, 2012.